Spectroscopic Studies For State-To-State Reaction Dynamics

G. Maitland

The University of Edinburgh

Abstract

A series of experiments was undertaken to establish the spectroscopic basis of subsequent dynamical studies of elementary bimolecular reactions in the gas phase, in which laser methods are used both for the preparation of reagents and the state-specific detection of products.

An apparatus was constructed which allowed gas phase molecules to be detected spectroscopically at very low densities in a state-specific fashion by either laser-induced fluorescence (LIF) or resonance-enhanced multiphoton ionization (REMPI). In REMPI experiments, further species discrimination was achieved by time-of-flight detection of the ions produced.

The [2+1] REMPI spectroscopy of HCl was thoroughly investigated to determine which transitions would be suitable for the measurement of potential ground state rovibrational populations and any spatial anisotropy of the rotational vectors of the nascent HCl produced in a chemical process. The observed linestrengths and polarization properties of the various bands were compared with rigorous theoretical predictions. Certain vibronic bands of the $V^1\Sigma^+(0^+)$-$X^1\Sigma^+(0^+)$ system were found to be sufficiently unperturbed to be suitable candidates for population studies. The $F^1\Delta_2(2)$-$X^1\Sigma^+(0^+)$ system, although subject to minor irregularities in observed linestrengths, could be used for both population and anisotropy measurements.

An attempt was made to investigate the dynamics of reactions of the type $Cl(^2P)$ + HX (where X=Br, I) by combining REMPI detection of the products with laser photolytic production of the $Cl(^2P)$ atoms. It was successfully demonstrated, by direct REMPI detection, that $Cl(^2P)$ atoms were produced with an anisotropic spatial distribution. Due to heterogeneous reactions occurring on the surfaces of the inlets necessary to introduce the reagent precursor gases, it was, however, not possible to unambiguously identify any nascent HCl product molecules.

Some preliminary measurements were also made of coherent anti-Stokes Raman spectroscopy (CARS) of HCl, with the intention of establishing the viability of the intimately related stimulated Raman pumping process for the state-selective preparation of molecular reagents in dynamical studies. In particular, the polarization properties of different spectroscopic branches were examined, allowing the feasibility of the preparation of a spatially anisotropic sample to be assessed.

Acknowledgements

There are many people who deserve my thanks and acknowledgements for their contribution to this work. Firstly, I must thank the SERC for the award of a postgraduate studentship and for their funding of the project. I also thank my supervisor, Dr. Kenneth McKendrick, for his enthusiasm throughout the project, his great attention to detail and seemingly never-ending supply of ideas.

Running these experiments alone would have been impossible and I was fortunate to work with a fellow student, Allister Watson, who made the experiments more manageable.

I would also like to thank the people who have patiently supported and encouraged me during the course of this work.

Declaration

I declare that this thesis has been composed by me and that the work described in it is my own, except where due acknowledgement is made, and was carried out at The University of Edinburgh.

Signed :

Date :

Table of Contents

List of Figures

List of Tables

Chapter 1

Introduction

The long term aim of the work presented in this thesis was the fully state-to-state study of the dynamics of reactions between atoms and diatomic molecules with the investigation of the effects of relative translational energy of the reagent and internal state of the molecular reagent on the product species. In addition a study of the correlation between the collision velocity vector and product rotational alignment was to be performed. The progress which has been made towards this ultimate objective is described in several stages.

Chapters 2 and 3 cover the apparatus used and the design and development of the computer-based data acquisition system. Chapter 4 is concerned with the two-photon rotational line strengths required for the calculation of the angular momentum multipole moments, with chapter 5 being a spectroscopic study of the two-photon REMPI of the chosen product molecule, HCl. Following this, chapter 6 details the bimolecular reactions selected for study and the experiments performed. Finally chapter 7.1 reports some preliminary measurements of CARS spectroscopy related to the production of state and polarization selected diatomic reagents.

The field of reaction dynamics essentially grew out of the study of kinetics. Initial work in kinetics is of profound significance and furthered the understanding of chemical reactions a great deal. The importance of reaction dynamics is that it greatly supplements and enriches the work on macroscopic aspects of kinetics. The disadvantage of macroscopic kinetic investigations is that the reactant

molecules are present in a range of energy states, so that one gains only indirect information about the individual molecular events that occur during a chemical reaction. Statistical treatments have been applied to understand the behavior of bulk systems, and such methods are essential to an understanding of how chemical change occurs under thermalized conditions. Over recent years these studies have been greatly assisted by both experimental and theoretical investigations in reaction dynamics.

There are two main justifications for performing dynamical studies. Firstly, the validity of some of the results from macroscopic kinetic theory, such as transition state theory, have been called into question [1,2,3,4,5,6,7]. Experimental and theoretical studies in reaction dynamics provide an alternative approach to the problem. A second reason is that there are many applications where it is important to have information about the precise quantum states of reactant and product molecules, such as laser gain media ,plasmas, and rarified environments such as the upper atmosphere and interstellar gas clouds where there are insufficient collisions to efficiently thermalize the nascent distribution of energies in species produced in chemical processes.

It was recognized that information on all of the features of a chemical reaction was given by the associated potential energy surface (PES) in conjunction with some method of calculating the trajectories on the PES of interest. Using these techniques, properties such as rate constants at extreme temperatures which would be very difficult to measure experimentally could be calculated in a relatively straight forward manner. The earliest work in this field was that of London, Eyring and Polanyi [8] who calculated the PES for the $H+H_2$ reaction with the first dynamical computations being carried out by Hirschfeld *et al.* [9]. These early computations were on a point-to-point basis and involved a great deal of laborious manual calculation. The first calculations using digital computers were those by Wall and his coworkers [10,11] for the $H+H_2$ system. It was this work which gave reaction dynamics its theoretical base. Not until the advent of high vacuum technology and lasers, however, did experimental reaction dynamics mature as a field in its own right and modern reaction dynamics has reached a stage where it

is possible to compare theoretical and experimental predictions on a regular basis, e.g for the H+D_2 [12,13,14,15,16,17,18] and Ba+HI [19,20] reactions.

1.1 Experimental Approaches to Reaction Dynamics

Throughout the short history of reaction dynamics there have been two schools of experimental work which have in very recent times merged to a large extent such that the distinctions are blurred. The first of these involves the molecular beam experiments which originate from the pioneering work done by Stern and Gerlach in the late 1920's and early 1930's [21]. These experiments use high vacuum technology and at least one, or ideally two crossed, molecular beams of the two reagent species of interest. In those experiments using only one molecular beam, bimolecular reaction studies are carried out using beam-gas techniques where a molecular beam of one reagent is passed through a bulk gas containing the second reagent species. The scattered products are generally measured by particle flux detectors. The second type of experiment is optically based. In the original experiments of this type the electromagnetic emissions (usually in the UV-visible or infra-red regions) of the product species formed in the reaction were measured as a function of various experimental parameters. The advent of lasers made it possible to use detection techniques such as laser-induced-fluorescence (LIF) in which a signal is actively excited from molecules not necessarily produced in an excited state, increasing the number of reactions which could be studied. Lasers can also be employed to optically pump one or more of the reagents into well defined states prior to the reaction. In addition, reagents prepared in this way will, in general, be aligned with respect to the lab frame and in certain cases [22,23,24] the use of static multipole fields can preserve this alignment right up to the point at which the reaction takes place. Very recently ion-imaging techniques have been used [25, 26,27] where the three dimensional product velocity distribution is projected onto a two dimensional position sensitive detector. Modern reaction dynamics exper-

iments frequently exploit the benifits of both techniques using molecular beam scattering with laser based detection systems. The experiments described in the present work are optically based although time-of-flight detection techniques are also employed, and in fact, in the current development of the apparatus molecular beam valves are being incorporated for the introduction of reagent molecules.

1.1.1 Molecular Beam Approach

The first identifiably *chemical* molecular beam experiment was that of Rice *et al.* [28] who in 1928 studied the decomposition of nitrogen pentoxide in a narrow beam so as to reduce the effect of collisions. The first bimolecular reaction to be investigated was that between Cs and CCl_4 by Bull and Moon [29]. Shortly afterward, Taylor and Datz [30] and Greene, Roberts and Ross [31] carried out a detailed analysis of the K+HBr reaction. Since then a great deal of both crossed-beam and beam-gas experiments have been performed pricipally built around the work of Lee [32,33,34], Bernstein [35,36,37], Herschbach [38,39,40] etc. and concentrating largely on the reactions of alkali metals with the methly-halides. The principal advantages of molecular beam experiments are that it is relatively easy to measure the angular dependence of the scattering as well as the dependence of the reaction cross-section on collision velocity. In this type of experiment the recoil velocities of the products are measured with the time-of-flight resolution normally only being sufficient to obtain product vibrational state information, and only in certain cases, e.g. $F+H_2$ [33] and $F+D_2$ [34], can information on the product rotational state distribution be obtained. In some cases it is possible to utilize hexapole fields to select the angular momentum state of one of the reagents and then use a dipole field to orient the state selected species although this is true only for a very limited number of molecules, e.g. symmetric top molecules with a permanent electric dipole moment as for the $Rb+ICH_3$ [41] and $K+ICH_3$ [42] reactions where the ICH_3 reagent was prepared in a specific angular momentum state.

1.1.2 Spectroscopically Based Approach

The optical based reaction dynamics experiments started with the chemiluminescence studies performed by Michael Polanyi [43]. The advent of infra-red chemiluminescence pioneered by John Polanyi was an important milestone and made it possible to study reactions which did not result in an electronically excited product. Work of this type concentrated on atom+diatomic exchange reactions producing a hydrogen halide as the product due to the large cross section for infra-red emission of these molecules [44,45]. This lead to the study of stimulated emission from cavities containing nascent reaction products to obtain product population distributions. Although the analysis is not straightforward these studies were very valuable in their day for fundamental chemical dynamics and also led to the practical exploitation of chemical lasers, e.g HF and CO_2.

The use of lasers as an reaction probe was first introduced by Zare [46] extending studies of the metal atom+halide reactions. One of the first laser based techniques, and still one of the most important, is laser-induced fluorescence (LIF) [47] although this has been supplanted more recently by multi-photon ionization spectroscopy (MPI) [48,49,50,51,52,53] with energies typically corresponding to the visible and UV regions allowing detection of closed shell molecules with high lying first excited states. In addition to LIF and MPI, coherent anti-Stokes Raman scattering (CARS) [54,55,56] and other non-linear coherent spectroscopic techniques such as degenerate four wave mixing [57,58] have been introduced for dynamical measurements.

Lasers have also found use in photolytic production of reagents from suitable precursor molecules. This has been particularly exploited for the production of H atoms [59,60] since conservation of momentum ensures that most of the energy released is carried away by the hydrogen atom in the form of translational energy. Other atoms such as Cl, $O(^3P)$ and $O(^1P)$ [61] have also been produced using photolytic techniques.

The most recent use of lasers has been in the preparation of one or more of the reagents in specific quantum states prior to the reaction using optical transitions.

These include atoms in excited states and specific polarizations and molecular electronically excited states, e.g. N_2O^+ as well as direct infra-red pumping to achieve selected rovibronic states within the electronic ground state [61]. More recently the technique of stimulated Raman pumping has become more widespread as it is applicable to both hetero- and homonuclear diatomics [62].

1.2 State of Current Understanding

Today the ultimate goal is still to carry out a full quantum mechanical calculation of a chosen PES and then perform quantum mechanical scattering calculations to predict the fully state specific outcome of the reaction of interest. Unfortunately this is still a long way off for anything but the original $H+H_2$ reaction and systems such as $F+H_2$. To this end various approximate quantum methods have been necessarily introduced for systems with larger numbers of electrons. In some cases it is possible to perform the scattering calculations by reducing the number of dimensions in which the scattering takes place, i.e. constraining the collision geometry for the reaction. In addition, purely classical trajectory calculations pioneered by Polanyi [63] have been very successful in predicting the majority of features and only fail for systems involving very light atoms where electron tunneling and quantum mechanical resonances play an important part. For the potential energy surfaces themselves many alternatives to full quantum calculations have been tried varying from approximate quantum to semi-empirical methods [64].

At a more qualitative level the reasons for translational and vibrational excitation effects are well understood in terms of the early/late barrier to the reaction. Rotational aspects, however, are not well understood and a lot of work over the past decade has focussed on trying to gain a better understanding of the rotational and angular aspects of chemical reactions [65,61,66,67,68,69,70,71,72,73,74,75,76].

Bibliography

[1] Anderson J. B., *J. Chem. Phys.*, **58**, 4684 (1973)

[2] Tan K. G., laidler K. J., Wright J. S., *J. Chem. Phys.*, **67**, 5883 (1977)

[3] Laidler K. J., Tan K. G., Wright J. S., *Chem. Phys. Lett.*, **46**, 56 (1977)

[4] Johnston H. S., *Adv. Chem. Phys.*, **3**, 131 (1961)

[5] Johnston H. S., Rapp D., *J. Am. Chem. Soc.*, **83**, 1 (1961)

[6] Pacey P. D., *J. Chem. Phys.*, **71**, 2966 (1979)

[7] Furue H., Pacey P. D., *J. Chem. Phys.*, **83**, 2878 (1985)

[8] Eyring H., Polanyi M., *Z. Phys. Chem., B.*, **12**, 279 (1931)

[9] Hirschfelder J. O., Eyring H., Topley B., *J. Phys. Chem.*, **4**, 170 (1936)

[10] Wall F. T., Hiller F. A., Mazur J., *J. Chem. Phys.*, **29**, 255 (1958)

[11] Wall F. T., Hiller F. A., Mazur J., *J. Chem. Phys.*, **35**, 1284 (1961)

[12] Gerrity D. P., Valentini J. J., *J. Chem. Phys.*, **82**, 1323 (1985)

[13] Gerrity D. P., Valentini J. J., *J. Chem. Phys.*, **83**, 2207 (1985)

[14] Marinero E. E., Rettner C. T., Zare R. N., *J. Chem. Phys.*, **80**, 4142 (1984)

[15] Blais N. C., Truhlar D. G., *Chem. Phys. Lett.*, **102**, 120 (1983)

[16] Levine R. D., Berstein R. B., *Chem. Phys. Lett.*, **105**, 467 (1984)

[17] Schatz G. C., *Chem. Phys. Lett.*, **108**, 532 (1984)

[18] Blais N. C., Truhlar D. G., *J. Chem. Phys.*, **82**, 2300 (1985)

[19] Tsekouras A. A., Leach C. A., Kalogerakis K. S., Zare R. N., *J. Chem. Phys.*, **97**, 7220 (1992)

[20] Zhao D. Q., Zare R. N., *J. Chem. Phys.*, **97**, 6208 (1992)

[21] Gerlach W., Stern O., *Z. Physik*, **9**, 349 (1922)

[22] Loesch H. J., Stienkemeier F., *98*, **J. Chem. Phys.**, 9570 (1993)

[23] Loesch H. J., Moller J., *J. Chem. Phys.*, **97**, 9016 (1992)

[24] Loesch H. J., Stenzel E., Wustenbecker B., *J. Chem. Phys.*, **95**, 3841 (1991)

[25] Baldwin D. P., Buntine M. A., Chandler D. W., *J. Chem. Phys.*, **93**, 6578 (1990)

[26] Buntine M. A., Baldwin D. P., Zare R. N., Chandler D. W., *J. Chem. Phys.*, **94**, 4672 (1991)

[27] Kitsopoulos T. N., Buntine M. A., Baldwin D. P. Zare R. N. Chandler D. W., *Science*, **260**, 1605 (1993)

[28] Rice F. O., Urey H. C., Washburne R. N., *J. Am. Chem. Soc.*, **50**, 2402 (1928)

[29] Bull T. H., Moon P. B., *Discuss. Faraday Soc.*, **17**, 54 (1954)

[30] Taylor E. H., Datz S., *J. Chem. Phys.*, **23**, 1711 (1955)

[31] Greene E. F., Roberts R. W., Ross J., *J. Chem. Phys.*, **32**, 940 (1960)

[32] McDonald J. D., Le Breton P. R., Lee Y. T., Herschbach D. R., *J. Chem. Phys.*, **56**, 769 (1972)

[33] Neumark A. M., Wodtke A. M., Robinson G. M., Hayden C. C., Lee Y. T., *J. Chem. Phys.*, **82**, 3045 (1985)

[34] Neumark A. M., Wodtke A. M., Robinson G. M., Hayden C. C., Shobatake K., Sparks R. K., Schafer T. P., Lee Y. T., *J. Chem. Phys.*, **82**, 3067 (1985)

[35] Stolte S., Proctor A. E., Pope W. M., Bernstein R. B., *J. Chem. Phys.*, **66**, 3468 (1977)

[36] Kramer K. H., Bernstein R. B., *J. Chem. Phys.*, **42**, 767 (1965)

[37] Gandhi S. R., Curtiss T. J., Xu Q. X., Choi S. E., Bernstein R. B., *Chem. Phys. Lett.*, **132**, 6 (1986)

[38] Herschbach D. R., *Faraday Discuss. Chem. Soc.*, **55**, 233 (1973)

[39] Parish D. D., Herschbach D. R., *J. Am. Chem. Soc.*, **95**, 6133 (1973)

[40] Riley S. J., Herschbach D. R., *J. Chem. Phys.*, **58**, 27 (1973)

[41] Parker D. H., Chakrovorty K. K., Bernstein R. B., *Chem. Phys. Lett.*, **86**, 113 (1982)

[42] Loesch H. J., Remscheid A., *J. Phys. Chem.*, **95**, 8194 (1991)

[43] Atomic Reactions, *M. Polanyi* (Ernest Benn)

[44] Maylotte D. H., Polanyi J. C., Woodall K. B., *J. Chem. Phys.*, **57**, 1547 (1972)

[45] Anlauf K. G., Kuntz P. J., Maylotte D. H., Pacey P. D., Polanyi J. C., *Discuss. Faraday Soc.*, **44**, 183 (1967)

[46] Shultz A., Cruse H. W., Zare R. N., *J. Chem. Phys.*, **57**, 1354 (1972)

[47] Kinsey J. L., *Ann. Rev. Phys. Chem.*, **28**, 349 (1977)

[48] Boesl U., *J. Phys. Chem.*, **95**, 2949 (1991)

[49] Ashfold M. N. R., *Mol. Phys.*, **58**, 1 (1986)

[50] Ashfold M. N. R., Clement S. G., Howe J. D., Western C. M., *J. Chem. Soc. Faraday Trans.*, **89**, 1153 (1993)

[51] Ultrasensitive Laser Spectroscopy, *D. H. Parker* (Academic Press, New York, 1983)

[52] Johnson P. M., Otis C. E., *Ann. Rev. Phys. Chem.*, **32**, 139 (1981)

[53] Johnson P. M., *Acc. Chem. Res.*, **13**, 20 (1980)

[54] Germann G. J., Valentini J. J., *J. Chem. Phys.*, **92**, 3792 (1988)

[55] Valentini J. J., Gerrity D. P., Phillips D. L., Nieh J. C., Tabor K. D., *J. Chem. Phys.*, **86**, 6745 (1987)

[56] Nieh J. C., Valentini J. J., *J. Chem. Phys.*, **91**, 1370 (1987)

[57] Meijer G., Chandler D. W., *Chem. Phys. Lett.*, **192**, 1 (1992)

[58] van der Wal R. L., Holmes B. E., Jeffries J. B., Danehy P. M., Farrow R. L., Rakestraw D. J., *Chem. Phys. Lett.*, **191**, 251 (1992)

[59] Flynn G. W., Weston R. E., *Ann. Rev. Phys. Chem.*, **37**, 551 (1986)

[60] Wood C. F., Flynn G. W., Weston R. E., *J. Chem. Phys.*, **77**, 4776 (1982)

[61] Simpson W. R., Orr-Ewing A. J., Zare R. N., *Chem. Phys. Lett.*, **212**, 163 (1993)

[62] Rohlfing E. A., Chandler D. W., *J. Chem. Phys.*, **87**, 5229 (1987)

[63] Kinetics of Gas Reactions, vol. 6A, *J. C. Polanyi* (Academic Press, New York, 1974)

[64] Molecular Reaction Dynamics and Chemical Reactivity, *R. D. Levine, R. B. Bernstein* (Oxford University Press)

[65] Shafer N. E., Orr-Ewing A. J., Simpson W. R., Xu H., Zare R. N., *Chem. Phys. Lett.*, **212**, 155 (1993)

[66] Aoiz F. J., Brouard M., Duxon S. P., Enriquez P. A., Sayos R., *J. Chem. Soc., Faraday Trans.*, **89**, 1427 (1993)

[67] Brouard M., Duxon S. P., Enriquez P. A., Simons J. P., *J. Chem. Soc., Faraday Trans.*, **89**, 1435 (1993)

[68] Brouard M., Duxon S. P., Enriquez P. A., Sayos R., Simons J. P., *J. Phys. Chem.*, **95**, 8169 (1991)

[69] Brouard M., Duxon S. P., Enriquez P. A., Simons J. P., *Laser Chem.*, **11**, 265 (1991)

[70] Brouard M., Duxon S. P., Enriquez P. A., Simons J. P., *J. Chem. Phys.*, **97**, 7414 (1992)

[71] Green F., Hancock G., Orr-Ewing A. J., Brouard M., Duxon S. P., Enriquez P. A., Sayos R., Simons J. P., *Chem. Phys. Lett.*, **182**, 568 (1991)

[72] Green F., Hancock G., Orr-Ewing A. J., *Faraday Discuss. Chem. Soc.*, **91**, 79 (1991)

[73] Johnston G. W., Satyapal S., Bersohn R., Katz B., *J. Chem. Phys.*, **92**, 206 (1990)

[74] Katz B., Park J., Satyapal S., Chattopadhyag A., Tasaki S., Bersohn R., *Faraday Discuss. Chem. Soc.*, **91**, 73 (1991)

[75] Van der Zande W. J., Zhang R., Zare R. N., McKendrick K. G., Valentini J. J., *J. Phys. Chem.*, **95**, 8205 (1991)

[76] Gilbert E., Maitland G., Watson A., McKendrick K. G., *J. Chem. Soc., Faraday Trans.*, **89**, 1527 (1993)

Chapter 2

Experimental Apparatus

2.1 Introduction

Whilst the main aim of the present work was the investigation of state-to-state reaction dynamics, there were several several tasks to be performed before this could go ahead. The initial stages involved a detailed spectroscopic study of the molecule to be studied, HCl, to find states which were unperturbed and thus suitable for quantitative investigation. The technique chosen for this work was Resonance-Enhanced-Multi-Photon-Ionization Spectroscopy (REMPI) in conjunction with a Time-Of-Flight-Mass-Spectrometry (TOFMS) detection system.

2.2 Spectron Laser System

2.2.1 Nd:YAG Laser

A Spectron Laser Systems Nd:YAG laser (SL803S) formed the basis of the two photon REMPI detection setup. The laser contained two Neodymium doped YAG rods used as an oscillator/amplifier pair with the lasing occurring between the electronic levels of the Nd^{3+} ions.

Two main triggering modes were available. The first of these controlled the flashlamp to Q-switch delay internally via potentiometers on the front panel of the power supply. The triggering of the oscillator flashlamps from either an internal or external source initiated the charging of the Q-switch capacitors. When the specified flashlamp to Q-switch delay had elapsed the high voltage relay supplying the Pockels Cell was triggered. This produced a short (approximately 10ns FWHM) pulse with a total energy of approximately 1Joule when the Q-switch delay was 200μs.

The second triggering mode used separate external sources for triggering the flashlamps and Q-switch respectively. In this mode the initiation of the charging of the Pockels Cell capacitors was still handled internally. This triggering arrangement was necessary for polarization sensitive experiments where the laser triggering had to be phase locked with the photo-elastic-modulator described in section 2.4. In addition the timing jitter on the internal Q-switch delay circuit was of the order of microseconds which is the same order of magnitude as the phase cycle of the photo-elastic-modulator. This would have resulted in a large uncertainty in the polarization of the laser beam when performing polarization sensitive REMPI. The two external triggers (flashlamps and Q-switch) were taken from a LeCroy 4222PDG pulse delay generator (described in section 3.2.3 via a line driver module which converted the pulses to the necessary voltage and source current levels.

The Nd:YAG laser was optimized for a 10 Hz repetition rate, the maintainance of which was essential due to thermal lensing effects in the Nd:YAG rods. The constant repetition rate was achieved using a PC-AT computer as described in section 3.3.

The fundamental 1064nm output from the oscillator/amplifier unit was frequency doubled using a KDP crystal with the doubled output at 532nm being separated from the residual 1064 beam using a dichroic optic. The 532nm beam was used to pump the dye laser while the residual 1064nm was mixed with the doubled dye output to form the beam used for two photon REMPI, as described in section 2.2.3.

2.2.2 Dye Laser

A Spectron Laser Systems dye laser (SL4000G) was used to provide a tunable source of laser light either for direct use or for doubling/mixing to provide light at the required wavelength for two photon REMPI of the species being studied. This laser was pumped by the 532nm doubled output from the Nd:YAG laser described previously.

The laser comprised an oscillator and two amplifier stages with only a few percent of the pump beam being used to pump the oscillator. The reamainder of the 532nm beam was split equally between the two amplifier stages. The oscillator consisted of a transversely pumped flowing dye cell, an output coupler, a diffraction grating and wavelength tuning mirror and a prism beam expander.

The dye cell contained a correcting window which provided the correct angle of incidence on the diffraction grating. The grating was used in a grazing incidence configuration and wavelength tuning was achieved using a separate tuning mirror mounted on a stepper motor sine drive arrangement. The sine drive contained a mechanical counter and two proximity switches to detect the limits of the drive travel.

The amplifier section consisted of two longitudinally pumped dye cells at Brewter's angle with the pump light for each of the amplifiers being supplied via the main pump beam by two beam splitters, one for each dye cell.

The dye circulator contained two separate reservoirs. One each for oscillator and amplifier dye cells. Each reservoir contained approximately one litre of dye with the amplifier typically being far more concentrated than that for the oscillator stage.

2.2.3 Mixing Unit

For most of the present work a laser source at 220-250nm was required. This was achieved by either doubling the output from the dye laser only or by doubling the dye output and then mixing the doubled dye beam with the residual Nd:YAG

fundamental at 1064nm. These operations were performed by a Spectron Laser Systems SL4000EX mixing unit shown schematically in figure 2–1.

The mixing unit comprised a delay line for the Nd:YAG fundamental beam, a doubling unit for the dye beam and a mixing unit to sum frequency mix the doubled dye and 1064nm beams. The doubling and mixing units had separate stepper motor drives and heaters.

The SL4000EX employed parallel faced non-linear crystals for harmonic generation and sum frequency mixing with induced axial effects being corrected by plain quartz compensating blocks. Crystals were rotated in one angular plane by five phase stepper motors driving through a low backlash 100:1 reduction gearbox. The drives had limit switches built in to detect excessive rotation of the crystals. All crystals were temperature controlled to improve stability and prevent problems with water absorption, etc..

When mixing as well as doubling the 1064nm beam was directed around an optical delay line incorporating a beam diameter reducing telescope. The generated wavelengths were detected by photodiodes with local head amplifiers. These had adjustable gain. A dedicated BBC microcomputer monitored the respective doubled and mixed power outputs via sample and hold analogue to digital converters and whilst continually updating the orientation of the crystals to ensure the correct phase matching conditions. In this way the power output was being constantly optimized [1] .

[1] While this always ensured optimum power output it did mean that the beam's cross sectional profile was changing in contrast to spatial optimization techniques.

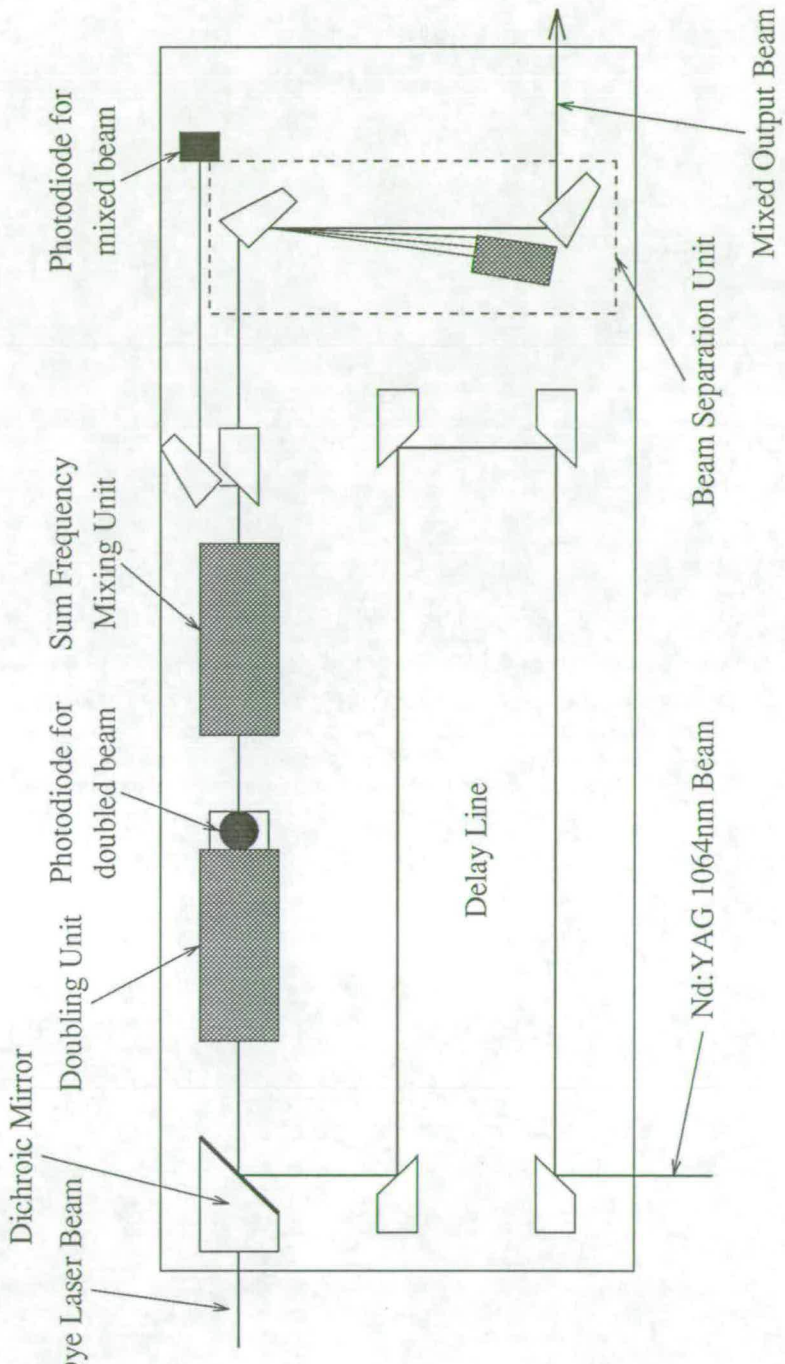

Figure 2–1: Spectron Laser Systems SL4000EX Mixing Unit

2.3 Vacuum Apparatus

The vacuum system (supplied by Vacuum Generators UK Ltd.) consisted of two differentially pumped chambers. This ensured that the high pressures required at the reaction zone for bimolecular dynamics studies were achievable whilst maintaining the necessary high vacuum (10^{-6}mbar) needed for the Microchannel Plate detector. All sections of the main chamber and TOF tube had a nominal 4″ internal diameter. The main vacuum components are shown schematically in figure 2–2.

Two 4″ Edwards diffusion pumps, (100/300M) one each for the reaction and TOFMS regions were used to evacuate the chamber. These were cryobaffled and backed by Edwards E2M8 rotary pumps. The reaction and TOF/detection regions were separated within the apparatus by a top-hat flange with all ions passing through a small hole in the face of the top-hat. The hole size was configurable between 2 and 10mm using various inserts. Additionally, a glass capillary array (Gallileo Corp.) with pore sizes from 10μm to 50μm could be placed in the top-hat to further improve the pressure differential between the two chambers whilst still maintaining good ion transmission into the TOF/detection region. The capillary arrays were conductively coated to prevent problems with charge build up on the surface.

The pressure in the two main chambers was monitored using a system of Pirani (Edwards PR10K) and ion gauges (Vacuum Generators VIG 8) connected to analogue controllers (Vacuum Generators IGC 17F).

A pneumatic gate valve was fitted half way along the TOF region. This allowed the detector to be isolated from the rest of the vacuum system whenever it was opened to the atmosphere to allow modifications to be made in the reaction chamber.

The ions formed at the focus of the probe laser beam in the reaction chamber were extracted using a draw-out-grid arrangement. The draw-out-grid consisted of

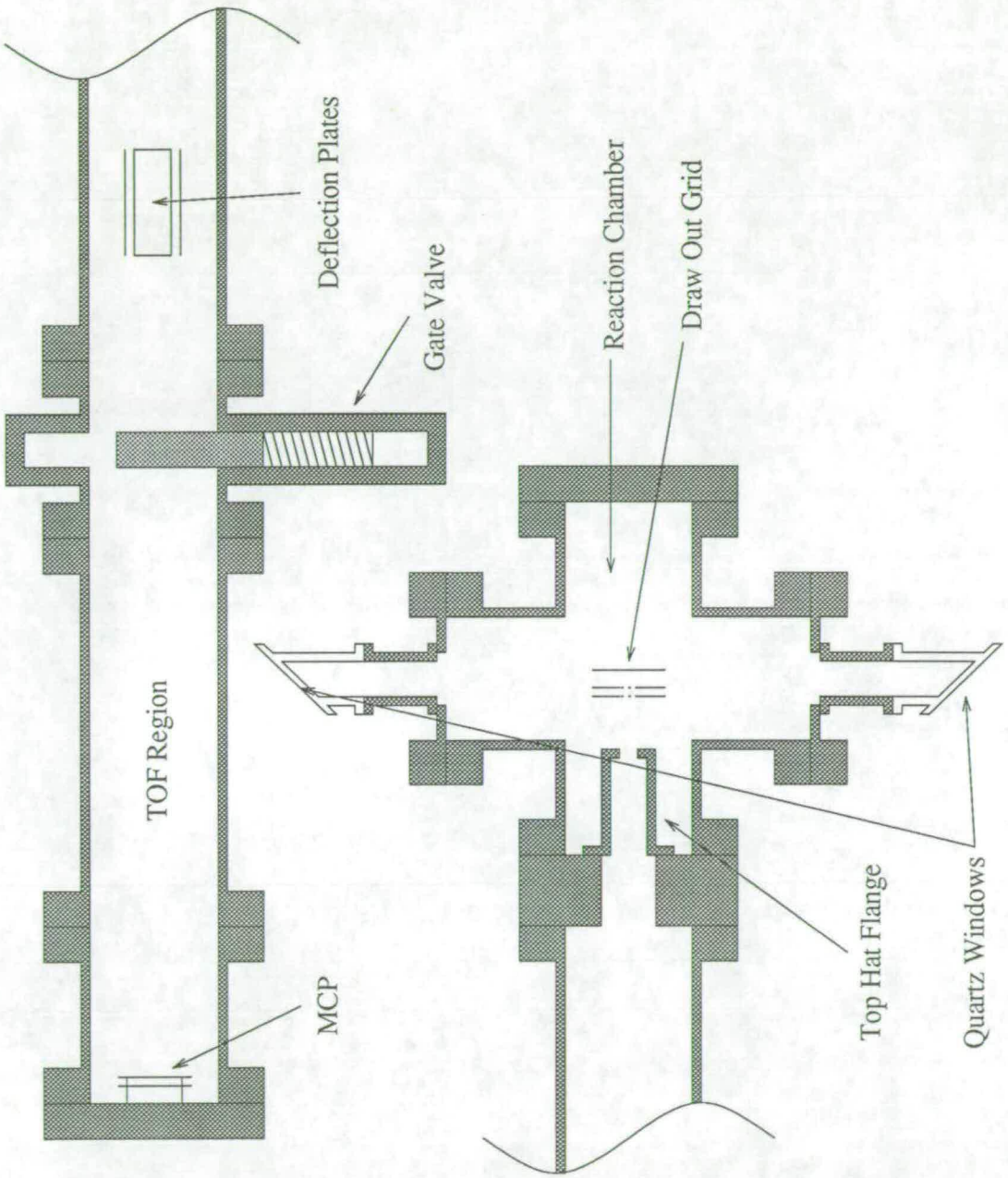

Figure 2–2: Schematic diagram of vacuum apparatus

repeller, retarder and ground plates conforming to the Wiley-McLaren [1] double field design which compensates for the spatial extent of the ion source. In later configurations the ground plate was dispensed with and the top-hat flange brought towards the repeller plate. This lessened the distance travelled by the ions before entering the high vacuum TOF region and improved overall sensitivity.

The plates forming the draw-out-grids were constructed from 0.5mm stainless steel 75mm in diameter. The retarder and ground plates had a 15mm diameter hole covered with nickel mesh (90% transmission, 0.074" spacing). The voltages to the grids were supplied via two high voltage power supplies (Bertan type 353, 0-2.5kV).

The ions then passed through the top-hat flange into the high vacuum field free TOF region. This region contained a two dimensional deflection plate arrangement to correct the ion path and thus maximize the ion flux at the detector. The ion signal was monitored using a Microchannel Plate (MCP) detector (R. M. Jordan Company) at the end of the TOF region. The detector consisted of two microchannel plates with up to 2kV potential difference between the front and rear surfaces of each plate. Additionally an accelerating potential of approximately 1kV was applied between the rear face of the first plate and the front surface of the second plate. In this configuration each plate had a gain of 10^3 resulting in a net gain of approximately 10^6. The output from the MCP was amplified (Stanford Research Systems SR240) and collected using the data acquisition system described in chapter 3.

For the present work the gases employed entered the reaction chamber via simple effusive sources. The simplest of these involved bleeding gases in via inlets in the rear flange of the reaction chamber as shown in figure 2–3.

This was sufficient when the transitions being studied were fairly intense. For situations where for some reason the signal was very weak a more direct source was used as shown in figure 2–4. In this case a hypodermic needle was used to feed the reagent(s) into the chamber at a point approximately 2mm from the focal point of the laser beam. This provided a dramatic ($\approx$ 10 fold) increase in the number density at the laser focus.

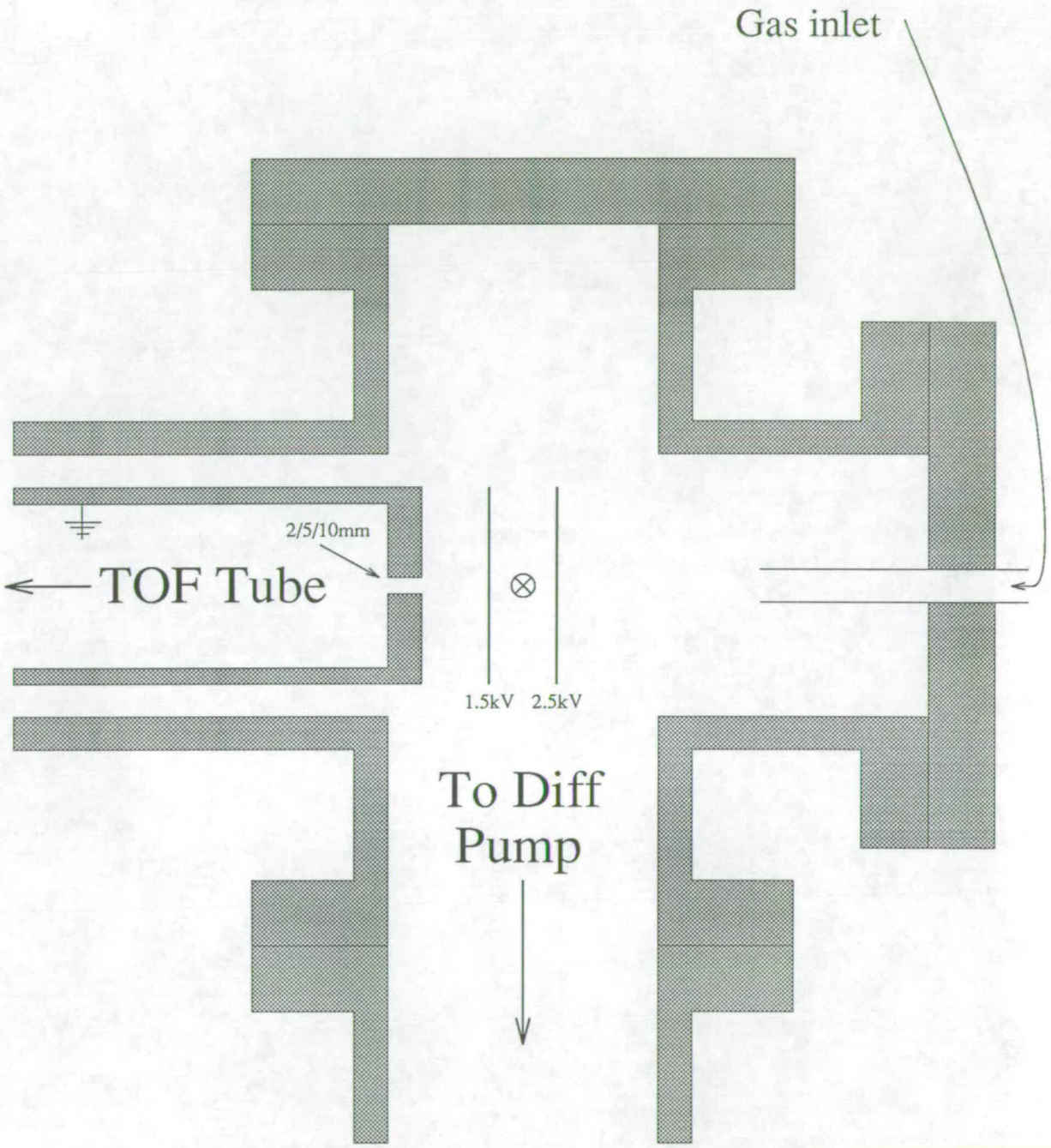

Figure 2–3: Diagram of reaction chamber with gas inlet at back flange

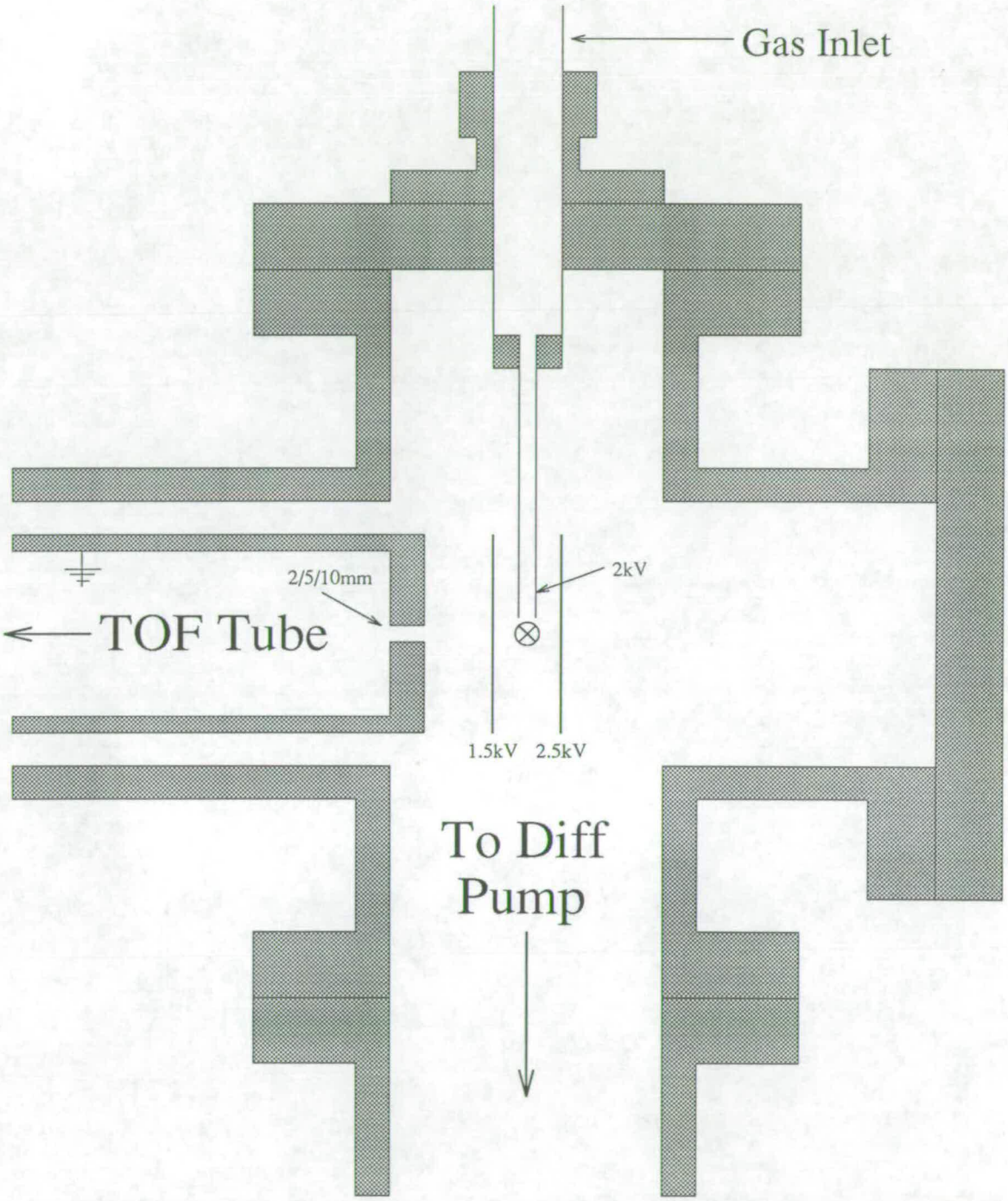

Figure 2–4: Diagram of reaction chamber with gas entering via a hypodermic needle

Using this injector arrangement caused problems with ion extraction since the injector voltage was effectively floating but the tip was in the fixed extraction field set up by the draw-out-grids. This was eventually cured by connecting the injector tip to a separate power supply and 'tuning' its voltage to optimize the ion signal. For cases where glass and quartz injectors were used the tip was coated in colloidal graphite and then wrapped in aluminium foil to provide a good electrical contact.

The laser beams passed through focusing lenses before entering the chamber via quartz windows. For the purposes of detection using a single polarization the windows were arranged at Brewsters angle and oriented to facilitate maximum transmission of the laser light [2] . In cases where a long (> 50cm) focal length lens was used extension arms were placed between the main vacuum chamber and the entrance and exit windows. This was necessary since the normal placing would have resulted in the beam being focussed at the point of incidence with the window with the risk of subsequent damage.

For polarization sensitive work the entrance window for the polarized beam was arranged such that the beam was normally incident ensuring the same transmission for all polarizations used.

To prevent laser light being scattered inside the chamber a baffle arrangement was used. This also provided the possibility of mounting the focusing lens inside the chamber for very short (< 10cm) focal length lenses.

---

[2]One problem with this arrangement was that the larger diameter windows required for Brewster angle incidence deformed under the large pressure differential to which they were subjected. In several cases this appeared to make the windows act as depolarizing elements.

2.4 Photoelastic Modulator

To carry out polarization sensitive REMPI some form of polarization modulation was required. This was accomplished using a Hinds PEM-80 photo-elastic-modulator (PEM).

The PEM is based on a optical element, transparent at the wavelength region of interest, which vibrates at its lowest frequency of standing compression sound waves. At the centre of the element a time varying birefringence is observed with a frequency equal to the natural standing sound wave frequency of the optical element itself. To sustain these vibrations the element is bonded to a quartz transducer tuned to the same frequency. In this way the amplitude of the vibrations and therefore the magnitude of the birefringence can be controlled. The effect of the induced birefringence on the incident beam is shown in figure 2–5.

The input beam can be resolved into two components, one lying along each of the major optical axes of the optical element. When the element is compressed or elongated along one of its axes the component of the input beam lying along that axis sees an apparent change in refractive index of the element. Thus this component of the input beam will experience a phase change relative to the other component on exiting the optical element. The resulting polarization can be described in terms of its Jones or Stokes vector [2,3].

The two special cases most commonly used for the present work were $\frac{1}{4}$ and $\frac{1}{2}$ wave retardance. When operating on a linearly polarized input beam lying at 45 degrees to the major axes of the crystal these produced circularly polarized output in the case of $\frac{1}{4}$ wave retardance and a linearly polarized beam at 90 degrees to the input beam in the case of $\frac{1}{2}$ wave retardance. This is shown in figure 2–6 [3] .

---

[3]For the present work the notion of handedness of the beam was irrelevant since the systems under study contained no net orientation and thus interacted with left and right handed beams in exactly the same manner.

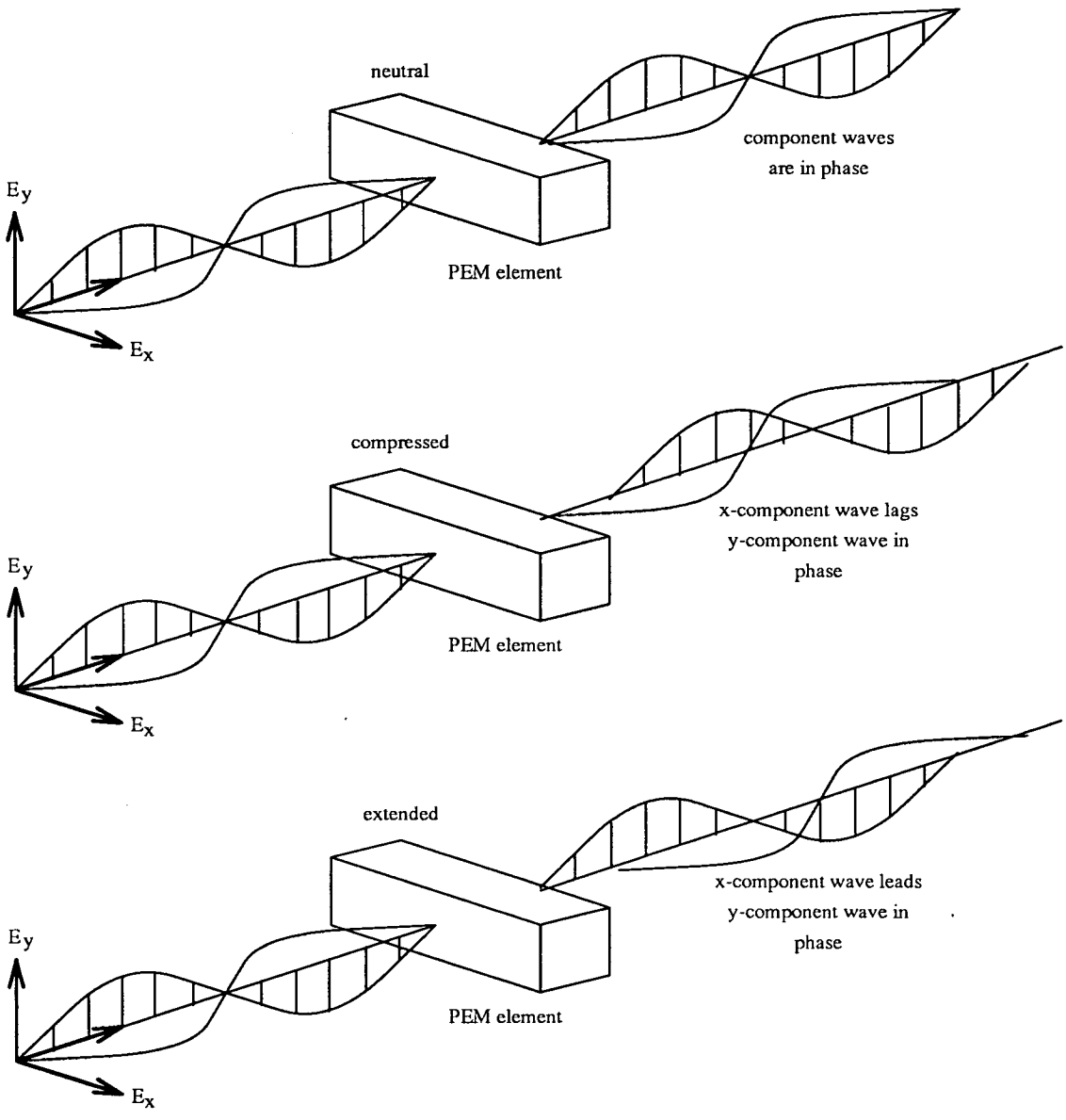

Figure 2–5: PEM Operation

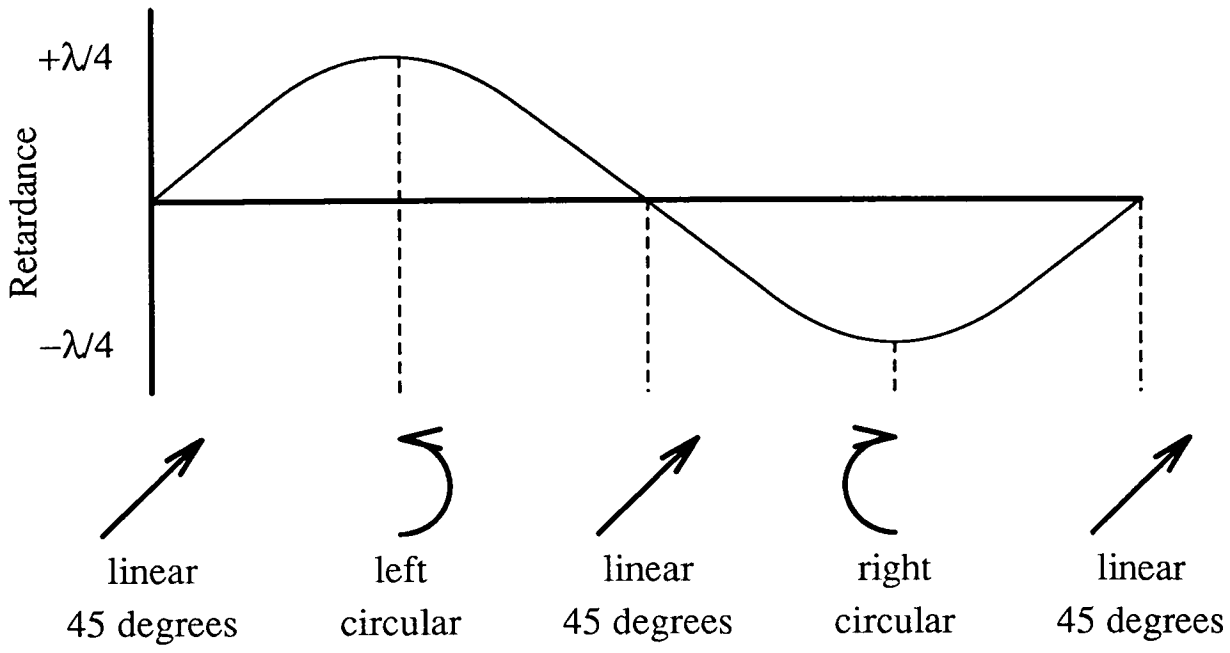

a) Retardance vs time for 1/4 wave maximum retardance

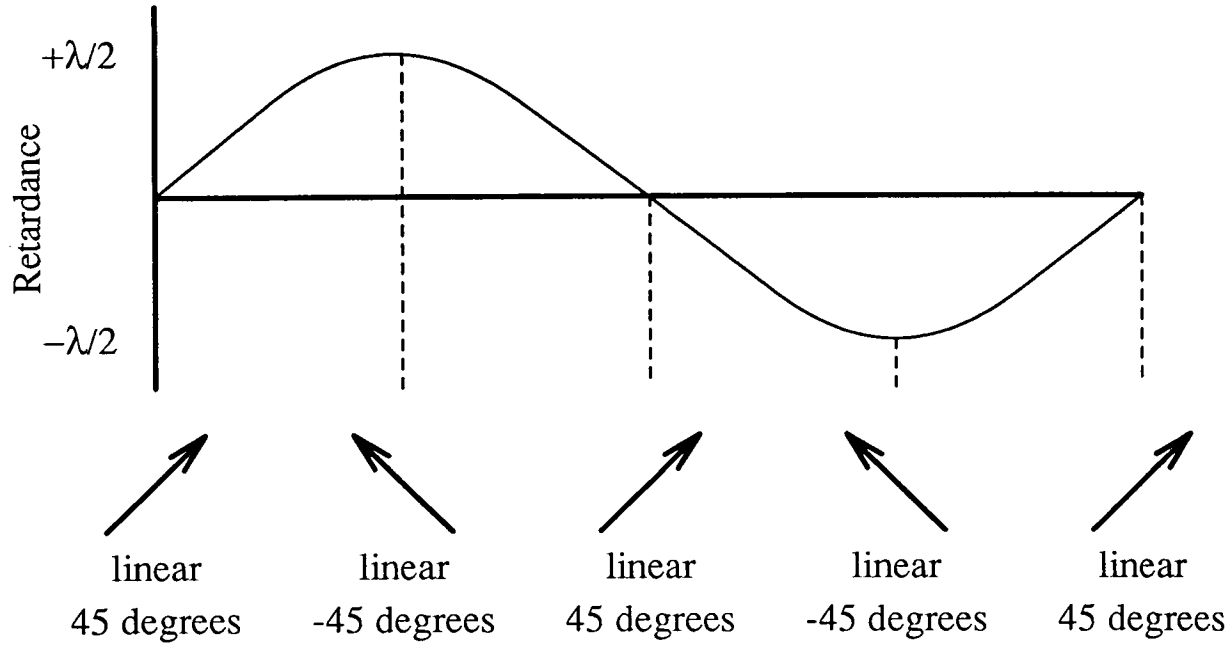

b) Retardance vs time for 1/2 wave maximum retardance

Figure 2–6: Retardance vs Time for $\frac{1}{4}$ and $\frac{1}{2}$ wave maximum retardance

The PEM optical element (fused silica in this case) had a fixed oscillatory period of 20μs. A phase locked output on the front panel of the controller was used to trigger all other electronics to achieve the phase locked conditions necessary for the experiment.

2.5 Rochon Polarizing Prism

As stated in the previous section a photo-elastic modulator was used for polarization modulation when performing polarization sensitive REMPI. For the polarization of the output beam from the PEM to be well characterized, however, the input beam had to have a well defined polarization. The output from the laser system used was fairly well polarized [4] . The polarization of the beam was further enhanced using a magnesium fluoride Rochon prism (Halbo Optics). This is a polarizer of the double image type comprising two prisms with the direction of the optical axes being shown in figure 2–7. When the 'unpolarized' light enters the prism the two plane polarized components are separated by double refraction at the interface between the two prisms with the O-ray being transmitted without deviation for all wavelengths [5] . It should be noted that the light must pass through the Rochon prism in the direction indicated in figure 2–7. If the light passes through the prism in the opposite direction then the plane of vibration will be rotated by the left hand component of the prism with the angle of rotation depending on the wavelength of the light.

---

[4]Vertical/linear for the doubled beam and horizontal/linear in the case of the mixed beam.

[5]This is the major advantage of the Rochon prism over the Wollaston configuration in which both the O and E-rays deviate from the normal path although the angular separation is greater in the case of the Wollaston prism.

2.6 Quanta-Ray Laser System

For certain parts of the present work a second laser source was required. In this case a Quanta-Ray Nd:YAG pumped dye system, shown in figure 2–8 was made available to us from the SERC laser loan pool.

2.6.1 Nd:YAG

The Nd:YAG laser was a Quanta-Ray GCR-11-2 comprising laser head, power supply and remote control. The unit had a built in harmonic generator which was used to generate 532nm doubled output for pumping the dye laser and also 355nm tripled output used for photolysis of precursor molecules. The harmonics were separated using a DHS-2 dichroic harmonic separator. In the configuration used for the present work no intra cavity etalon was fitted which resulted in a line width of approximately $1.0cm^{-1}$.

2.6.2 Dye Laser

The tunable output was obtained from a model PDL-3 dye laser as shown in figure 2–8. This was pumped using the 532nm doubled output from the Nd:YAG laser and was used almost exclusively with DCM dye over a wavelength range of 620-660nm. The apparatus described in the previous sections was configured as shown in figure 2–9.

2.6.3 CARS apparatus

For later work (see section 7) the apparatus described previously was reconfigured to perform Coherent Anti-Stokes Raman Spectroscopy (CARS). The CARS setup is shown in figure 2–10.

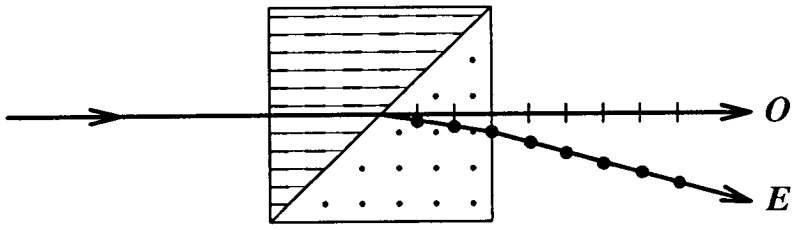

Figure 2–7: Rochon Polarizing Prism

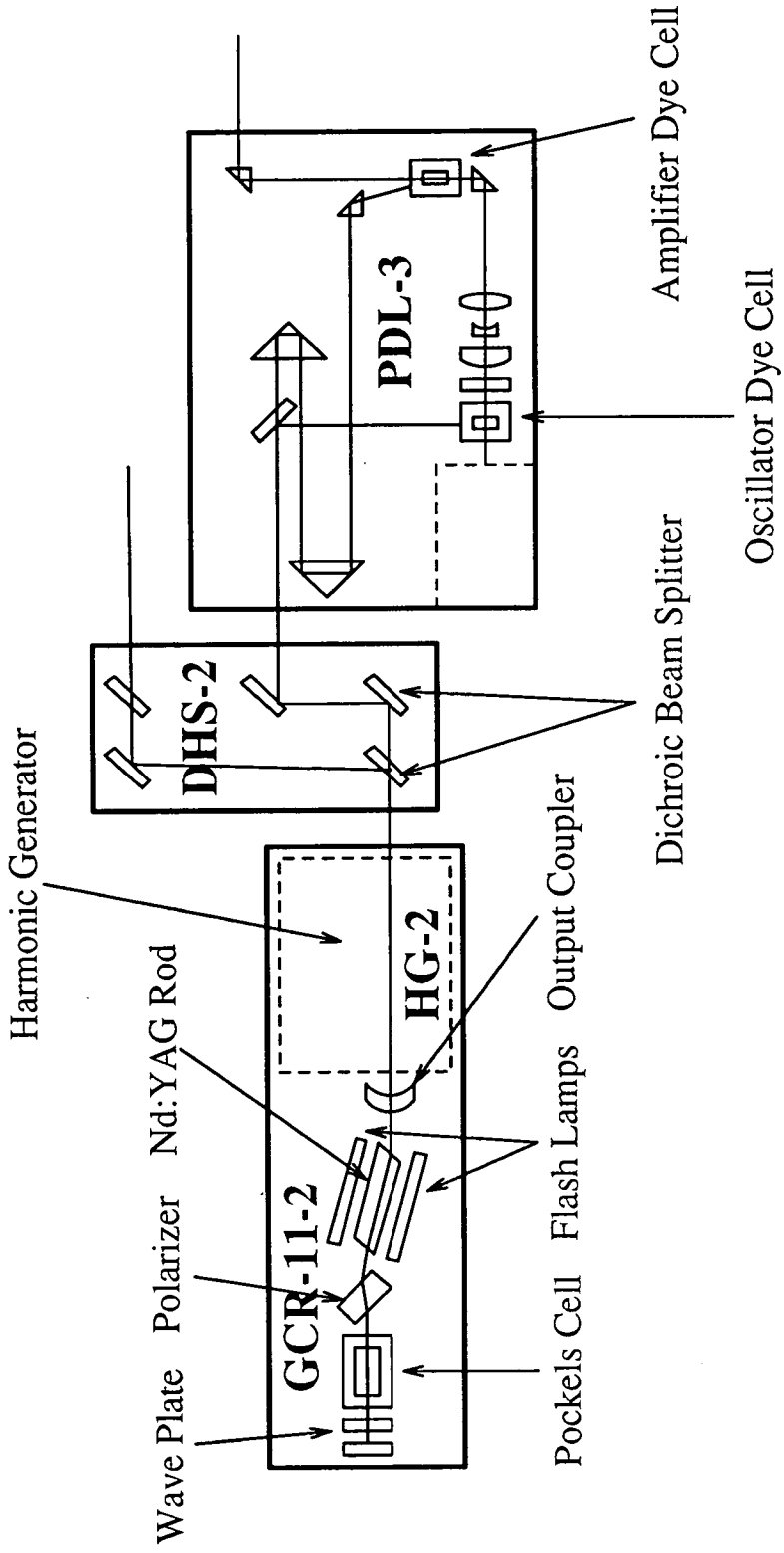

Figure 2–8: Scematic of Quanta-Ray Laser system

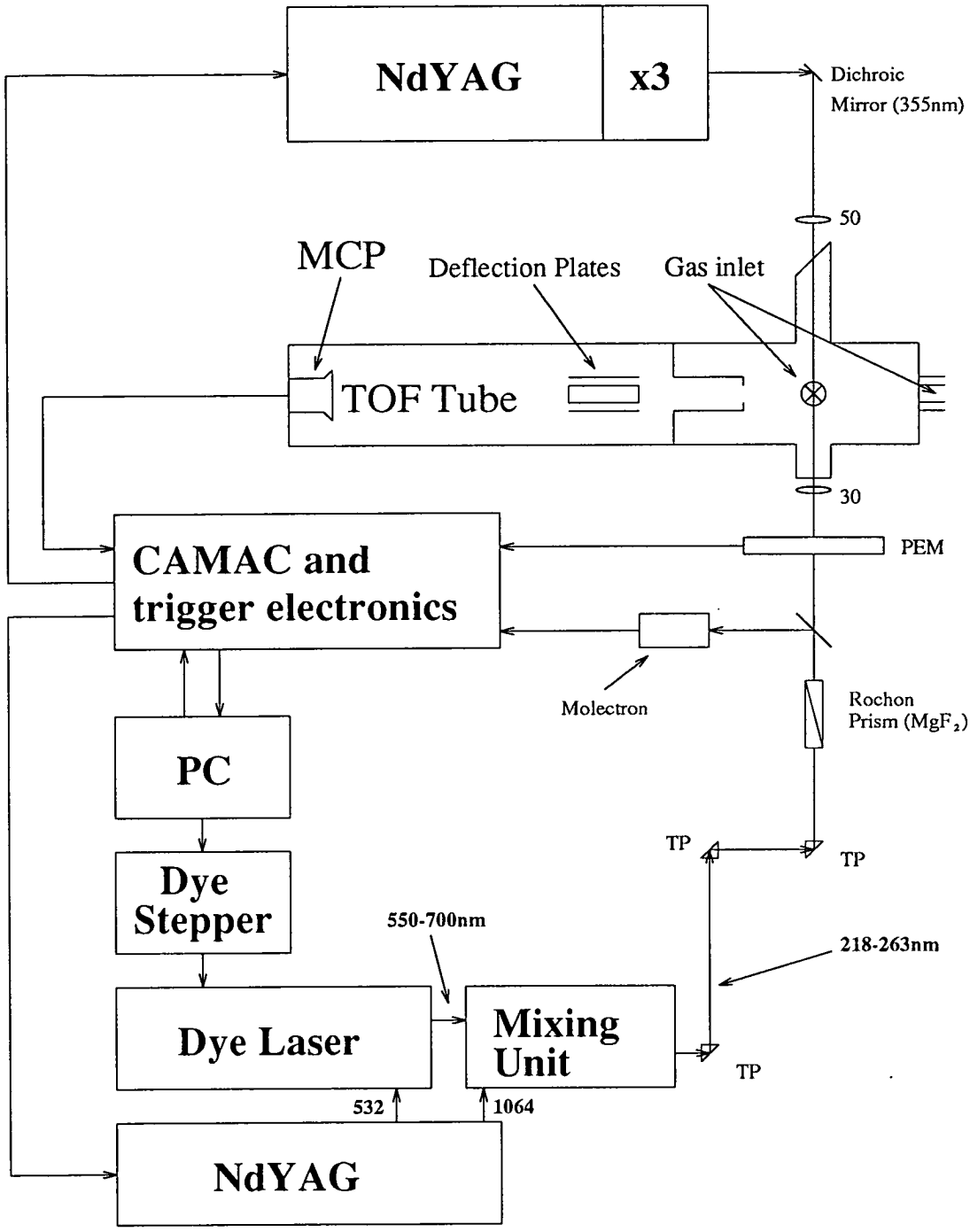

Figure 2–9: Diagram showing configuration of experimental apparatus

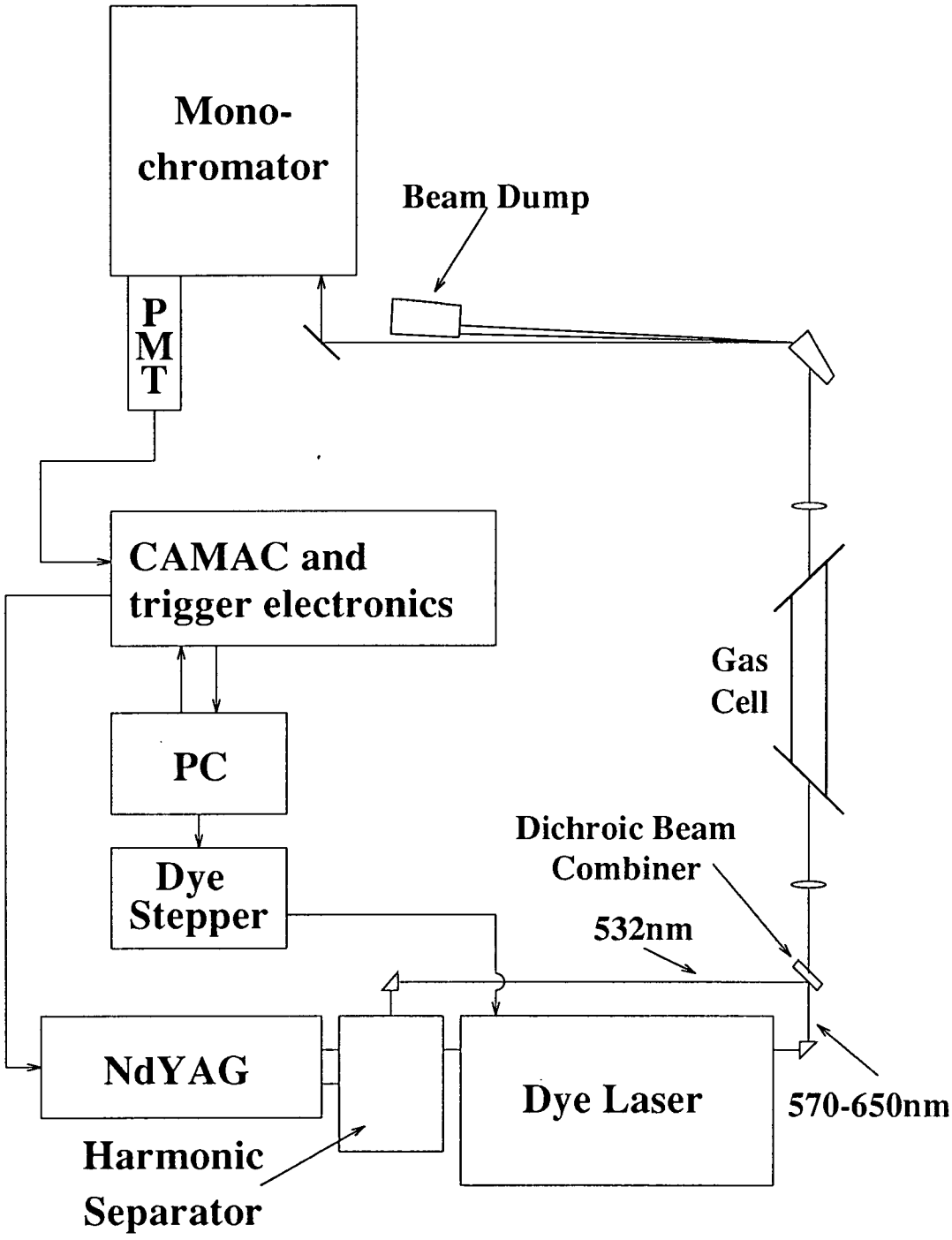

Figure 2–10: Diagram of experimental setup used for recording CARS spectra

Bibliography

[1] Wiley W.C., McLaren I.H., *Rev. Sci. Instum.*, **26**, 1150 (1955)

[2] Geometrical and Physical Optics, *R. S. Longhurst* (Longman, New York, 1973)

[3] Polarized Light in Optics and Spectroscopy, *D. S. Kliger, J. W. Lewis, C. E. Randall* (Academic Press, 1990)

Chapter 3

Design and Development of Data Acquisition Software

3.1 Introduction

One of the first tasks in the present work was to decide on a method to be used for gathering and processing the large amounts of data generated by the proposed experiments. It was decided at an early stage to use a computer based data acquisition system since this would entail all data being in computer readable form from the outset and thus simplify subsequent analysis as well as making it a relatively simple job to save and recall various parameter settings. In addition, in the likely event it became necessary to adjust various parameters during an experiment, having everything controlled from a single source would make it easier to perform validity checks on values of interdependent variables.

Having made the decision to use a computer based data acquisition system there only remained the choice as to which one. The two predominant systems in this field are GPIB (General Purpose Interface Bus. IEEE Std 488-1978) and CAMAC (Computer Aided Control And Measurement). A CAMAC system interfaced to an IBM compatible PC-AT was chosen due to its superior data transfer rate and wider range of instrumentation available making it a more suitable choice for

real-time data acquisition. This chapter describes the instrumentation used and the software developed to control it.

3.2 CAMAC Instrumentation

CAMAC is an international standard of modularized electronics whose function is to allow a wide range of instruments to be interfaced to a common dataway which can in turn be interfaced to a computer. In this way additions to a data transfer system may be made by simply plugging in additional modules and updating the control software to make use of them. The common dataway used by the modules takes the form of a backplane in the crate into which the modules are placed. The two rightmost stations are used to hold a dedicated crate controller which acts as the main interface between the instrumentation modules and the computer.

In a typical CAMAC read cycle the controlling computer would send a station number (N), a module subaddress (A) and a function code (F) to the crate controller. In response the module being addressed would write its data (1,2 or 3 bytes depending on the module and function code) to the relevant read registers to be read by the computer and generate a valid command accepted (X) response. Write commands proceed in much the same way with the write data registers being loaded by the computer with the relevant data before executing the CAMAC cycle.

In addition the status of modules and commands is conveyed by LAM (Look At Me) and response (Q) signals. When data within a module is available for reading the module issues a LAM signal which can be tested by the controlling software. The Q responses are generated by the individual CAMAC cycles, ie after a cycle has been completed the software can test the Q response with Q equal to one meaning all is well and a Q of zero implying an error of some sort has occurred.

The following sections describe the CAMAC instrumentation used for the present work.

3.2.1 dsp6001 Crate Controller

The crate controller used in all experiments was a dsp Technologies model 6001 mounted in a dsp crate (model "optima 860"). The 6001 has an integral dataway display for monitoring dataway activity which proved useful for debugging purposes and was interfaced to the PC using a dsp PC004 interface card. All commands are transferred via a four bit address bus with the 6001 controller appearing to the PC as a set of external registers plus one on-board register used to set up and initiate direct memory access [1] (DMA) data transfers. These registers were read or written using simple software commands and are described in table 3–1.

3.2.2 dsp2001A Transient Digitizer

When performing TOFMS for purposes of MPI a waveform digitizer is required to sample the incoming TOF waveform at high speed. In all of the experiments carried out this operation was performed by a dsp model 2001A 100MHz Transient Digitizer. The digitizer when used in conjunction with the control software allowed up to ten pairs of gates to be defined. The TOF signal between pairs of adjacent gates could then be integrated to give the ion signal arising from various selected mass channels.

The digitizer allowed waveforms to be sampled at rates up to 100MHz, ie 10ns sampling interval with the number of samples stored ranging from 256 to 32768 samples in powers of two. Once the digitizer had been armed a trigger was sent to the front panel and the unit then proceeded to digitize and store the required number of samples. Segments of the input waveform arriving before the start trigger could also be digitized and stored by setting the number of pre-trigger samples required. All major settings could be altered either from software or from front panel switches.

---

[1] Few problems were associated with the 6001 crate controller, the one notable exception being its apparent inability to perform DMA transfers for high speed data acquisition. This problem was never solved.

Register no'	Description
0	Write only register for CAMAC write data high byte (bits 16-23)
1	Write only register for CAMAC write data middle byte (bits 8-15)
2	Write only register for CAMAC write data low byte (bits 0-7)
3	Write only register for CAMAC A subaddress (0-15)
4	Write only register for CAMAC F function code (0-31)
5	Write only register for CAMAC N station address (1-23)
6	Write only register for CAMAC initialize (Z), clear (C) and inhibit (I) commands
7	Addressing this register initiates a 1.1μs CAMAC cycle
8	Read only register to read LAM (Look At Me) status, Q and X. The Q and X bits reflect the status of the last CAMAC write cycle performed. LAM lines are priority-encoded, ie., station 1 has the highest priority and station 23 the lowest
9	Read only register for CAMAC read data high byte (bits 16-23)
10	Read only register for CAMAC read data middle byte (bits 16-23)
11	Read only register for CAMAC read data low byte (bits 16-23)
12	Read only register for crate controller status

Absolute addresses of the various registers are set via switches on board the PC004 interface card.

Table 3–1: Description of CAMAC registers

The 2001A was an 8 bit unit with a maximum input voltage of 512mV implying a resolution of 2mV. This was perfectly adequate for the present work when used in conjuction with a variable gain fast preamp. A summary of functions is given in table 3–2.

Command	Function Performed
F(0) A(0)	Reads pre-trigger samples, number of samples and sampling interval
F(2) A(0)	Reads waveform data from memory. Q = 1 is returned until last data read.Thereafter Q = 0
F(3) A(0)	Reads module ID
F(8) A(0)	Test module LAM
F(9) A(0)	Reset module LAM and start sampling
F(10) A(0)	Reset module LAM
F(11) A(0)	Computer single sample
F(16) A(0)	Writes pre-trigger samples, number of samples and sampling interval
F(24) A(0)	Disable module LAM
F(25) A(0)	Computer stop trigger
F(26) A(0)	Enable LAM and computer readout
F(27) A(0)	Enables reading of module's input dc. offset

F(n) implies function code 'n' and A(n) implies module subaddress 'n'

Table 3–2: dsp2001A Transient Digitizer functions

3.2.3 LeCroy 4222PDG Pulse Delay Generator

Several of the experiments carried out required that separate trigger pulses be sent with very little (< 2ns) timing jitter. This task was accomplished using a LeCroy model 4222 pulse delay generator.

This unit has four independent channels each of which has its own delay. The delays are specified by 24 bits with 1ns resolution implying a delay range of 0 to 16777215ns with each channel having a choice of three output pulse types. These

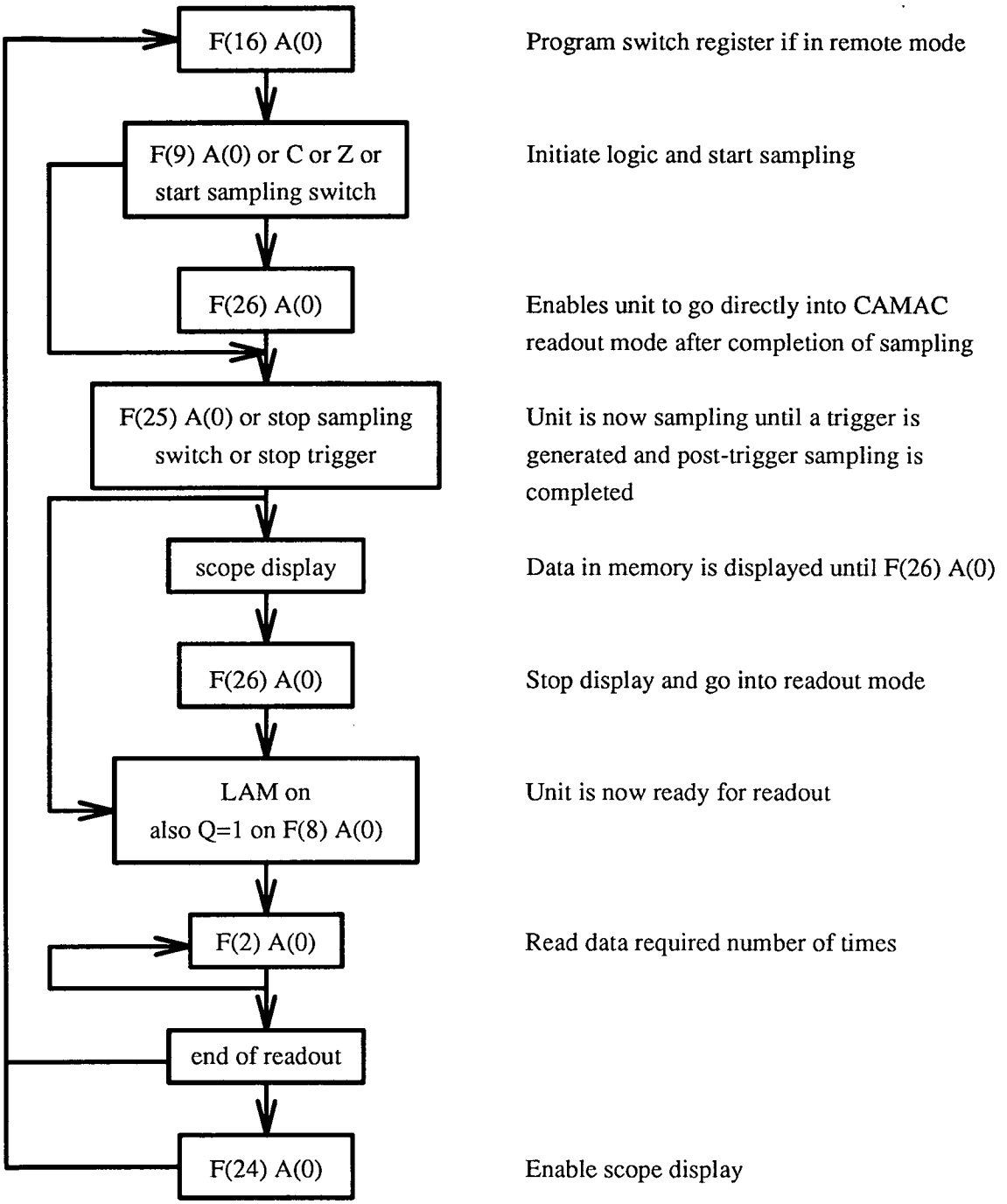

Figure 3–1: General control sequence for dsp2001A

are NIM, $\overline{\text{NIM}}$ and fast 5V into 50Ω. There are three distinct triggering modes. The first of these allows the unit to be retriggered anytime 100ns after the last input trigger, the second allows the unit to be triggered anytime after the longest programmed delay has elapsed. These are both retrigger modes. The third mode, non-retrigger mode, requires the module to be re-armed from the PC after it has been triggered before it may be triggered again.

For the purposes of the present work the non-retrigger mode proved the most useful since one of the triggering devices (PEM) [2] supplied the trigger pulses at a rate far in excess of the 10Hz repetition rate required by the laser devices. The non-retrigger mode shown schematically in figure 3–2 made it possible to use this device as a trigger for phase locking purposes whilst still maintaining the required repetition rate of approximately 10Hz. A summary of the module's functions is given in table 3–3.

A typical timing sequence is shown in figure 3–3.

Command	Function Performed
F(0) A(0-3)	Reads selected programmed delay for channel in 24 bits
F(1) A(0)	Reads status via read lines 1 to 4
F(9) A(0)	Resets all channels
F(16) A(0-3)	If CAMAC access enabled, writes delay to selected channel in 24 bits. Q = 1 if CAMAC enabled; Q = 0 otherwise.
F(24) A(0)	Disable module
F(25) A(0)	Triggers the unit. Q = 1 if unit was ready for trigger; Q = 0 otherwise
F(26) A(0)	Enables unit

F(n) implies function code 'n' and A(n) implies module subaddress 'n'

Table 3–3: LeCroy 4222PDG functions

[2]The Hinds PEM-80 has a 50kHz base frequency.

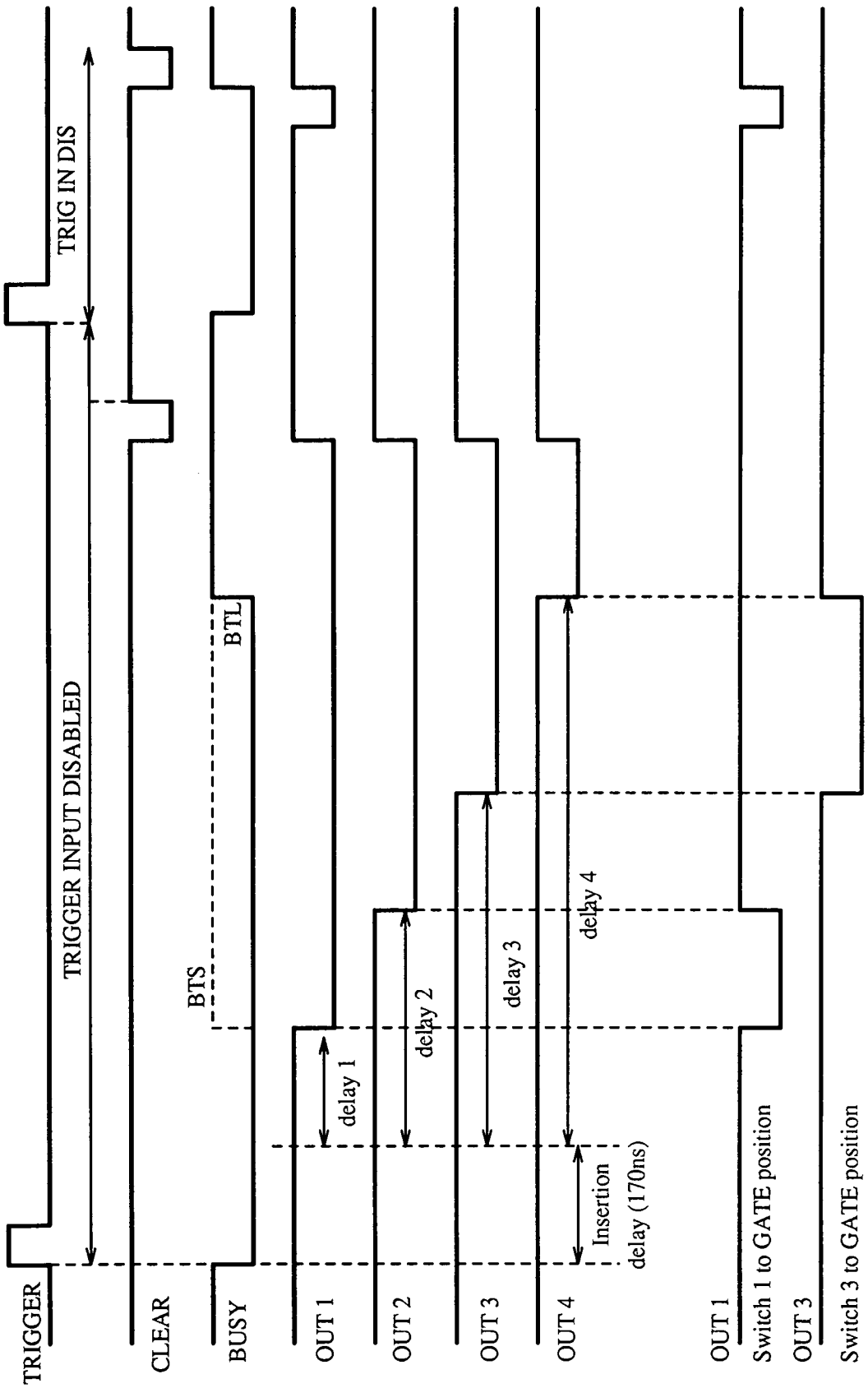

Figure 3–2: Schematic diagram of LeCroy 4222PDG pulse delay generator non-retrigger mode. BTS and BTL denote the 'busy til shortest' and 'busy til last' modes respectively

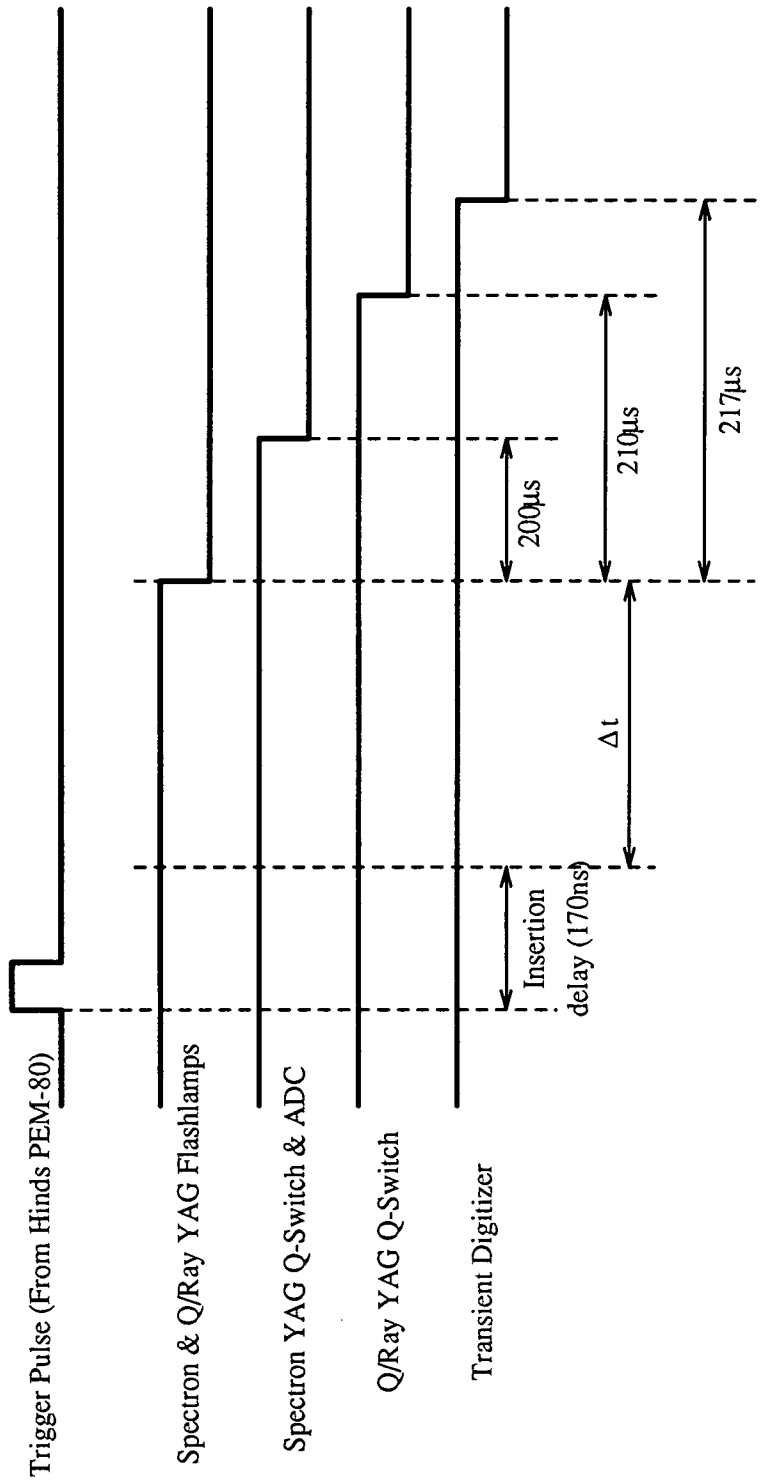

Figure 3–3: Timing sequence for LeCroy 4222PDG during two laser experiment

3.2.4 Hytec ADC520 Analogue to Digital Converter

While the transient digitizer performed the necessary fast waveform sampling function there were several other sources to be monitored during an experiment particularly for power normalization purposes. This was handled by a Hytec model ADC520 four channel analogue to digital converter. This unit had a conversion time of approximately 20μs with each channel also having a preamp for independently programmable gain [3] .

Command	Function Performed
F(0) A(0-3)	Reads data for channel 0-3
F(1) A(0)	Reads control register
F(8) A(15)	Test module LAM
F(16) A(0)	Writes programmable gain register
F(16) A(15)	Writes test mode data into all data registers, disables ADC's and enters test mode
F(17) A(0)	Writes control register
F(24) A(0)	Disable module LAM
F(25) A(15)	Resets module and exits test mode
F(26) A(0)	Enable LAM
F(27) A(0)	Tests to see if LAM enabled

F(n) implies function code 'n' and A(n) implies module subaddress 'n'

Table 3–4: Hytec ADC520 functions

3.2.5 Spectron SL4000SC Scan Controller

A SL4000SC scan controller from Spectron Laser Systems was used to control the grating position of the dye laser. In contrast to the the other devices used this

[3]This feature was never fully debugged.

was not under CAMAC control but instead used one of the RS-232 serial ports on the PC [1].

The scan controller provided a number of low level functions on which the device drivers for the dye laser were based. These included reading/writing the target value, start/stop scan, etc.. The commands sent to and received from the scan controller were coded in a specific frame structure incorporating full cyclic redundancy check (CRC) data validation with all commands returning an acknowledge packet. A summary of the functions provided by the SL4000SC is given in table 3–5.

Command (hex)	Function
00	Null command. Used for testing SL4000SC status
15	Write target value
16	Read target value
1A	Write present position value
1B	Save present position value
1C	Read present position value
1D	Start scan
1E	Send pulses
1F	Stop scan

Table 3–5: Spectron Laser Systems SL4000SC functions

The dye laser was used in two basic modes of operation. Firstly a continuous scan could be initiated to a predefined target. In this mode the output from the various instruments, eg digitizer, ADC, could be monitored whilst scanning the wavelength. In the second mode the dye laser stepped a predefined amount and then a fixed number of shots were fired before stepping to the next wavelength. This was the mode used when colecting spectra.

3.3 IBM PC-AT Hardware

To allow full use of the CAMAC instrumentation several low level features of the PC-AT type computer had to be used, the most important of which is the interrupt structure.

A conventional program running under normal conditions would have to continually poll all of the devices it controlled at regular intervals to read, write or update them. For the purposes of the present work, however, this was not sufficient since devices such as the Nd:YAG laser must run at a precise repetition rate. If the polling method were used then the time taken between successive Nd:YAG laser triggers would depend on the amount of time taken to update the other devices under the control of the computer.

The PC-AT family of computers provide what are known as interrupts. These are special conditions which arise from within the CPU, from external devices (ie. keyboard), or in software. When one of these conditions is detected a special routine known as an exception handler or interrupt service routine is executed. This task completed, the computer then continues to do whatever it was doing before the interrupt occurred [2,3].

An important question is establishing which interrupt service routine to execute. Each interrupt condition has associated with it a number in the range 0 to 255 and this number is used as an index into a table lying in the lowest 1kByte of memory. Each entry in the table (commonly called the Interrupt Vector Table) is four bytes long and contains the address of the service routine associated with the interrupt detected. As an example, if interrupt number 12 was generated the computer would multiply this number by four. It would then read four bytes from absolute address 48 and execute the routine at the address given by these four bytes. The interrupt vector table is shown schematically in figure 3–4.

The addresses in the vector table are set when the computer boots up initially. However, knowing how the interrupt service works means that the programmer

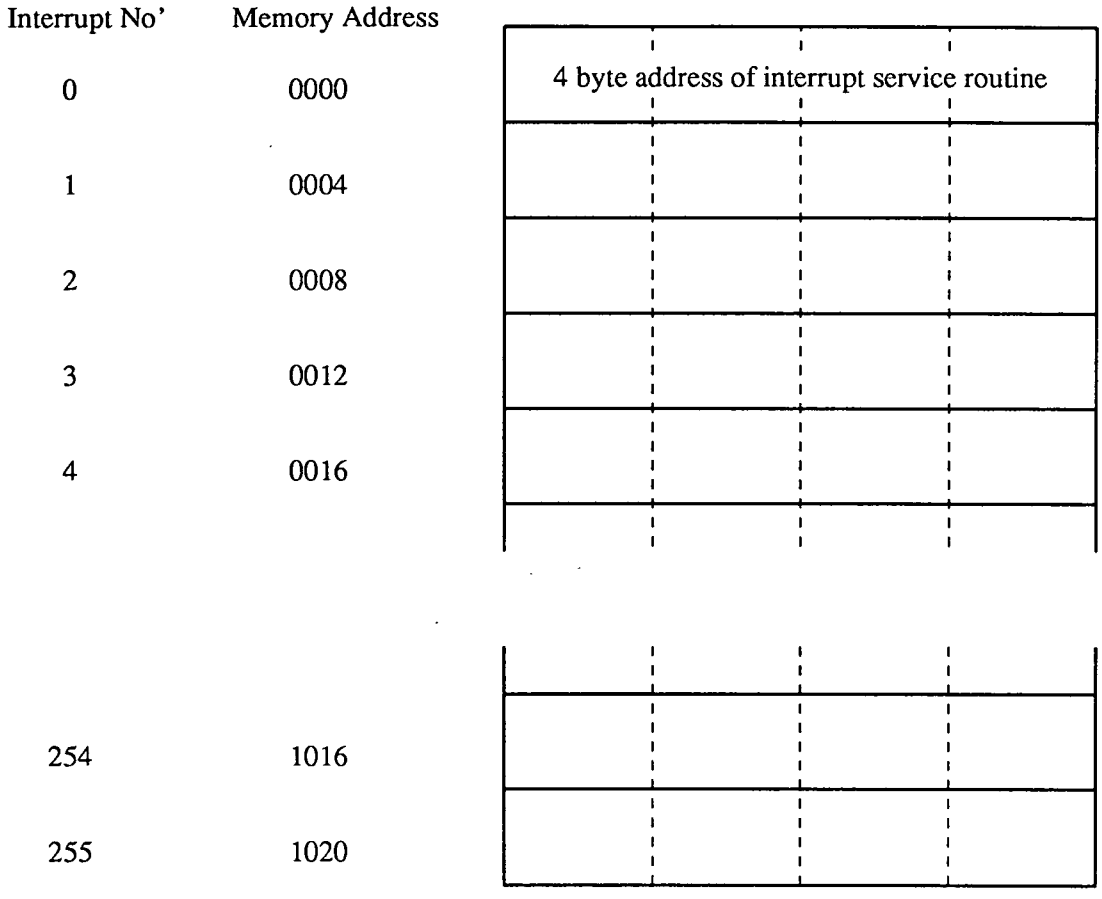

Figure 3–4: Structure of PC-AT Interrupt Vector Table

is free to replace the addresses in the table with those of alternative routines. For instance, if a programmer wanted to take control of interrupt number 12 as explained earlier then they would simply replace the four bytes at absolute address 48 with the four byte address of their own interrupt service routine. Having done this the new routine will now be executed every time an interrupt number 12 occurs.

The main reason for wishing to use interrupts is that all PC-AT type computers have an on-board timer unit which generates an interrupt number 8 at precise intervals. In addition, the interval between interrupts is programmable and lies in the range 18.2Hz (the default) and approximately 1.2MHz. By taking control of this interrupt it was possible to perform functions, ie. Nd:YAG laser trigger and data acquisition, at a precise repetition rate and with minimal timing jitter. [4]

3.4 Data Acquisition Code

The data acquisition code developed had to perform several basic functions.

Firstly, it had to provide some means of setting the parameters for and monitoring the output from the various instruments under its control, particularly the CAMAC modules and the laser system. Secondly, it had to synchronize all active modules with the dye laser scanning and phase output from the photo-elastic-modulator when carrying out a wavelength scan. In addition, several other 'utilities' were found to be useful. The next sections describe the various code components in outline. Most of the code was written in 'C' [4] [5] with small sections of assembly language [6] for machine-specific code [2,3].

---

[4]Typically less than 50ns.

[5]Microsoft 'C' version 5.10.

[6]IBM Macro Assembler version 2.00.

3.4.1 Digitizer Setup Routines

For the present work the main source of data was the transient digitizer. Having recorded the required number of TOFMS waveform samples the data was then down-loaded to the PC for processing. The processing stage consisted of integrating discrete segments of the wave form (with background subtraction), power normalization (if required) and saving the processed data to temporary buffers before writing to disk.

The code for setting up the digitizer and the various parameters associated with it allowed the waveform output of the digitizer to be monitored in real time for fairly short record lengths and also allowed zooming in on individual parts of the waveform [5]. Gates could then be set specifying start and stop points for integration (i.e. for different mass channels on TOFMS data) along with the associated start/stop pairs for the required background subtraction gates (one for each signal gate).

For very light ions, especially H^+, the ion signal was often difficult to observe due to the Q-switch noise from the Nd:YAG laser which appeared at the same point on the TOF signal. Since the H^+ signal was often used as a check it was important to be able to monitor this fairly easily. This was done by summing a number of waveforms with no signal other than background, Q-switch noise etc., and then actively subtracting the resulting waveform from the signal bearing waveform on each shot. A mass calibration scale could also be placed on the TOF spectrum by choosing two points on the waveform along with their known associated masses.

The setup code for the digitizer was also used to check the relative phase of the Hinds PEM-80 photo elastic modulator. This was achieved by scanning over one $20\mu s$ cycle of the PEM and plotting a digitized signal on the screen. This scanning process was then repeated with successive scans being summed. For purposes of phase checking the signal was usually that from a Molectron power meter (J3-09DW) which collected the laser beam taken from a Brewster angle optic as shown in figure 3–5 although the signal from the MCP could also be used

thus giving a quantitative measure of how the line strength varied with changes in polarization.

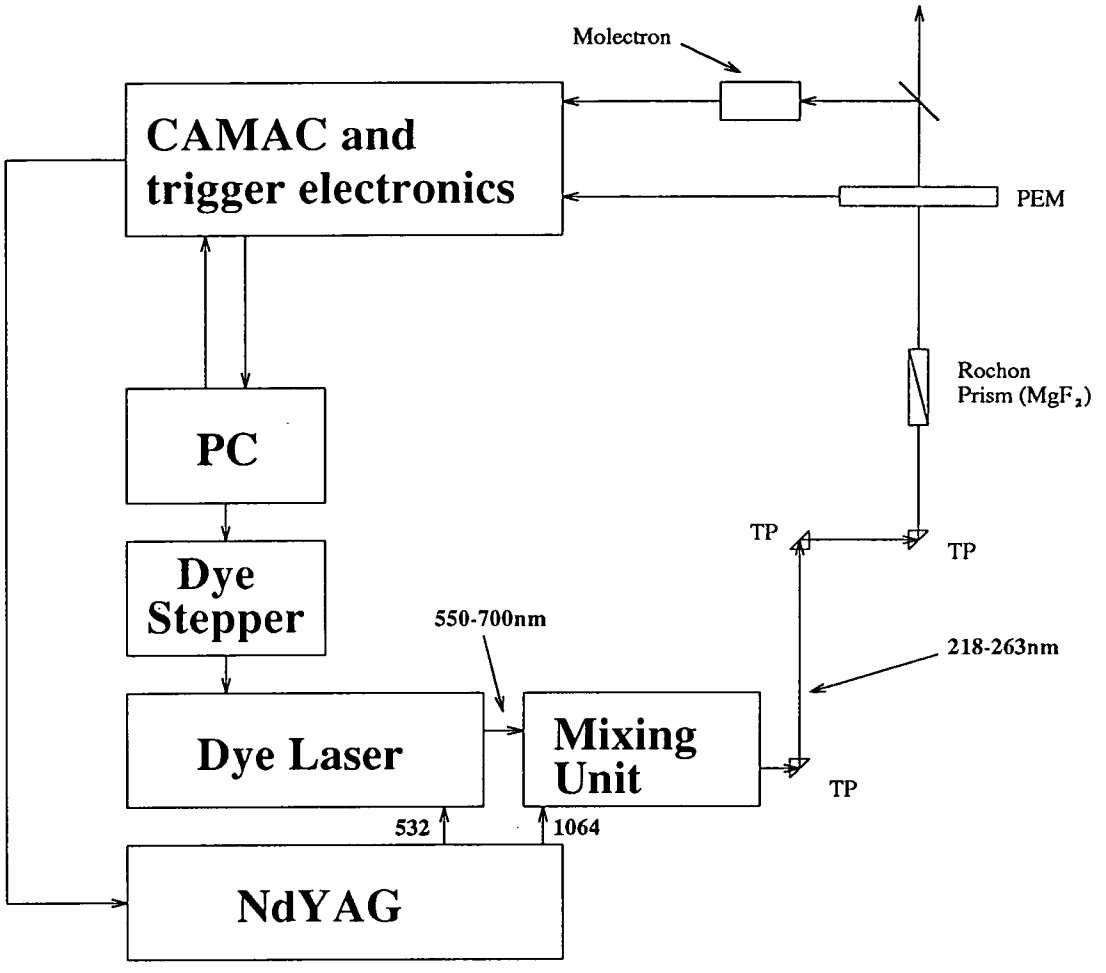

Figure 3–5: Experimental setup for phase checking Hinds PEM-80

The signal collected in this way clearly showed the variation in intensity of the collected component of the beam with the delay between the PEM phase output and firing the YAG Q-switch and enabled any phase corrections to be made fairly easily.

In addition to the above facilities routines were also added to view data from only a single chosen delay set, e.g. one polarization, and to enable the dye laser to stop scanning automatically if the signal within a gate reached a certain level.

3.4.2 Delay Pulse Module Setup Routines

The LeCroy model 4222PDG pulse delay generator was responsible for firing of the lasers and subsequently the data acquisition modules. When using more than one polarization it received an external trigger from the Hinds PEM-80 and was therefore in direct control of the polarization of the probe beam used. This meant that careful setting of the delays and phase relative to the PEM was very important.

The setup routines allowed delay sets [7] to be added or deleted to those already being used. A maximum of ten delay sets, ie. ten polarizations, could be active at any one time with the trigger code automatically cycling through the delay sets on successive laser shots. Using the delay sets in this manner ensured that spectra collected for different polarizations were all directly comparable since no single spectrum would suffer excessively from long term changes in the experimental conditions. [8] .

3.4.3 ADC Setup Routines

Only basic routines were required for the Hytec ADC520 since the configuration was determined largely by internal DIP switches and links. The input for the four individual channels was continually monitored and displayed on screen as four 'bar charts' along with a number representing the digitized value. The software was used to set various parameters for each ADC channel such as zeros, polarity and programmable gain.

One major problem did arise with the ADC520 unit. When using this module to monitor the power output from the laser system with subsequent power normalization it became apparent that the signal was being normalized with respect to

---

[7]Each delay set consisted of four delays, with one for each channel of the 4222PDG.

[8]The LeCroy unit introduces a base delay of 170ns on all delays. Thus a programmed delay of 0ns actually corresponds to a delay of 170ns

the power signal from the previous shot [9] . This was cured by introducing at least one dummy shot at the start of each data point to synchronize all units correctly.

3.4.4 Wavelength Scan Setup

These routines allowed the setting of the various parameters governing the data acquisition process during a wavelength scan. Each module, and individual channels in the case of the ADC, could be switched on or off depending on the signal source.

The software allowed a maximum of ten wavelength ranges in a single scan. Two separate scan speeds were used during scanning. The 'slow scan' variable controlled the scanning speed on a data-point to data-point basis within a given wavelength range whereas 'fast scan' controlled the scanning speed between the end of one range and the beginning of the next (if any).

The laser repetition rate, and thus the overall rate of data acquisition, was variable between 9.1 and 20Hz with 10Hz being the normal choice repetition rate.

Throughout the wavelength scan the doubling and mixing crystals in the Spectron laser system were continually reoriented using stepper motors controlled by a dedicated BBC micro-computer to optimize the power in the output beam. This meant that after changing the wavelength, ie moving to the next point in a scan or going to the start of the next wavelength range, the tracking system occasionally required some time to stabilize the power output. To compensate for this a user definable number of shots were ignored at the start of each data point [10] .

The software also allowed one of several power normalization modes to be selected. With the autotracking system used the shot-to-shot power fluctuations

---

[9]Detected due to an apparent anticorrelation in the power versus normalized signal plot.

[10]This number had to be greater than or equal to one to compensate for an idiosynchracy with the ADC unit used.

were fairly large. This meant that the signal had to be power normalized on a shot-to-shot basis since for $n > 1$, $\sum_i \frac{signal_i}{power_i^n} \neq \frac{\sum_i signal_i}{\sum_j power_j^n}$, i.e. on each shot the signal was divided by the an appropriate power of the pulse energy and then the normalized signals were averaged, rather than averaging the signal and pulse energy separately and then dividing the averaged signal by the square of the averaged power . This made it necessary to store the signal and power values in an extra data buffer until power normalization could take place.

Having set up the parameters as required, the scan was initiated using a control-g keystroke. This allowed the output from any of the modules or analysis of other data files to take place whilst the data acquisition continued in the background.

When the data acquisition was complete (or aborted using a control-a keystroke) the data could then be saved to disk. The main data saving routine split the data into a number of files given by the number of wavelength ranges times the number of masses saved times the number of polarizations used, i.e. each file contained data for one mass using a single polarization over one wavelength range. The extension on the filename indicated the specific mass, etc., of the data in a particular file.

The files were in 'humanly readable' ASCII format to aid interpretation. Each data type within the files was contained in a separate field whose size was determined by the data type itself. This made it relatively easy to add new data types without having to convert older data files to the new format.

3.4.5 Data Acquisition

As mentioned in section 3.3 the program took over control of the PCs' interrupt number 8 in order to maintain the constant 10Hz repetition rate required in these experiments. The new interrupt handler installed was a fairly short routine written

in assembler [11] which called the 'harvest' routine on alternate shots to do the processing [12] .

Once all of the data acquisition modules and parameters had been initialized and configured the wavelength scan was initiated using a control-g keystroke. From that point on until the data acquisition was completed (or aborted as mentioned previously) the harvest routine and main program code communicated using blocks of shared data. This was necessary because these two threads of execution were not synchronized in any normal programming sense. This meant that great care had to be taken when choosing data types to be used for shared data and also in accessing the data [13] .

A basic flow diagram of the data collection and processing procedure is shown in figure 3–6.

After checking the status of various flags, data from the 'active' modules were read into memory. Having done this the relevant modules were re-enabled, the pulse delay generator re-armed and, if necessary, triggered from the dataway [14] . This done, the data were then processed in the required manner. If data were being collected from the digitizer then the datum in each mass bin was integrated

---

[11] Although the Microsoft C compiler had language extensions to enable routines coded in C to be installed as interrupt handlers this did not seem to work for several of the hardware interrupts controlled by the Intel 8259 programmable interrupt controller (PIC). This made it necessary to produce some code in Intel 80x86 assembly language.

[12] Although the interrupt timing is programmable it cannot be any less than approximately 18.2Hz. For this reason 10Hz was achieved by programming the interrupt timer for 20Hz and only processing on every second shot.

[13] If the harvest routine read data when the main program was half way through updating it a serious program error and in most cases a program crash could have resulted.

[14] The 4222PDG delay generator was usually triggered externally by the Hinds PEM-80.

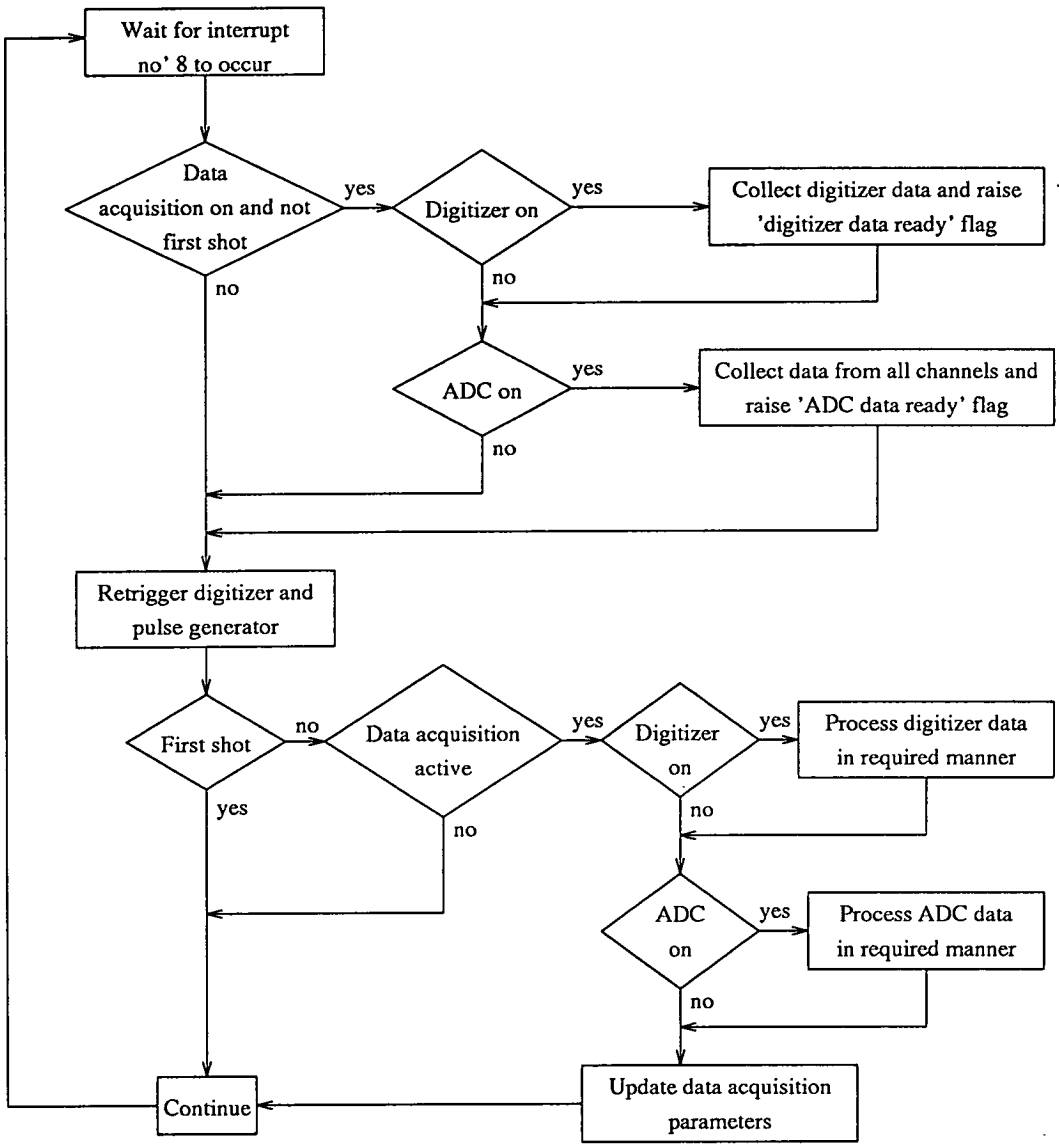

Figure 3–6: Flow chart for data acquisition code

with background subtraction being performed and then corrected for input signal polarity [15] . The processed digitizer data were then saved in a power normalization buffer if required. Next, data from each channel of the ADC were checked, corrected for signal polarity and saved in power normalization buffers as required. Having processed the raw data all relevant parameters, i.e. number of shots multiplexed, delay set used, etc., were updated before returning to the main thread of execution.

Rather than saving all data in internal arrays which would have required too much memory, a small number of data points were buffered in memory before being flushed to a temporary file on disk. The power normalization process was also carried out just before saving the buffered data to disk.

For the present work the record length of the digitizer was limited to 4096 samples. This was perfectly adequate for the relatively light ions of interest. With the code in its present form this quantity of data could easily be processed at 20Hz implying that a switch to 8192 samples at 10Hz would be possible. With some changes to the structure of "harvest" this could be doubled to 16k samples at 10Hz without too much trouble. A listing of the main data acquisition routine is given in appendix A.

3.4.6 Data Analysis

Data saved to disk could be read back into the program for data analysis and subsequent processing.

The display was configurable into windows with each window showing different data sets or alternative segments of the same data set. This allowed easy visual comparison of data sets that should have been similar (or otherwise). By default all data types collected, ie digitizer, ADC, were displayed and data sets collected

---

[15]The incoming signal from the MCP was negative going for ion signal.

over slightly different wavelength ranges could be synchronized on screen to further aid comparison of spectra.

For quantitative data analysis the main requirement was the ability to integrate the areas under individual peaks. This was accomplished using one set of gates for defining the signal and a second set of gates to define the background level to be subtracted. The data within any window could be scaled in both directions to aid viewing of the data.

In certain cases, as will become apparent in section 5, different electronic transitions of a molecule being studied will result in different ions being formed and subsequently detected. If a wavelength scan was taken over a region where different electronic transitions were contributing to the overall signal intensity the resulting spectrum often became very congested. However, knowing which ions were produced by the different contributing transitions made it possible to unscramble the spectrum since multiples of the spectra from different masses could be subtracted from one another with the resulting difference spectrum representing (hopefully) the contributions to the signal intensity from the transition of interest only.

Bibliography

[1] C Programmers Guide to Serial Communications, *J. Campbell* (Sams)

[2] Assembly Language Tools & Techniques for the IBM Microcomputers, *J. Sanchez* (Prentice Hall)

[3] IBM PC Assembler Language & Programming, *P. Abel* (Prentice Hall)

[4] The C Programming Language, *B. W. Kernighan, D. M. Ritchie* (Prentice Hall)

[5] Programmers Guide to the EGA and VGA Cards, *R. F. Ferraro* (Addison-Wesley)

Chapter 4

Rotational Line Strengths

4.1 Introduction

The long term aim of this work was to measure the multipole moments of the angular momentum distribution in a reaction product using polarization sensitive REMPI and in this section an introduction to orientation and alignment in samples will be presented.

As with any spatial property, if we are to describe quantitatively any anisotropy within the system we require a basis set for the expansion. In general the basis set chosen would be the set of spherical harmonics given by

$$Y_q^k(\theta,\phi) = (-1)^q \left[\frac{2q+1}{4\pi} \cdot \frac{(k-q)!}{(k+q)!}\right]^{1/2} \cdot P_q^k(\cos\theta) e^{iq\phi} \tag{4.1}$$

where k and q are the rank and component of the basis function respectively, θ and ϕ are the polar and azimuthal angles associated with the usual spherical coordinate system, and $P_q^k(x)$ is the associated Legendre function [4]. These functions would then form a complete orthonormal basis set with which to describe the system anisotropy. The set of coefficients so describing the system in terms of this basis set is called a Laplace series expansion.

For the present work however this is not quite sufficient since we are describing a quantum system whereas the method outlined above assumes a classical system.

Density matrix theory states that all eigenvalues of the density matrix must be positive definite and sum to unity. This places strict limits on the description of the system and means that for low **J** the basis functions are not orthogonal. As **J** increases, however, the basis functions quickly revert to their classical limit of the spherical harmonics.

The first four cylindrically symmetric basis functions, (not including the zeroth order which is simply spherical), are shown in figures 4–1 to 4–4 with the relevant mathematical expressions for the basis functions and the moments, $\mathcal{A}_{0+}^{\{k\}}$, in tables 4–1 and 4–2 respectively.

$$J_{0+}^{\{0\}} = 1$$
$$J_{0+}^{\{1\}} = J_z$$
$$J_{0+}^{\{2\}} = 6^{-1/2}\left(3J_{z^2} - \mathbf{J}^2\right)$$
$$J_{0+}^{\{3\}} = 10^{-1/2}J_z\left(5J_{z^2} - 3\mathbf{J}^2 + 1\right)$$
$$J_{0+}^{\{4\}} = \left(70^{-1/2}/2\right)\left(3\mathbf{J}^4 - 6\mathbf{J}^2 - 30J_{z^2}\mathbf{J}^2 + 25J_{z^2} + 35J_{z^4}\right)$$

Operators with multiple subscripts represent symmetric sums of all unique permutations, i.e. $J_{xy} = J_xJ_y + J_yJ_x$ but $J_{x^2} = (J_x)^2 \cdot \langle|\mathbf{J}^2|\rangle$ is the magnitude of the vector squared, i.e. $\langle|\mathbf{J}|\rangle = [J\,(J+1)]^{1/2}$

Table 4–1: Angular momentum spherical tensor operators [6] expressed using the Hertel-Stoll normalization [1]

$$\mathcal{A}_{0+}^{\{0\}} = 1$$
$$\mathcal{A}_{0+}^{\{1\}} = \langle(J_i|J_z/\mathbf{J}|J_i)\rangle$$
$$\mathcal{A}_{0+}^{\{2\}} = \langle(J_i|(3J_{z^2} - \mathbf{J}^2)/\mathbf{J}^2|J_i)\rangle$$
$$\mathcal{A}_{0+}^{\{3\}} = (1/2)\,\langle(J_i|J_z(5J_{z^2} - 3\mathbf{J}^2 + 1)/\mathbf{J}^3|J_i)\rangle$$
$$\mathcal{A}_{0+}^{\{4\}} = (1/8)\,\langle(J_i|(3\mathbf{J}^4 - 6\mathbf{J}^2 - 30J_{z^2}\mathbf{J}^2 + 25J_{z^2} + 35J_{z^4})/\mathbf{J}^4|J_i)\rangle$$

J_i represents the angular momentum of the state whose distribution is required

Table 4–2: Definitions for the moments of the ground state angular momentum distribution [6] using the Hertel-Stoll normalization [1]

The alignment parameters lie in general within the respective ranges

$$-1 \leq \mathcal{A}_{0+}^{\{2\}} \leq 2 \tag{4.2}$$

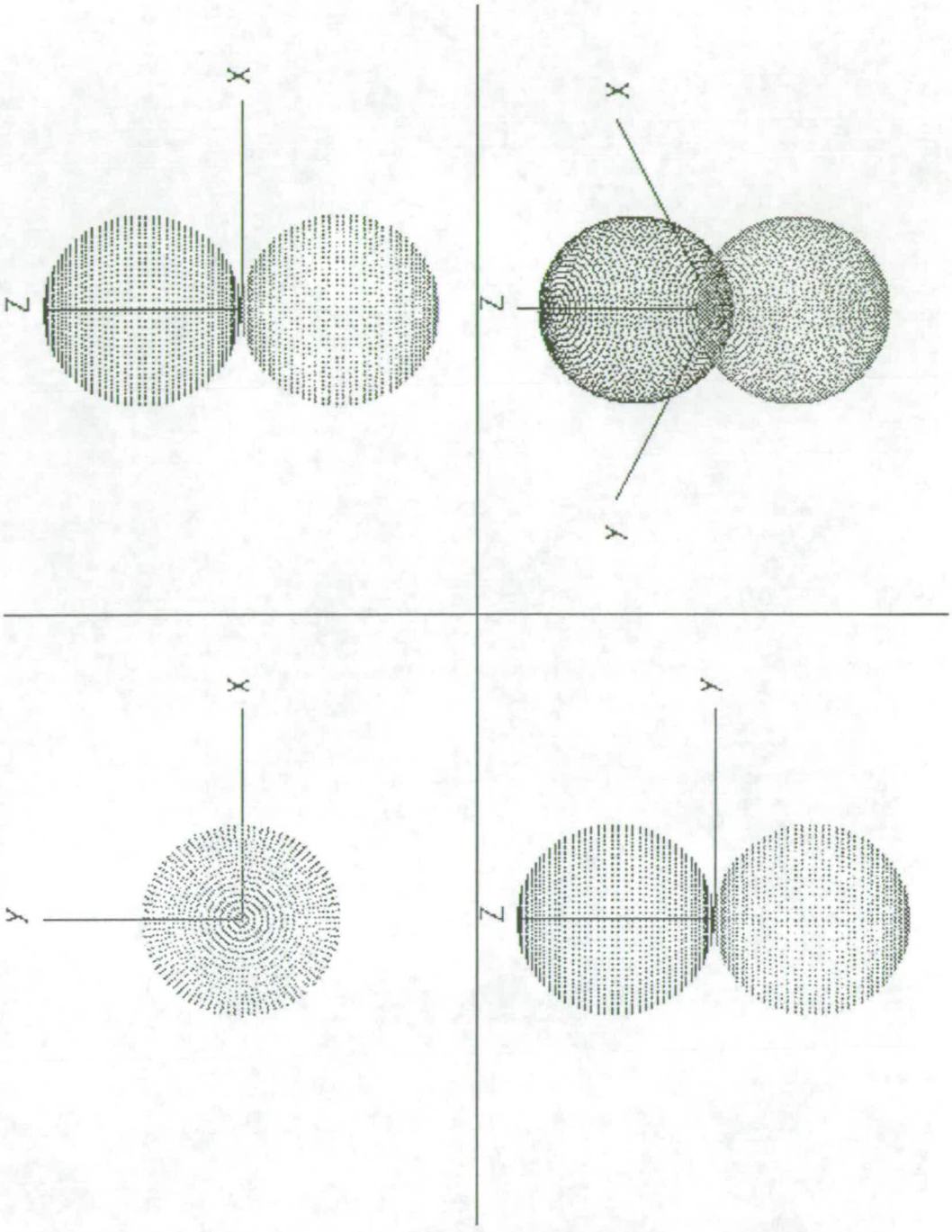

Figure 4–1: Illustration of $J_{0+}^{\{1\}}$ basis function

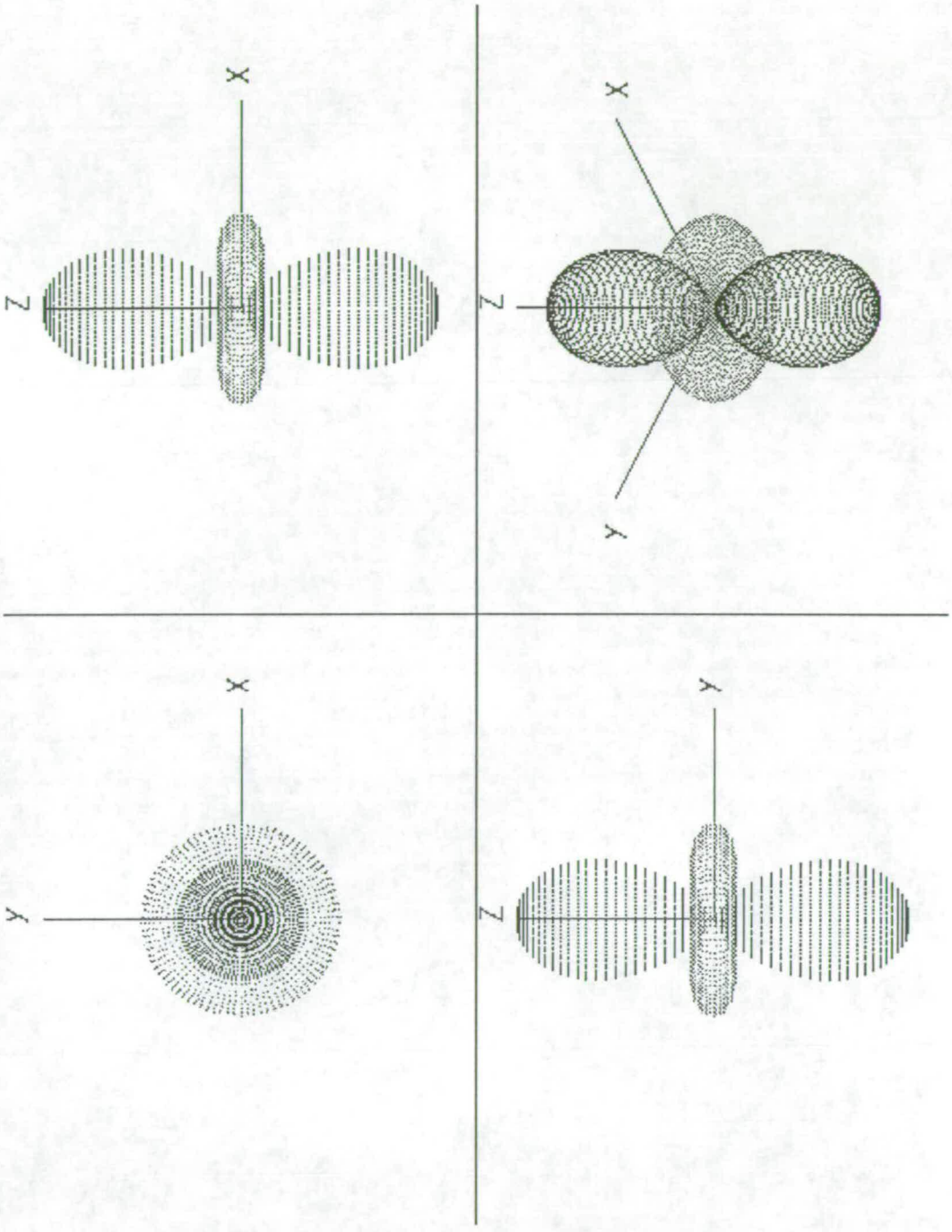

Figure 4–2: Illustration of $J_{0+}^{\{2\}}$ basis function

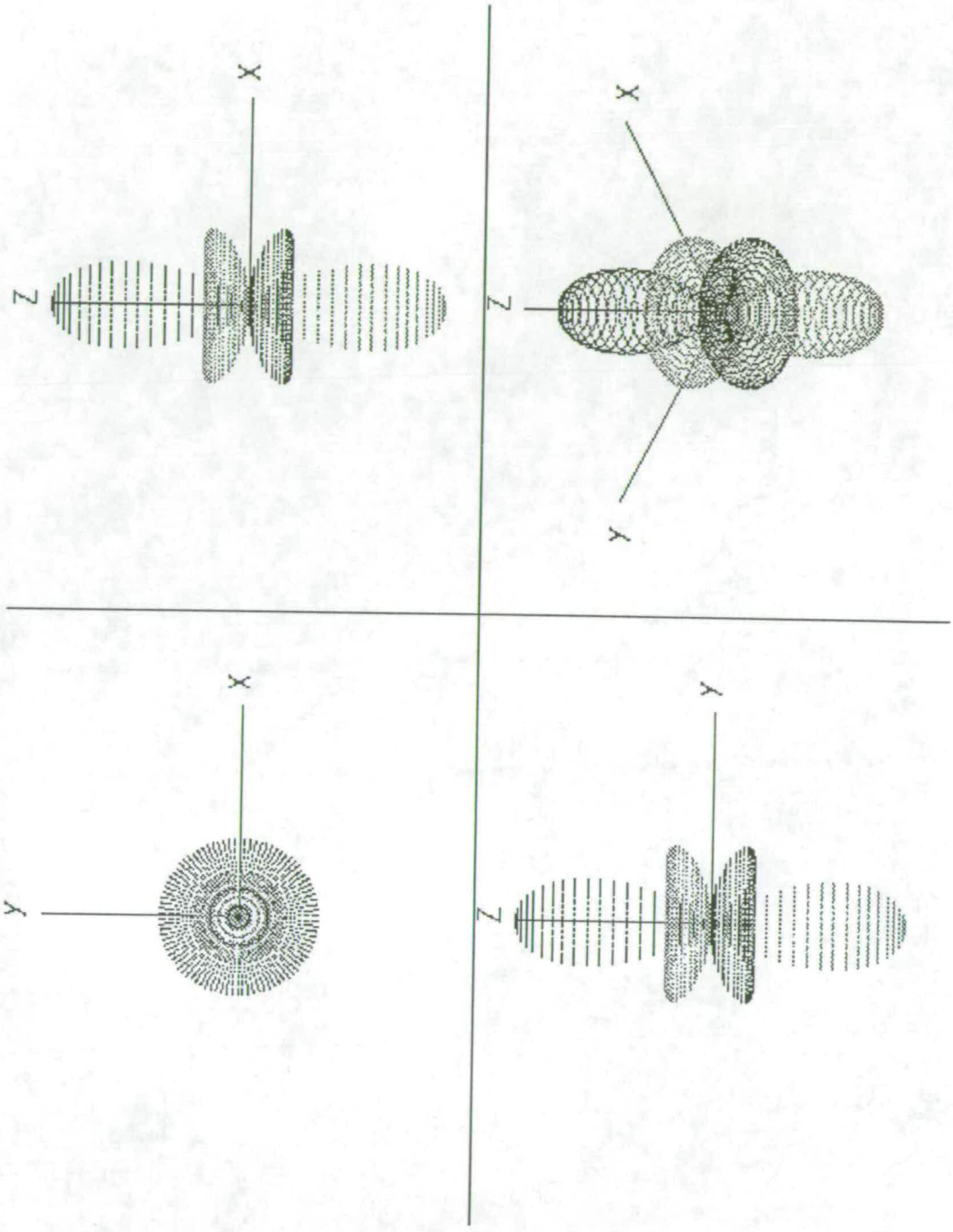

Figure 4–3: Illustration of $J_{0+}^{\{3\}}$ basis function

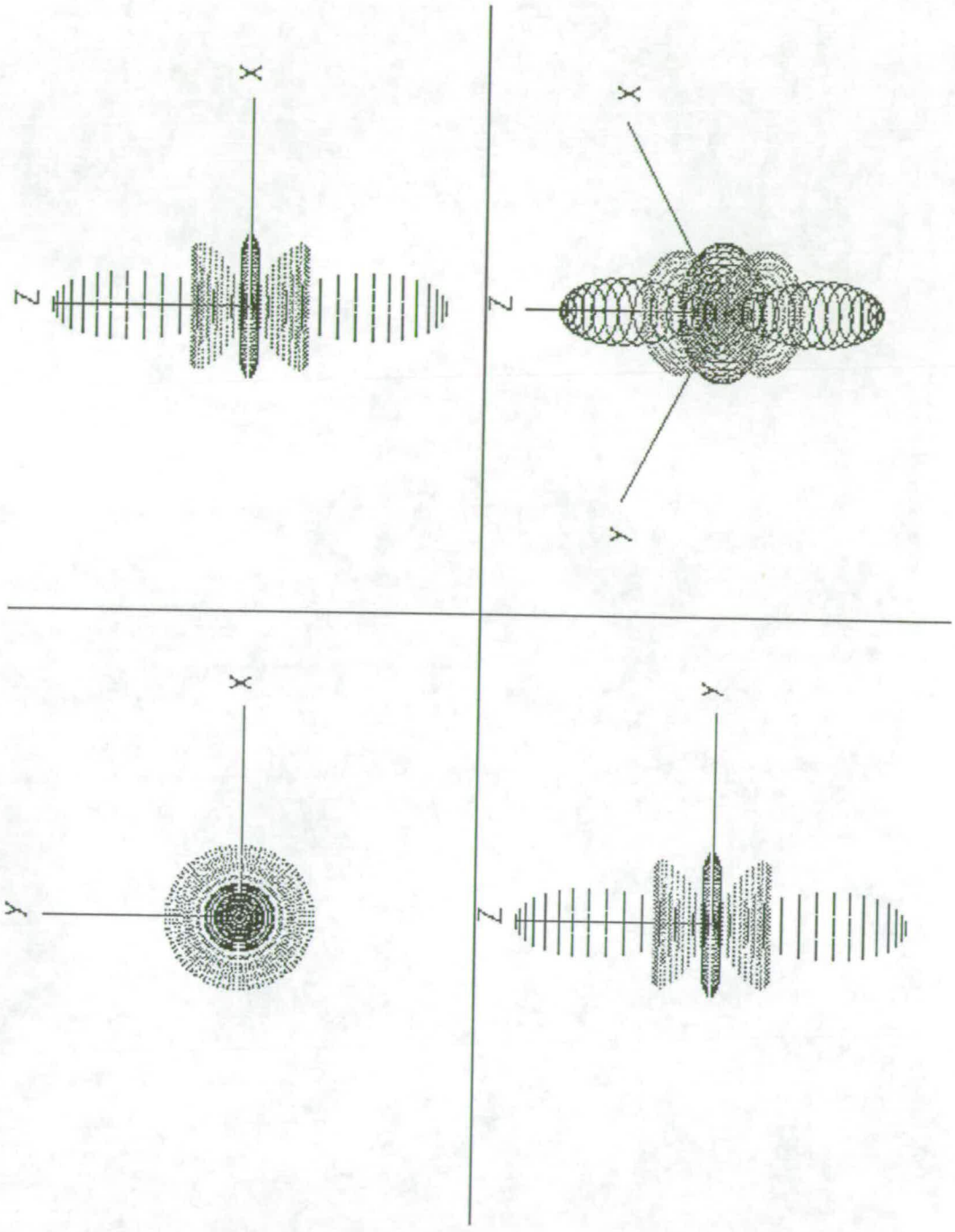

Figure 4–4: Illustration of $J_{0+}^{\{4\}}$ basis function

and

$$-\frac{3}{7} \leq \mathcal{A}_{0+}^{\{4\}} \leq 1 \tag{4.3}$$

If, however, the alignment is created via a photofragmentation process then $\mathcal{A}_{0+}^{\{4\}} = 0$ and $\mathcal{A}_{0+}^{\{2\}}$ lies between 1 and $\frac{4}{5}$ which becomes $-\frac{2}{5}$ and $\frac{4}{5}$ in the high **J** limit.

The most noticable property of these functions is the fact that the even order moments ($k = 0, 2, 4$) are symmetric with respect to a reflection in the x-y plane whereas the odd order moments ($k = 1, 3$) are antisymmetric. Consider a system where the angular momentum vectors are 'aligned' along the z axis but with neither the -z or the +z direction being preferred. In this case the second order, or quadrupole, moment would be positive but the first order, or dipole, moment would be zero since the positive and negative contributions would cancel each other out. It is therefore the case that for the system to posses any non-zero odd moments then the angular momentum vectors must point preferentially along a given direction, ie have a net helicity. This is termed orientation. If, on the other hand, the angular momentum vectors lie preferentially along one axis but pointing with equal probability in both directions then only the even moments of the system can be non-zero. This is termed alignment. These two cases are illustrated in figure 4–5

One further important point to be considered is that to create a system with a net orientation non-linearly polarized light must be used. In the present work all anisotropies in the samples were created by photolysis using linearly polarized light. This meant that the system had no net helicity and therefore could possess even moments (alignment) only.

The geometry used throughout the present work is shown in figure 4–6. The lab frame, labeled x, y, z, is determined by the electric vector of the (linearly polarized) photolysis beam and is chosen such that the electric vector coincides with the lab z axis. The detector frame, labelled x_{det}, y_{det}, z_{det}, is determined by the geometry of the variable wave plate used with the y_{det} and z_{det} axes of the detector frame chosen to coincide with the major and minor axes of the wave

a)

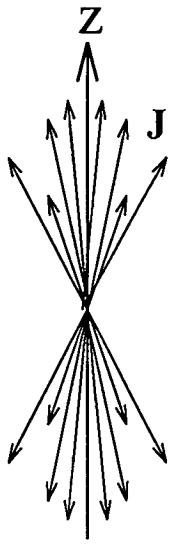

Molecule rotates preferentially in xy-plane but both directions equally probable

b)

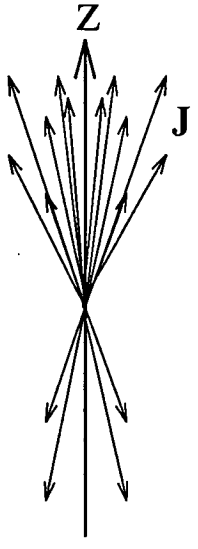

Molecule rotates in xy-plane but one direction of rotation preferred

Figure 4–5: Illustration of the differences between even moments (alignments) and odd moments (orientations). In a) the angular momentum vectors, denoted **J**, lie predominantly along the z direction but with equal probability in either direction. This implies that the molecules rotate in the x-y plane but without a preferred sense of rotation. This is alignment. In b) again the angular momentum vectors lie along the z axis but in this case the preferred direction is in the positive z sense implying a preferred sense of rotation. This is orientation.

plate. In the present work the anisotropy was created by the photolysis process and thus the angular momentum distribution in the products is fixed relative to the lab frame, x, y, z. It is then by altering the geometry of the wave plate, i.e. orientation and retardance, that the probe beam polarization is modified and the line strengths monitored as a function of the polarization.

4.2 Line Strengths for Isotropic Samples

Before looking at the full theory, however, it is important to realize that the line strength factors depend on the polarization of the probe beam even for a sample in which the spatial distribution of the angular momentum vectors is isotropic. Indeed, a study of exactly how the line strength varies with polarization is, in certain cases, essential to gain enough information to perform a full study on an anisotropic sample.

The two-photon rotational line strengths for an isotropic sample are given by the Bray-Hochstrasser theory [2]. The relevant equations are given in tables 4–3 and 4–4 [1] where J denotes the angular momentum of the initial state and Λ is the modulus of the projection of the electronic orbital angular momentum on the internuclear axis for a Hunds case (a) diatomic molecule.

Using the line strengths in tables 4–3 and 4–4 the required intensity is given by

$$I(J) = C \cdot n(J) \cdot \mathcal{A}_{0+}^{\{0\}}(J) \cdot P_{0+}^{\{0\}}(J) \tag{4.4}$$

where

C is a constant of proportionality (detection efficiency, etc.)

---

[1] The formulae presented in these tables differ slightly from those in reference [2] due to the different phase convention used for the $R^{\pm 1}$ component. In [2] $R^{\pm 1} = 2^{-1/2}(R_x \pm iR_y)$ whereas the formulae presented use $R^{\pm 1} = \mp 2^{-1/2}(R_x \pm iR_y) \equiv \mp \langle \Lambda \pm 1 | er^{\pm} | \Lambda \rangle$. Here $r^{\pm} = \mp 2^{-1/2}(r_x \pm ir_y)$ where $r_\alpha (\alpha = x, y, z)$ are the cartesian components of the electric dipole operator.

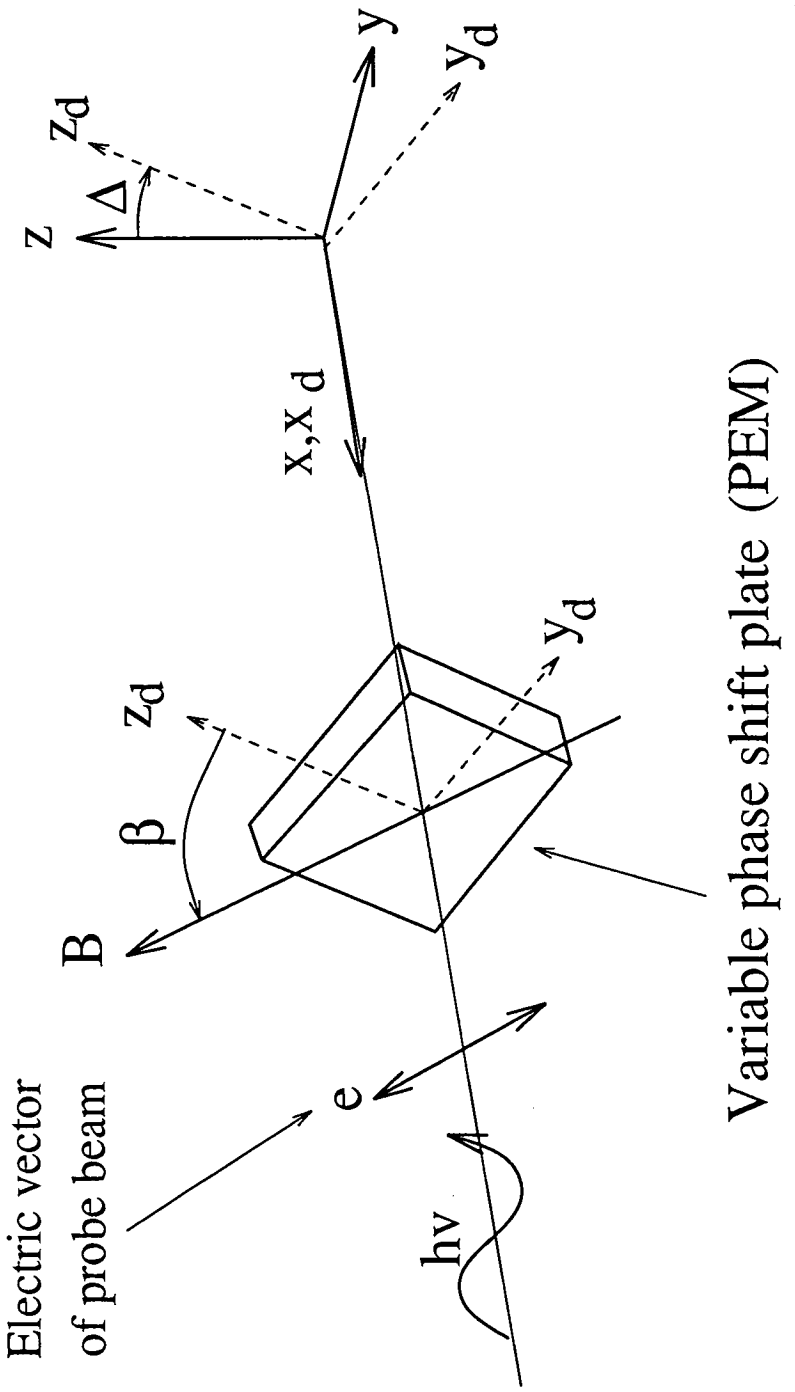

Figure 4–6: Geometry used throughout the present work. The lab frame, x, y, z, is determined by the electric vector of the photolysis beam with the detector frame, x_{det}, y_{det}, z_{det}, determined by the geometry of the variable wave plate

	$\Delta\Lambda = \pm 1^{\dagger}$	$\Delta\Lambda = \pm 2^{\ddagger}$
O branch	$\frac{K_0(J\mp\Lambda-1)(J\mp\Lambda)(J\mp\Lambda-2)(J\pm\Lambda)}{15J(J-1)(2J-1)}$	$\frac{K_0(J\mp\Lambda)(J\mp\Lambda-1)(J\mp\Lambda-2)(J\mp\Lambda-3)}{30J(J-1)(2J-1)}$
P branch	$\frac{K_0(J\mp\Lambda-1)(J\mp\Lambda)(J\pm2\Lambda+1)^2}{30J(J+1)(J-1)}$	$\frac{K_0(J\mp\Lambda)(J\mp\Lambda-1)(J\mp\Lambda-2)(J\pm\Lambda+1)}{15J(J+1)(J-1)}$
Q branch	$\frac{K_0(J\pm\Lambda+1)(2\Lambda\pm1)^2(2J+1)(J\mp\Lambda)}{10J(J+1)(2J-1)(2J+3)}$	$\frac{K_0(J\mp\Lambda)(J\mp\Lambda-1)(J\pm\Lambda+1)(J\pm\Lambda+2)(2J+1)}{5J(J+1)(2J-1)(2J+3)}$
R branch	$\frac{K_0(J\pm\Lambda+1)(J\pm\Lambda+2)(J\mp2\Lambda)^2}{30J(J+1)(J+2)}$	$\frac{K_0(J\mp\Lambda)(J\pm\Lambda+1)(J\pm\Lambda+2)(J\pm\Lambda+3)}{15J(J+1)(J+2)}$
S branch	$\frac{K_0(J\pm\Lambda+1)(J\pm\Lambda+2)(J\pm\Lambda+3)(J\mp\Lambda+1)}{15(J+1)(J+2)(2J+3)}$	$\frac{K_0(J\pm\Lambda+1)(J\pm\Lambda+2)(J\pm\Lambda+3)(J\pm\Lambda+4)}{30(J+1)(J+2)(2J-3)}$

$K_0 = (4\pi/3)^2(2J_i+1)^{-1}$

† All expressions for $\Delta\Lambda = \pm 1$ to be multiplied by $\mu^2_{\Delta\Lambda=\pm1} = |R^0_{ei}R^{\pm1}_{fe} + R^{\pm1}_{ei}R^0_{fe}|^2$

‡ All expressions for $\Delta\Lambda = \pm 2$ to be multiplied by $\mu^2_{\Delta\Lambda=\pm2} = |R^{\pm1}_{ei}R^{\pm1}_{fe}|^2$

Values are for linearly polarized light. Line strengths for circularly polarized light are obtained by multiplying the values above by 3/2. The subscripts on R^0 and $R^{\pm1}$ are used to label the one-photon transition which the factor denotes, i.e. R^0_{ei} denotes the amplitude for a $\Delta\Lambda = 0$ one-photon transition from the initial to excited, (virtual), state whereas $R^{\pm1}_{fe}$ denotes the amplitude for a $\Delta\Lambda = \pm1$ one-photon transition from the excited, (virtual), to final state

Table 4–3: Two photon rotational line strength factors for $\Delta\Lambda = \pm1$ and ±2 transitions

	linear	circular
O branch	$\frac{K_0(J^2-\Lambda^2)[(J-1)^2-\Lambda^2]}{30J(J-1)(2J-1)}\mu_s^2$	linear $\times 3/2$
P branch	$\frac{2K_0\Lambda^2(J^2-\Lambda^2)}{30J(J+1)(J-1)}\mu_s^2$	linear $\times 3/2$
Q branch	$\frac{K_0(2J+1)}{9}\mu_i^2 + \frac{K_0(2J+1)[J(J+1)-3\Lambda^2]^2}{45J(J+1)(2J-1)(2J+3)}\mu_s^2$	$\frac{K_0(2J+1)[J(J+1)-3\Lambda^2]^2}{30J(J+1)(2J+3)(2J-1)}\mu_s^2$
R branch	$\frac{2K_0\Lambda^2[(J+1)^2-\Lambda^2]}{30J(J+1)(J+2)}\mu_s^2$	linear $\times 3/2$
S branch	$\frac{K_0[(J+1)^2-\Lambda^2][(J+2)^2-\Lambda^2]}{30(J+1)(J+2)(2J+3)}\mu_s^2$	linear $\times 3/2$

$K_0 = (4\pi/3)^2(2J_i+1)^{-1}$

$\mu_i^2 = |R^0_{ei}R^0_{fe} - R^{+1}_{ei}R^{-1}_{fe} - R^{-1}_{ei}R^{+1}_{fe}|^2$

$\mu_s^2 = |2R^0_{ei}R^0_{fe} + R^{+1}_{ei}R^{-1}_{fe} + R^{-1}_{ei}R^{+1}_{fe}|^2$

Table 4–4: Two photon rotational line strength factors for $\Delta\Lambda = 0$ transitions

$n(J)$ is the population of the lower level involved in the transition
$\mathcal{A}_{0+}^{\{0\}}(J)$ is the coefficient of the lowest order multipole moment, (always normalized to one) and
$P_{0+}^{\{0\}}(J)$ is the relevant line strength factor from tables 4–3 and 4–4.

One important quantity to consider is the ratio of line strength for linearly polarized light (σ_{ll}) to that for circularly polarized light (σ_{cc}). This turns out to be a constant value of $\frac{2}{3}$ except for the special case of a $\Delta\Lambda = 0$ Q branch transition. In this case

$$\frac{\sigma_{ll}}{\sigma_{cc}} = \frac{10J(J+1)(2J+3)(2J-1)}{3[J(J+1)-3\Lambda^2]^2} \cdot \frac{\mu_i^2}{\mu_s^2} + \frac{2}{3} \tag{4.5}$$

which in the high J limit becomes

$$\frac{\sigma_{ll}}{\sigma_{cc}} = \frac{2}{3}\left[1 + 20\left(\frac{\mu_i^2}{\mu_s^2}\right)\right] \tag{4.6}$$

From the footnotes to tables 4–3 and 4–4 it can be seen that the quantity $\frac{\mu_i^2}{\mu_s^2}$ depends on the three factors R^0, R^{+1} and R^{-1}. These represent the probability at each stage of the two photon transition of a change in Λ of 0, +1 or -1 respectively [2] . The value of each of the components R^0, R^{+1} and R^{-1} depends upon the Λ values of the real states which lie in the proximity of the one-photon non-resonant level.

The variations of $\frac{\sigma_{cc}}{\sigma_{ll}}$ and $\frac{\mu_s^2}{\mu_i^2}$ with different values of R^0, R^{+1} and R^{-1} are shown in figures 4–7 and 4–8. Here the factors have been normalized such that

$$\left|R^0\right|^2 + \left|R^{+1}\right|^2 + \left|R^{-1}\right|^2 = 1 \tag{4.7}$$

$\frac{\sigma_{cc}}{\sigma_{ll}}$ varies from $\frac{1}{14}$ for purely perpendicular transitions through 0 when perpendicular and parallel transitions are equally probable to $\frac{1}{4}$ for purely parallel transitions.

---

[2]It is always the case that $|R^{+1}| = |R^{-1}|$. The relative sign of the quantities, however, depends upon the relative symmetries of the wavefunctions of the upper and lower states under a σ_v symmetry operation. If the two wavefunctions have the same symmetry then $R^{+1} = -R^{-1}$ otherwise $R^{+1} = R^{-1}$.

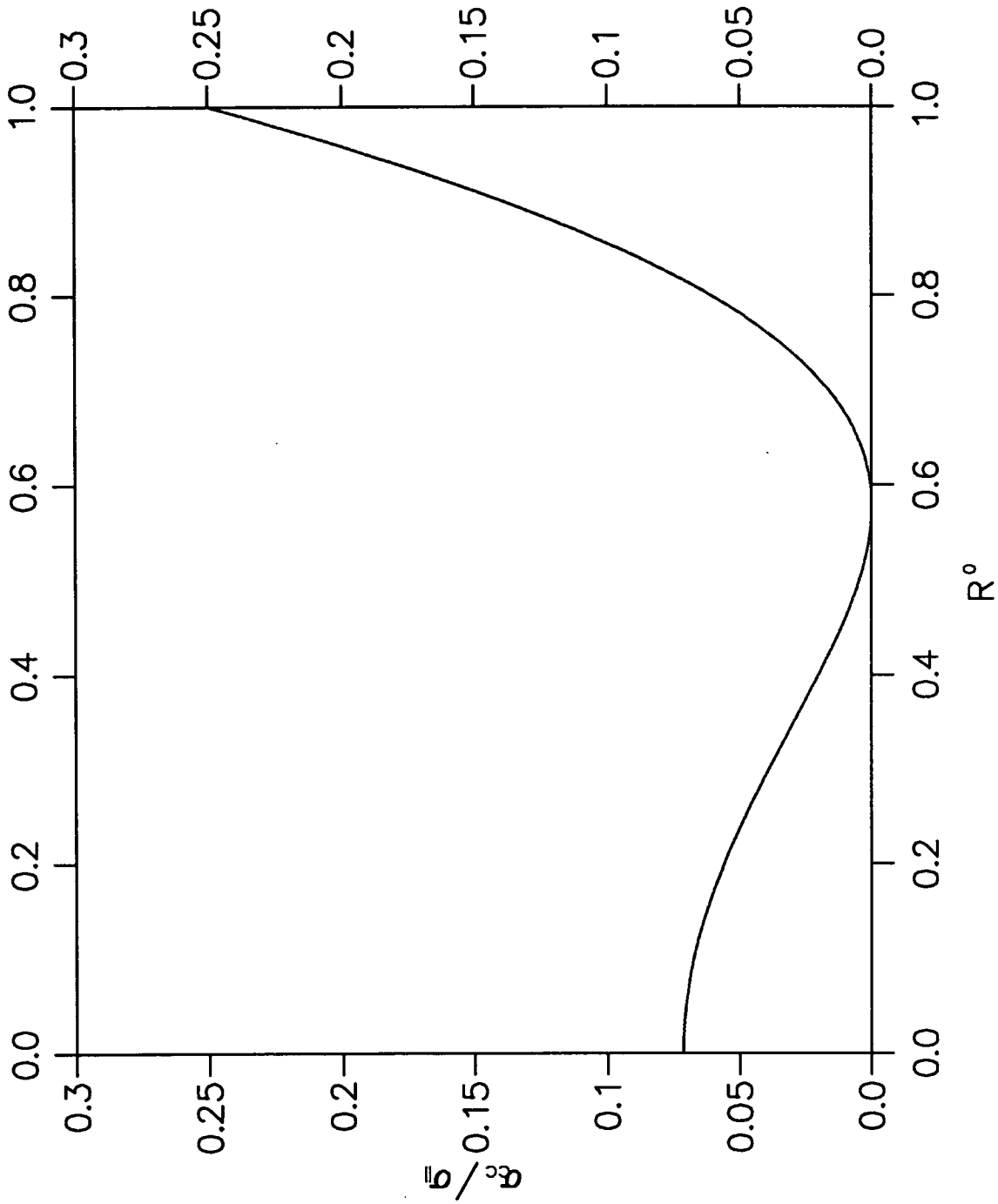

Figure 4–7: Plot showing $\frac{\sigma_{cc}}{\sigma_{||}}$ as a function of R^0, R^{+1} and R^{-1} for Q-branch of a $\Delta\Lambda = 0$ two-photon transition . The axes are constructed such that $|R^{+1}| = |R^{-1}| = \sqrt{(1 - |R^0|^2)/2}$ and $R^{+1} = -R^{-1}$

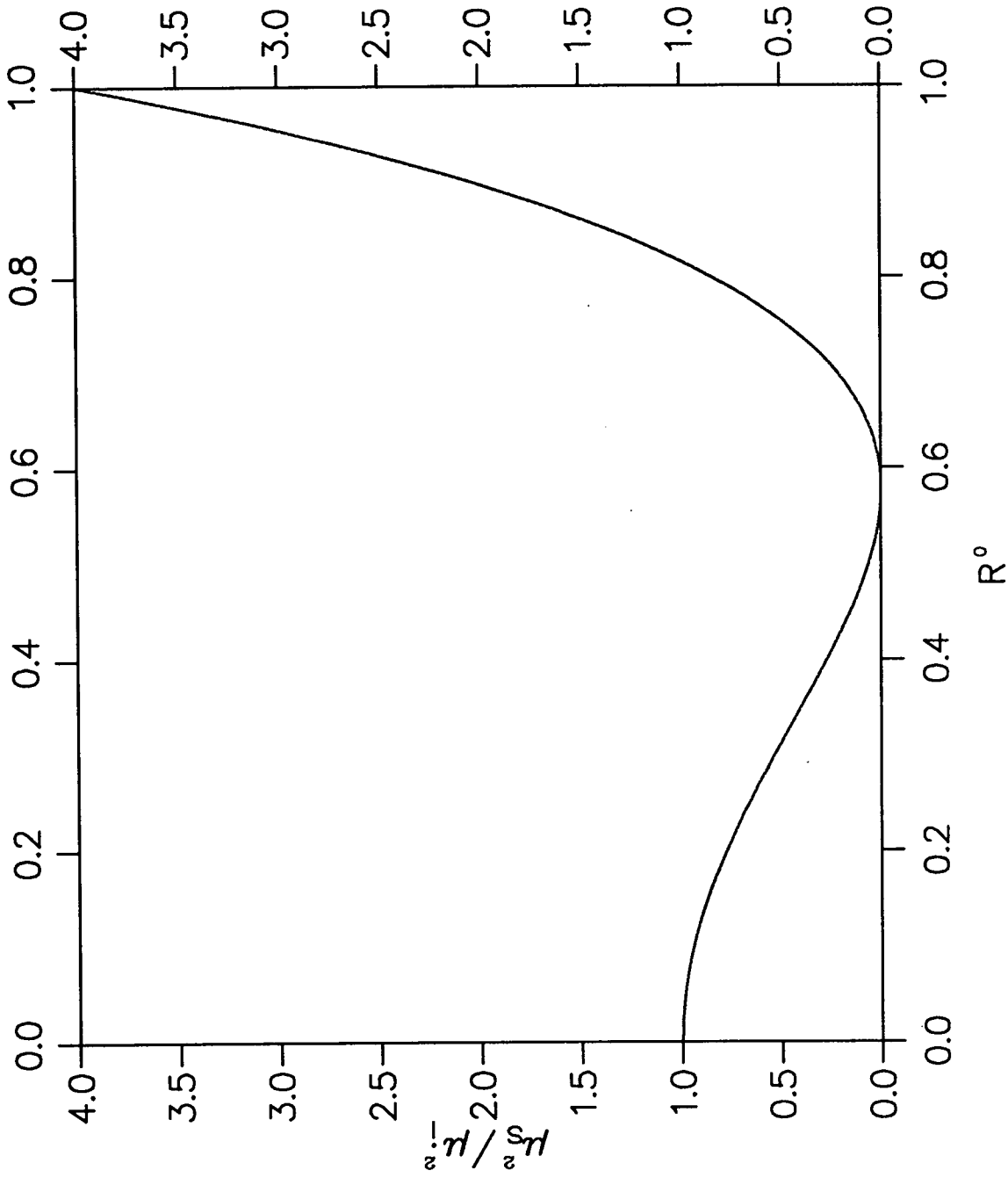

Figure 4–8: Plot showing $\frac{\mu_{fi}^2}{\mu_{ii}^2}$ as a function of R^0, R^{+1} and R^{-1} for Q-branch of a $\Delta\Lambda = 0$ two-photon transition . The axes are constructed such that $|R^{+1}| = |R^{-1}| = \sqrt{(1 - |R^0|^2)/2}$ and $R^{+1} = -R^{-1}$

In the case of two photon $\Delta\Lambda = 0$ transitions the quantities $\frac{\mu_s^2}{\mu_i^2}$, R^0, R^{+1} and R^{-1} are especially important since they are required by the formulae presented in the next section in order to perform a full multipole moment analysis using these transitions. eg $\Sigma \leftarrow \Sigma$. Qualitatively, the observable quantity $\frac{\mu_s^2}{\mu_i^2}$ governs how much alignment information can be obtained using the transition in question. In particular, if $\mu_s^2 = 0$ then there is no alignment information contained within the spectrum.

This poses a problem when trying to use certain $\Delta\Lambda = 0$ transitions for alignment measurements since, as can be seen from figure 4–8, for values of $\frac{\mu_s^2}{\mu_i^2} < 1$ there exists two independent sets of probabilities R^0, R^{+1} and R^{-1}. This doesn't affect the line strengths for an isotropic sample but will do so for an anisotropic sample, i.e. the populations in an isotropic sample can still be measured but no alignment measurements can be performed on an anisotropic sample. In this particular case there is insufficient information available to carry out an alignment study using the transition in question [3] .

The value of $\frac{\mu_s^2}{\mu_i^2}$ for any given transition can be obtained using one of two methods. Firstly by comparing the line strengths of Q-branch ($\sigma_{II}(Q)$) and S-branch ($\sigma_{II}(S)$) (or O-branch) lines using linearly polarized light [4]

---

[3] Using $\frac{\mu_s^2}{\mu_i^2} = \frac{|2R^{0^2} - 2R^{-1^2}|^2}{|R^{0^2} + 2R^{-1^2}|^2}$
for $2R^{0^2} - 2R^{-1^2}$ and $R^{0^2} + 2R^{-1^2}$ both positive this implies
$R^{-1} = R^0\sqrt{\left(2 - \sqrt{\frac{\mu_s^2}{\mu_i^2}}\right) / \left(2 + 2\sqrt{\frac{\mu_s^2}{\mu_i^2}}\right)}$
otherwise either $2R^{0^2} - 2R^{-1^2}$ or $R^{0^2} + 2R^{-1^2}$ negative gives
$R^{-1} = R^0\sqrt{\left(\sqrt{\frac{\mu_s^2}{\mu_i^2}} + 2\right) / \left(2 - 2\sqrt{\frac{\mu_s^2}{\mu_i^2}}\right)}$
These two equation give the ratio of $R^0 : R^{-1}$ for cases where $\frac{\mu_s^2}{\mu_i^2} < 1$

[4] In cases where $\Lambda \neq 0$ the $\sigma_{II}(Q)$ to $\sigma_{II}(P)$ or $\sigma_{II}(R)$ ratio could be taken.

. This gives

$$\frac{\mu_s^2}{\mu_i^2} = \frac{10(2J+1)(J+1)(J+2)(J+3)}{3[(J+1)^2-\Lambda^2][(J+2)^2-\Lambda^2]} \times \left[\frac{\sigma_{II}(Q)}{\sigma_{II}(S)} - \frac{2(2J+1)(J+2)(J+3)[J(J+1)-3\Lambda^2]^2}{3J(2J-1)(2J+3)[(J+1)^2-\Lambda^2][(J+2)^2-\Lambda^2]}\right]^{-1} \tag{4.8}$$

The second method involves comparing the line strengths for a $\Delta\Lambda = 0$ Q branch for linearly and circularly polarized light. This gives [5]

$$\frac{\mu_s^2}{\mu_i^2} = \frac{10J(J+1)(2J-1)(2J+3)}{3\left[J(J+1)-3\Lambda^2\right]^2\left(\frac{\sigma_{II}}{\sigma_{cc}}-\frac{2}{3}\right)} \tag{4.9}$$

4.3 Line Strengths for Anisotropic Samples

For anisotropic samples in general equation 4.4 must be modified to include contributions to the line strength from the higher order moments. i.e. $\mathcal{A}_{q+}^{\{k\}}$, $\forall k \neq 0$. Equation 4.4 then becomes

$$I(J) = C \cdot n(J)\left[\sum_{k,q} \mathcal{A}_{q+}^{\{k\}}(J) \cdot P_{q+}^{\{k\}}(J)\right] \tag{4.10}$$

where k is a positive integer and for any given value of k, q is an integer lying between $-k$ and k inclusive.

For samples, such as those produced by photolysis of a precursor, where there exists an axis of cylindrical symmetry then all $\mathcal{A}_{q+}^{\{k\}}$ with $q \neq 0$ vanish leaving

$$I(J) = C \cdot n(J)\left[\sum_{k} \mathcal{A}_{0+}^{\{k\}}(J) \cdot P_{0+}^{\{k\}}(J)\right] \tag{4.11}$$

---

[5] Care must be taken when using this method to determine $\frac{\mu_s^2}{\mu_i^2}$. If the linearly polarized light is not perfectly polarized, ie contains an ellipticity, then this will lead to the calculated value of $\frac{\mu_s^2}{\mu_i^2}$ being too large.

In addition, for the present work there was no net orientation in the sample and only the first two anisotropic moments were finite. The line intensity then finally reduces to

$$I(J) = C \cdot n(J) \left[\mathcal{A}_{0+}^{\{0\}}(J) \cdot P_{0+}^{\{0\}}(J) + \mathcal{A}_{0+}^{\{2\}}(J) \cdot P_{0+}^{\{2\}}(J) + \mathcal{A}_{0+}^{\{4\}}(J) \cdot P_{0+}^{\{4\}}(J) \right] \tag{4.12}$$

For a case where we wish to measure the first n even moments $\mathcal{A}_{0+}^{\{0\}}, \mathcal{A}_{0+}^{\{2\}}, \ldots \mathcal{A}_{0+}^{\{2n-2\}}$ we must therefore make a minimum of n independent sets of two photon REMPI measurements and carry out a least squares fit on the data to obtain the required moments.

The formulae for the line strength factors $P_{q+}^{\{k\}}$ taken from reference [6] are presented in tables 4–5 and 4–6 with the notation used being outlined in table 4–7. Each of the terms is explained briefly below.

4.3.1 Reduced matrix elements of the spherical tensor angular momentum operators, $b^k(J_i)$

The $b^k(J_i)$, presented in table 4–8, can be considered as scaling factors and are proportional to the reduced matrix elements of the angular momentum spherical tensor operators in the ground state. The $c(k)$ are normalizing factors.

4.3.2 The hyperfine and fine structure depolarization, $g^k(J_i)$ and $g^k(N_i)$

For molecules with nonzero nuclear spin the direction of **J** is not fixed in space. Instead **J** is coupled to the nuclear spin **I** to form a resultant **F**, the total angular momentum. Initially **J** may be aligned but within a short space of time it randomizes due to the coupling with **I**. The physical interpretation of this being the precession of **J** about **F**. If, as in most cases, the hyperfine structure is unresolved

$$I = C \cdot n(J_i) \sum_{k,q} \left[P_{q+}^{\{k\}}(J_i, \Lambda_i, J_f, \Lambda_f; \Omega) \mathcal{A}_{q+}^{\{k\}}(J_i) + P_{q-}^{\{k\}}(J_i, \Lambda_i, J_f, \Lambda_f; \Omega) \mathcal{A}_{q-}^{\{k\}}(J_i) \right] \tag{4.13}$$

$$P_{q+}^{\{k\}}(J_i, \Lambda_i, J_f, \Lambda_f; \Omega) = b^k(J_i) g^k(J_i) \sum_{k_d, k_a} \left[(-1)^{(k)} \epsilon_{q+}^{\{k\}}(k_d, k_a; \Omega_{\rm lab}) \times \sum_{J_e, \Lambda_e, J'_e, \Lambda'_e} S(J_i, \Lambda_i, J_e, \Lambda_e, J'_e, \Lambda'_e, J_f, \Lambda_f) \times h(k_d, k_a, k, J_i, J_e, J'_e, J_f) \right] \tag{4.14}$$

$$\mathcal{A}_{q\pm}^{\{k\}}(J_i) = c(k) \left\langle (J_i M_i \Lambda_i | J_{q\pm}^{\{k\}} | J_i M_i \Lambda_i) \right\rangle / \left[(J_i M_i \Lambda_i | \mathbf{J}^2 | J_i M_i \Lambda_i) \right]^{k/2} \tag{4.15}$$

$$\epsilon_{q+}^{\{k\}}(k_d, k_a; \Omega_{\rm lab}) = (-1)^q (2 - \delta_{q,0})^{1/2} \, \mathcal{R}e \left[\epsilon_q^{(k)}(k_d, k_a; \Omega_{\rm lab}) \right] \tag{4.16}$$

$$\epsilon_{q-}^{\{k\}}(k_d, k_a; \Omega_{\rm lab}) = (-1)^q (2)^{1/2} (1 - \delta_{q,0}) \, \mathcal{I}m \left[\epsilon_q^{(k)}(k_d, k_a; \Omega_{\rm lab}) \right] \tag{4.17}$$

$$\epsilon_q^{(k)}(k_d, k_a; \Omega_{\rm lab}) = \sum_{q'} e^{iq'\chi} d^k_{q',q}(-\theta) e^{iq\phi} \sum_m (-1)^{k_a - k_d - q'} (2k+1)^{1/2} \times \begin{pmatrix} k_d & k_a & k \\ m & q'-m & -q' \end{pmatrix} E^{k_d}_m E^{k_a}_{q'-m} \tag{4.18}$$

$$E^k_q = \left[e^{*(1)} \otimes e^{(1)} \right]^k_q \tag{4.19}$$

$$b^k(J_i) = c(k)^{-1} \left[(J_i M_i \Lambda_i | \mathbf{J}^2 | J_i M_i \Lambda_i) \right]^{k/2} / (J_i || J^{(k)} || J_i) \tag{4.20}$$

$$g^k(J_i) = \sum_I \sum_{F_i} (2F_i + 1)^2 \begin{Bmatrix} F_i & F_i & k \\ J_i & J_i & I \end{Bmatrix}^2 \tag{4.21}$$

$$g^k(N_i) = \sum_{J_i} (2J_i + 1)^2 \begin{Bmatrix} J_i & J_i & k \\ N_i & N_i & S \end{Bmatrix}^2 g^k(J_i) \tag{4.22}$$

From reference [6]

Table 4–5: Formulae for the calculation of the line strength moments $P_q^{\{k\}}$

$$S(J_i,\Lambda_i,J_e,\Lambda_e,J'_e,\Lambda'_e,J_f,\Lambda_f) = (J'_e\Lambda'_e||r^{(1)}||J_i\Lambda_i)^*(J_e\Lambda_e||r^{(1)}||J_i\Lambda_i) \times (J_f\Lambda_f||r^{(1)}||J'_e\Lambda'_e)^*(J_f\Lambda_f||r^{(1)}||J_e\Lambda_e) \quad (4.23)$$

$$(J_2\Lambda_2||r^{(1)}||J_1\Lambda_1) = (4\pi/3)^{1/2}R_{21}^{(\Lambda_2-\Lambda_1)}(2J_2+1)^{1/2}(2J_1+1)^{1/2} \times(-1)^{(J_2-\Lambda_2)}\begin{pmatrix} J_1 & J_2 & 1 \\ \Lambda_1 & -\Lambda_2 & \Lambda_2-\Lambda_1 \end{pmatrix} \quad (4.24)$$

$$(J_2\Lambda_2||r^{(1)}||J_1\Lambda_1)^* = (-1)^{(J_2-J_1)}(J_1\Lambda_1||r^{(1)}||J_2\Lambda_2) \quad (4.25)$$

$$h(k_d,k_a,k,J_i,J_e,J'_e,J_f) = (-1)^{(J_f+J'_e-k_d+1)}[(2k_d+1)(2k_a+1)(2k+1)]^{1/2} \times\begin{Bmatrix} J'_e & J_e & k_d \\ 1 & 1 & J_f \end{Bmatrix}\begin{Bmatrix} J'_e & 1 & J_i \\ J_e & 1 & J_i \\ k_d & k_a & k \end{Bmatrix} \quad (4.26)$$

From reference [6]

Table 4–6: Formulae for the calculation of the line strength moments $P_q^{\{k\}}$ (continued)

J_i = Rotational quantum number of the initial state apart from nuclear spin.

J_e = Rotational quantum number of the virtual state apart from nuclear spin.

J_f = Rotational quantum number of the final state apart from nuclear spin.

Λ_i = Orbital angular momentum quantum number of the initial state.

Λ_e = Orbital angular momentum quantum number of the virtual state.

Λ_f = Orbital angular momentum quantum number of the final state.

k_a = The rank for the square of the first photon.

k_d = The rank for the square of the second photon.

k = The rank for the ground state distribution.

q = The component for the ground state distribution.

Ω = Angles describing the geometry of the laser beam with respect to the coordinate system for the moments of the ground state distribution.

ϕ, θ, χ = Euler angles which rotate the lab into the detector frame.

$\hat{\mathbf{B}}$ = The vector along which the laser light is linearly polarized before passing through the variable wave plate.

β = The angle between the laser polarization vector and the major axis of the variable wave plate.

Δ = The angle between the major axis of the variable wave plate and the z axis of the lab frame.

ζ = The phase shift between the x_d and y_d components of the electric field vector of the light. ie $\zeta = \pi/2$ for a quarter wave plate.

F_i = Total angular momentum quantum number of the initial state including nuclear spin.

I = Nuclear spin quantum number.

S = Electronic spin quantum number.

N_i = Total angular momentum quantum number apart from spin for Hund's case (b) molecules.

From reference [6]

Table 4–7: Notation and terms used in formulae

then this depolarization must be taken into account by multiplying each $P_{q+}^{\{k\}}$ by the relevent depolarization factor, equation 4.21, for $g^k(J_i)$ [6] .

For Hunds case b molecules the randomly polarized spin **S** is also responsible for depolarization of **J**. In this case it is the moments of **N** that are being measured rather then those of **J** and each $P_{q+}^{\{k\}}$ should be multiplied by the corresponding $g^k(N_i)$, equation 4.22.

4.3.3 System geometry, $\epsilon_{q\pm}^{\{k\}}(k_a, k_d; \Omega_{lab})$

This term describes the relative orientations of the two space fixed frames of reference used to describe the system geometry as shown in figure 4–6. For the present work where an axis of cylindrical symmetry was present this axis must be designated the lab z axis and case II geometry as defined in reference [6] is used throughout the calculations. The components of the electric vector cross product, E_q^k, are given in table 4–9.

The reduced Wigner rotation matrices, $d_{q'q}^k$, and the 3j symbols,

$$\begin{pmatrix} k_d & k_a & k \\ m & q'-m & -q' \end{pmatrix},$$

are introduced in appendix B.

4.3.4 Reduced matrix elements of the dipole moment operator, $S(J_i, \Lambda_i, J_e, \Lambda_e, J_e', \Lambda_e', J_f, \Lambda_f)$

The S terms in equation 4.14 when squared are equal to the normal single photon line strength or Hönl-London factors. These then can be thought of as that part of the total line strength which is independent of the coupling betwen photons, the

---

[6] Care must be taken here as to which **J** couple to which **I**. For heteronuclear diatomics all **J** couple to all **I**. For homonuclears, however, even **J** couple to even **I** and vice versa for gerade symmetry and even **J** couple to odd **I** and vice versa for ungerade symmetry.

$$b^0(J_i) = (2J_i + 1)^{-1/2}$$

$$b^1(J_i) = (2J_i + 1)^{-1/2}$$

$$b^2(J_i) = \left[\frac{J_i(J_i+1)}{(2J_i+3)(2J_i+1)(2J_i-1)}\right]^{1/2}$$

$$b^3(J_i) = \frac{2J_i(J_i+1)}{[(J_i-1)(2J_i-1)(2J_i+1)(2J_i+3)(J_i+2)]^{1/2}}$$

$$b^4(J_i) = \frac{4J_i^2(J_i+1)^2}{[(J_i+2)(J_i+1)J_i(J_i-1)(2J_i+5)(2J_i+3)(2J_i+1)(2J_i-1)(2J_i-3)]^{1/2}}$$

From reference [6]

Table 4–8: The scaling factors $b^k(J_i)$

E_0^0	$-1/\sqrt{3}$
$E_{\pm1}^1$	$(\pm1/2)\sin 2\beta \sin\zeta$
E_0^1	0
$E_{\pm2}^2$	$(-1/2)\sin^2\beta$
$E_{\pm1}^2$	$(i/2)\sin 2\beta\cos\zeta$
E_0^2	$(1/\sqrt{6})(3\cos^2\beta - 1)$

From reference [6]

Table 4–9: The electric vector cross product terms E_q^k for the geometry used

coupling between the angular momentum vectors and the anisotropy of the ground state distribution. Each matrix element is a function of two intermediate states labeled by the ket vectors $|J_e\Lambda_e\rangle$ and $|J'_e\Lambda'_e\rangle$ with the amplitudes for each of the two possible two-photon transitions interfering. A summation is then performed over all possible pairs of interfering pathways to arrive at the final two-photon probability amplitude. Each of the terms is dependent on a 3j symbol or vector coupling coefficient described in appendix B.

4.3.5 Angular momentum coupling terms, $h(k_d, k_a, k, J_i, J_e, J'_e, J_f)$

The h terms show how the moments of the electric field vectors of the photons and the moments of the ground state alignment distribution are coupled to the angular momentum vectors of the ground, intermediate and final states. They are a function of the 6j and 9j symbols described in appendix B.

4.4 Calculated Moments of Line Strengths and Interpretation of Higher Order Moments

As stated in section 4.1 the values of the higher order alignment parameters $\mathcal{A}_{0+}^{\{2\}}$ and $\mathcal{A}_{0+}^{\{4\}}$ provide information on the spatial distribution of the angular momentum vectors J_i of the product molecules. As can be seen from figure 4–2, $\mathcal{A}_{0+}^{\{2\}}$ is negative when low M_i sublevels ($M_i \ll J_i$) are primarily populated, implying that J_i lies predominantly at right angles to the axis of cylindrical symmetry z. When J_i lies mainly along the z axis and large values of M_i are populated ($M_i \approx J_i$) $\mathcal{A}_{0+}^{\{2\}}$ is positive. The physical interpretation of $\mathcal{A}_{0+}^{\{4\}}$ isn't quite as straight forward. As can be seen from figure 4–4 in the limit of high M_i excitation $\mathcal{A}_{0+}^{\{4\}}$ is positive. As M_i is reduced so $\mathcal{A}_{0+}^{\{4\}}$ becomes negative before finally going positive again when the lowest values of M_i ($M_i \ll J_i$) are primarily populated. Thus one of the effects of $\mathcal{A}_{0+}^{\{4\}}$ is to give an indication of the 'sharpness' or 'narrowness' of the distribution.

The calculated line strength moments for the various electronic transitions investigated are shown in figures 4–9 to 4–19. These correspond to the $J_i = 5$ Q-branch line. These figures show how the $P_{0+}^{\{0\}}$, $P_{0+}^{\{2\}}$ and $P_{0+}^{\{4\}}$ line strength moments vary as a function of the retardance and orientation of the variable wave plate used, with the retardance being a function of the phasing of the photoelastic modulator as described in section 2.4. The retardance varies between 0 and 2π radians with $\pi/2$ corresponding to a 1/4 wave plate and π corresponding to a 1/2 wave plate. The two parameters β and Δ describe the orientation of the major axis of the variable wave plate relative to the lab and detector frames. Rotating the wave plate about the lab x axis by an angle ψ corresponds to setting $\beta = \psi$ and $\Delta = -\psi$ in the expression for the geometric factor $\epsilon_{q\pm}^{\{k\}}$.

For values of $\beta, -\Delta = n\pi/2, n \in Z$ the wave plate has no effect since the electric vector of the input beam lies along either the major or minor axis of the wave plate. Thus for these configurations the light remains vertically polarized. For cases where $\zeta = 2n\pi, n \in Z$ then the wave plate is again transparent and has no effect on the input beam.

When $\zeta = \pi$ we have a 1/2 wave plate and the light will be transformed from vertically polarized to horizontally polarized as β and $-\Delta$ go from 0 to $\pi/4$ and finally back to vertically polarized when $\beta = -\Delta = \pi/2$. This is repeated four times along the cross section for $\zeta = \pi$.

The cases where $\zeta = (2n+1)\pi/2$ with $\beta = -\Delta = (2n+1)\pi/4$ correspond to circularly polarized light [7] .

Figures 4–9 to 4–11 correspond to a $\Delta \leftarrow \Sigma$ two photon transition. For an isotropic sample the observed line intensity is a function of $P_{0+}^{\{0\}}$ only and as can be seen from figure 4–9 the $\frac{\sigma_{cc}}{\sigma_{ll}}$ value of 3/2 agrees directly with that predicted by the Bray-Höchstrasser theory in section 4.2.

---

[7]Left and right hand circular polarizations are not distinguished in the present work since only even moments are of interest

Figure 4–10 showing $P_{0+}^{\{2\}}$ gives an indication as to how any anisotropy in the sample will affect the observed line intensity. The transition proceeds via two single photon perpendicular transitions. For $\zeta = 0, 2\pi$ or $\beta = -\Delta = \frac{\pi}{2}, \pi, \frac{3\pi}{2}$ the light is vertically polarized. This will promote detection of molecules whose **J** lies along the z axis and produce a positive contribution to the overall line strength. For $\zeta = \pi$ and $\beta = -\Delta = \frac{\pi}{4}, \frac{3\pi}{4}, \frac{5\pi}{4}, \frac{7\pi}{4}$ the light is horizontally polarized. This will enhance the detection of molecules whose **J** lies in the xy plane and thus give a negative contribution to the overall line strength.

Figures 4–12 to 4–15 correspond to a $\Sigma \leftarrow \Sigma$ two photon transition. The first of these, 4–12 and 4–13 are for the case where the transition goes through a virtual Σ state, ie $\Sigma \leftarrow \Sigma \leftarrow \Sigma$. Again as can be seen from figure 4–12 representing the $P_{0+}^{\{0\}}$ moment of the line strength, the $\frac{\sigma_{\mu}}{\sigma_{cc}}$ value of 4 agrees with that of Bray-Höchstrasser. In the $\Sigma \leftarrow \Sigma \leftarrow \Sigma$ case the process proceeds via two single photon parallel transitions. For $\zeta = 0, 2\pi$ or $\beta = -\Delta = \frac{\pi}{2}, \pi, \frac{3\pi}{2}$ the light is vertically polarized. This will promote detection of molecules whose **J** lies in the xy plane and produce a negative contribution to the overall line strength. For $\zeta = \pi$ and $\beta = -\Delta = \frac{\pi}{4}, \frac{3\pi}{4}, \frac{5\pi}{4}, \frac{7\pi}{4}$ the light is horizontally polarized. This will enhance the detection of molecules whose **J** lies along the z axis and thus give a positive contribution to the overall line strength.

Figures 4–14 and 4–15 correspond to a $\Sigma \leftarrow \Pi \leftarrow \Sigma$ two photon transition where the virtual level is a Π state. The $\frac{\sigma_{\mu}}{\sigma_{cc}}$ value of 14 derived from figure 4–14 once more agrees with that of Bray-Höchstrasser. The $\Sigma \leftarrow \Pi \leftarrow \Sigma$ two photon transition proceeds via two single photon perpendicular transitions. For $\zeta = 0, 2\pi$ or $\beta = -\Delta = \frac{\pi}{2}, \pi, \frac{3\pi}{2}$ the light is vertically polarized. This will promote detection of molecules whose **J** lies along the z axis and produce a positive contribution to the overall line strength. For $\zeta = \pi$ and $\beta = -\Delta = \frac{\pi}{4}, \frac{3\pi}{4}, \frac{5\pi}{4}, \frac{7\pi}{4}$ the light is horizontally polarized. This will enhance the detection of molecules whose **J** lies in the xy plane and thus give a negative contribution to the overall line strength.

Figures 4–16 to 4–19 represent the case outlined in section 4.2 in which $\frac{\mu_z^2}{\mu_i^2} < 1$ resulting in two distinct sets of $R^0, R^{\pm 1}$ values. The results shown are for $\frac{\mu_z^2}{\mu_i^2} = .5$. The two sets of $R^0, R^{\pm 1}$ values are given in table 4–10.

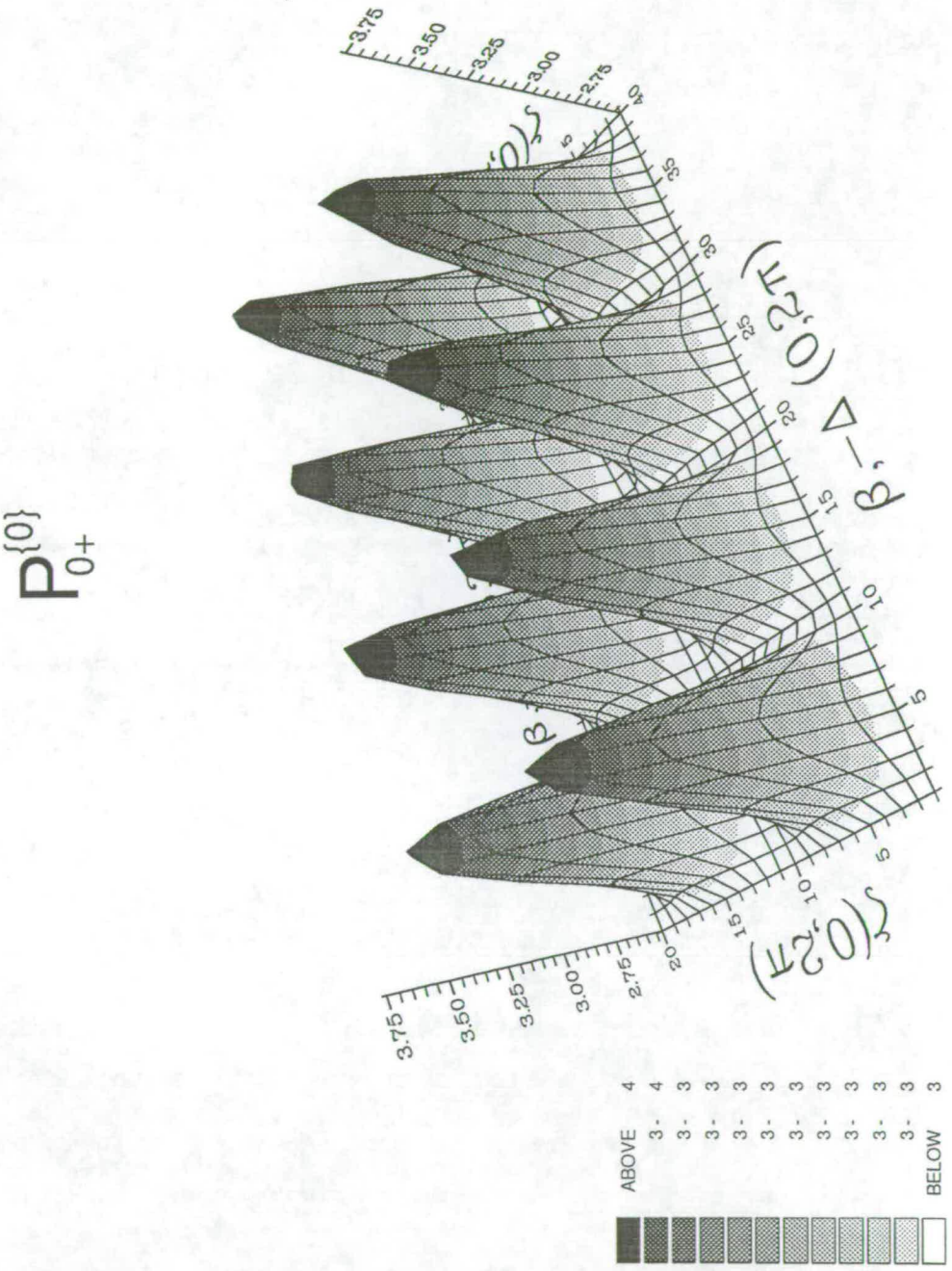

Figure 4–9: Plot of the line strength moment $P_{0+}^{\{0\}}$ for a two-photon $\Delta \leftarrow \Pi \leftarrow \Sigma$ transition as a function of the experimental parameters ζ, β and Δ with $\beta = -\Delta$. The line strength is for a Q-branch line originating from $J_i = 5$. This two-photon transition comprises two perpendicular single-photon transitions with $R^0 = 0$, $R^{+1} = \sqrt{2}$ and $R^{-1} = \sqrt{2}$

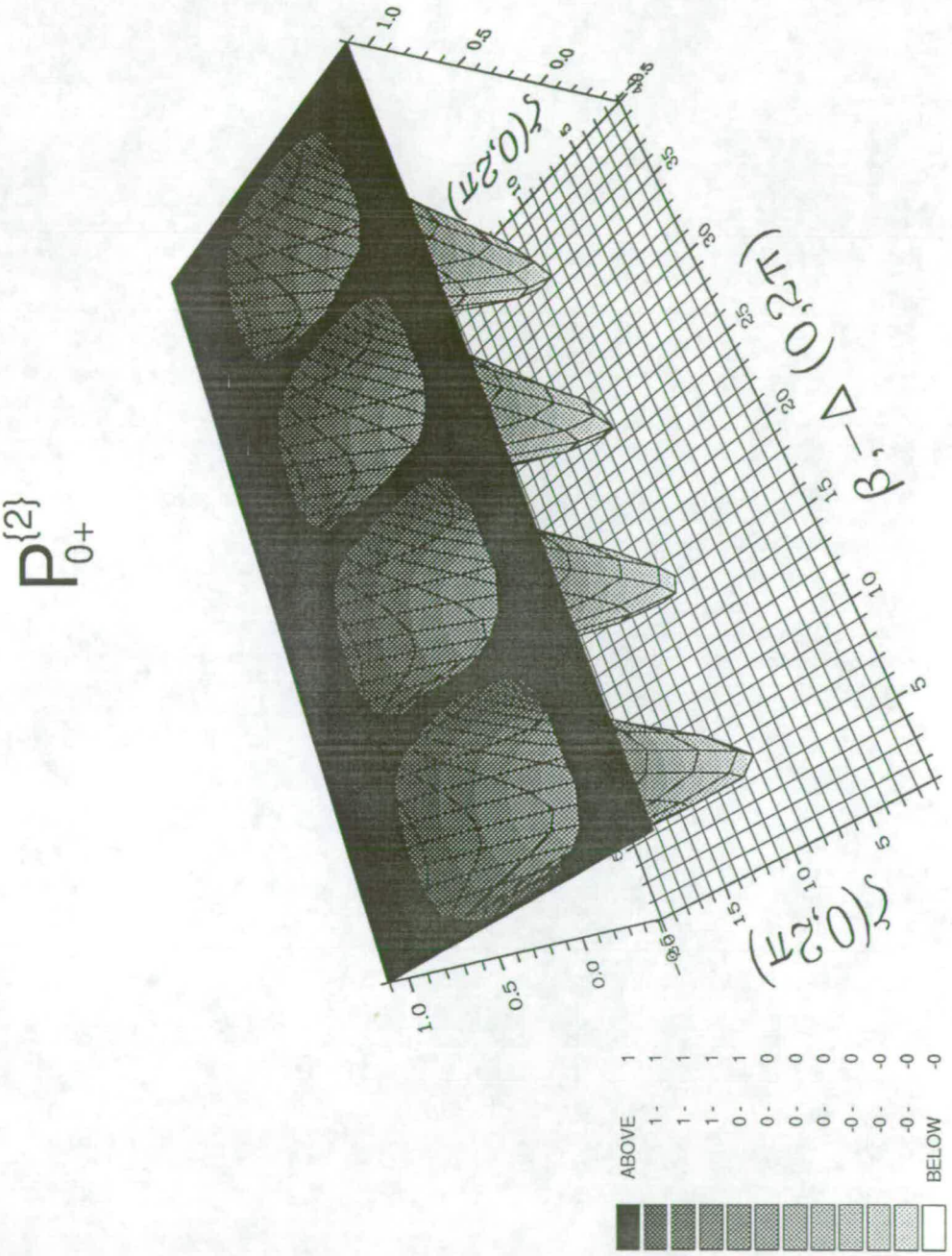

Figure 4–10: Plot of the line strength moment $P_{0+}^{\{2\}}$ for a two-photon $\Delta \leftarrow \Pi \leftarrow \Sigma$ transition as a function of the experimental parameters ζ, β and Δ with $\beta = -\Delta$. The line strength is for a Q-branch line originating from $J_i = 5$. This two-photon transition comprises two perpendicular single-photon transitions with $R^0 = 0$, $R^{+1} = \sqrt{2}$ and $R^{-1} = \sqrt{2}$

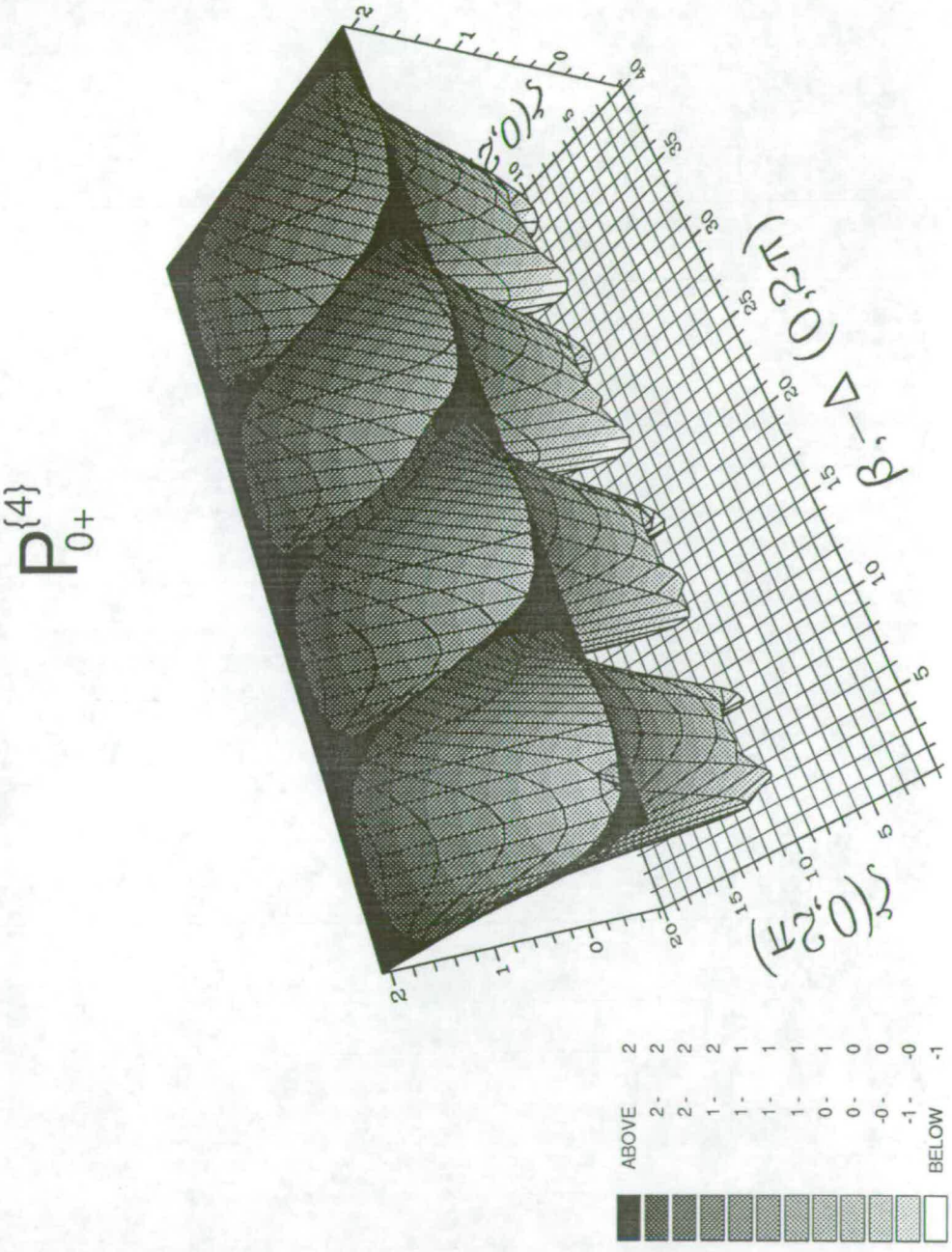

Figure 4–11: Plot of the line strength moment $P_{0+}^{\{4\}}$ for a two-photon $\Delta \leftarrow \Pi \leftarrow \Sigma$ transition as a function of the experimental parameters ζ, β and Δ with $\beta = -\Delta$. The line strength is for a Q-branch line originating from $J_i = 5$. This two-photon transition comprises two perpendicular single-photon transitions with $R^0 = 0$, $R^{+1} = \sqrt{2}$ and $R^{-1} = \sqrt{2}$

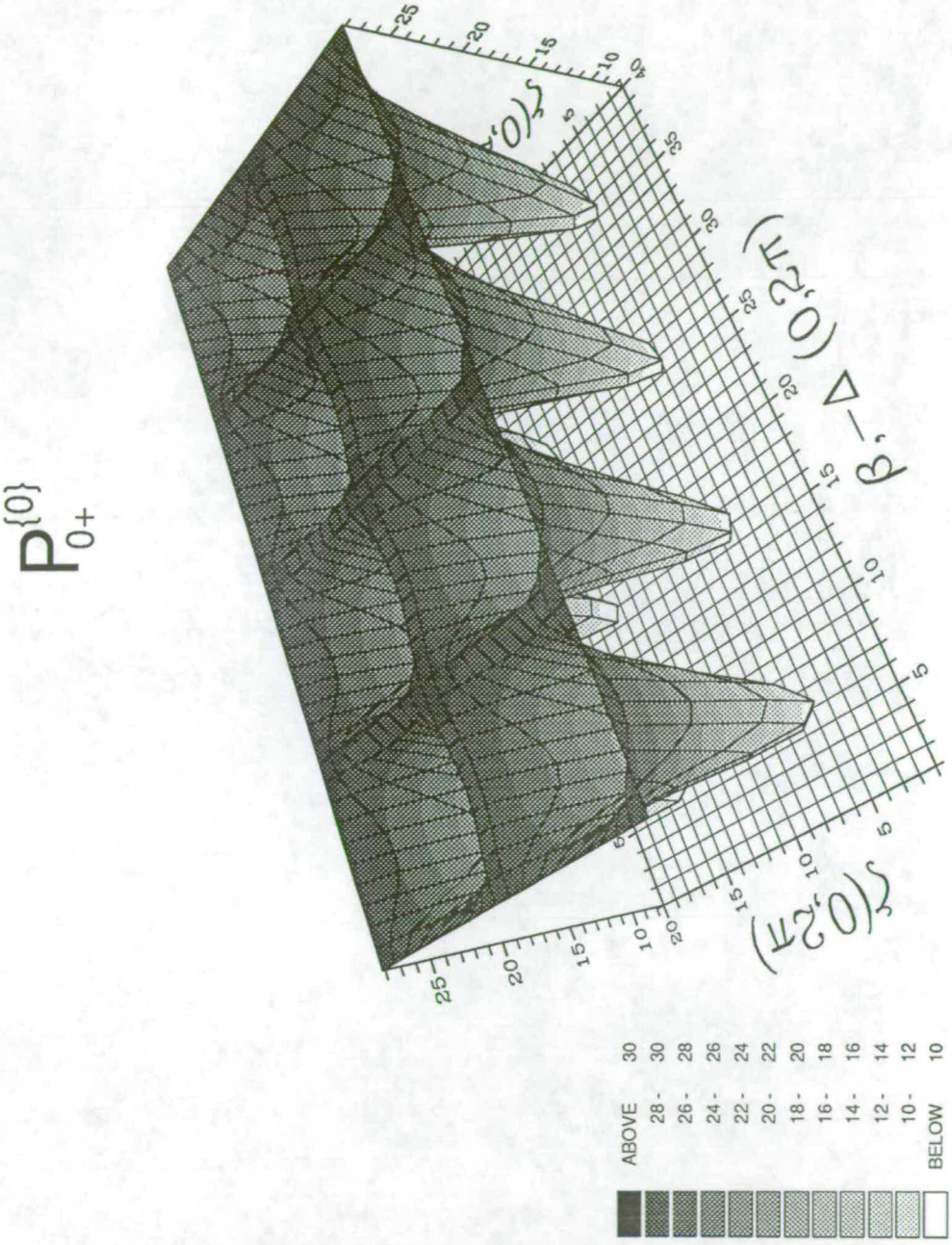

Figure 4–12: Plot of the line strength moment $P_{0+}^{\{0\}}$ for a two-photon $\Sigma \leftarrow \Sigma \leftarrow \Sigma$ transition as a function of the experimental parameters ζ, β and Δ with $\beta = -\Delta$. The line strength is for a Q-branch line originating from $J_i = 5$. This two-photon transition comprises two parallel single-photon transitions with $R^0 = 1$, $R^{+1} = 0$ and $R^{-1} = 0$

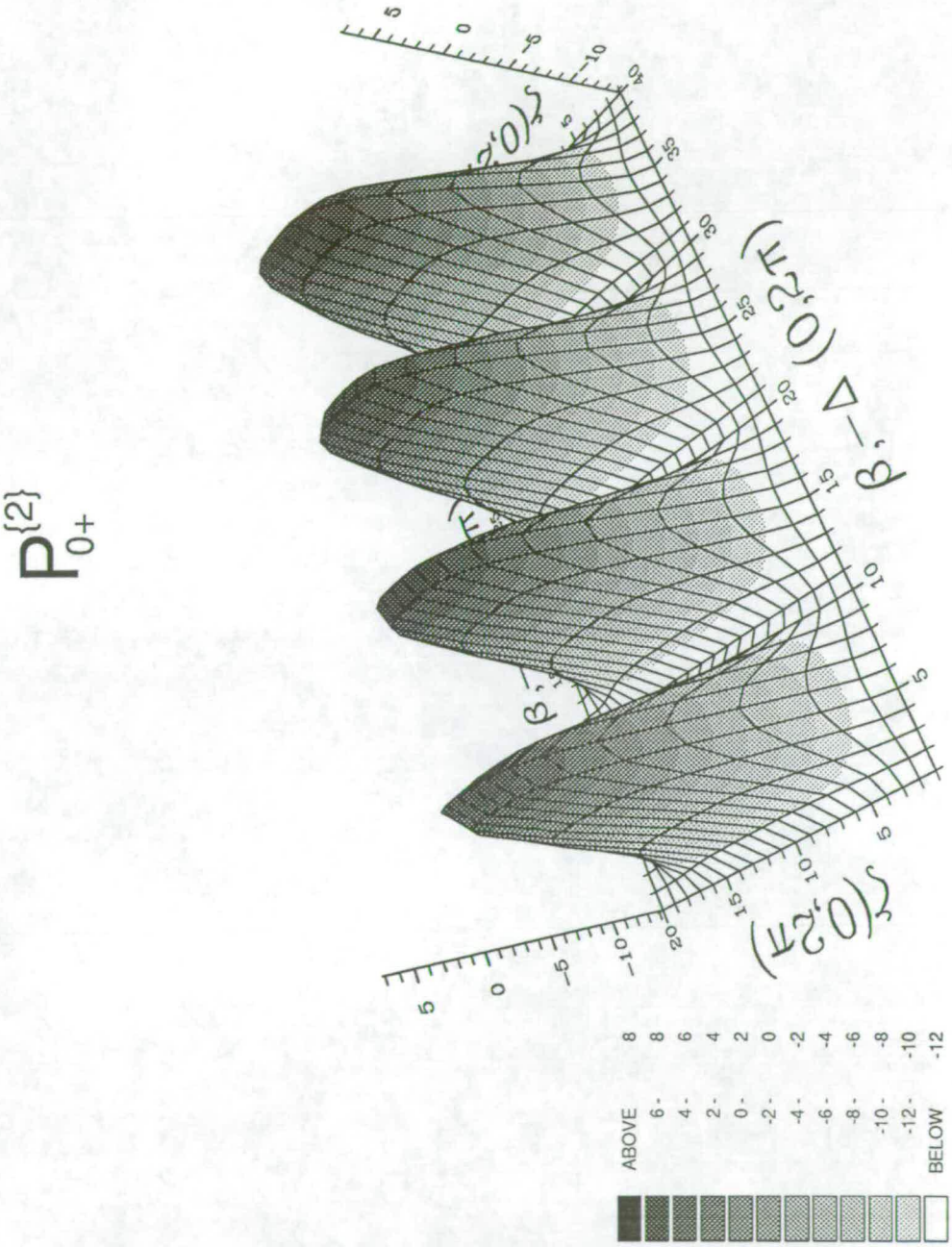

Figure 4–13: Plot of the line strength moment $P_{0+}^{\{2\}}$ for a two-photon $\Sigma \leftarrow \Sigma \leftarrow \Sigma$ transition as a function of the experimental parameters ζ, β and Δ with $\beta = -\Delta$. The line strength is for a Q-branch line originating from $J_i = 5$. This two-photon transition comprises two parallel single-photon transitions with $R^0 = 1$, $R^{+1} = 0$ and $R^{-1} = 0$

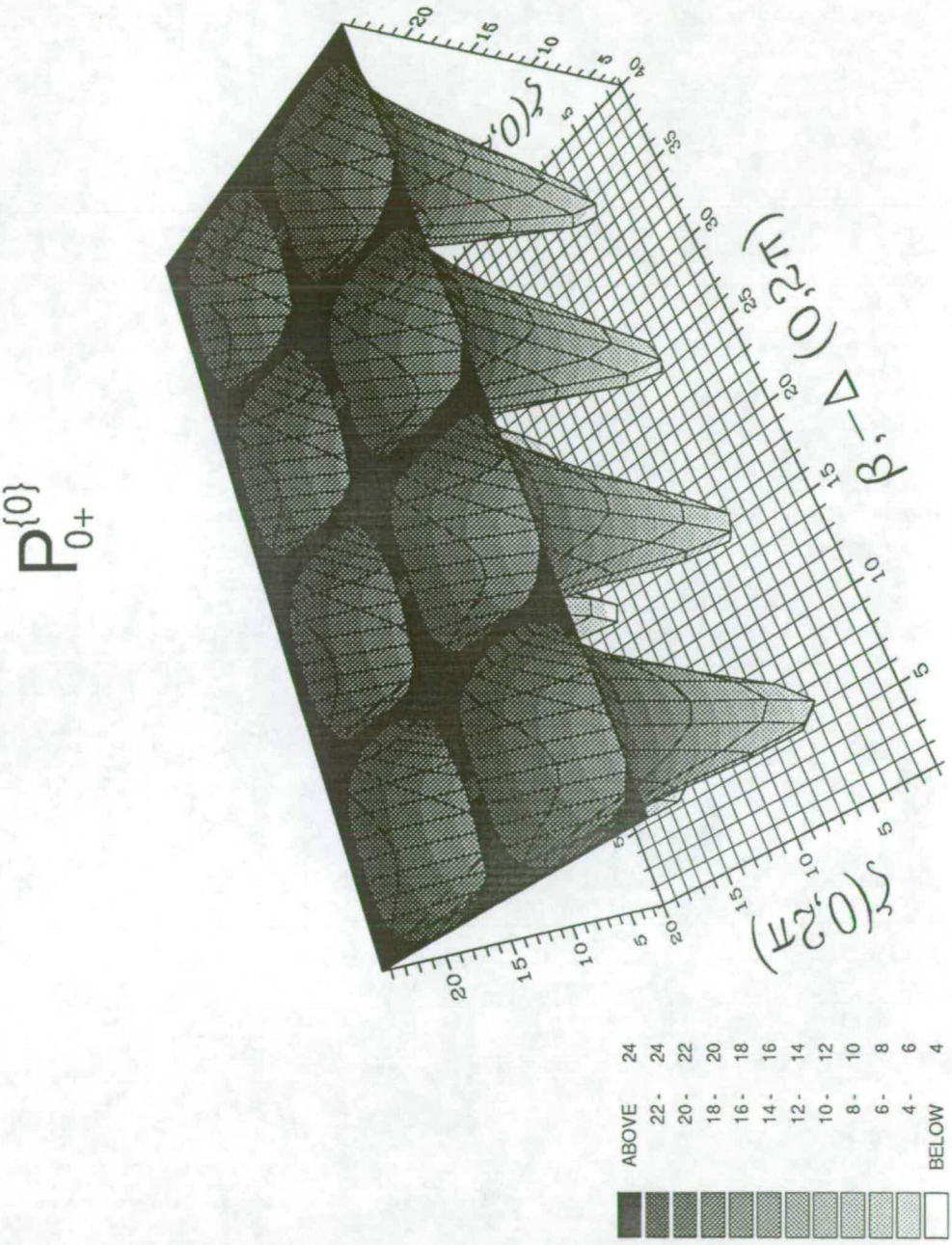

Figure 4–14: Plot of the line strength moment $P_{0+}^{\{0\}}$ for a two-photon $\Sigma \leftarrow \Pi \leftarrow \Sigma$ transition as a function of the experimental parameters ζ, β and Δ with $\beta = -\Delta$. The line strength is for a Q-branch line originating from $J_i = 5$. This two-photon transition comprises two parallel single-photon transitions with $R^0 = 0$, $R^{+1} = -\sqrt{2}$ and $R^{-1} = \sqrt{2}$

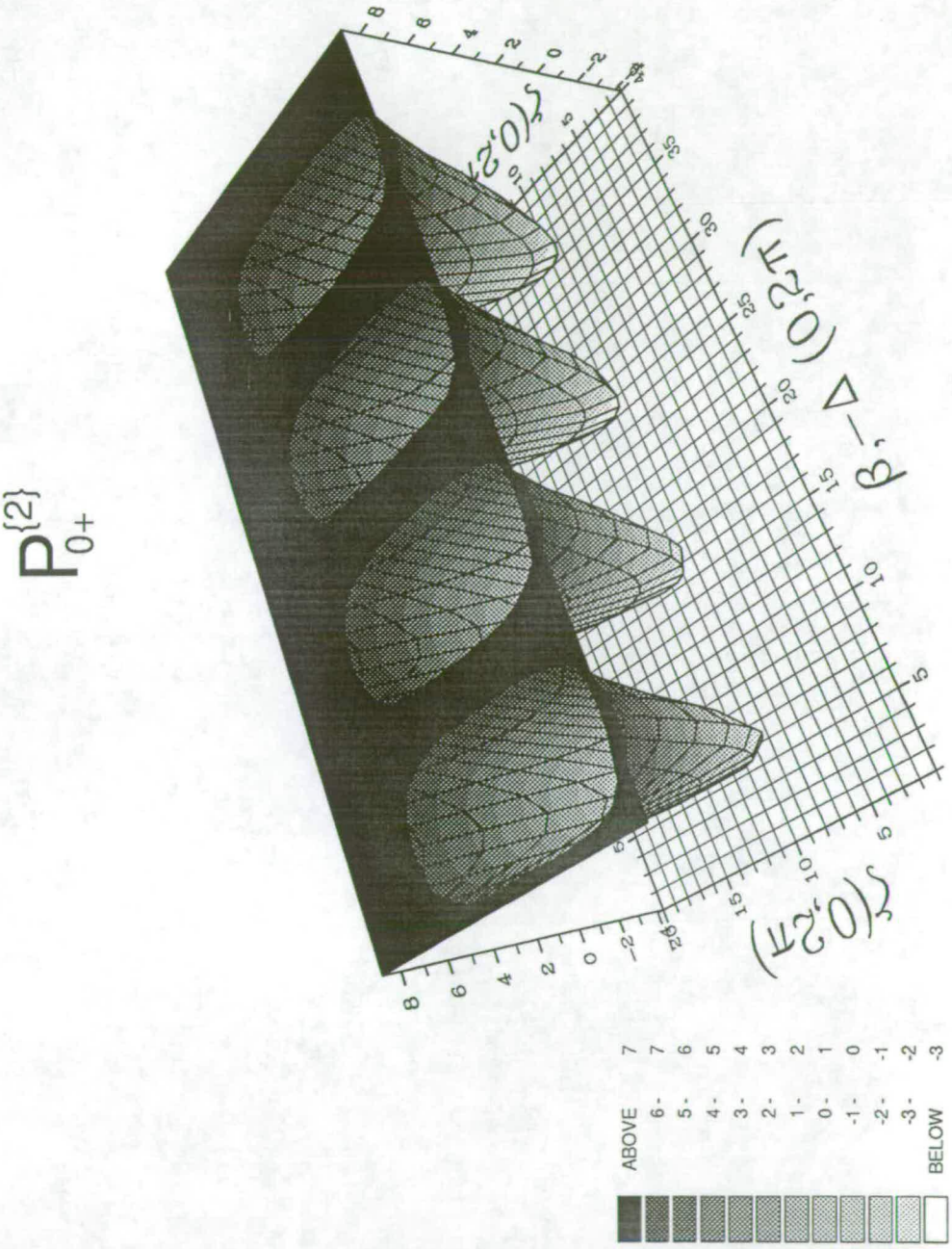

Figure 4–15: Plot of the line strength moment $P_{0+}^{\{2\}}$ for a two-photon $\Sigma \leftarrow \Pi \leftarrow \Sigma$ transition as a function of the experimental parameters ζ, β and Δ with $\beta = -\Delta$. The line strength is for a Q-branch line originating from $J_i = 5$. This two-photon transition comprises two parallel single-photon transitions with $R^0 = 0$, $R^{+1} = -\sqrt{2}$ and $R^{-1} = \sqrt{2}$

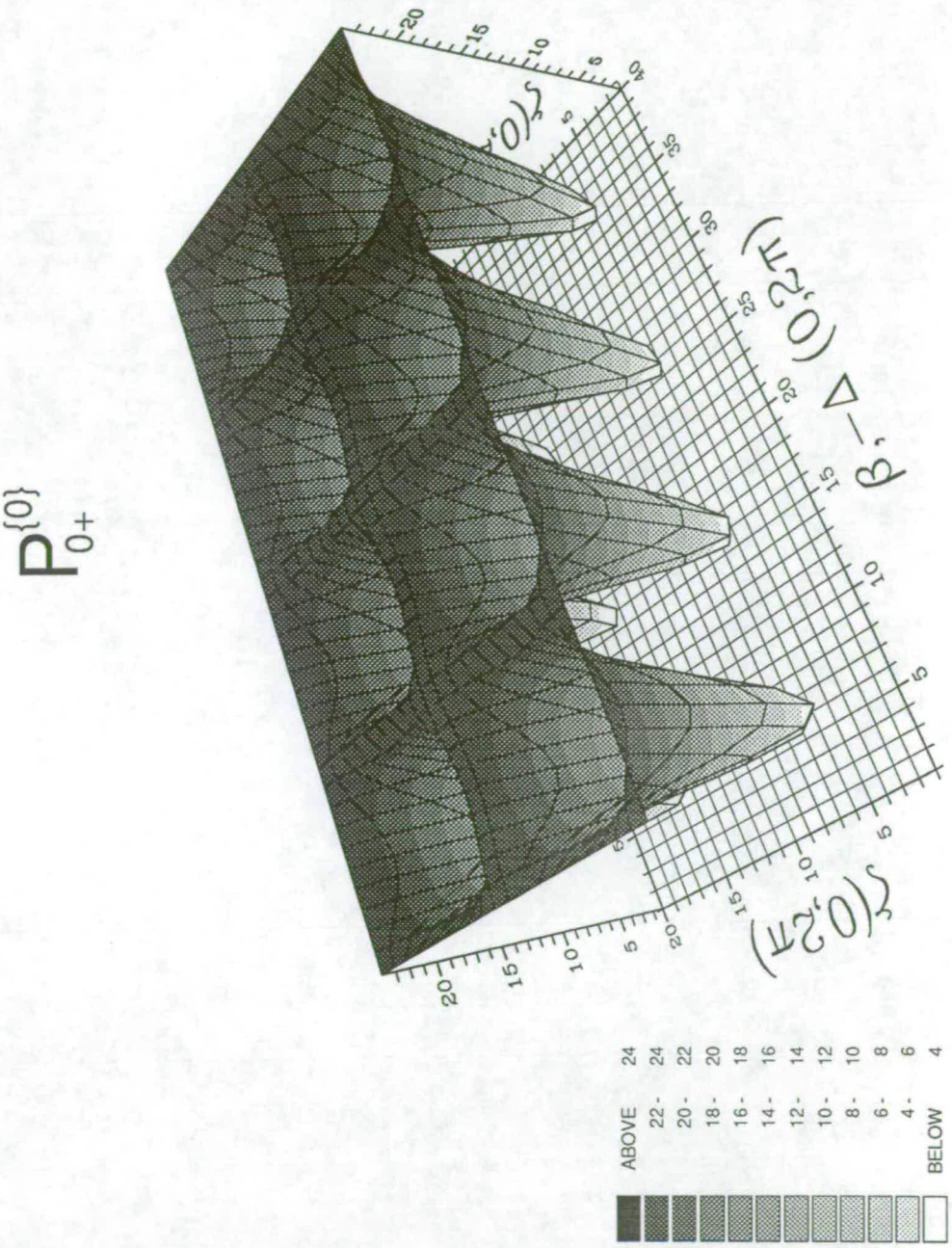

Figure 4–16: Plot of the line strength moment $P_{0+}^{\{0\}}$ for a two-photon $\Sigma \longleftarrow \Sigma$ transition as a function of the experimental parameters ζ, β and Δ with $\beta = -\Delta$. The line strength is for a Q-branch line originating from $J_i = 5$. This two-photon transition comprises two parallel single-photon transitions with $R^0 = 0.75434$, $R^{+1} = -0.46420$ and $R^{-1} = 0.46420$

The first two figures, 4–16 and 4–17 correspond to the first case in table 4–10 where $|R^0| > |R^{\pm 1}|$. This implies that the process goes predominantly via two single photon parallel transitions. For $\zeta = 0, 2\pi$ or $\beta = -\Delta = \frac{\pi}{2}, \pi, \frac{3\pi}{2}$ the light is vertically polarized. This will promote detection of molecules whose **J** lies in the xy plane and produce a negative contribution to the overall line strength. For $\zeta = \pi$ and $\beta = -\Delta = \frac{\pi}{4}, \frac{3\pi}{4}, \frac{5\pi}{4}, \frac{7\pi}{4}$ the light is horizontally polarized. This will enhance the detection of molecules whose **J** lies along the z axis and thus give a positive contribution to the overall line strength.

Alternatively, the second two figures correspond to the second case in table 4–10 where $|R^0| < |R^{\pm 1}|$. In this case the two photon transition proceeds predominantly via two single photon perpendicular transitions analagous to the $\Delta \leftarrow \Sigma$ or $\Sigma \leftarrow \Pi \leftarrow \Sigma$ cases. For $\zeta = 0, 2\pi$ or $\beta = -\Delta = \frac{\pi}{2}, \pi, \frac{3\pi}{2}$ the light is vertically polarized. This will promote detection of molecules whose **J** lies along the z axis and produce a positive contribution to the overall line strength whilst for $\zeta = \pi$ and $\beta = -\Delta = \frac{\pi}{4}, \frac{3\pi}{4}, \frac{5\pi}{4}, \frac{7\pi}{4}$ the light is horizontally polarized, enhancing the detection of molecules whose **J** lies in the xy plane and thus give a negative contribution to the overall line strength.

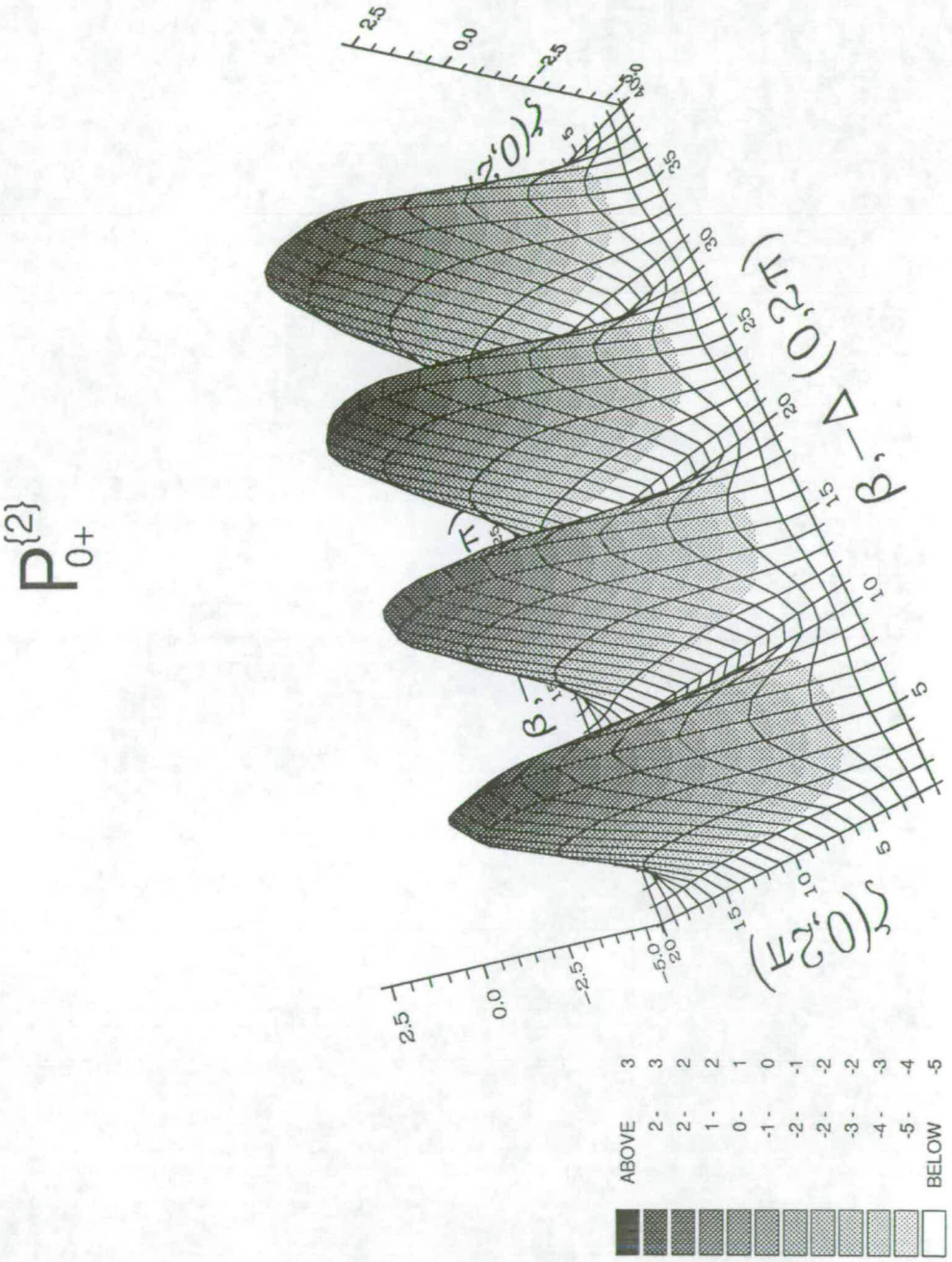

Figure 4–17: Plot of the line strength moment $P_{0+}^{\{2\}}$ for a two-photon $\Sigma \longleftarrow \Sigma$ transition as a function of the experimental parameters ζ, β and Δ with $\beta = -\Delta$. The line strength is for a Q-branch line originating from $J_i = 5$. This two-photon transition comprises two parallel single-photon transitions with $R^0 = 0.75434$, $R^{+1} = -0.46420$ and $R^{-1} = 0.46420$

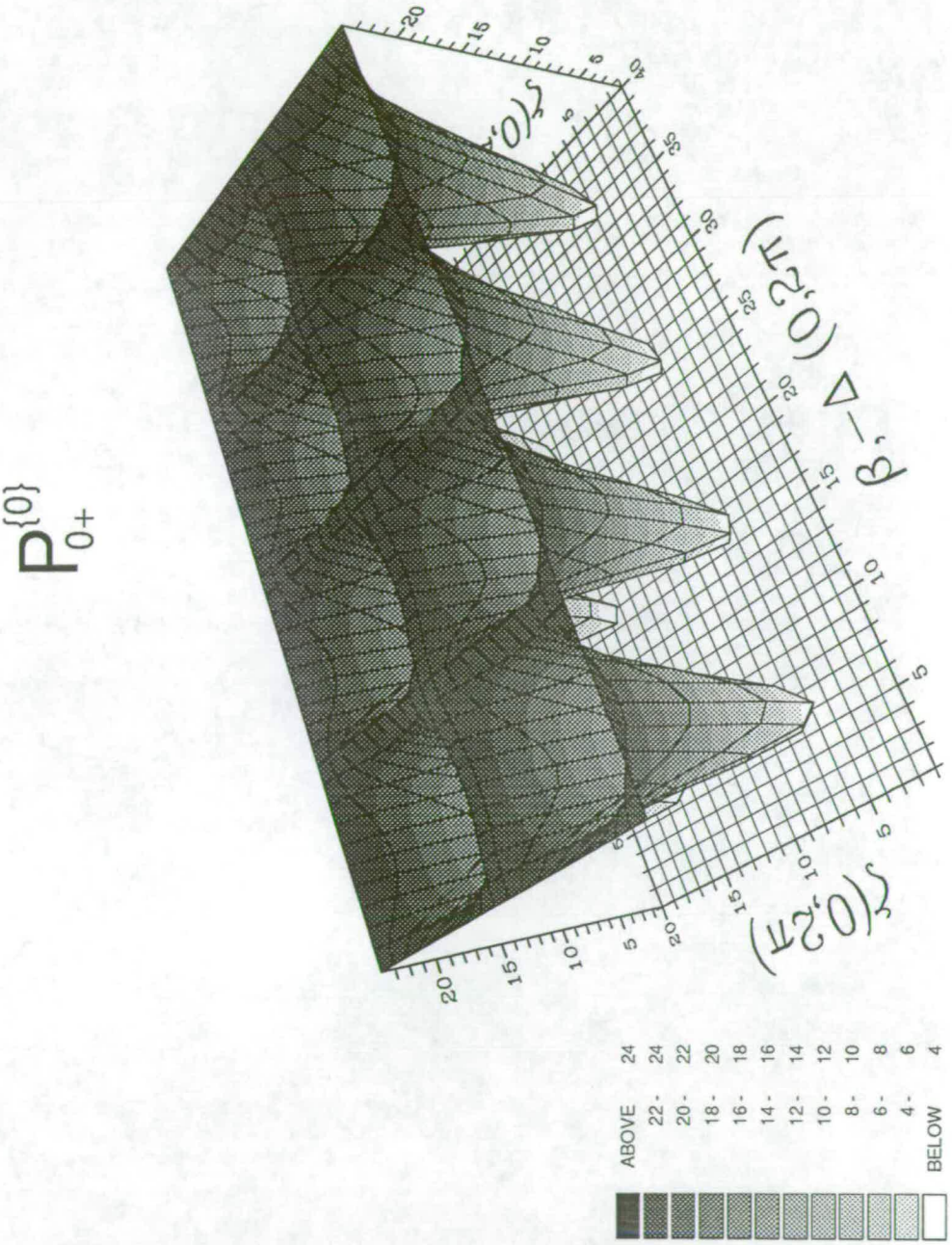

Figure 4–18: Plot of the line strength moment $P_{0+}^{\{0\}}$ for a two-photon $\Sigma \longleftarrow \Sigma$ transition as a function of the experimental parameters ζ, β and Δ with $\beta = -\Delta$. The line strength is for a Q-branch line originating from $J_i = 5$. This two-photon transition comprises two parallel single-photon transitions with $R^0 = 0.31246$, $R^{+1} = -0.67170$ and $R^{-1} = 0.67170$

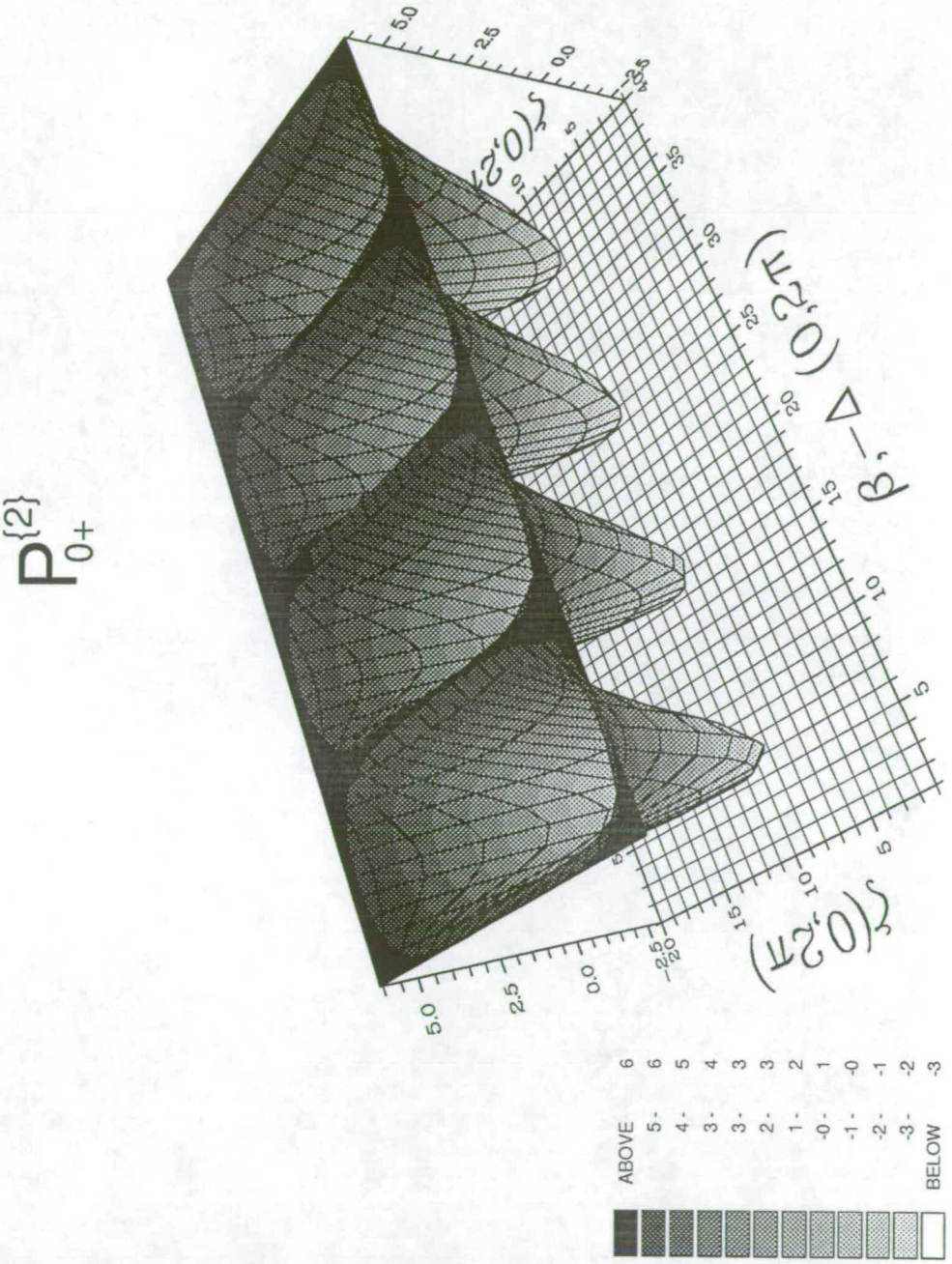

Figure 4–19: Plot of the line strength moment $P_{0+}^{\{2\}}$ for a two-photon $\Sigma \longleftarrow \Sigma$ transition as a function of the experimental parameters ζ, β and Δ with $\beta = -\Delta$. The line strength is for a Q-branch line originating from $J_i = 5$. This two-photon transition comprises two parallel single-photon transitions with $R^0 = 0.31246$, $R^{+1} = -0.67170$ and $R^{-1} = 0.67170$

R^0	R^{+1}	R^{-1}
0.75434	-0.46420	0.46420
0.31246	-0.67170	0.67170

Table 4–10:

Bibliography

[1] Hertel I. V., Stoll W., *Adv. At. Mol. Phys.*, **13**, 113 (1978)

[2] Bray R.G., Hochstrasser R.M., *Mol. Phys.*, **31**, 412 (1976)

[3] Polarized Light in Optics and Spectroscopy, *D. S. Kliger, J. W. Lewis, C. E. Randall* (Academic Press, 1990)

[4] Mathematical Methods for Physicists, *G. Arfken* (Academic Press, 1985)

[5] Kummel A. C., Sitz G. O., Zare R. N., *J. Chem. Phys.*, **85**, 6874 (1986)

[6] Kummel A. C., Sitz G. O., Zare R. N., *J. Chem. Phys.*, **88**, 6707 (1988)

[7] Greene C. H., Zare R. N., *J. Chem. Phys.*, **78**, 6741 (1983)

[8] Greene C. H., Zare R. N., *Ann. Rev. Phys. Chem.*, **33**, 119 (1982)

Chapter 5

Two Photon REMPI of HCl

5.1 Introduction

The main aim of the present work was to investigate the dynamics of small molecule-atom reactions by observing the product state distributions and the degree of alignment (if any) in the product species created by the reactions.

The chosen method of population and alignment measurement was via two photon Resonance-Enhanced-Multi-Photon-Ionization spectroscopy (REMPI or R2PI).

To make the required measurements and reduce the spectra to populations and angular momentum alignment moments, reliable values for the rotational line strengths had to be obtained. To this end the main objective of this spectroscopic study was to find bands whose rotational structure gave reliable and reproducible line strengths. The evaluation of absolute line positions was relatively unimportant.

It should be noted that a transition involving a perturbed upper or lower state does not necessarily result in unreliable line strengths. If the line strengths prove to be relatively constant irrespective of experimental conditions such as laser power, etc. then a set of empirical line strength correction factors can be derived which

are then multiplied by the 'true' theoretical line strengths to give the observed line strength factors.

5.2 REMPI Spectroscopy

The chosen method of spectroscopic study, REMPI, is one which has become increasingly prominent over the past decade due to the increased availability of powerful coherent light sources in the form of pulsed dye lasers (ref [1]).

An '$n+m$' photon ionization scheme is shown schematically in figure 5–1 The molecule in state E_i undergoes simultaneous absorption of n photons to reach state E_f with ionization being caused by absorption of a further m photons. The $n+m$ photons may come from either a single laser beam passing through the absorbing sample or they may come from two or more beams emitted from one or several lasers. The added complexity makes multiphoton spectroscopy harder experimentally than single-photon work but has the compensatory advantage that more factors contribute to the appearance of the resulting spectra and thus more information can be obtained on the excitation process as a whole.

The $2+1$ REMPI scheme used throughout this work has two principal advantages over single photon spectroscopic techniques.

1) Excited levels can be reached via two-photon transitions that are forbidden by parity or other selection rules for single-photon dipole radiation.

2) The accessible spectral range of multiphoton spectroscopy can be extended into the vacuum ultraviolet region if the photons come from visible or uv lasers. By combining tunable lasers or by using combinations of fixed frequency lasers with a tunable laser, continuous tuning ranges in the uv and vuv ranges are possible.

The probability A_{if} for a two-photon transition between an initial state E_i and an excited state E_f can be written as a product of two factors:

$$A_{if} \propto \frac{\gamma_{if}}{\left[\omega_{if} - \omega_1 - \omega_2 - \underline{v}\cdot(\underline{k}_1 + \underline{k}_2)\right]^2 + (\gamma_{if}/2)^2}$$

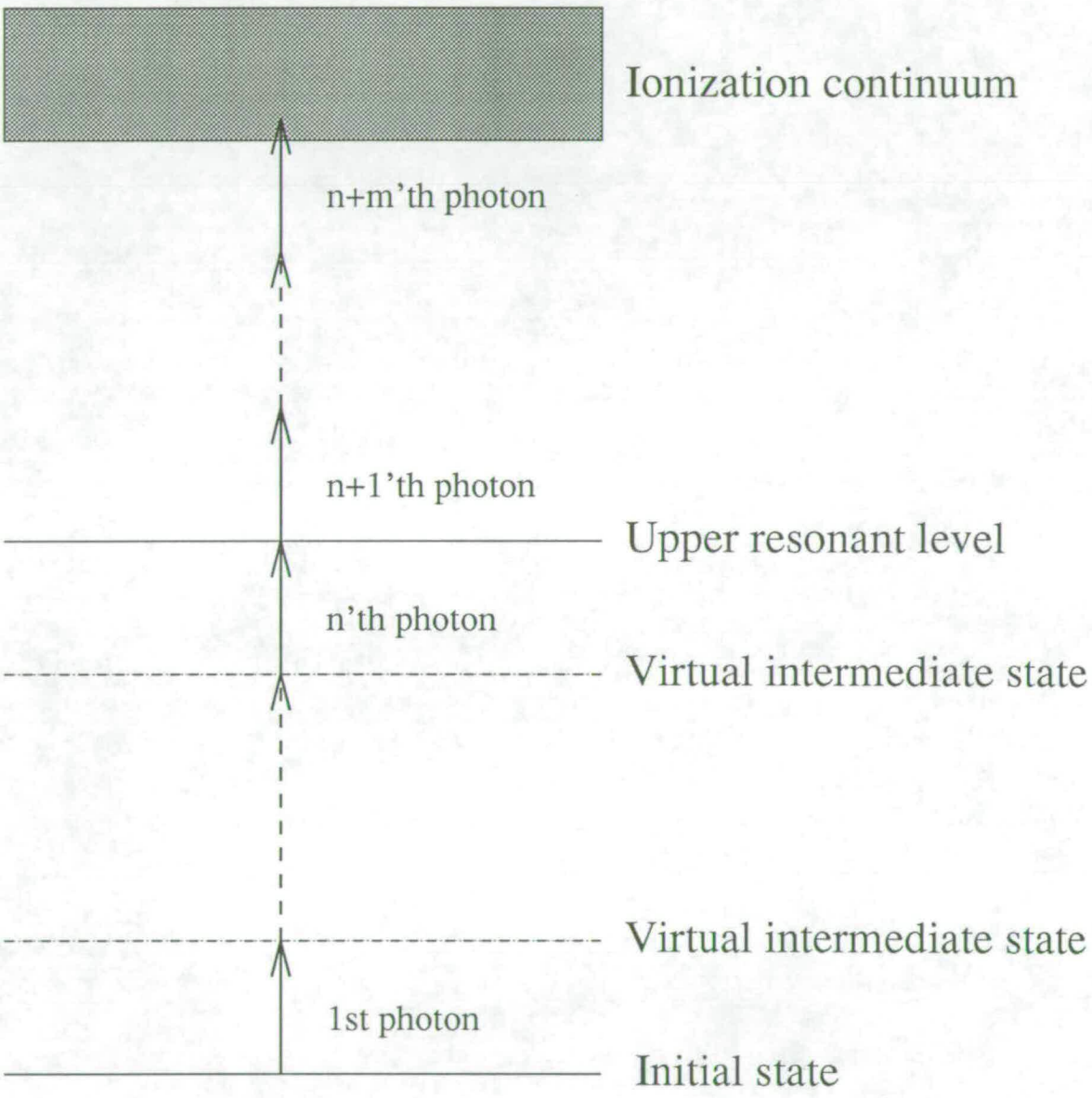

Figure 5–1: Schematic of an '$n + m$ photon' REMPI process

$$\times \left| \sum_k \frac{(\underline{R}_{ik} \cdot \underline{e}_1)(\underline{R}_{kf} \cdot \underline{e}_2)}{(\omega_{ki} - \omega_1 - \underline{k}_1 \cdot \underline{v})} + \frac{(\underline{R}_{ik} \cdot \underline{e}_2)(\underline{R}_{kf} \cdot \underline{e}_1)}{(\omega_{ki} - \omega_2 - \underline{k}_2 \cdot \underline{v})} \right|^2 \cdot I_1 I_2 \qquad (5.1)$$

where $\hbar\omega_1$ and $\hbar\omega_2$ are the energies of the first and second photons with wave vectors $\underline{k}_1$ and $\underline{k}_2$, polarization vectors $\underline{e}_1$ and $\underline{e}_2$ and intensities I_1 and I_2, and $\underline{v}$ is the molecular velocity.

The first factor gives the spectral line profile of the two-photon transition. It corresponds exactly to that of a single-photon transition of a moving molecule at a centre frequency $\omega_{if} = \omega_1 + \omega_2 + \underline{v} \cdot (\underline{k}_1 + \underline{k}_2)$ with a homogeneous linewidth γ_{if}. Integration over all molecular velocities $\underline{v}$ of a thermal sample gives a Voigt profile with a halfwidth which depends on the relative orientation of $\underline{k}_1$ and $\underline{k}_2$. If both light waves are parallel, the Doppler width which is proportional to $|\underline{k}_1 + \underline{k}_2|$ becomes maximum and is in general large compared to the homogeneous width γ_{if}. For $\underline{k}_1 = -\underline{k}_2$, i.e. counterpropagating beams, the Doppler broadening vanishes and we obtain a pure Lorentzian line profile with a homogeneous line width γ_{if} provided that the laser linewidth is small compared to γ_{if}.

Because the transition probability is proportional to the product of the intensities $I_1 I_2$, pulsed lasers are generally required to deliver sufficiently large peak powers. The spectral linewidth of these lasers is often comparable or larger than the Doppler width and the terms in the denominator of equation 5.1 of the form $(\omega_{ki} - \omega - \underline{k} \cdot \underline{v})$ can be approximated by $(\omega_{ki} - \omega)$.

The second factor in equation 5.1 describes the transition probability for the two-photon transition. It can be derived quantum mechanically by second-order perturbation theory [2]. This factor contains a sum of products of matrix elements $R_{ik}R_{kf}$ for transitions between the initial state i and intermediate molecular levels k and between these levels k and the final state f. The summation extends over all molecular levels k. The denominator shows, however, that only those levels k which are not too far off resonance with one of the Doppler-shifted laser frequencies $\omega_n' = \omega_n - \underline{k}_n \cdot \underline{v}$ $(n = 1, 2)$ will contribute significantly to the overall process.

As stated, the two-photon transition probability is proportional to I^2 for a single colour experiment ($\omega_1 = \omega_2$) requiring very high photon fluxes. Typical cross-sections for two-photon absorption are 10^{-50}cm^2 . It is these small cross-

sections combined with the I^2 power dependence that have made pulsed dye lasers the only viable source of light. The current generation of pulsed dye lasers can produce in the region of 10^{-3}Joules in 10ns requiring the beam to be focussed to a radius of approximately 100μm to achieve a two-photon transition probability of 10^{-2} per pulse. The very high peak powers used do, however, lead to several line broadening processes, in addition to the Doppler broadening already discussed, that can have a marked effect on the observed spectra.

Another major cause of line broadening is the AC Stark effect [3,4,5]. The degree of broadening can be quite extensive even at moderate laser powers, about 60GHz/GWcm^{-2}. The Stark effect shows itself as an asymmetric broadening rather than a shift because of the temporal and spatial variation in intensity during any particular pulse.

A lesser cause of line broadening arises due to the fact that the excitation and ionization processes must take place within the duration of a single laser pulse. For a 5ns pulse the uncertainty principle limits the linewidth to a minimum of approximately 200MHz. It is usually the case, however, that the ionization step is much more probable than the excitation step (by two orders of magnitude or so) so that when reasonable signal levels are achieved the excited state lifetime is considerably shortened and the linewidth is correspondingly broadened. For an '$n+m$' multiphoton ionization process the degree of lifetime broadening is a function of $\frac{n}{m}$ thus the broadening for a $3+1$ process would be greater than that for a $2+1$ process.

A major factor affecting the power dependance of the REMPI signal arises from the conical geometry of the focused light beam and the high order of non-linearity of the ionization. For the Rayleigh length (shown in figure 5–2) the focus region is more or less cylindrical, but away from that the conical geometry of the beam creates a rapid intensity variation and the intensity drops off in proportion to the square of the distance from the focus. It is often quite easy to saturate the ionization in the focus region. When this happens, continuing to increase the laser intensity creates no more signal within the Rayleigh length, but the ionization region begins to move out into the conical focus regions. In this case it

can be shown that the power dependence becomes $I^{3/2}$ irrespective of the number of photons involved in the ionization [6] [1] .

5.3 Two Photon REMPI of HCl - General Considerations

The two-photon REMPI spectroscopy of HCl is characterized by the two-photon electric dipole selection rules. States described by Hund's case (a), (Λ, S) basis, shown in figure 5–3, are subject to a restriction on the change in axial component of the orbital angular momentum, $|\Delta\Lambda| \leq 2$. For states following Hund's case (c), (Ω, ω) basis, there is a restriction on the change in axial component of the total angular momentum, $|\Delta\Omega| \leq 2$. In practice there is a relaxation of these selection rules suggesting more intermediate coupling cases.

One-photon spectroscopy of HCl has detected transitions which are totally forbidden under dipole selection rules where one assumes the Born-Oppenheimer approximation with no spin-orbit coupling and a totally symmetric ground state [8, 9,10]. This demonstrates the weakening of the (Λ, S) coupling. Generally, as the principal quantum number, n, increases the axial component of the total angular momentum for the ion core and the excited electron play a more dominant role, characteristic of (Ω, ω) coupling. When the excited states involve a core within which strong spin-orbit coupling is present, Ω is the conserved quantity. This Hund's case (c) basis is thus expected to describe more adequately the allowed transitions and the spacings of the multiplet states.

---

[1] For a multiphoton process involving an n photon excitation to the resonant state it can be shown that the actual ion yield is proportional to f^{4-2n} where $n \geq 2$ (see [7]) where f is the focal length of the lens being used. At first sight therefore it appears that there is little to gain by using short focal length lenses for two photon REMPI. However, although the ion yield remains unchanged the detection efficiency will in general depend on the volume in which the ions are made.

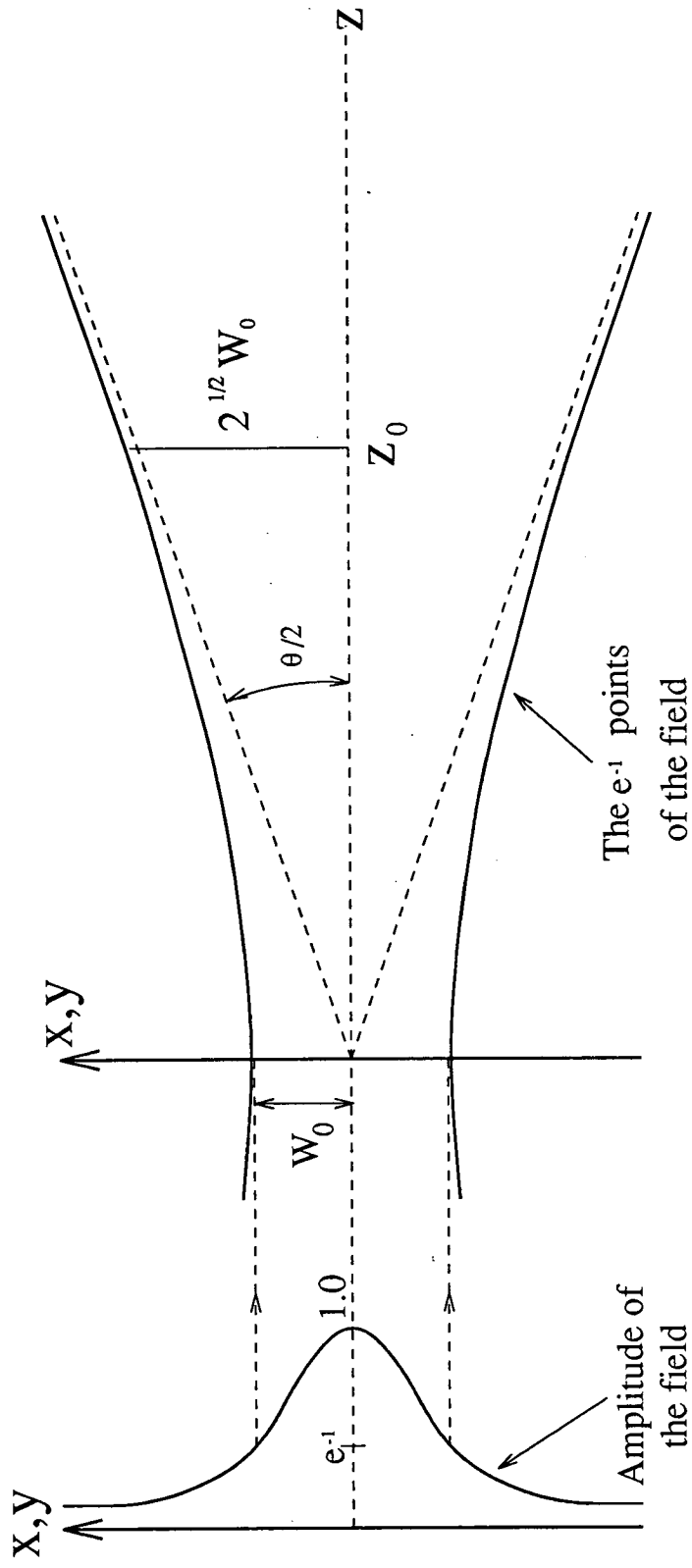

Figure 5–2: Rayleigh length z_0 within focused Gaussian beam

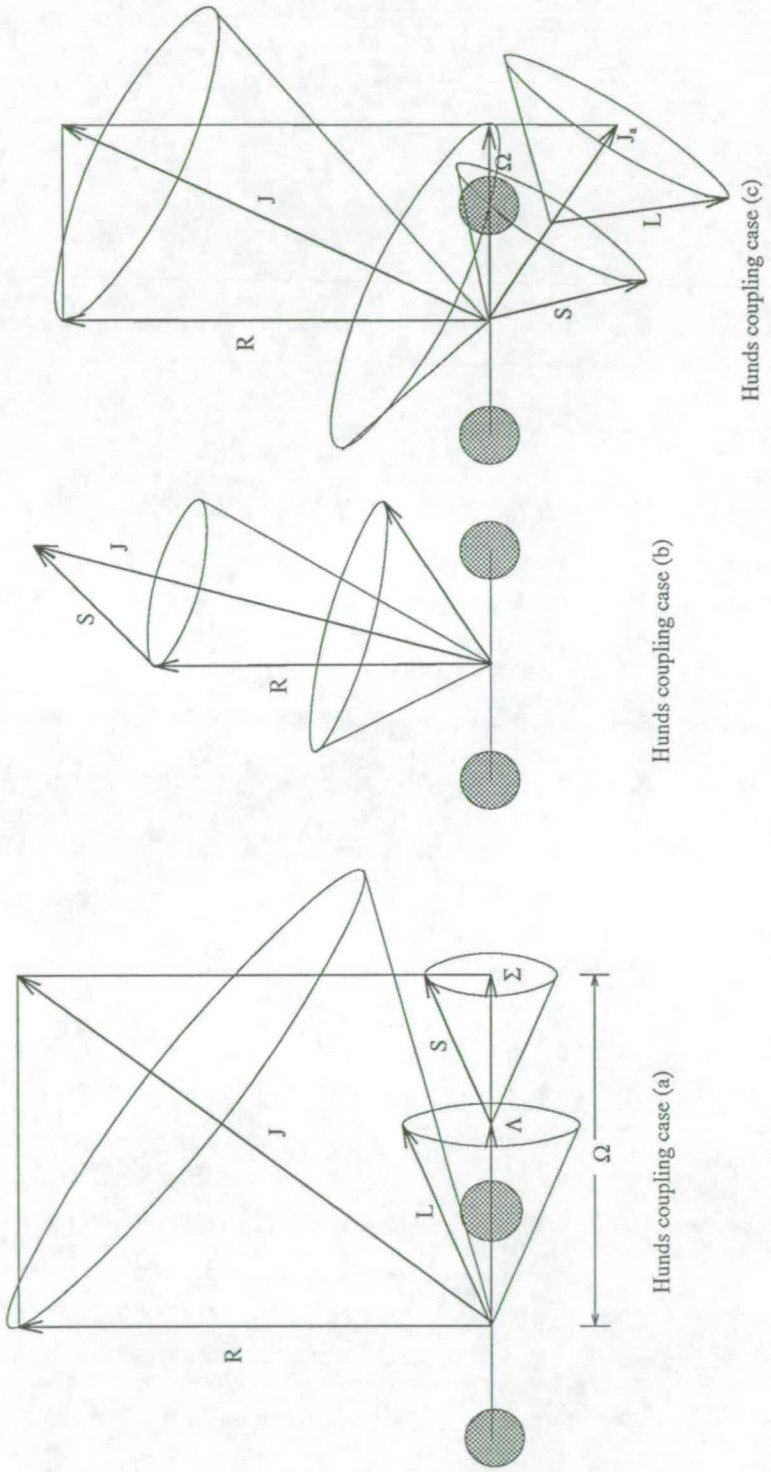

Figure 5–3: Hunds coupling cases

For transitions from the $X^1\Sigma^+(0^+)$ ground electronic state, the relevant rotational and parity [2] selection rules are: $|\Delta J| = 0$ or 2, and $e(A') \leftarrow e(A')$; $|\Delta J| = 1$, and $f(A'') \leftarrow e(A')$. In hydrogen chloride where the ground state levels are all $e(A')$, the two-photon transition to the O, Q and S-branch lines access $e(A')$ components while transitions to P and R-branches access the $f(A'')$ components. With a proper choice of photon frequency it is possible to select not only a specific rotational-vibrational-electronic intermediate resonant state but one with a known parity.

The choice as to exactly which transitions to study was largely a question of the photon energies that could be generated. Using the laser system described in section 2.2 the single photon energies ranged from approximately 30000cm^{-1} using DCM dye and doubling only to 45100cm^{-1} using Rhodamine 590 dye and mixing the doubled dye output with the Nd:YAG fundamental at 1064nm giving a maximum two-photon excitation energy of approximately 90200cm^{-1}. This can be compared to the energies of several of the main electronic states as shown in figure 5–4

A comprehensive list of the states accessible to us is given in tables 5–1 and 5–2 as derived from reference [12]. A large number of initial survey spectra were collected and identified prior to the systematic catalogue by Greene *et al.* [12] including those from $V^1\Sigma^+(0^+) \leftarrow X^1\Sigma^+(0^+)$, $E^1\Sigma^+(0^+) \leftarrow X^1\Sigma^+(0^+)$, $F^1\Delta(2) \leftarrow X^1\Sigma^+(0^+)$, $I^1\Delta(2) \leftarrow X^1\Sigma^+(0^+)$, $H^1\Sigma^+(0^+) \leftarrow X^1\Sigma^+(0^+)$, $j^3\Sigma^-(1) \leftarrow X^1\Sigma^+(0^+)$, $\Omega'(0^+) \leftarrow X^1\Sigma^+(0^+)$, $\Omega'(2) \leftarrow X^1\Sigma^+(0^+)$, $\Omega'(\leq 2) \leftarrow X^1\Sigma^+(0^+)$, $f^3\Delta \leftarrow X^1\Sigma^+(0^+)$ and $g^3\Sigma^- \leftarrow X^1\Sigma^+(0^+)$.

Many of the alignment effects were expected to lead to very subtle changes in the line strengths and thus the lines chosen with which to monitor these effects had to have the highest possible absolute detection sensitivities. Initial measurements

---

[2]The labeling of parity doublet components adheres to the scheme used in [11] . ie rotational levels with parity $+(-1)^J$ are labeled e or A' and levels with parity $-(-1)^J$ are labeled f or A''.

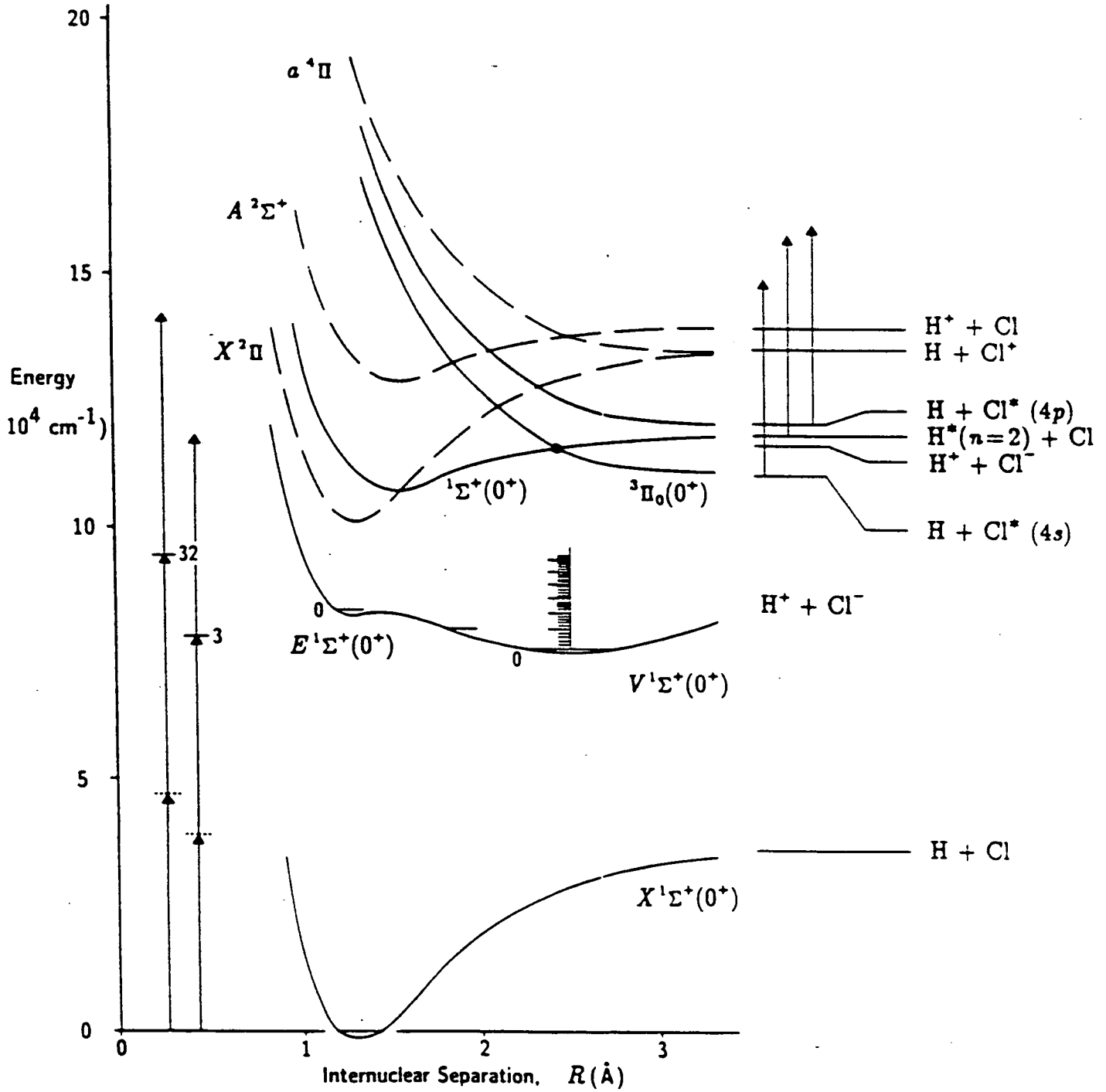

Figure 5–4: Energy level diagram for HCl

State	v	$\nu_0(v)$	B_v	$D_v \times 10^3$
$V^1\Sigma^+(0^+)$	3 A'	78697.9	2.85	0.5
$V^1\Sigma^+(0^+)$	4 A'	79453.7	2.89	0.8
$V^1\Sigma^+(0^+)$	5 A'	80183.4	2.929	0.711
$V^1\Sigma^+(0^+)$	6 A'	80887.9	2.97	0.19
$V^1\Sigma^+(0^+)$	7 A'	81569.8	3.05	2.54
$f^3\Delta_3(3)$	0 A'	81826.5	9.44	0.240
	A''	81827.6	9.32	-2.63
$f^3\Delta_2(2)$	0 A'	82014.6	10.915	4.382
	A''	82014.9	10.896	3.562
$V^1\Sigma^+(0^+)$	8 A'	82225.8	3.165	0.725
$f^3\Delta_1(1)$	0 A'	82523.6	10.293	-0.267
	A''	82523.4	10.32	-0.87
$V^1\Sigma^+(0^+)$	9 A'	82839.7	3.709	5.318
$F^1\Delta(2)$	0 A'	82847.2	10.3246	0.9837
	A''	82847.4	10.3228	1.0925
$g^3\Sigma^-(0^+)$	0 A'	83087.7	7.629	-5.726
$g^3\Sigma^-(1)$	0 A'	83263.6	11.94	100.6
$V^1\Sigma^+(0^+)$	10 A'	83434.0	5.05	-24.1
$E^1\Sigma^+(0^+)$	0 A'	83780.0	6.6257	3.1134
$V^1\Sigma^+(0^+)$	11 A'	84208.0	4.348	-6.872
$f^3\Delta_3(3)$	1 A'	84341.1	9.56	1.27
	A''	84240.9	9.59	2.00
$f^3\Delta_2(2)$	1 A'	84531.4	10.87	0.64
	A''	84530.2	10.070	7.264
$V^1\Sigma^+(0^+)$	12 A'	84747.1	3.997	0.1876
$f^3\Delta_1(1)$	1 A'	85021.6	10.61	6.7
	A''	85021.4	10.65	8.8
$V^1\Sigma^+(0^+)$	13 A'	85278.4	4.1196	1.0493

Π states not included in table since intrinsically weaker for two photon work than $\Delta\Lambda = 0$ or 2 transitions.

Table 5–1: States accessible via two-photons using current experimental setup. From reference [12]

State	v	$\nu_0(v)$	B_v	$D_v \times 10^3$
$F^1\Delta(2)$	1 A'	85363.7	10.143	1.0659
	A''	85363.8	10.1447	1.7346
$V^1\Sigma^+(0^+)$	14 A'	85671.7	6.126	4.529
$g^3\Sigma^-(0^+)$	1 A'	85782.6	10.70	107.3
$E^1\Sigma^+(0^+)$	1 A'	85919.8	6.028	-79.55
$V^1\Sigma^+(0^+)$	15 A'	86404.6	4.01	-3.648
$V^1\Sigma^+(0^+)$	16 A'	86931.8	3.753	-0.926
$f^3\Delta_2(2)$	2 A'	86949.6	11.2	
$i^3\Delta_3(3)$	0 A'	87409.8	9.051	1.7780
$V^1\Sigma^+(0^+)$	17 A'	87465.2	3.455	-3.494
$i^3\Delta_2(2)$	0 A'	87657.0	9.830	1.396
	A''	87656.4	9.893	3.032
$F^1\Delta(2)$	2 A'	87772.4	10.256	5.153
	A''	87772.4	10.248	5.004
$V^1\Sigma^+(0^+)$	18 A'	87967.4	4.3411	6.0767
$i^3\Delta_1(1)$	0 A'	88121.5	9.8441	0.6500
	A''	88121.5	9.8465	0.6789
$V^1\Sigma^+(0^+)$	19 A'	88565.5	3.778	-7.405
$I^1\Delta(2)$	0 A'	88582.4	9.5490	0.7016
	A''	88582.4	9.549	0.5683
$H^1\Sigma^+(0^+)$	0 A'	88685.2	8.3687	-0.599
$j^3\Sigma^-(1)$	0 A'	88971.7	9.747	3.392
	A''	88970.5	9.76	2.918
$V^1\Sigma^+(0^+)$	20 A'	89086.1	3.403	1.057
$j^3\Sigma^-(0^+)$	0 A'	89282.2	9.657	0.871
$V^1\Sigma^+(0^+)$	21 A'	89607.3	3.302	-2.378
$i^3\Delta_3(3)$	1 A'	89996	9.0	
$V^1\Sigma^+(0^+)$	22 A'	90106.8	3.297	-0.757

Π states not included in table since intrinsically weaker for two photon work than $\Delta\Lambda = 0$ or 2 transitions.

Table 5–2: States accessible via two-photons using current experimental setup. From reference [12] (continued)

suggested that the most favourable transitions were those involving the $E^1\Sigma^+(0^+)$, $V^1\Sigma^+(0^+)$ and $F^1\Delta(2)$ states and only spectra of these transitions are presented. In addition these states also had the largest amount of two-photon data gathered for them which provided a useful comparison with our own results.

5.4 $^1\Sigma^+(0^+)$ States

The features due to the $E^1\Sigma^+(0^+)$ and $V^1\Sigma^+(0^+)$ states are the most abundant in the two-photon spectroscopy of HCl. Molecular orbital calculations [13] show that these states result from strongly interacting covalent and ionic configurations. At small interatomic separations the V and E states arise predominantly from the molecular orbital configurations $^1\Sigma^+(\sigma^2\pi^3)c\pi$ and $^1\Sigma^+(\sigma^2\pi^3)d\pi$ respectively. There is considerable distortion of the potential curves due to avoided crossings. In the case of the V state this leads to a potential well with a double minimum as shown in figure 5–4. The interaction of the E and V states to form the so called B double minimum state is manifest in the non Franck-Condon vibrational band intensities observed for these transitions [13]. With respect to the double minimum of the $B^1\Sigma^+(0^+)$ state, the vibrational wave functions of the outer well mix with those of the inner well and the molecular constants and transition moments reflect an effective or average equilibrium bond length.

5.4.1 $E^1\Sigma^+(0^+) \leftarrow X^1\Sigma^+(0^+)$ transitions

The $(0-0)$ band of the $E^1\Sigma^+(0^+) \leftarrow X^1\Sigma^+(0^+)$ transition was found to be very heavily perturbed due to interaction of the $E^1\Sigma^+(0^+)v = 0$ level with the $V^1\Sigma^+(0^+)v = 10$ level. As a result it would be far too weak in absolute terms to be used for purposes of alignment detection in the products of bimolecular reactions, and derivation of populations would be even more difficult. A representative spectrum of the $(1-0)$ band of the $E^1\Sigma^+(0^+) \leftarrow X^1\Sigma^+(0^+)$ transition obtained using the apparatus described in section 2 is shown in figure 5–5 . As can be seen the $E^1\Sigma^+(0^+) \leftarrow X^1\Sigma^+(0^+)$ transitions are dominated by a strong Q-branch with

very weak O and S-branches. Mass to charge ratios of 36, 35 and 1 corresponding to $H^{35}Cl^+$, $^{35}Cl^+$ and H^+ ions respectively were observed on all TOFMS signals arising from excitation to the $E^1\Sigma^+(0^+)$ and $V^1\Sigma^+(0^+)$ levels as well as peaks for the ^{37}Cl equivalents. It was observed that the $H^{35}Cl^+$ to $^{35}Cl^+$ ratio varied only very weakly with the laser power (in agreement with [14]). This power dependence would make it difficult to apply the two-photon line strength formula presented in sections 4.2 and 4.3 which assumes that the initial two-photon excitation step is unsaturated with the final ionization step being completely saturated. The threshold for Cl^+ ion production from HCl requires at least four photons with the present experimental setup and several mechanisms have been put forward [15, 14]. A diagram showing the relevant energy levels is given in figure 5–6.

The first possibility for Cl^+ ion production is that a pair of sequential two-photon absorptions produces HCl^+ in an electronic state that dissociates directly into atomic ions. This, however, would result in a HCl^+ to Cl^+ ratio which depended on the photon flux raised to the power one or more since HCl^+ from the resonant two-photon HCl state requires a single photon whereas the formation of the Cl^+ ion from the same HCl state requires a further two photons.

A second possibility is that HCl^+ is formed by a three photon absorption with a further single photon resulting in the production of Cl^+ via excitation to a repulsive state in HCl^+. This, however, would not explain why the HCl^+ to Cl^+ ratio depends to such a large extent on the intermediate state encountered in the process.

The most likely possibility, however, is that following two-photon excitation of an electronic state, absorption of a photon to produce HCl^+ competes with absorption by a dissociative state in HCl which correlates with excited atomic products (see figure 5–6). Due to the very high photon flux being used in a typical two-photon REMPI experiment one photon ionization of excited Cl is then very likely. In this case the HCl^+ to Cl^+ ratio would depend only very weakly on the power since each of the one photon steps should be very nearly saturated. This would explain why the atomic ions are observed only for transitions through states with long bond length character, i.e. $E^1\Sigma^+(0^+)$ and $V^1\Sigma^+(0^+)$, and not for the

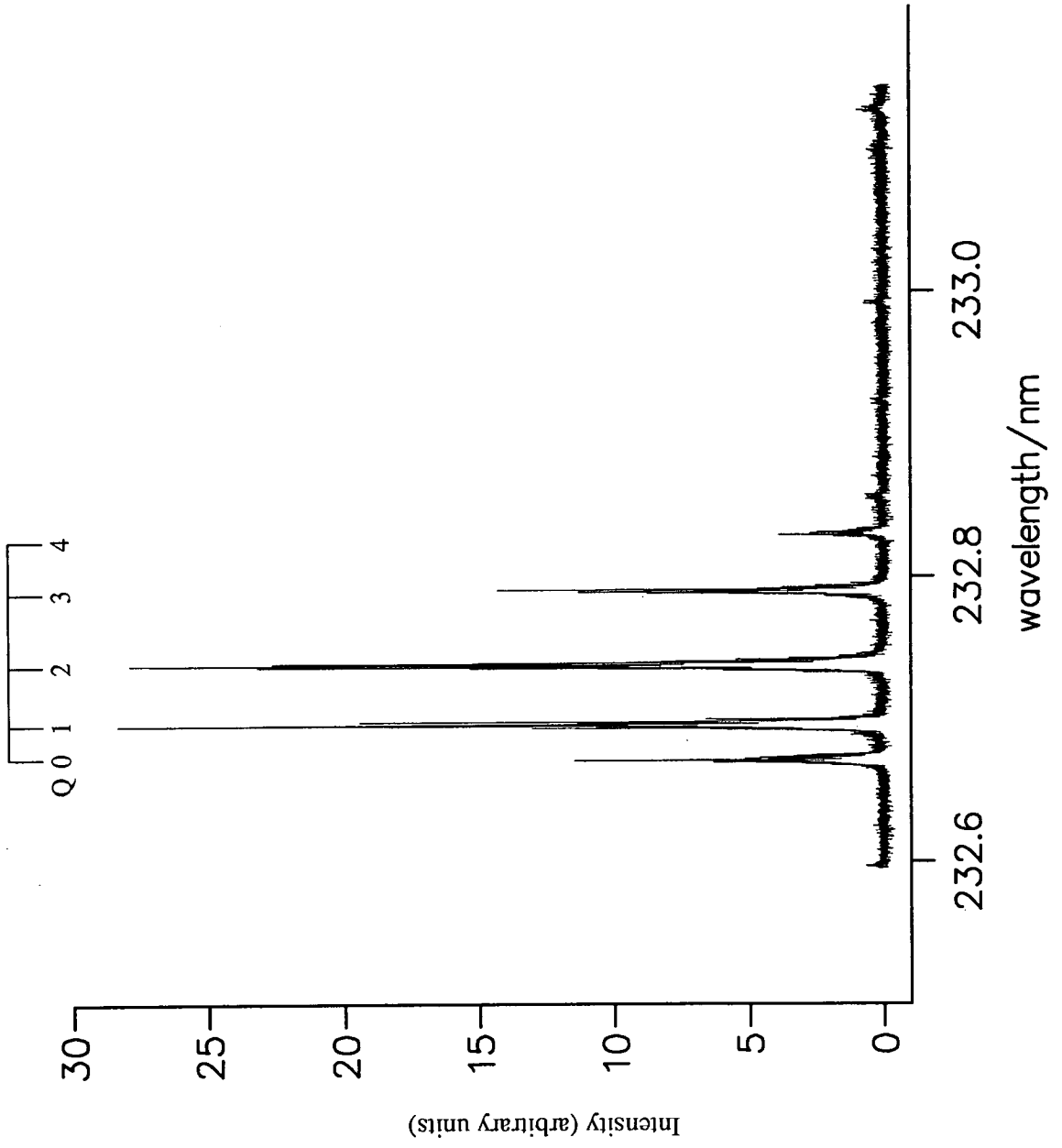

Figure 5–5: $2+1$ REMPI spectrum of HCl at room temperature for the $(1-0)$ band of the $E^1\Sigma^+(0^+) \leftarrow X^1\Sigma^+(0^+)$ transition

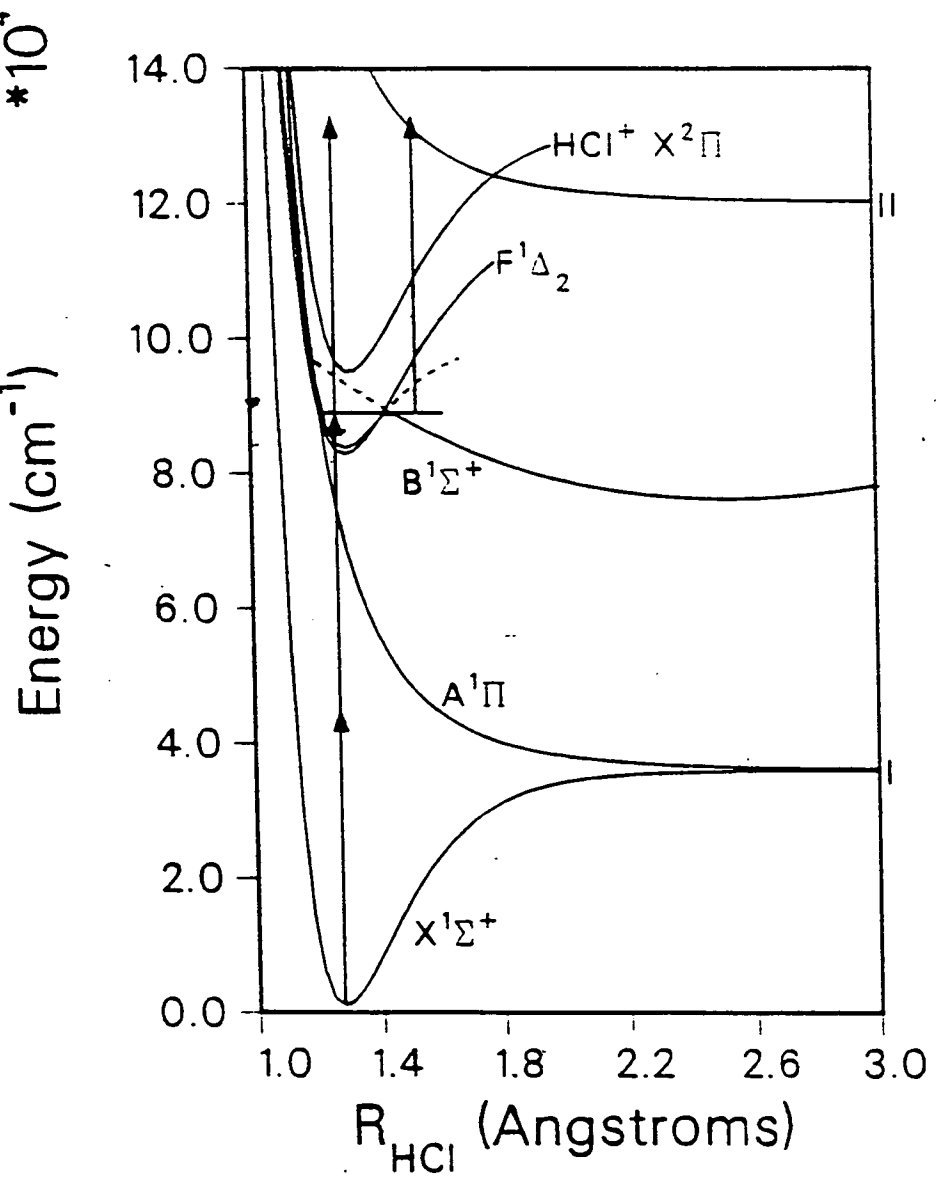

Figure 5–6: Energy level diagram for HCl showing possible atomic ion production channels

$F^1\Delta(2)$ state transitions. This same mechanism can also be used to explain H^+ ion production.

5.4.2 $V^1\Sigma^+(0^+) \leftarrow X^1\Sigma^+(0^+)$ transitions

The (11-0), (12-0), (15-0) and (16-0) bands of the $V^1\Sigma^+(0^+) \leftarrow X^1\Sigma^+(0^+)$ transition are shown in figures 5–7 to 5–10. The intensity, I_e, of any rotational line is given by

$$I_e = C \cdot g(J_i) P_{0+}^{\{0\}}(J_i) \exp(\frac{-\mathrm{E}_{rot}}{kT}) \tag{5.2}$$

where C is a proportionality constant, $g(J_i)$ is the degeneracy of the J_i'th rotational level, $\exp(\frac{-\mathrm{E}_{rot}}{kT})$ is the population of each level and $P_{0+}^{\{0\}}(J_i)$ is the rotational line strength factor as presented in tables 4–3 and 4–4 in section 4.2. This can be rearranged to give

$$\ln\left(\frac{I_e}{g(J_i)P_{0+}^{\{0\}}(J_i)}\right) = \frac{-\mathrm{E}_{rot}}{kT} + \ln C \tag{5.3}$$

From equation 5.3 it is clear that a plot of $\ln\left(\frac{I_e}{g(J_i)P_{0+}^{\{0\}}(J_i)}\right)$ vs E_{rot} should result in a straight line with gradient $\frac{-1}{kT}$ where T is the temperature of the sample gas. This is known as a Boltzmann plot. Boltzmann plots for the (11-0) and (12-0) bands in figures 5–11 and 5–12. All plots were evaluated using the combined ion signal from $H^{35}Cl^+$ and $^{35}Cl^+$.

The Boltzmann plot for the $(11-0)$ band of the $V^1\Sigma^+(0^+) \leftarrow X^1\Sigma^+(0^+)$ transition shown in figure 5–11 results in a temperature of 295K($\pm$10K) and as can be seen no points deviate significantly from the straight line plot. A similar plot for the $(12-0)$ band of the same transition shown in figure 5–11, however, shows a significant, and reproducible, perturbation in the $Q(5)$ rotational line strength. The resulting temperature is 222K($\pm$22K) when the $Q(5)$ line is included in the data and 273K($\pm$16K) when it is discarded. Boltzmann plots for the $(15-0)$ and $(16-0)$ bands showed their rotational line strengths to be perturbed also.

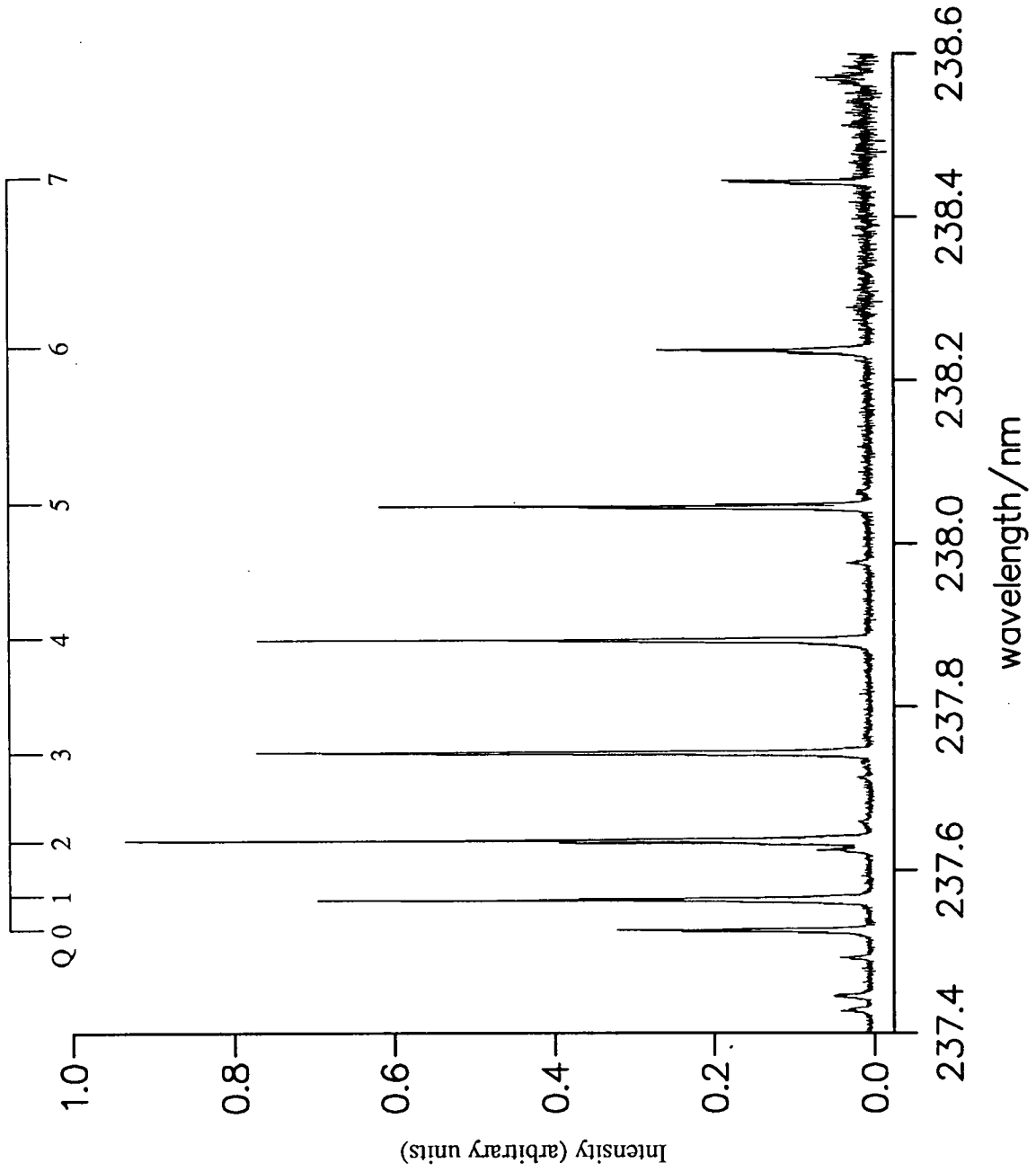

Figure 5–7: $2+1$ REMPI spectrum of HCl at room temperature for the $(11-0)$ band of the $V^1\Sigma^+(0^+) \leftarrow X^1\Sigma^+(0^+)$ transition

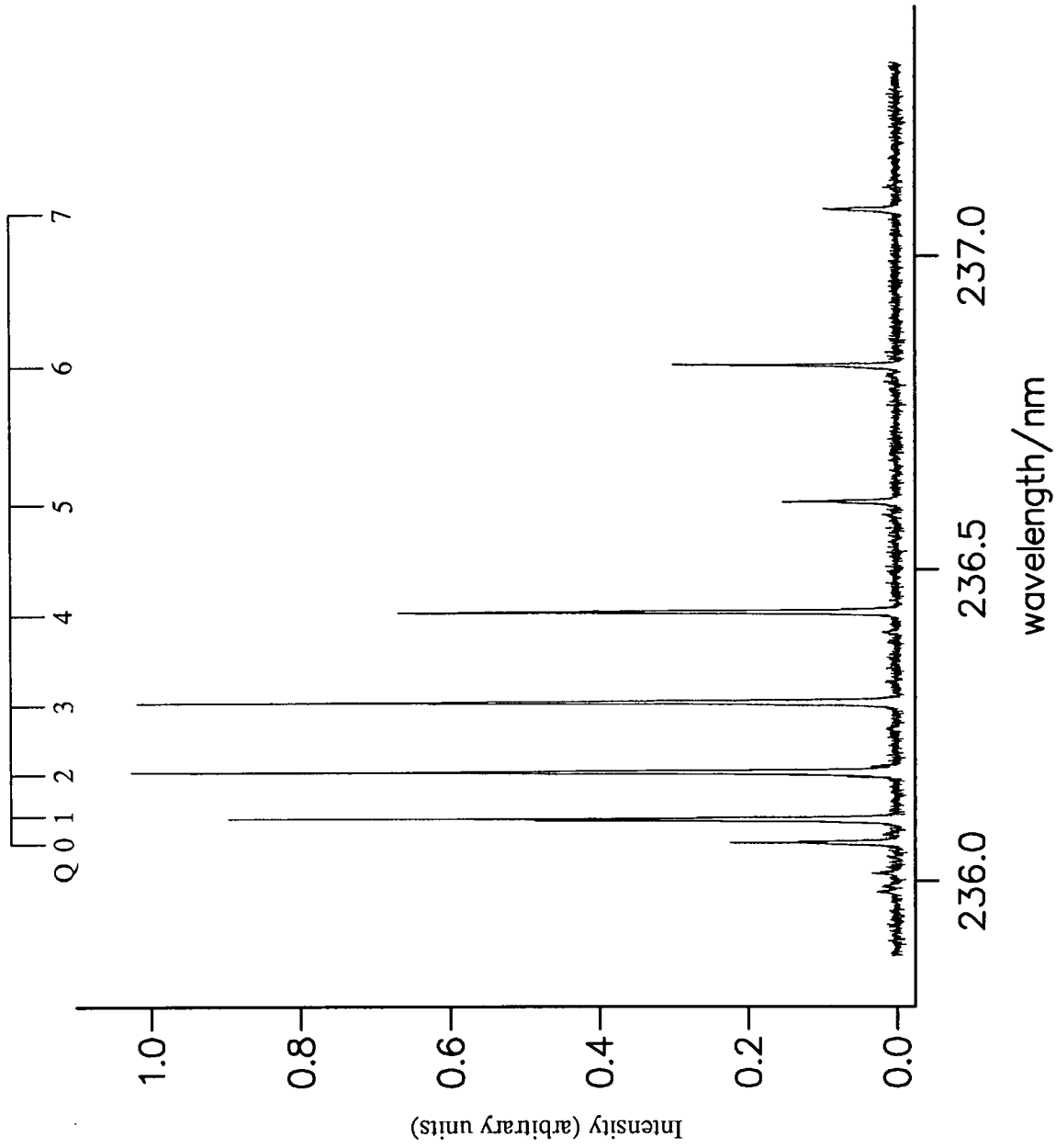

Figure 5–8: $2+1$ REMPI spectrum of HCl at room temperature for the $(12-0)$ band of the $V^1\Sigma^+(0^+) \leftarrow X^1\Sigma^+(0^+)$ transition

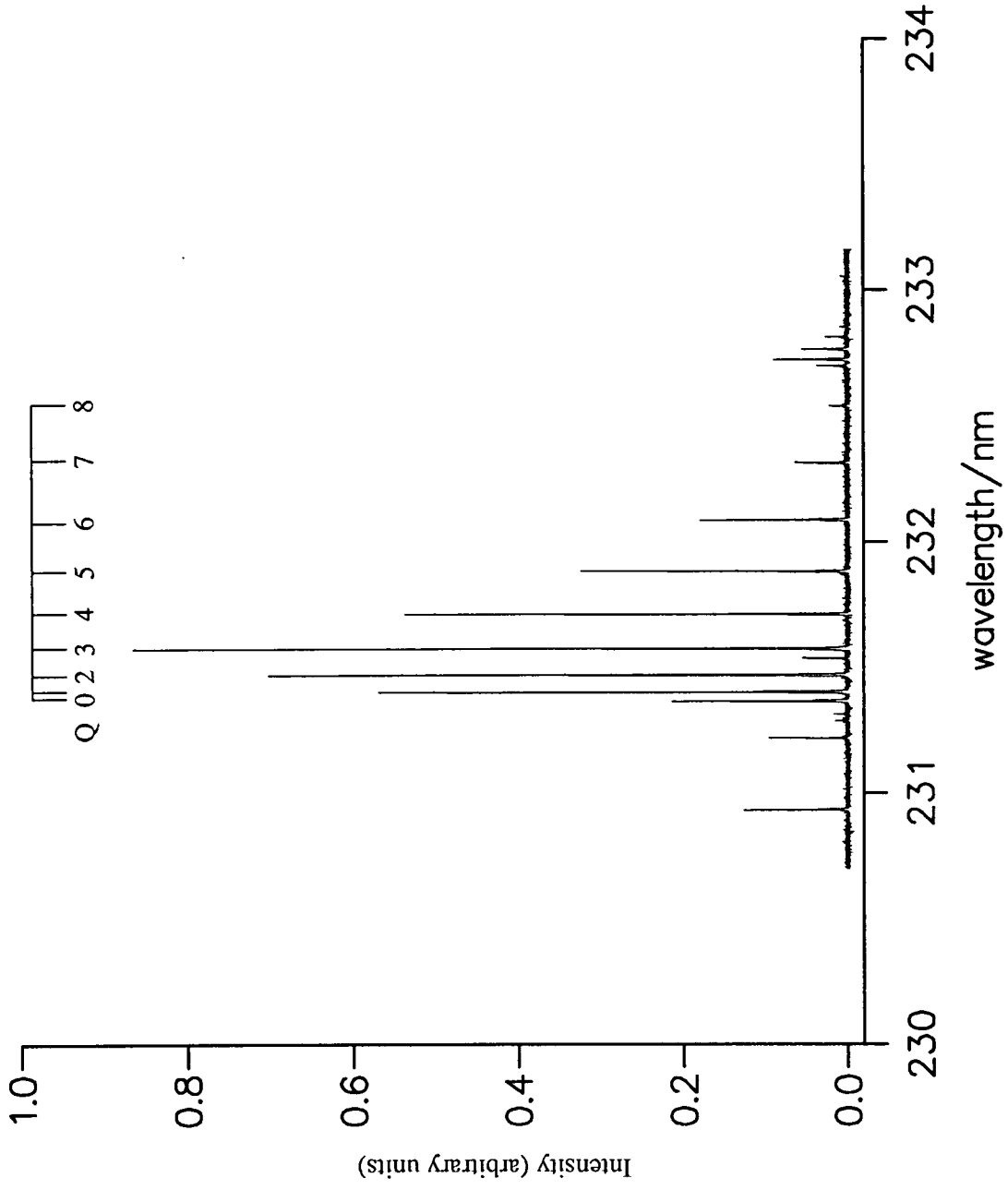

Figure 5–9: $2+1$ REMPI spectrum of HCl at room temperature for the $(15-0)$ band of the $V^1\Sigma^+(0^+) \leftarrow X^1\Sigma^+(0^+)$ transition

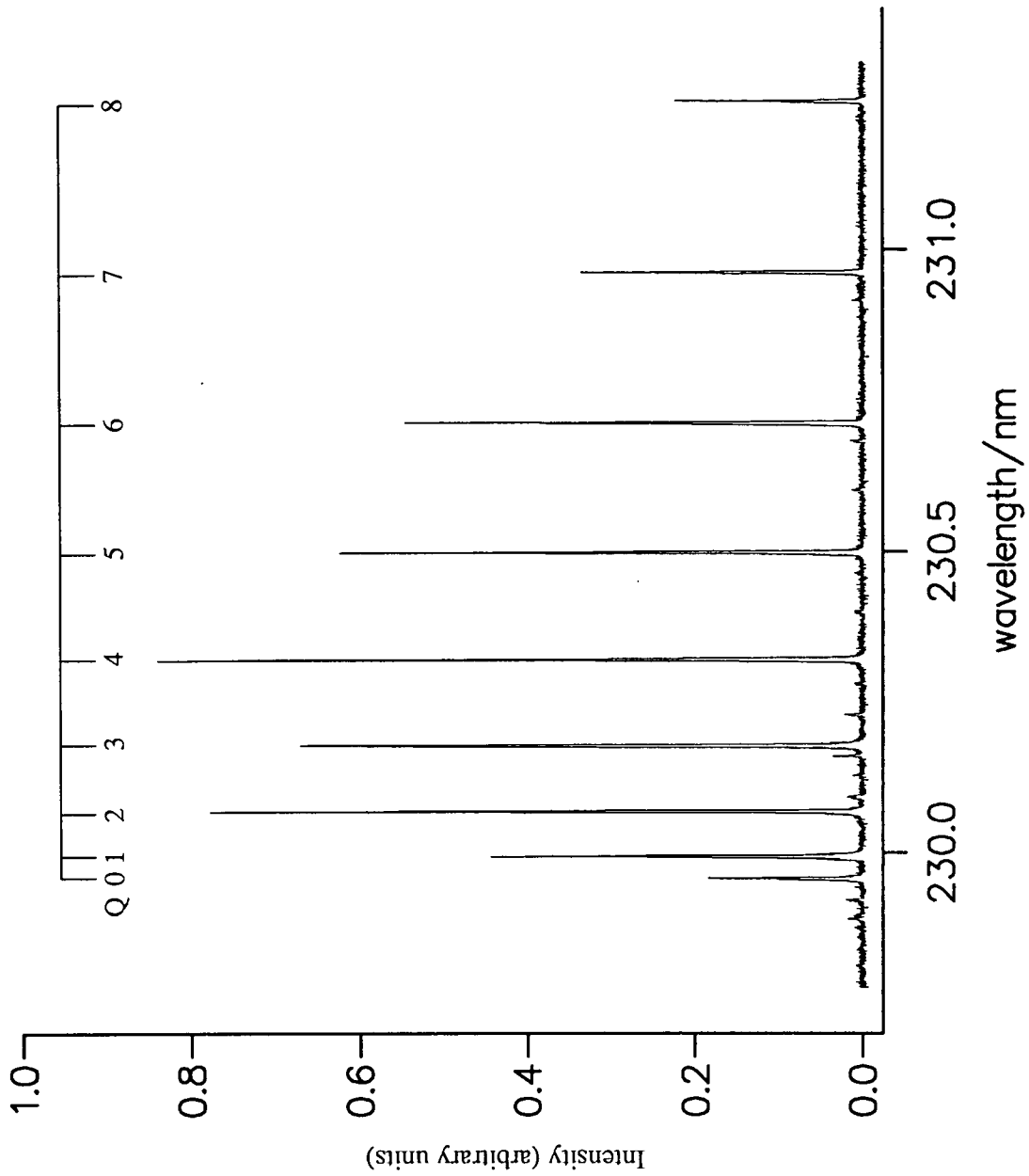

Figure 5–10: 2+1 REMPI spectrum of HCl at room temperature for the (16−0) band of the $V^1\Sigma^+(0^+) \leftarrow X^1\Sigma^+(0^+)$ transition

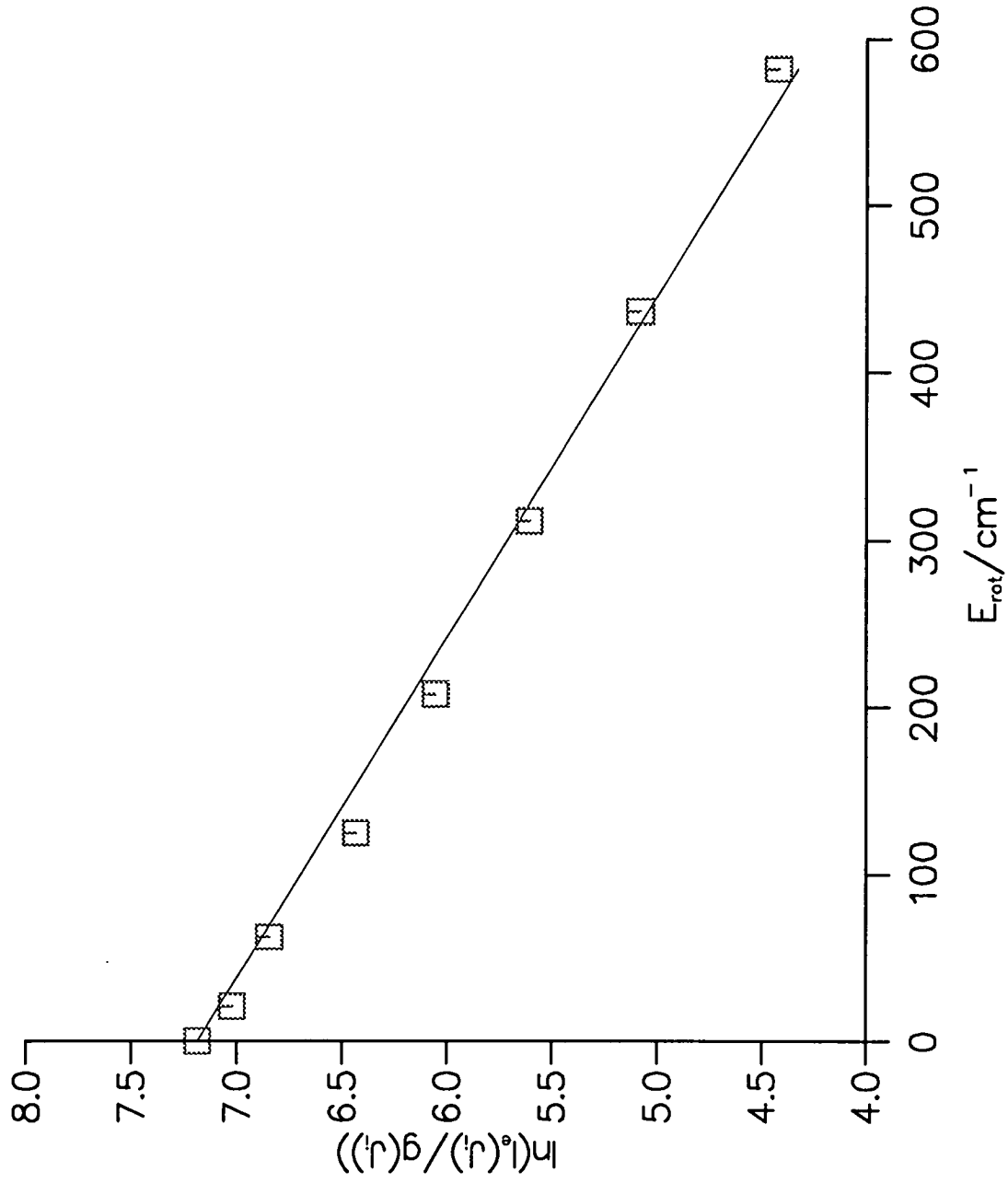

Figure 5–11: Boltzmann plot for the (11−0) band of the $V^1\Sigma^+(0^+) \leftarrow X^1\Sigma^+(0^+)$ transition in room temperature HCl

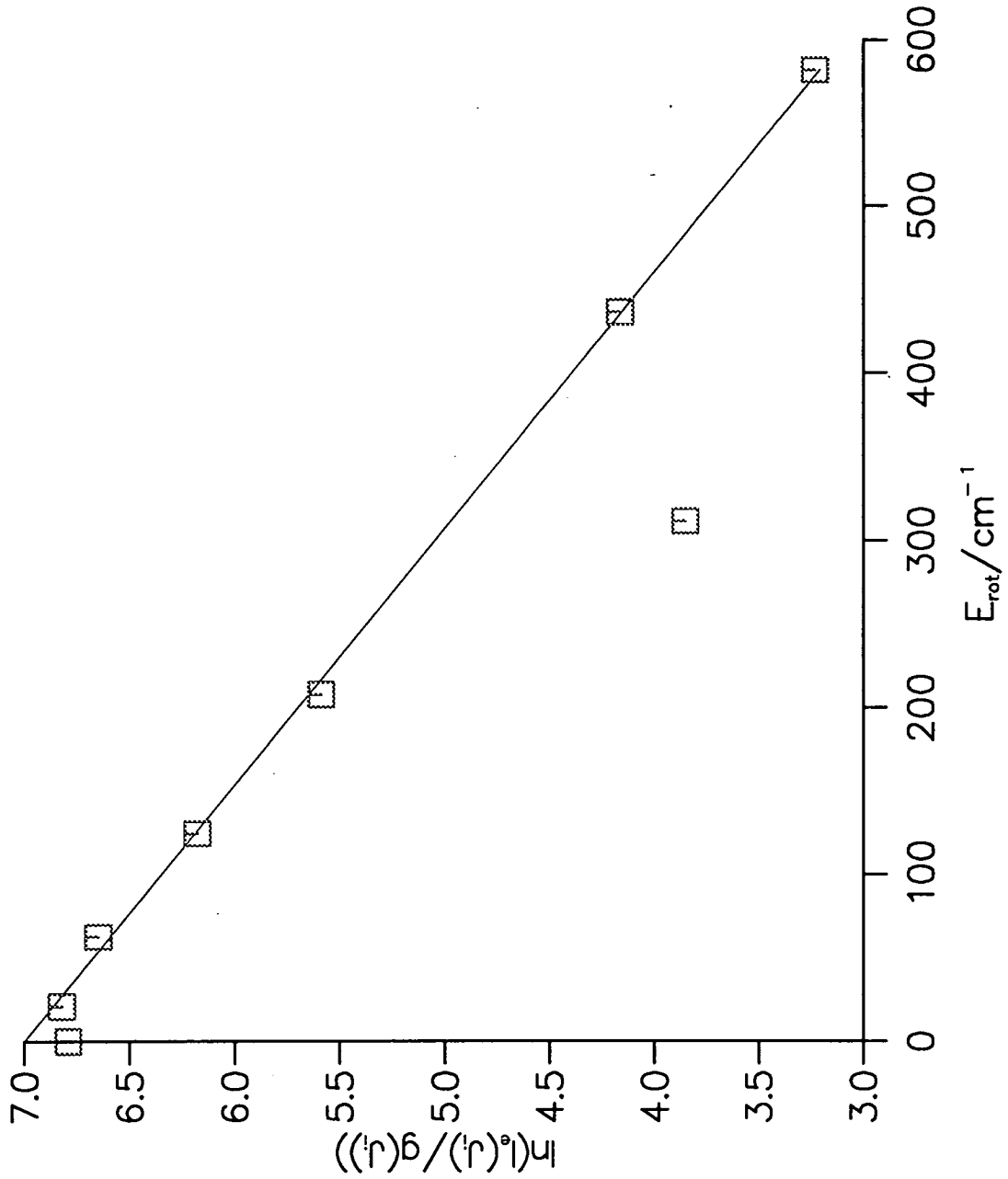

Figure 5–12: Boltzmann plot for the (12−0) band of the $V^1\Sigma^+(0^+) \leftarrow X^1\Sigma^+(0^+)$ transition in room temperature HCl

5.5 $F^1\Delta(2)$ State

The $F^1\Delta(2) \leftarrow X^1\Sigma^+(0^+)$ transitions were amongst the most intense features observed in the two-photon REMPI of HCl. The TOFMS revealed *only* $H^{35}Cl$ and $H^{37}Cl$ mass channels with no apparent fragmentation into atomic ion channels. The $F^1\Delta(2)$ state correlates with the $n = 4$ members of the $[\cdots\sigma^2\pi^3]np\pi$ Rydberg series [12] which converges on the $X^2\Pi_{1/2}$ ion limit and angular momentum coupling lies between Hund's cases (a) and (c). This is consistent with the argument given in section 5.4.1 that the Cl^+ ions arise from absorption of a third photon by neutral HCl at long internuclear distances and is thus ineffective for the $F^1\Delta(2)$ state which has a short internuclear distance.

Two-photon REMPI spectra of the O, P, Q, R and S-branches of the $F^1\Delta(2) \leftarrow X^1\Sigma^+(0^+)$ transition are shown in figures 5–13 and 5–14. These were obtained using linearly and circularly polarized probe beams, respectively, with the circularly polarized light causing the lines due to the $g^3\Sigma^-(0^+)$ state to be suppressed. This is in agreement with the line strength formulae presented in tables 4–3 and 4–4 in section 4.2.

One major feature of the $(0-0)$ band of the $F^1\Delta(2) \leftarrow X^1\Sigma^+(0^+)$ transition is that the rotational line strengths appear anomalously low for intermediate J values and pick up again at higher J (approximately $J = 9, 10$). This effect was also noted elsewhere [16]. Higher resolution spectra of the Q-branch are shown in figures 5–15 and 5–16 and the R-branch in figures 5–17 and 5–18. The R-branch was obtained using both linear (figure 5–17) and circular (figure 5–18) polarizations to enable the lines from the two states, $F^1\Delta(2)$ and $g^3\Sigma^-(0^+)$, to be more easily identifiable.

The data from figures 5–13 to 5–18 were then used to construct Boltzmann plots from which quantitative measurements of the rotational line strength perturbations could be taken. The Boltzmann plot used the formulae given in section 4.2 and is shown in figure 5–19.

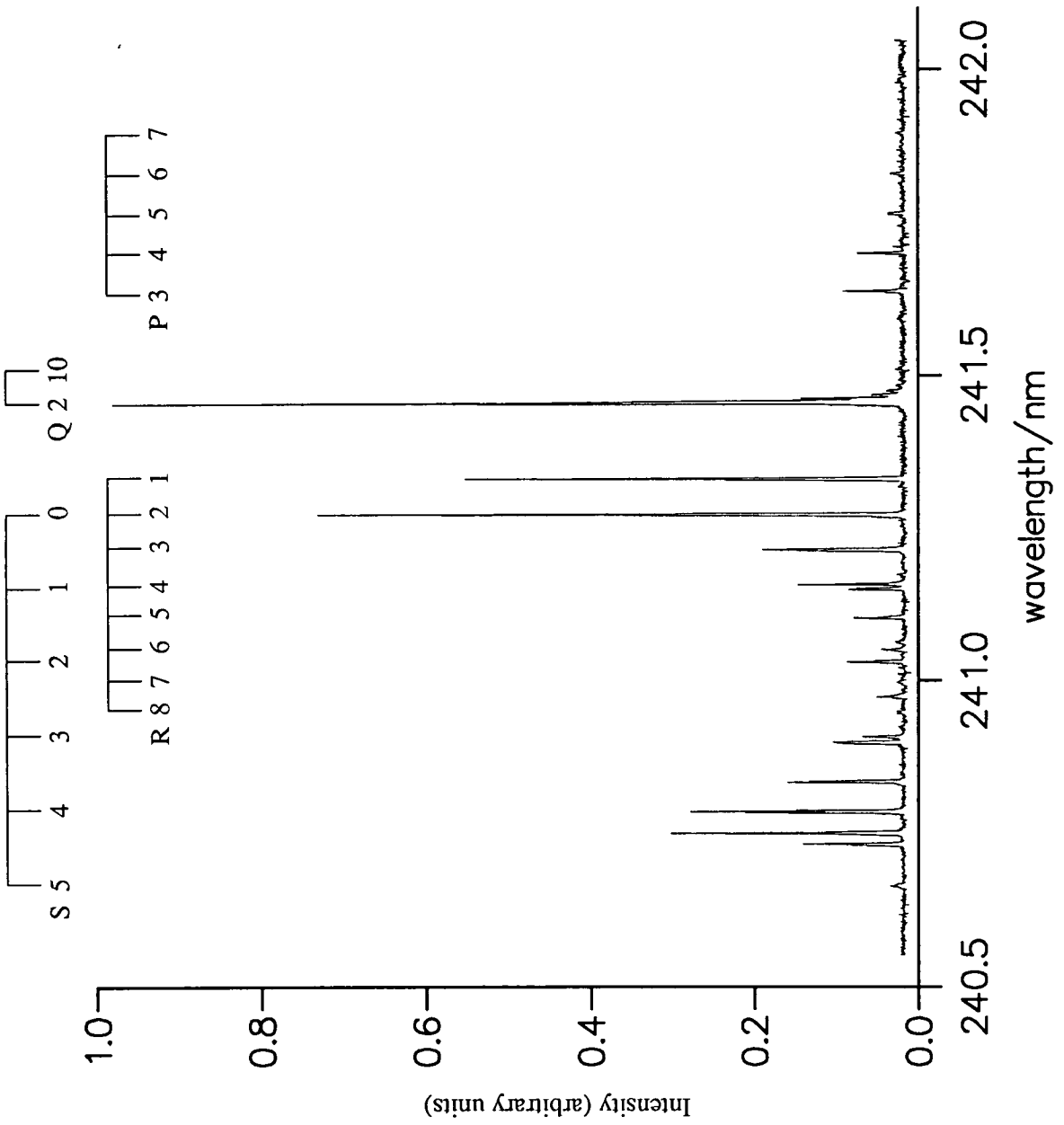

Figure 5–13: $2+1$ REMPI spectrum of HCl at room temperature for the $(0-0)$ band of the $F^1\Delta(2) \leftarrow X^1\Sigma^+(0^+)$ transition. Spectrum was obtained using a linearly polarized probe beam

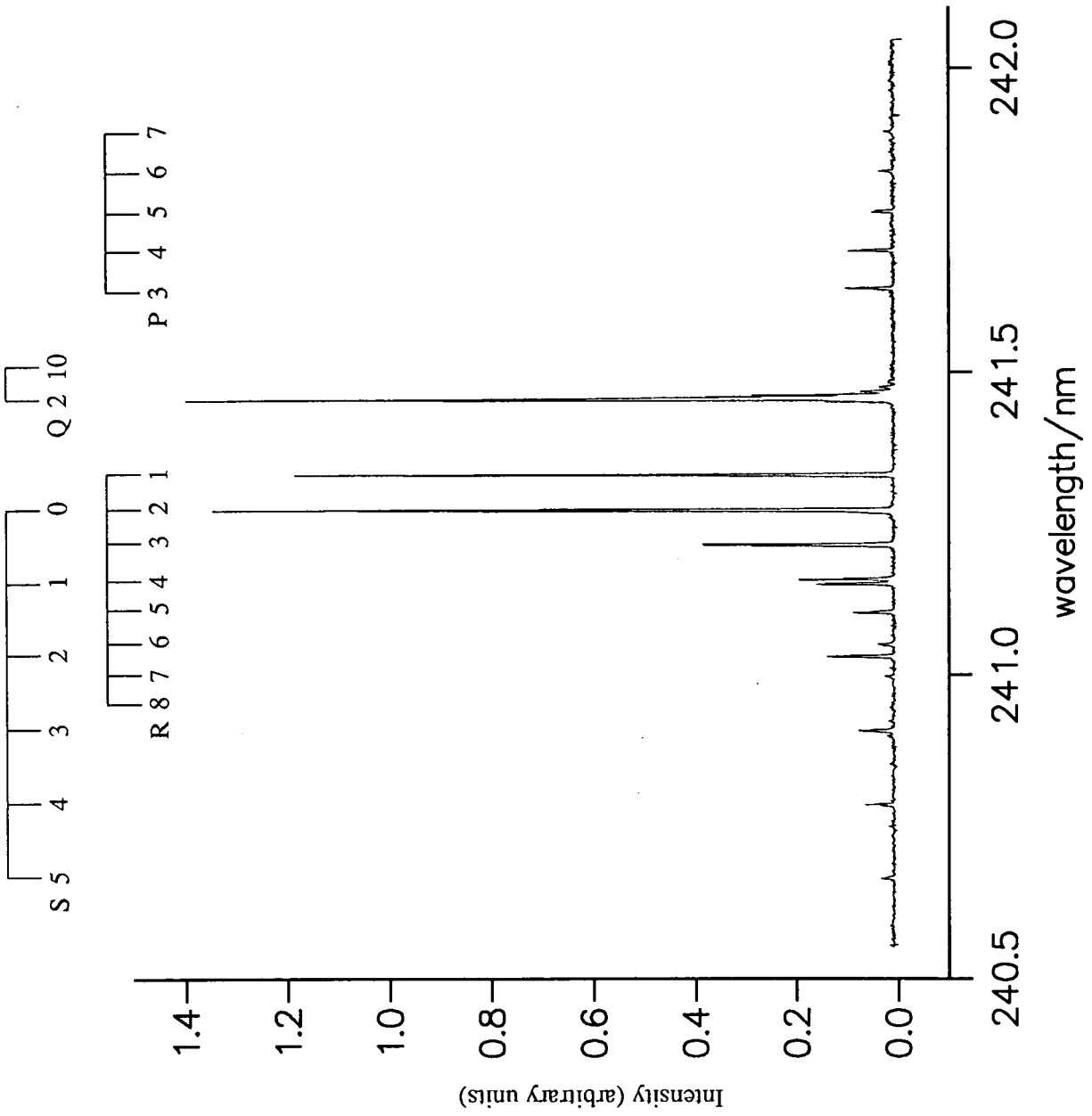

Figure 5–14: $2+1$ REMPI spectrum of HCl at room temperature for the $(0-0)$ band of the $F^1\Delta(2) \leftarrow X^1\Sigma^+(0^+)$ transition. Spectrum was obtained using a circularly polarized probe beam

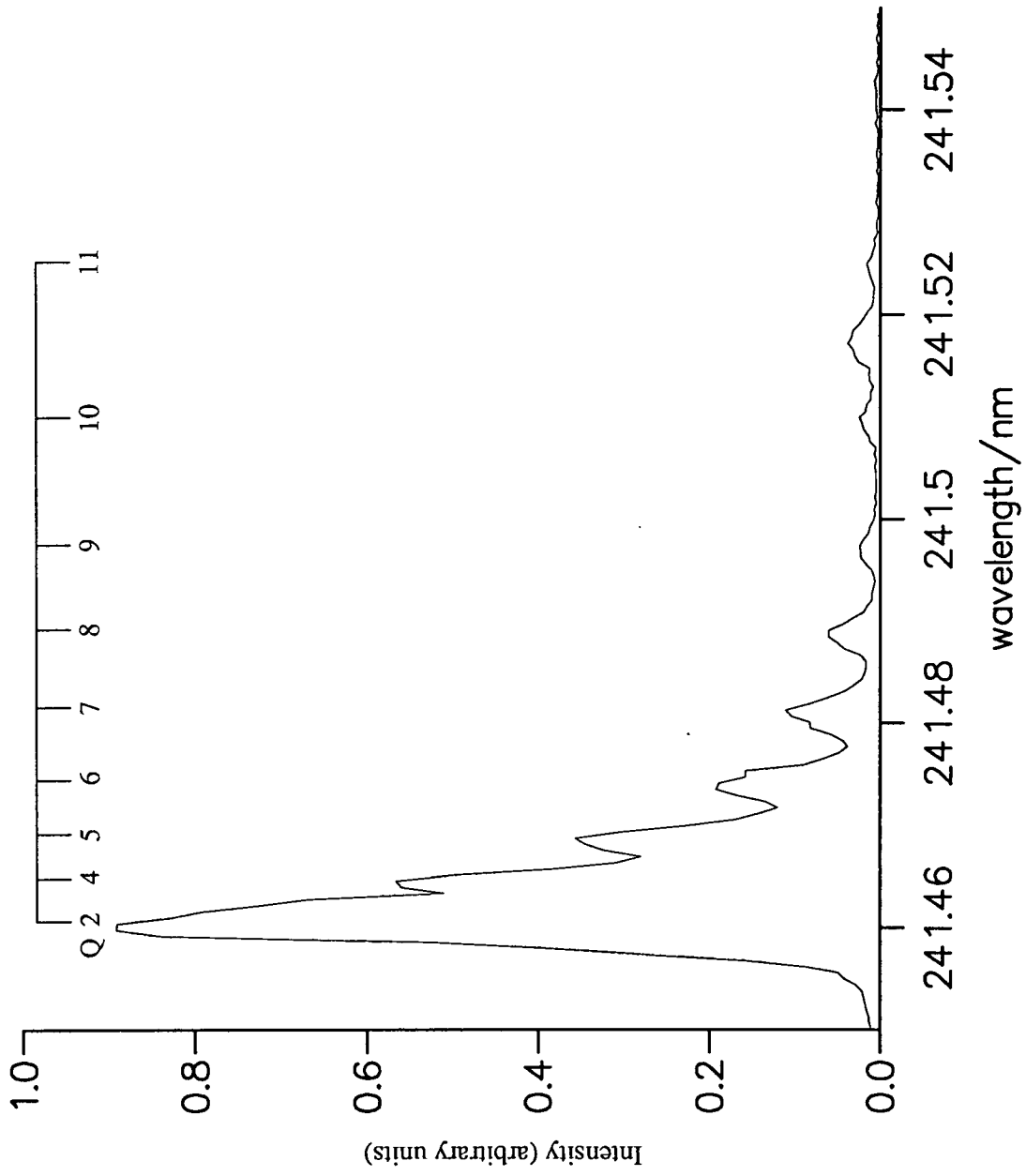

Figure 5–15: $2 + 1$ REMPI spectrum of HCl at room temperature showing the Q-branch of the $(0 - 0)$ band for the $F^1\Delta(2) \leftarrow X^1\Sigma^+(0^+)$ transition

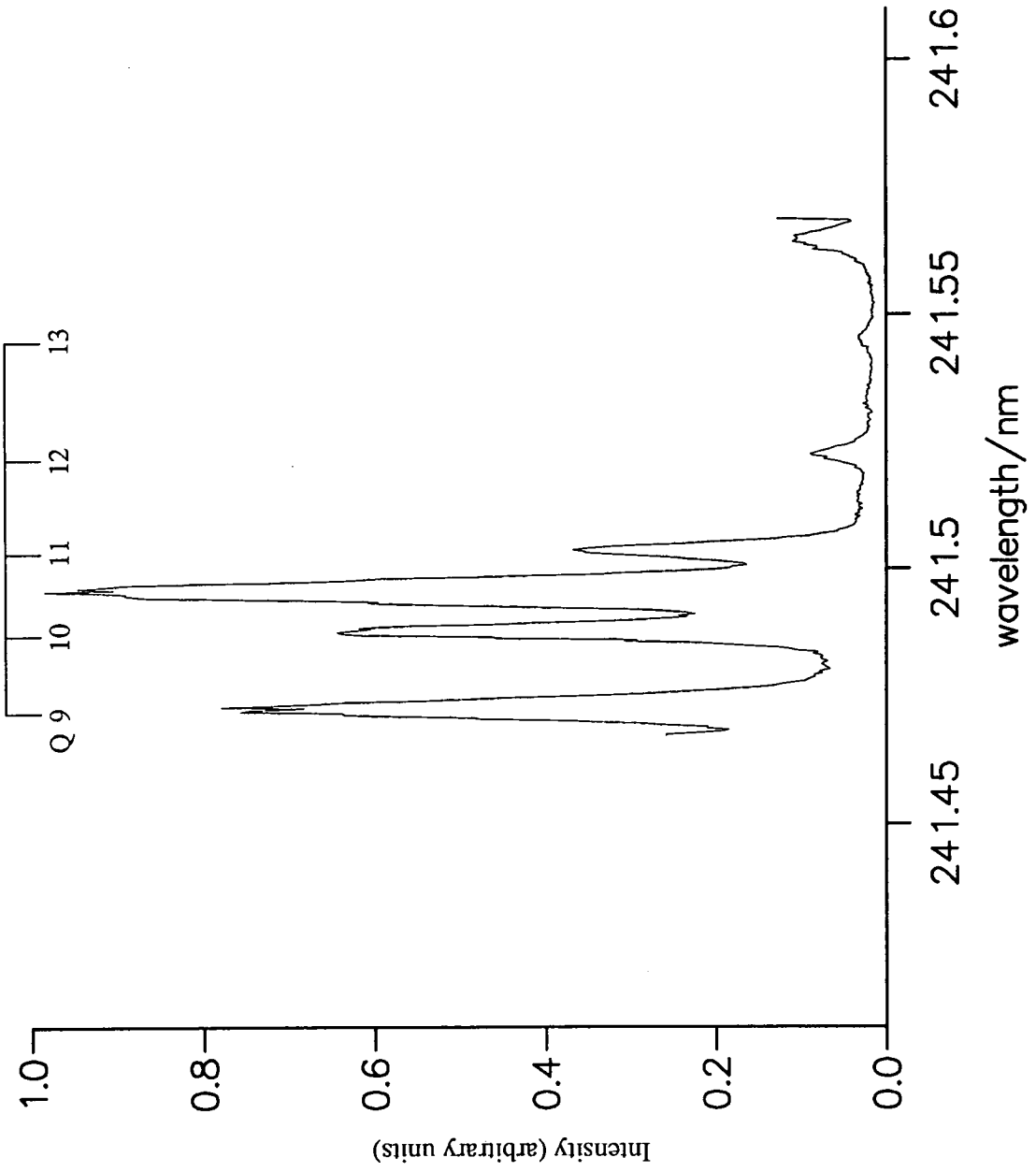

Figure 5–16: $2+1$ REMPI spectrum of HCl at room temperature showing the higher J lines within the Q-branch of the $(0-0)$ band for the $F^1\Delta(2) \leftarrow X^1\Sigma^+(0^+)$ transition

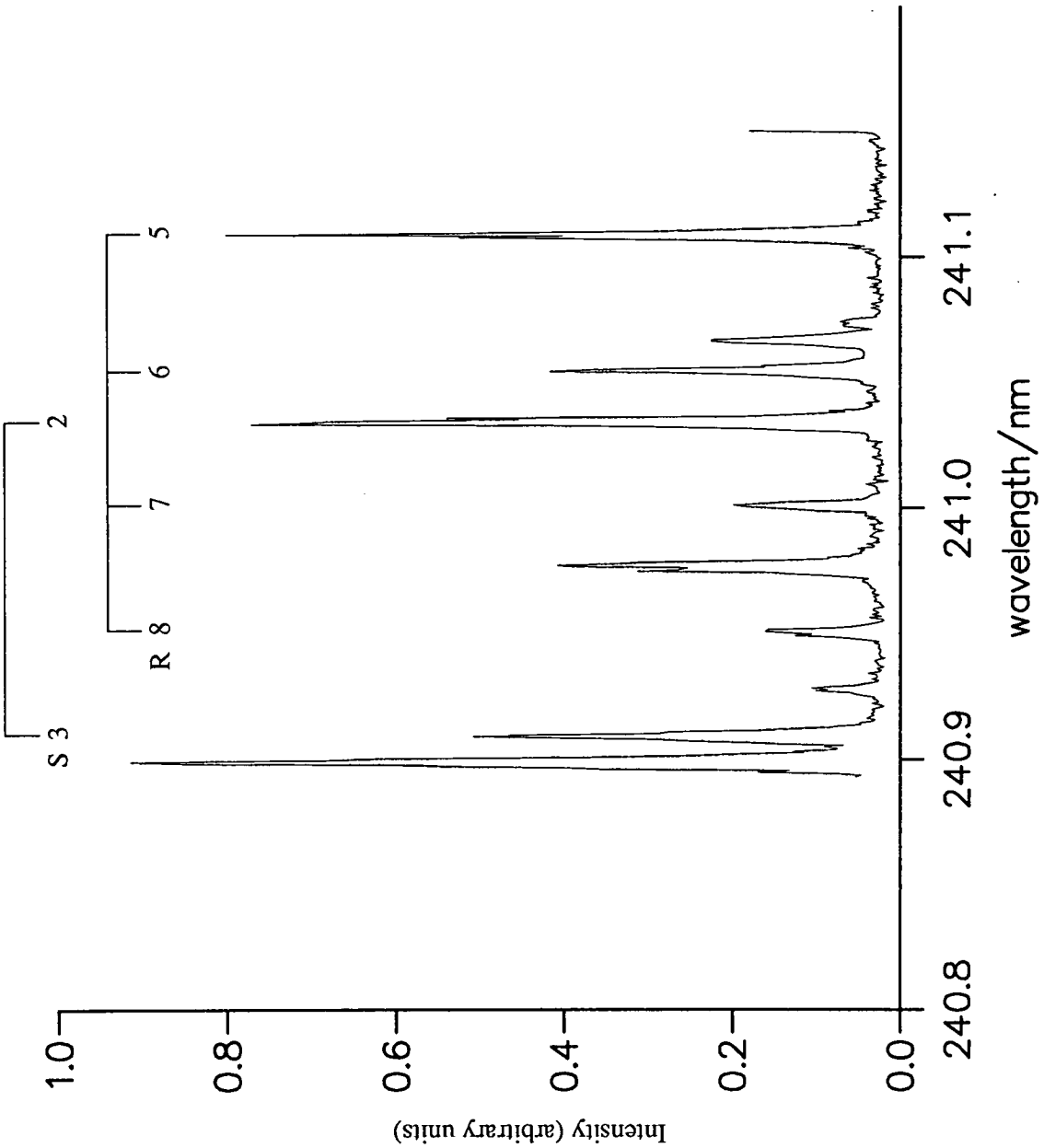

Figure 5–17: $2 + 1$ REMPI spectrum of HCl at room temperature showing the R-branch of the $(0 - 0)$ band for the $F^1\Delta(2) \leftarrow X^1\Sigma^+(0^+)$ transition. Spectrum was obtained using a linearly polarized probe beam

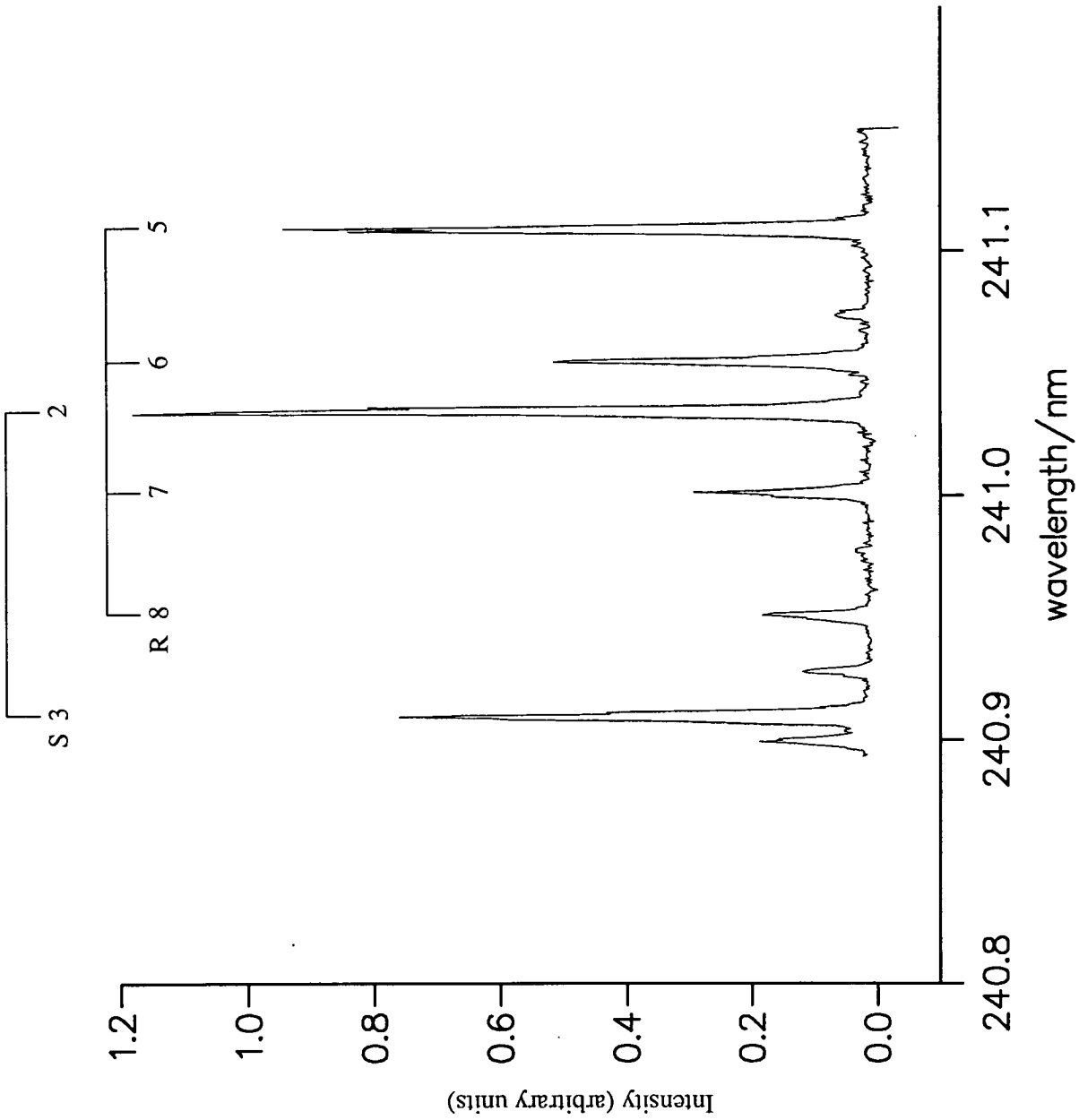

Figure 5–18: $2 + 1$ REMPI spectrum of HCl at room temperature showing the R-branch of the $(0 - 0)$ band for the $F^1\Delta(2) \leftarrow X^1\Sigma^+(0^+)$ transition. Spectrum was obtained using a circularly polarized probe beam

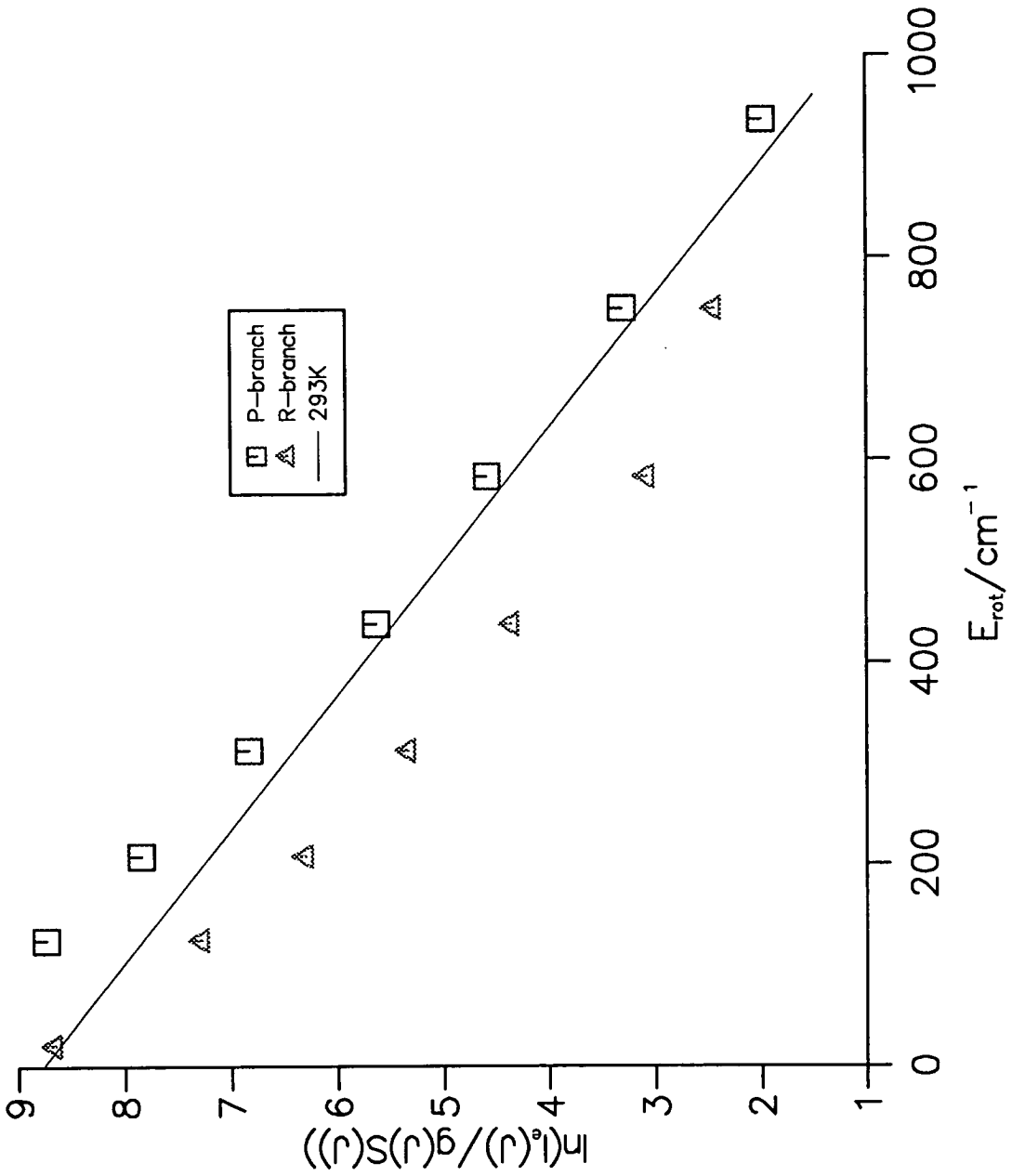

Figure 5–19: Boltzmann plot for the $(0-0)$ band of the $F^1\Delta(2) \leftarrow X^1\Sigma^+(0^+)$ transition in room temperature HCl

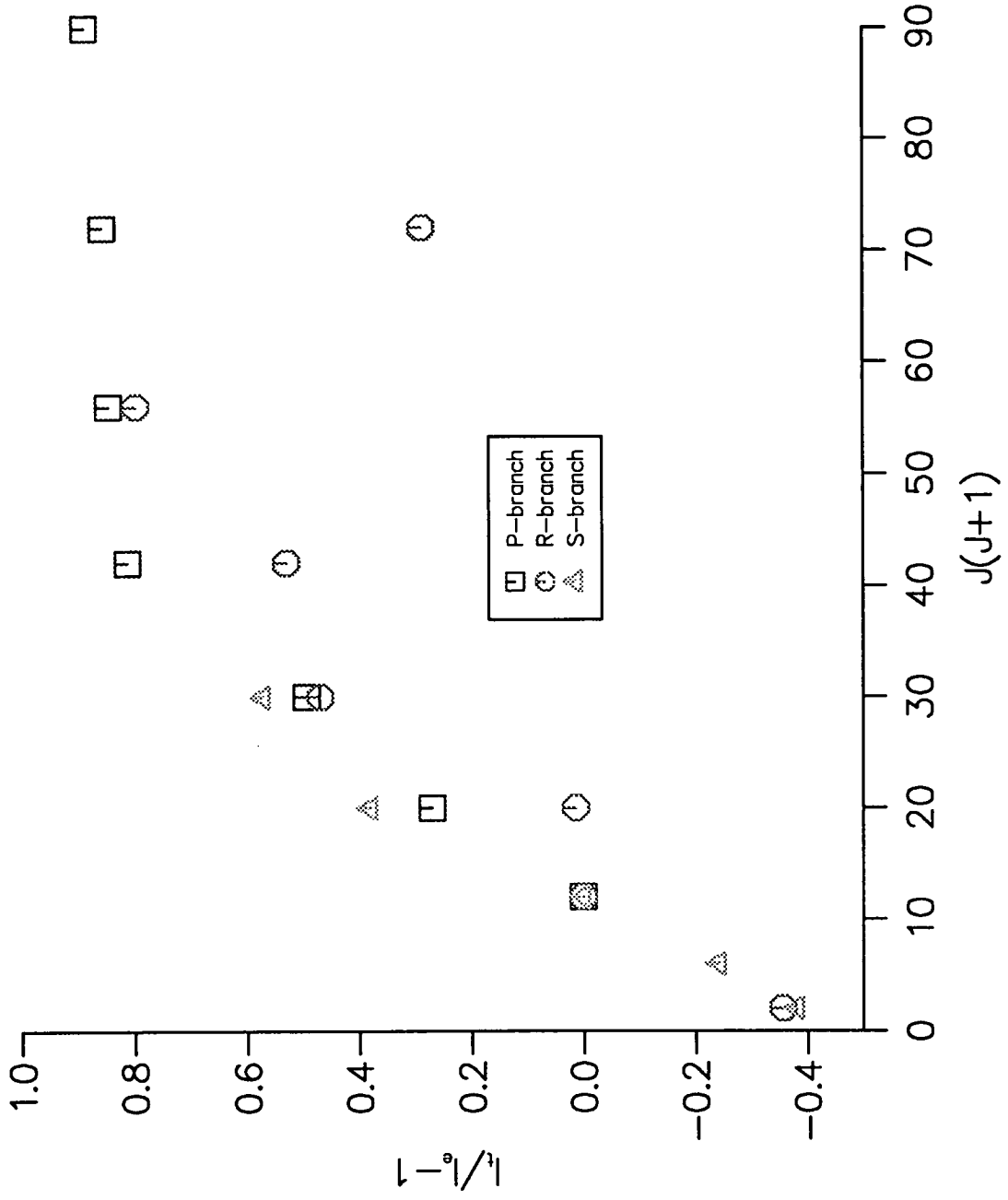

Figure 5–20: Plot of $I_t/I_e - 1$ as a function of $J(J+1)$ for the $(0-0)$ band of the $F^1\Delta(2) \leftarrow X^1\Sigma^+(0^+)$ transition in room temperature HCl where I_t is the theoretical rotational line strength and I_e is the experimental line strength. Data are normalized for $J_i = 3$

The Boltzmann plot for the $(0-0)$ band of the $F^1\Delta(2) \leftarrow X^1\Sigma^+(0^+)$ transition shown in figure 5–19 shows clearly the decrease in rotational line strength with respect to the theoretical value for $J = 3$ to 9. An important point from figure 5–19 that has not been commented on elsewhere is that not only are the rotational line strength inconsistent within any given branch but the relative intensities between the O, P, Q, R and S-branches are incorrect. The rotational line strength formulae from section 4.2 predict a $P(3)$ to $R(3)$ ratio of $\frac{1}{6}$ whereas experimental measurements give a $P(3)$ to $R(3)$ ratio of 0.3689. The fact that the deviations from the theoretical line strengths shown in the Boltzmann plots are the same for all branches measured indicates that the perturbation occurs at the two-photon resonant level. The perturbation could be due to intensity borrowing by a nearby state with a suitably long lifetime, interaction with a dissociative state or alternatively interaction with some predissociative state. The first of these, intensity borrowing by a nearby state, is very unlikely since a state with a long enough lifetime to cause a perturbation in this way would have led to unassigned rotational lines in the spectra and this was not the case.

The possibility of direct predissociation by interaction with a repulsive state can be ruled out. In this case the plot of $I_t/I_e - 1$ vs $J(J+1)$ shown in figure 5–20 takes the form

$$I_t/I_e - 1 = k_p/k_i \tag{5.4}$$

where I_t is the theoretical line strength, I_e is the observed line strength and k_i and k_p are the ionization and predissociation rates respectively [17]. As can be seen from figure 5–20 the deviation from the predicted line strength increases with J. As noted by Xie *et al.* [16] the deviation is greatest for $J_i = 8$ and then decreases to a mimumum at $J_i = 11, 12$ before increasing again.

Assuming a harmonic oscillator function for the F state and a repulsive exponential for the predissociating state Xie *et al.* [16] have calculated the semiclassical Franck-Condon factor as a function of energy and shown it to oscillate too slowly as a function of J for the perturbation to be of this kind.

The remaining possibility is indirect predissociation due to interaction with a bound state. As demonstrated by Xie *et al.* [16] the nature of the perturbation in

the $F^1\Delta(2)$ state transitions is very similar for all branches. This tends to indicate that the perturbing state has e and f levels with very similar rotational constants and thus implies a perturbing state with $\Omega \neq 0$.

5.6 Conclusions on Linestrengths

As stated at the beginning of this chapter, the aim of this spectroscopic study was to identify two-photon REMPI transitions within HCl for which the line strengths were predictable enough to enable those transitions to be used for evaluation of populations. The assessment of angular momentum multipole moments is considered in the next section.

Of the $^1\Sigma^+(0^+)$ states studied, the (1-0) band of the $E^1\Sigma^+(0^+) \leftarrow X^1\Sigma^+(0^+)$ transition is fairly weak. It also displayed perturbations which were dependent on laser intensity and can therefore be ruled out for the present work. Of the $V^1\Sigma^+(0^+) \leftarrow X^1\Sigma^+(0^+)$ branches observed only the (11-0) band has reproducible and predictable rotational line strengths. It was also one of the most intense transitions studied and these two facts would at first seem to suggest it be a strong candidate for population studies.

The (0-0) band of the $F^1\Delta(2) \leftarrow X^1\Sigma^+(0^+)$ transition is also an interesting candidate. Although much has been made of the fact that the line strengths, both within a given rotational branch and relative branch to branch, do not appear to fit any of the predictions for isolated states of a given symmetry, it was found that the deviations of the observed line strengths from the calculated vales remained essentially constant over a wide range of experimental conditions. This suggests that a set of empirical rotational line strength correction factors $F(\Delta J, J)$, could be calculated such that the intensity of a spectral line be given by

$$I(J) = C \cdot n(J) \cdot P_{0+}^{\{0\}}(J) \cdot F(\Delta J, J). \tag{5.5}$$

Here C is a constant of proportionality (detection efficiency etc.)
$n(J)$ is the population of the lower level involved in the transition

	Rotational Branch			
J	P	Q	R	S
0	-	-	-	-
1	-	-	1	.6823
2	-	2.116	-	.5567
3	1.747	-	.6444	.4222
4	1.377	-	.5005	.3059
5	1.171	-	.4389	.2689
6	.9654	-	.4216	-
7	.9486	.7395	.3591	-
8	.9432	.6628	.5009	-
9	.9279	.5418	-	-

Table 5–3: Rotational line strength correction factors for the two-photon REMPI $F^1\Delta(2) \leftarrow X^1\Sigma^+(0^+)$ transition in HCl. All factors are normalized with respect to the $R(1)$ line.

$P_{0+}^{\{0\}}(J)$ is the relevant line strength factor from tables 4–3 and 4–4 in section 4.2. The experimentally derived correction factors are given in table 5–3.

In addition to having predictable line strengths the (0-0) band of the $F^1\Delta(2) \leftarrow X^1\Sigma^+(0^+)$ transition was also the most intense feature of the two-photon REMPI of HCl observed making it a suitable transition with which to carry out angular momentum alignment studies.

5.7 Detailed Polarization Properties

To be suitable for use in alignment studies a transition must have rotational line strengths which vary with the polarization of the probe beam in accordance with the theory presented in section 4

5.7.1 $V^1\Sigma^+(0^+) \leftarrow X^1\Sigma^+(0^+)$ transitions

A $\frac{\mu_2^2}{\mu_1^2}$ value of 0.774 ($\pm$ .02) was calculated for the $(11-0)$ band of the $V^1\Sigma^+(0^+) \leftarrow X^1\Sigma^+(0^+)$ transition by comparing the relative intensities of the Q and S-branch lines. As explained in section 4.2, however, a $\frac{\mu_2^2}{\mu_1^2}$ value of < 1 implies that two different sets of R^0, R^{+1}, R^{-1} factors are possible and are given in table 5–4. This suggests that a polarization sensitive study on a sample of known alignment would be necessary to enable the correct set of R^0, R^{+1}, R^{-1} factors to be selected.

R^0	R^{+1}	R^{-1}
0.7916	-0.4321	0.4321
0.2002	-0.6928	0.6928

Table 5–4: Two sets of R^0, R^{+1}, R^{-1} factors possible for the (11-0) band of the two-photon $V^1\Sigma^+(0^+) \leftarrow X^1\Sigma^+(0^+)$ transition in HCl

5.7.2 $F^1\Delta(2) \leftarrow X^1\Sigma^+(0^+)$ transitions

The formulae presented in section 4.2 suggest that the ratio of the line strength for circularly polarized light to linearly polarized light, $\frac{\sigma_{cc}}{\sigma_{ll}}$, is $\frac{3}{2}$ for all branches of a $F^1\Delta(2) \leftarrow X^1\Sigma^+(0^+)$ transition. To evaluate the observed polarization dependance the apparatus was set up to continuously vary the PEM, described in section 2.4, through a 20 microsecond cycle with the oscillatory amplitude adjusted to give either $\frac{1}{4}$ wave or $\frac{1}{2}$ wave maximum retardance.

Figures 5–21, 5–22 and 5–23 show the polarization dependance of the $Q(2)$, $R(4)$ and $P(3)$ lines respectively.

The value of $\frac{\sigma_{cc}}{\sigma_{ll}}$ [3] for each of the rotational lines measured lies within 7% of the theoretical value. This fact, combined with the predictable line strengths as a function of J, suggests that the $(0-0)$ band of the $F^1\Delta(2) \leftarrow X^1\Sigma^+(0^+)$ transition is the best overall candidate for use in alignment studies of HCl.

[3]The actual value of $\frac{\sigma_{cc}}{\sigma_{ll}}$ was calculated using an iterative method.

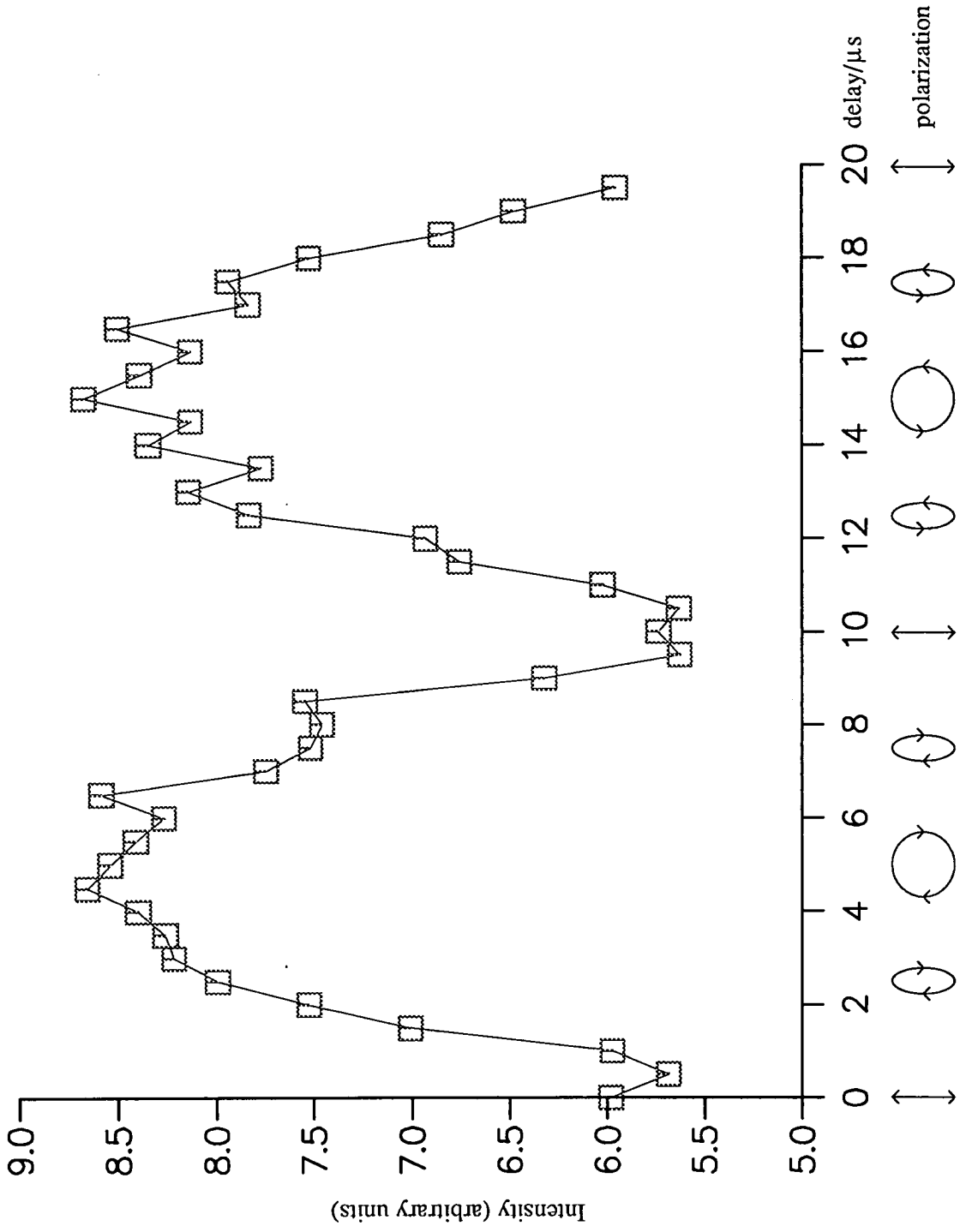

Figure 5–21: Polarization scan for the (0-0) band of the two-photon $F^1\Delta(2) \leftarrow X^1\Sigma^+(0^+)$ transition in HCl. Scan is for the $Q(2)$ line

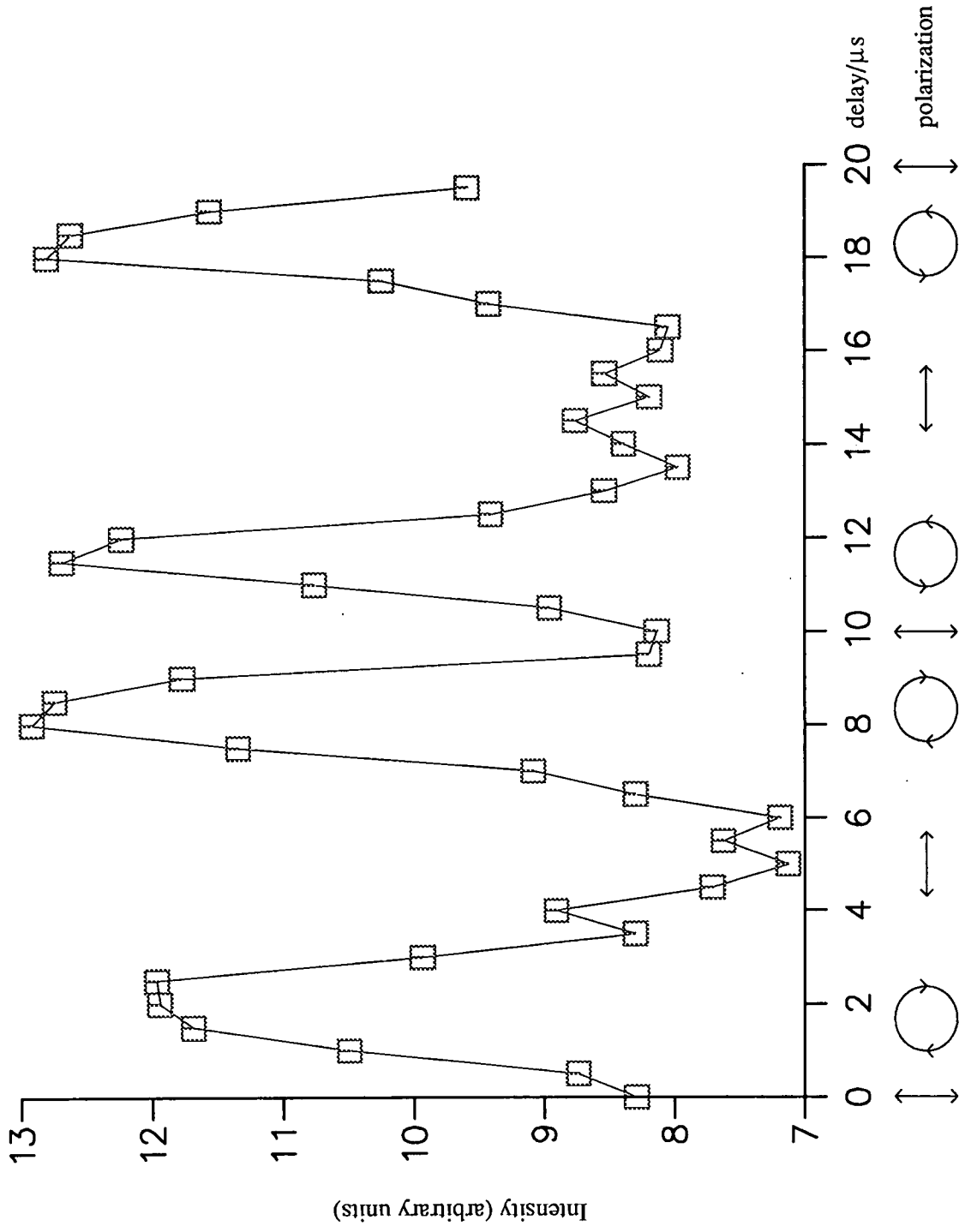

Figure 5–22: Polarization scan for the (0-0) band of the two-photon $F^1\Delta(2) \leftarrow X^1\Sigma^+(0^+)$ transition in HCl. Scan is for the $R(4)$ line

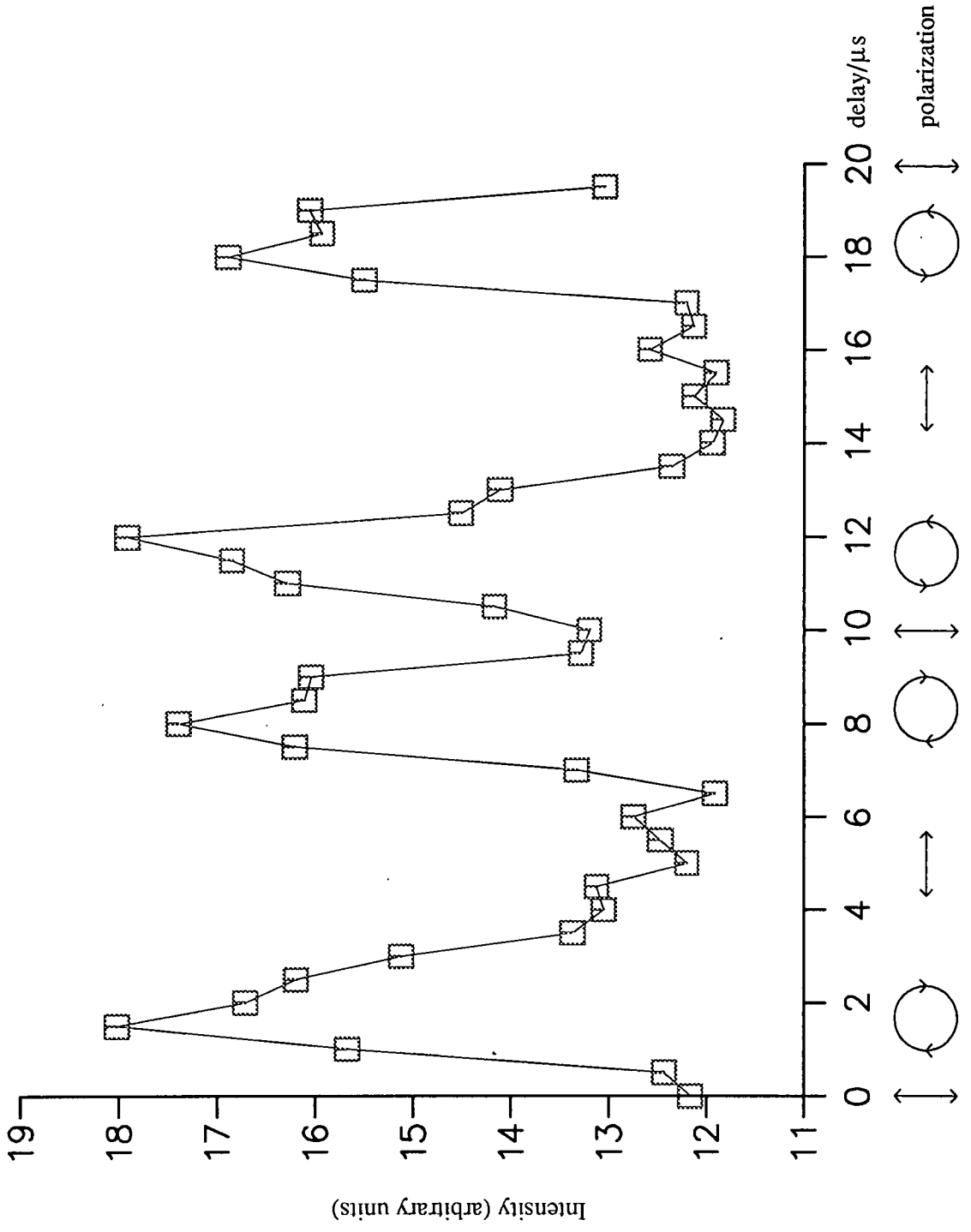

Figure 5–23: Polarization scan for the (0-0) band of the two-photon $F^1\Delta(2) \leftarrow X^1\Sigma^+(0^+)$ transition in HCl. Scan is for the $P(3)$ line

Bibliography

[1] Friedrich D. M., McClain W. M., *Ann. Rev. Phys. Chem.*, **31**, 559 (1980)

[2] Multiphoton Spectroscopy in *Progress in Atomic Spectroscopy, Bräunlich P.* (Plenum Press, 1978)

[3] Morellec J., Normand D., Petite G., *Phys. Rev.*, **14**, 300 (1976)

[4] Demaray R. E., Otis C. A., Johnson P. M., *J. Chem. Phys.*, **72**, 5772 (1980)

[5] Mainfray G., Manus C., *Appl. Opt.*, **19**, 3934 (1980)

[6] Johnson P. M., Otis C. E., *Ann. Rev. Phys. Chem.*, **32**, 139 (1981)

[7] Gandi S. R., Bernstein R. B., *Chem. Phys.*, **105**, 423 (1986)

[8] Tilford S. G., Ginter M. L., Vanderslice J. T., *J. Mol. Spec.*, **33**, 505 (1970)

[9] Tilford S. G., Ginter M. L., *J. Mol. Spec.*, **40**, 568 (1971)

[10] Ginter D. S., Ginter M. L., *J. Mol. Spec.*, **90**, 177 (1981)

[11] Brown J. M., Hougen J. T., Huber K. P., Johns J. W. C., Kopp I., Lefebrve-Brion H., Merer A. J., Ramsay D. A., Rostas J., Zare R. N., *J. Mol. Spec.*, **55**, 500 (1975)

[12] Green D. S., Bickel G. A., Wallace S. C., *J. Mol. Spec.*, **150**, 303 (1991)

[13] Bettendorff M. L., Peyerimoff S. D.,Buenker R. J., *Chem. Phys.*, **66**, 261 (1982)

[14] Spiglanin T. A., Chandler D. W., *Chem. Phys. Lett.*, **137**, 414 (1987)

[15] Green D. S., Wallace S. C., *J. Chem. Phys.*, **96**, 5857 (1992)

[16] Xie Y., Reilly P. T. A., Chilukuri S., Gordon R. J., *J. Chem. Phys.*, **95**, 854 (1991)

[17] Park H., Li L., Chupka W. A., *Chem. Phys. Lett.*, **162**, 317 (1989)

Chapter 6

Bimolecular Reaction Dynamics

6.1 Introduction

Having completed the necessary ground work it was possible to perform some initial bimolecular reaction studies. Several reactions were considered including

$$H + Cl_2 \longrightarrow HCl + Cl \tag{6.1}$$

$$Cl + HI \longrightarrow HCl + I \tag{6.2}$$

$$Cl + HBr \longrightarrow HCl + Br \tag{6.3}$$

$$H + C_3H_7Cl \longrightarrow HCl + C_3H_7 \tag{6.4}$$

$$H + CH_2Cl_2 \longrightarrow HCl + CH_2Cl \tag{6.5}$$

Of these the first three had been studied previously in the greatest detail [1,2,3,4, 5,6,7].

Since one of the main aims was the measurement of any potential angular momentum alignment in the product HCl, at least one of the reagents had to have an anisotropic vector quantity associated with it prior to reacting with the other reagent. This was achieved by creating the atomic reagent via photolysis of a parent molecule which resulted in an anisotropic distribution of the photofragment velocity vectors.

When a molecule is fragmented via a photolysis process it can be shown that [8] the final recoil distribution of the fragments in the molecular frame is given in general by

$$f(\theta_m, \phi_m) = \sum_{k,q} b_{kq} Y_q^k(\theta_m, \phi_m) \tag{6.6}$$

where $Y_q^k(\theta_m, \phi_m)$ are the spherical harmonics and θ_m and ϕ_m are the polar and azimuthal angles about the direction of the transition dipole moment μ. The expansion coefficients, b_{kq} are given by

$$b_{kq} = \int_0^{2\pi} \int_0^{\pi} (-1)^q Y_{-q}^k(\theta_m, \phi_m) f(\theta_m, \phi_m) \sin\theta_m d\theta_m d\phi_m \tag{6.7}$$

If we let $I(\theta_s, \phi_s)$ denote the angular distribution of the fragments in the lab frame where θ_s and ϕ_s are the polar and azimuthal angles about the electric vector of the photolysis light, then the complete fragment angular distribution is obtained by integrating over all possible molecular orientations giving

$$I(\theta_s, \phi_s) = \int_0^{2\pi} \int_0^{\pi} \int_0^{2\pi} P_{diss}(\phi, \theta, \chi) f(\theta_m, \phi_m) d\chi \sin\theta d\theta d\phi \tag{6.8}$$

where

$$P_{diss}(\phi, \theta, \chi) = \frac{3\cos^2\theta}{8\pi^2} \tag{6.9}$$

If the photofragmentation process takes place using a linearly polarized beam then only b_{00} and b_{20} are non zero and from this the final distribution can be calculated. Normalized it becomes the very well known expression [8]

$$I(\theta_s, \phi_s) = \frac{1}{4\pi} [1 + \beta P_2(\cos\theta)] \tag{6.10}$$

where $\beta = 2\langle P_2(\cos\theta_m)\rangle$ is the anisotropy parameter ranging from 2 ($\cos^2$ distribution) for parallel transitions to -1 ($\sin^2$ distribution) for perpendicular transitions. This is shown diagramatically in figure 6–1.

The main factor concerning the choice of atomic reagent, H or Cl, was the yield available from the photolysis process. The most easily obtainable H atom production was via the processes

$$\mathrm{HI} \xrightarrow{\lambda \leq 403\mathrm{nm}} \mathrm{H} + \mathrm{I}$$

$$I = \frac{1}{4\pi}\left[1 + \beta P_2(\cos\theta)\right]$$

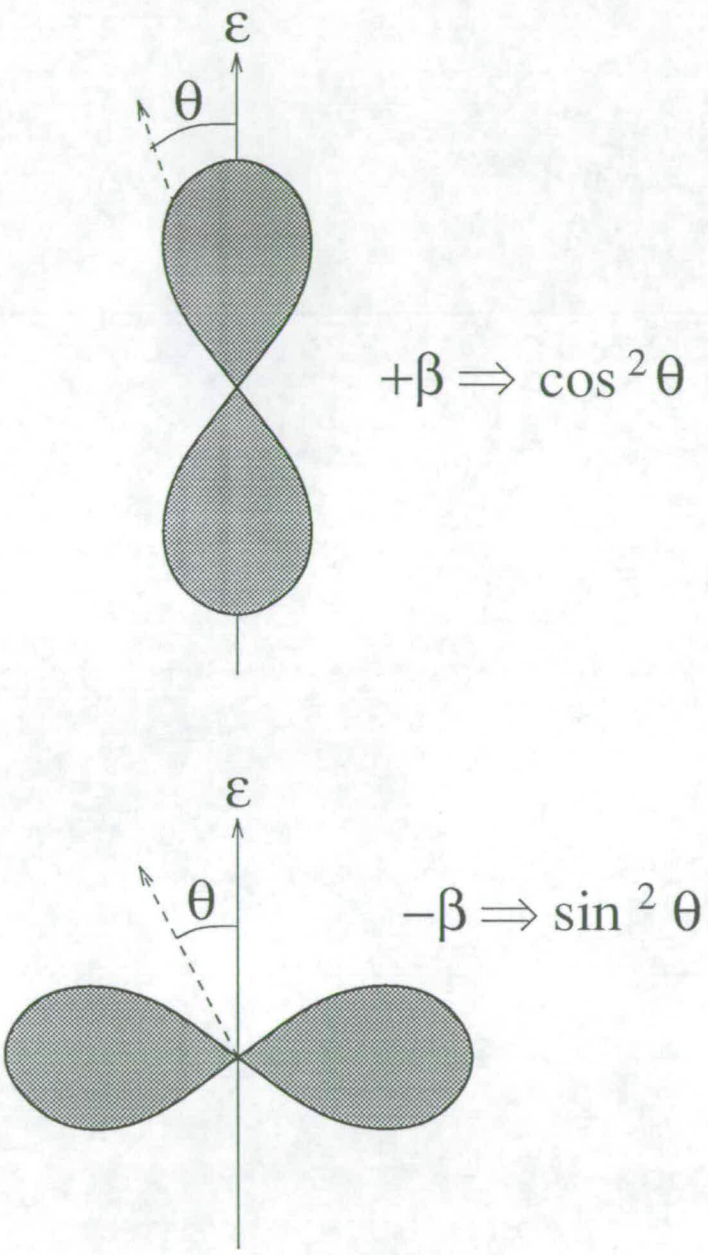

Figure 6–1: Schematic diagram illustrating effect of anisotropy parameter, β, on photofragment velocity vector distribution. ϵ denotes the polarization vector of the photolysis beam

where the wavelength shown corresponds to the dissociation energy of the parent molecule. The photolysis beam used was the tripled output of a Nd:YAG laser, described in section 2.6, at 355nm. Using this beam the atomic reagent yield from either of the above two processes would have been much less than the chlorine atom yield from photolysis of Cl_2 at 355nm. Thus it was decided to concentrate on the two reactions 6.2 and 6.3 which use atomic chlorine as one of the reagents

The photolysis of Cl_2 to produce Cl atoms results in the production of both the ground state atom, $Cl(^2P_{3/2})$, and the spin-orbit excited state $Cl^*(^2P_{1/2})$ which lies 0.109eV above the ground state. It is known [9] that the $^1\Pi(1_u) \leftarrow X^1\Sigma(0_g^+)$ transition produces two $Cl(^2P_{3/2})$ atoms whereas the $B^3\Pi(0_u^+) \leftarrow X^1\Sigma(0_g^+)$ transition gives a $Cl(^2P_{3/2})$ atom and one excited $Cl^*(^2P_{1/2})$ atom. The ratio of production of the two spin orbit states [9] is given as a function of photolysis wavelength in table 6–1.

As can be seen from the table the anisotropy parameter, β, is very different for the two spin orbit states. This arises from the fact that the ground state atom is produced predominantly via a perpendicular transition, ($\Delta\Omega = \pm 1$), whereas the spin-orbit excited atom results exclusively from a parallel transition, ($\Delta\Omega = 0$). This suggests that the angular distribution of velocity vectors in the chlorine atoms will be a superposition of the two more fundemental distributions, parallel and perpendicular, which could make the interpretation of HCl product alignment significantly more difficult than if all the chlorine atoms were created via the same transition. However, as is evident from the third column of table 6–1, the ratio of $Cl^*(^2P_{1/2})$ to $Cl(^2P_{3/2})$ atoms is less than two percent indicating that the velocity vector distribution would have an effective anisotropy factor of -1.0. A separate study by Park *et al.* [1] suggests the branching ratio is actually less than one percent.

The rate constants and energetics of the two reactions using thermalized isotropic atomic reagents from microwave discharges are well documented and are shown in table 6–2 while the vibrational distribution in the product HCl is given in table 6–3.

λ/nm	$I(Cl^*)/I(Cl)^\dagger$	$[Cl^*]/[Cl]^\ddagger$	β	
			Cl	Cl*
266			-1.0	
308	0.0038	0.0095	-1.0	-0.7
355	0.0064	0.016	-1.0	1.8
370			-1.0	2.0
375	0.017	0.043		
380	0.021	0.053		
385	0.036	0.090		
390	0.057	0.143		
395	0.070	0.175		
400	0.098	0.25	-0.7	2.0
405	0.110	0.28		
450	0.114	0.29		
455	0.146	0.37		
460	0.122	0.31		
465	0.170	0.43		
470	0.179	0.45		
475	0.187	0.47		
480	0.156	0.39		
485	0.105	0.26		

†Ratio of MPI signals

‡Corrected branching ratio

Table 6–1: Table showing branching ratio of $Cl^*(^2P_{1/2})$ to $Cl(^2P_{3/2})$ and anisotropy factor, β, as a function of photolysis wavelength. Reproduced from Matsumi *et al.* [9]

Reaction	Rate Constant† /cm^{3}molecule^{-1}s^{-1}	$\sigma^{\ddagger}$/Å^2	ΔH/kJmol^{-1}
6.2	1.64×10^{-10}	33.5	-133.4
6.3	7.4×10^{-12}	1.44	-65.5

† @295K

‡ Using the expression $\langle\sigma\rangle = k/\langle v\rangle$, where $\langle v\rangle$ is the average thermal velocity.

Table 6–2: Table showing rate constants and energetics for the reactions 6.2 and 6.3

Reaction	Relative HCl vibrational level population†			
	$v'' = 1$	$v'' = 2$	$v'' = 3$	$v'' = 4$
6.2	0.07	0.24	0.49	0.20
6.3	0.75	0.25	-	-

† From [7] . For reagents @295K

Table 6–3: Vibrational population distributions for reactions 6.2 and 6.3

6.2 Cl+HI

The first to be attempted was the Cl+HI reaction (6.2) as the absolute cross-section is a factor of 22.3 larger. This is offset somewhat by the fact that, as can be seen from table 6–3, only 7% of the HCl product lies in the first vibrationally excited state. The energy level diagram is shown in figure 6–2.

The reason for looking at $v' = 1$ was that the $(1 - 1)$ band of the $F^1\Delta(2) \leftarrow X^1\Sigma^+(0^+)$ transition had been studied in earlier work not presented in this thesis. Thus the exact wavelengths for the different rotational lines were known making it relatively easy to test for the presence of $v' = 1$ HCl. Having decided whether or not nascent $v' = 1$ HCl was present, the populations of other levels could then be measured accordingly.

As is evident from the energy level diagram the total energy available for the reaction is increased by some 40kJmol^{-1} over the room temperature reagents

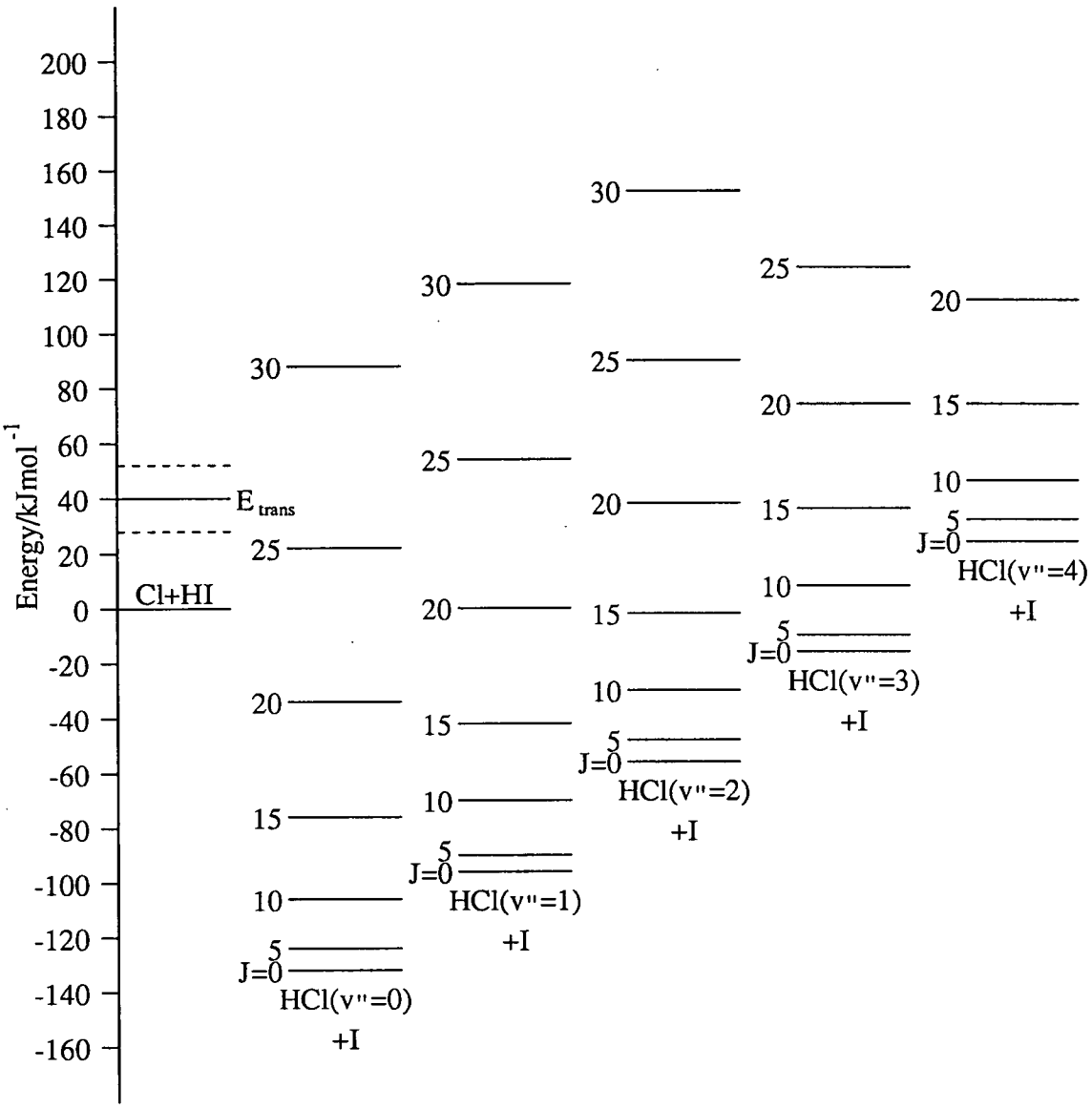

Figure 6–2: Energy level diagram for the Cl+HI⟶HCl+I reaction. The zero of energy corresponds to the room temperature energy of the reactants. The level labeled E_{trans} is the energy of the reactants with the chlorine atoms being produced via photolysis at 355nm with the dashed lines representing the spread in energy of the chlorine atoms due to thermal motion of the precursor CL_2 molecules and the HI reagent

by the fact that the chlorine atoms are produced via a photolysis process. The apparatus used to perform the experiment is shown schematically in section 2.6.2, figure 2–9.

One of the main concerns initially was to acheive high enough number densities of the reagents for a detectable amount of $HCl(v'' = 1)$ to be produced. The first gas injector used is shown in figure 6–3. Initial problems with distortion of the TOF extraction field led, after considerable experimentation, to the end 2″ of the glass injector being coated in colloidal graphite and then wrapped in aluminium foil. The foil was then connected to a high voltage supply and its potential tuned in order to correct the extraction field as far as was possible.

Both gases were allowed to mix within the injector before entering the reaction chamber. This was not anticipated to pose a problem since the rate constant for the homogeneous Cl_2+HI reaction is several orders of magnitude smaller than that for the atom-molecule process, resulting in an insignificant amount of HCl being produced via this molecule-molecule reaction.

Several attempts were made to observe the $HCl(v'' = 1)$ by monitoring the $(1 - 1)$ band of the $F^1\Delta(2) \leftarrow X^1\Sigma^+(0^+)$ transition using two-photon REMPI at short delays after the 355nm photolysis pulse. All of these failed to show any evidence of any vibrationally excited HCl. These attempts were repeated for varying Cl_2 to HI pressure ratios ranging from 10:1 to 1:10 , different total pressures and several different values for the height of the gas injector tip from the beam axis ranging from 2 to 20mm. Again no $HCl(v'' = 1)$ was observed. It was noted, however, that very large ground state HCl signals were produced when the Cl_2/HI mixture was admitted to the chamber.

It was known that the injector arrangement being used created sufficiently high number densities in the reaction zone to enable a detectable amount of HCl to be produced via this reaction assuming the rate constants in table 6–2.

First a check was made to ensure that both reagents were reaching the reaction zone. $2 + 1$ REMPI of the $(6 - 0)$ band of the $^1\Pi_g \leftarrow X^1\Sigma_g^+$ transition in Cl_2 were performed and are shown in figure 6–4.

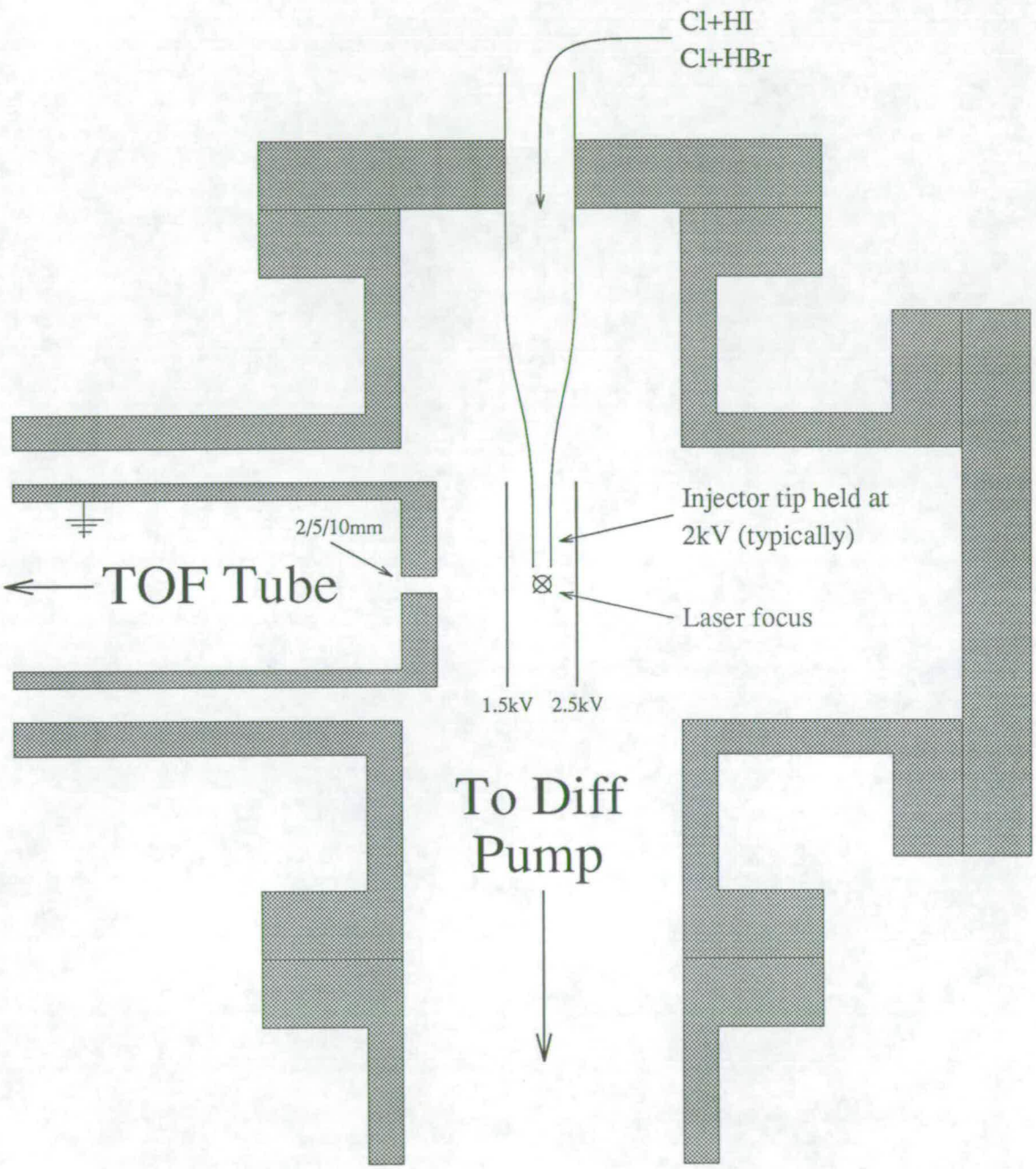

Figure 6–3: Diagram of gas inlet injector used for Cl+HI experiment

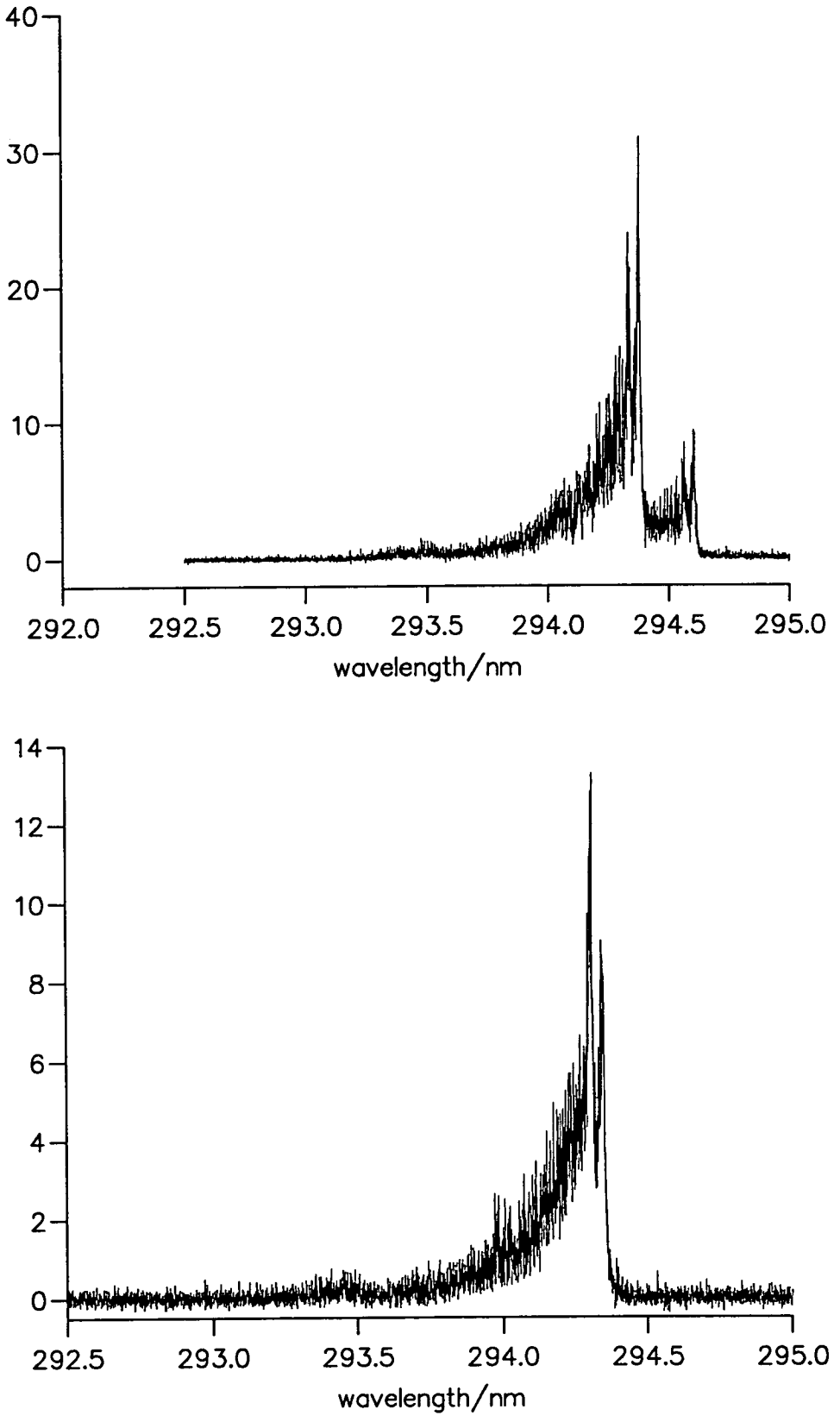

Figure 6–4: 2+1 REMPI spectra of Cl_2 at room temperature for the (6−0) band of the $^1\Pi_g \leftarrow X^1\Sigma_g^+$ transition. Top spectra was collected using mass channels 70, 72 and 74, lower spectra used mass channel 70 only

Following on from this a check was carried out to ensure that the molecular chlorine was in fact being photolysed by the 355 beam. The resulting 2+1 REMPI spectrum of the chlorine atom $4p\ ^2P_{3/2} \leftarrow 3p^5\ ^2P_{3/2}$ transition shown in figure 6–5 again confirms that both reagents for the Cl+HI reaction were present in the reaction chamber.

Further investigation into the Cl+HI reaction was impossible due to a lack of HI. At this point it was decided, therefore, to move over to the Cl+HBr reaction as described in the next section.

6.3 Cl+HBr

From table 6–2 it can be seen that the cross-section for the Cl+HBr reaction is much smaller than for Cl+HI although the product HCl is concentrated in the $v'' = 1$ and 2 levels rather than the much broader $v'' = 1$ to 4 spread as expected for Cl+HI. A full energy level diagram for the Cl+HBr reaction is given in figure 6–6.

Initially the same gas inlet injector arrangement was used for this reaction, as shown in figure 6–3. The same checks were performed on both the atomic (Cl) and molecular (HBr) reagents as for the previous reaction. The $2 + 1$ REMPI spectrum of the $(0 - 0)$ band of the $I^1\Delta_2 \leftarrow X^1\Sigma$ transition in HBr [10] is shown in figures 6–7 and 6–8. These were collected using masses 79 and 80 respectively..

Initial attempts at the reaction, monitoring the $(1 - 1)$ band of the $F^1\Delta(2) \leftarrow X^1\Sigma^+(0^+)$ transition, again failed to show any vibrationally excited HCl. It was known that both reagents were reaching the reaction zone when flowed separately through the injector. Additionally a plot of the chlorine atom REMPI signal versus the time delay between the photolysis to probe beams, figure 6–9, showed that the delay being used ($\approx$ 750ns) was close to optimal. The fact that the Cl atom signal in figure 6–9 does not peak instantaneously may be due to the photolysis and probe beams not being correctly overlapped. Once again several partial pressure ratios were used as well as altering the total flow of gas into the reaction zone but no vibrationally excited HCl was detected. Again, however it was noted that

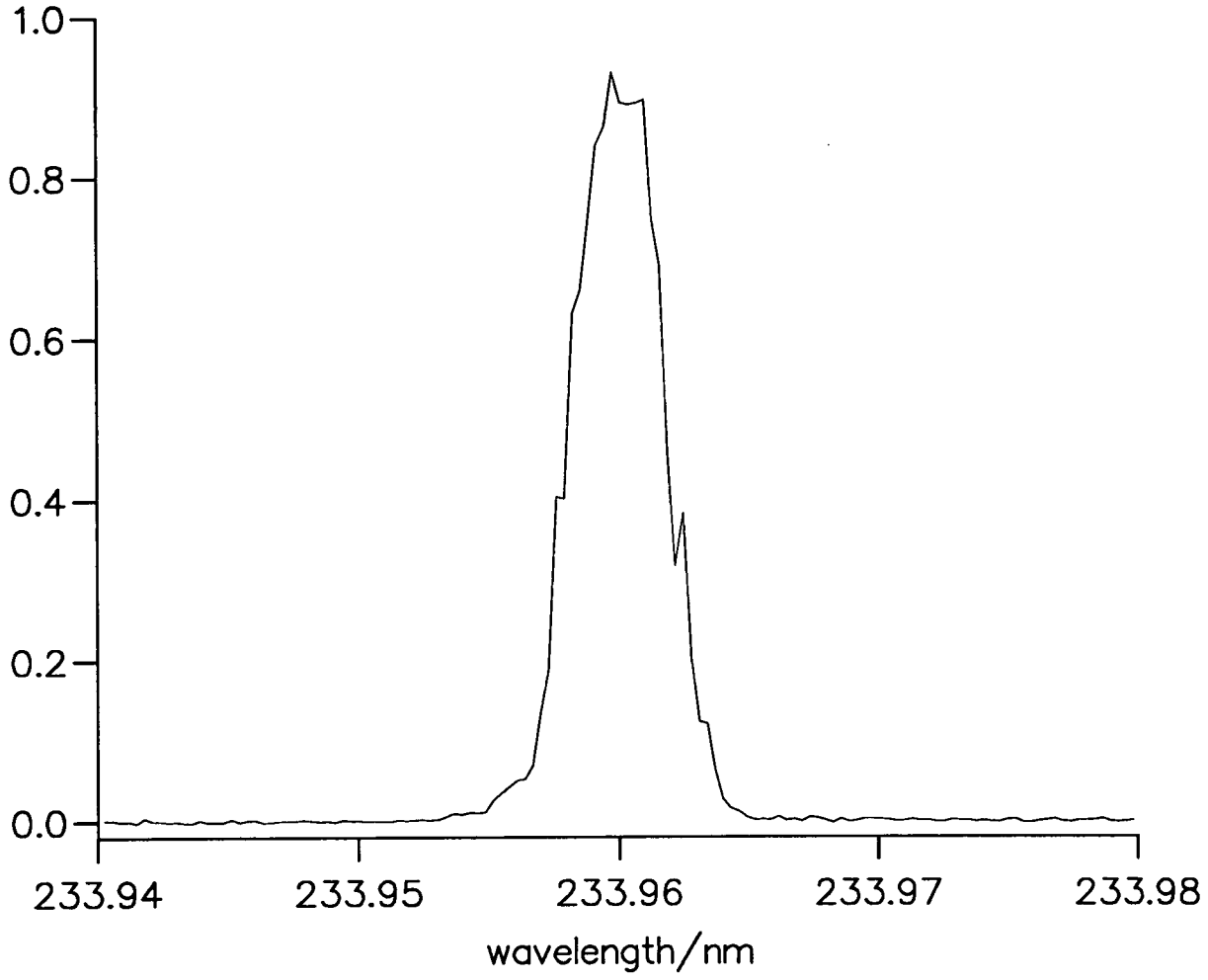

Figure 6–5: $2 + 1$ REMPI spectrum of atomic Cl at room temperature for the $4p\ ^2P_{3/2} \leftarrow 3p^5\ ^2P_{3/2}$ transition. Collected using mass channel 35

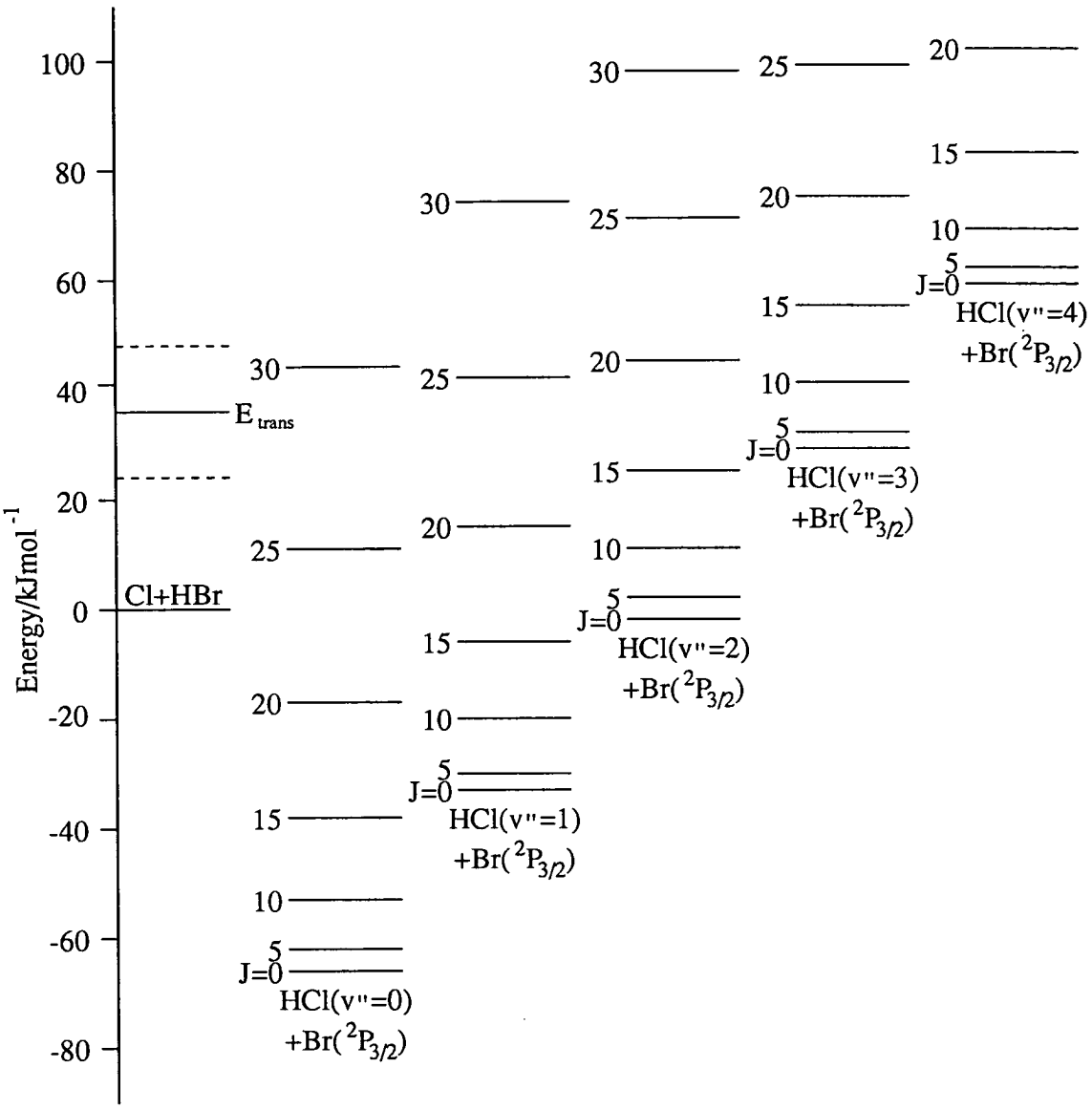

Figure 6–6: Energy level diagram for the Cl+HBr⟶HCl+Br reaction. The zero of energy corresponds to the room temperature energy of the reactants. The level labeled E_{trans} is the energy of the reactants with the chlorine atoms being produced via photolysis at 355nm with the dashed lines representing the spread in energy of the chlorine atoms due to thermal motion of the precursor Cl_2 molecules and HBr reagent

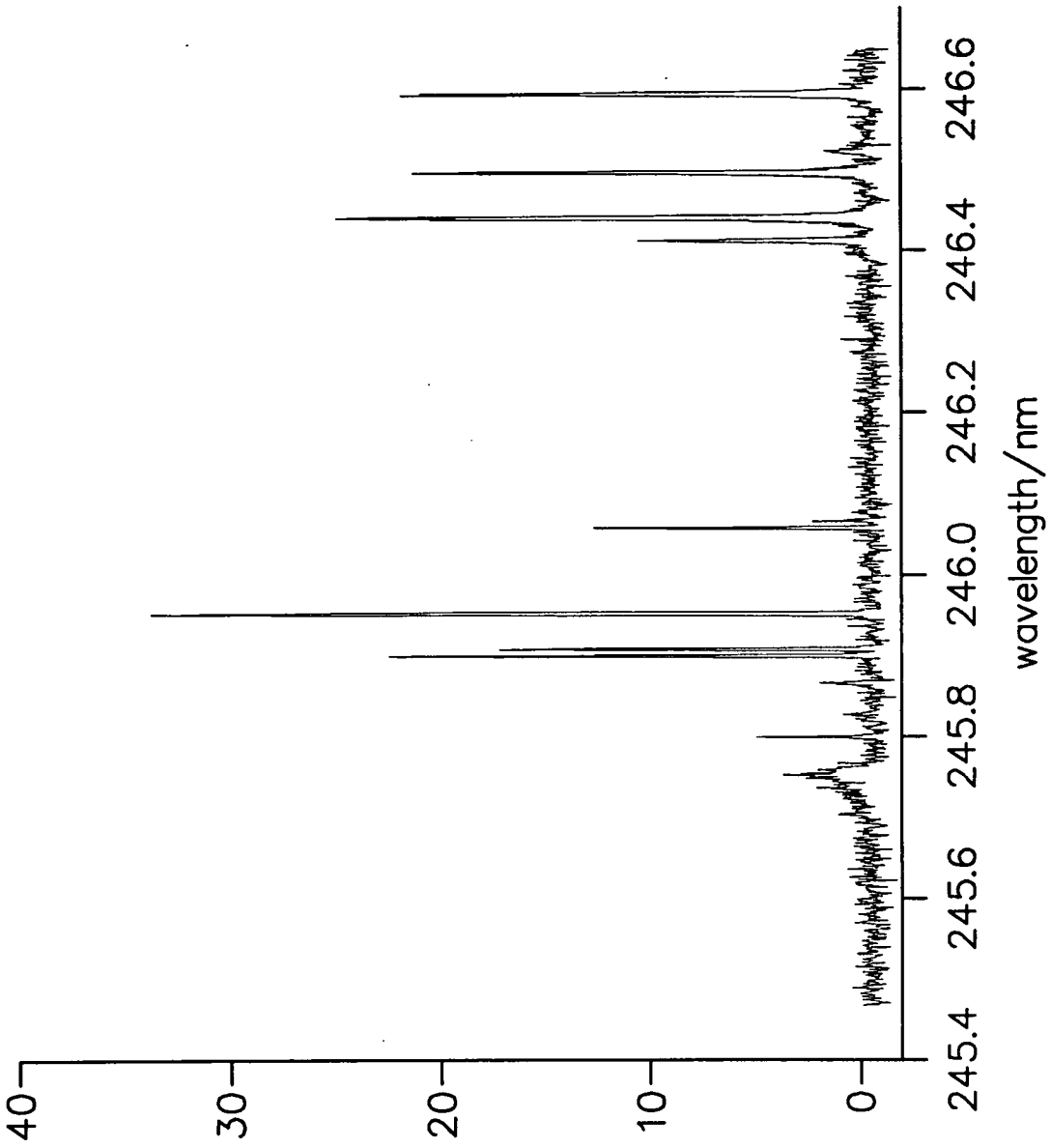

Figure 6–7: $2+1$ REMPI spectrum of HBr at room temperature for the $(0-0)$ band of the $I^1\Delta_2 \leftarrow X^1\Sigma$ transition. Collected using mass channel 79

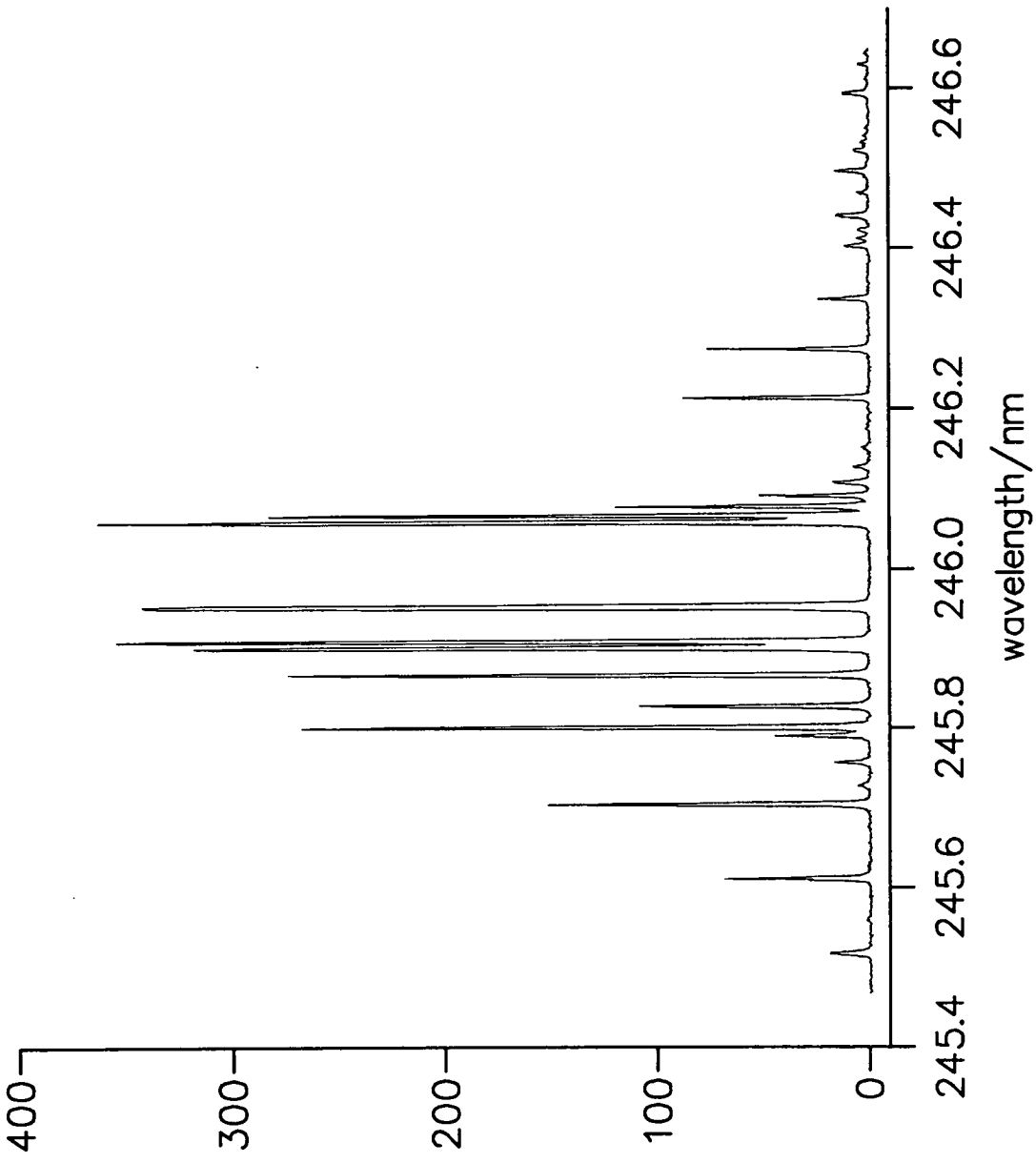

Figure 6–8: $2+1$ REMPI spectrum of HBr at room temperature for the $(0-0)$ band of the $I^1\Delta_2 \leftarrow X^1\Sigma$ transition. Collected using mass channel 80

very large ground state HCl signals were produced when the Cl_2/HI mixture was admitted to the chamber.

It was then decided to monitor the chlorine atom signal while altering the flow of HBr into the chamber. The chlorine atom REMPI signal did *indeed* get weaker as the HBr was added. Initially much of the decrease was due to the aluminium foil coating the injector reacting with the reagent gases causing the extraction field become less than optimal. However, once the voltage on the injector tip had been tuned to reoptimize the field there was still a measurable decrease in the chlorine atom REMPI signal.

Following this the HBr REMPI signal was monitored while altering the flow of Cl_2 into the chamber. Ideally the HBr REMPI signal should have remained constant irrespective of the amount of Cl_2 flowing into the chamber [1] . This was definitely not the case however. It was found that the HBr signal almost disappeared when any significant amount of Cl_2 was let into the injector. It was concluded, therefore, that a large amount of ground vibrational level HCl was being produced in some surface catalysed reaction proceeding within the injector itself.

The single inlet injector was then removed and replaced with a separate 500μm internal diameter injector for each of the two gases as shown in figure 6–10. Again each of the injector tips was connected to a high voltage supply to enable the TOF extraction fields to be optimized.

Using the separate injectors it was found that ratio of the number densities for the reaction zone versus the background had increased to a factor of approximately 100:1. Unfortunately the loan period for the photolysis laser being used ended before further investigation could take place and the work was curtailed at this point.

---

[1] Once the injector voltage had been reoptimized as for the previous check.

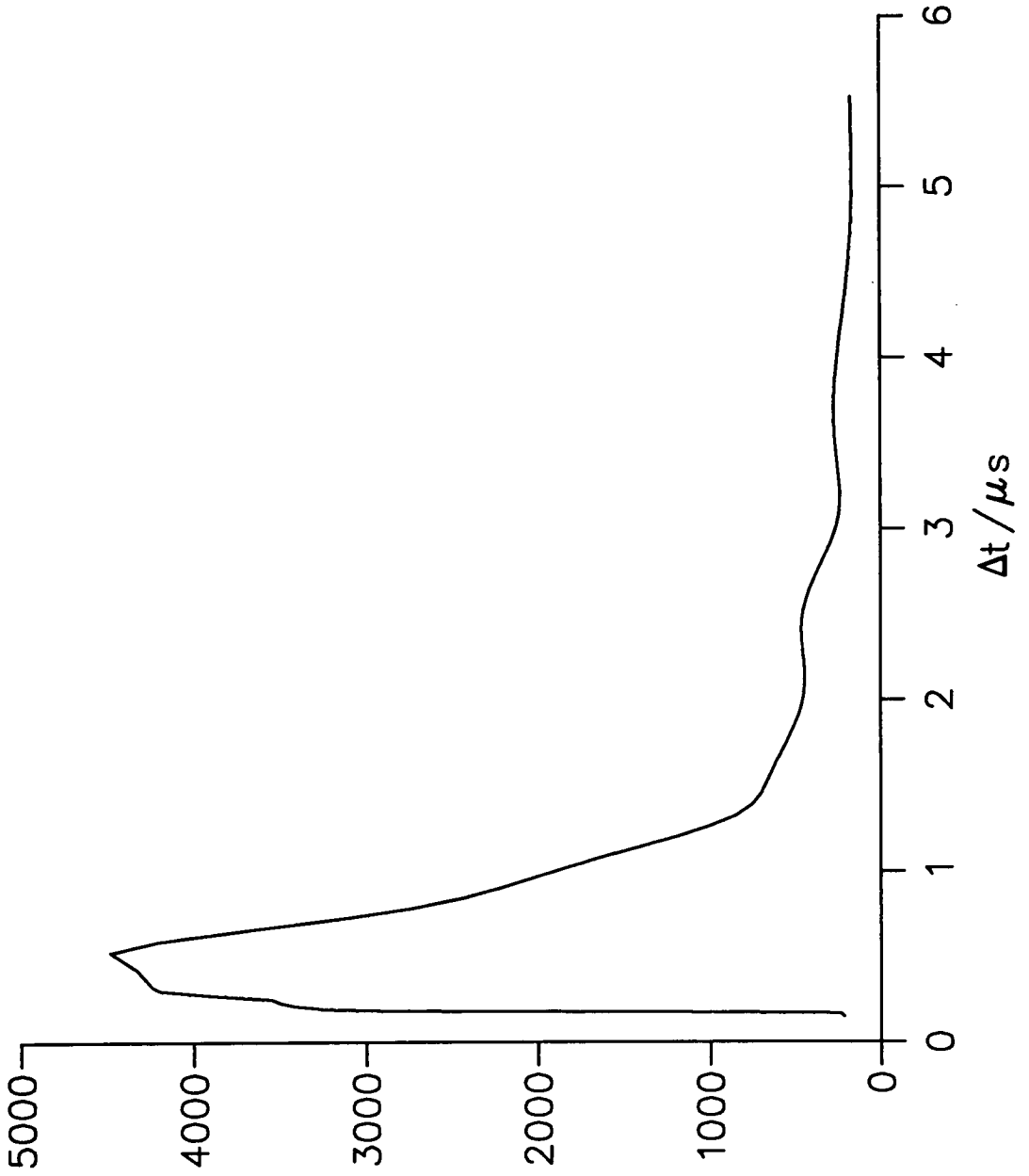

Figure 6–9: Plot of $2+1$ Cl atom REMPI signal as a function of the photolysis to probe delay time

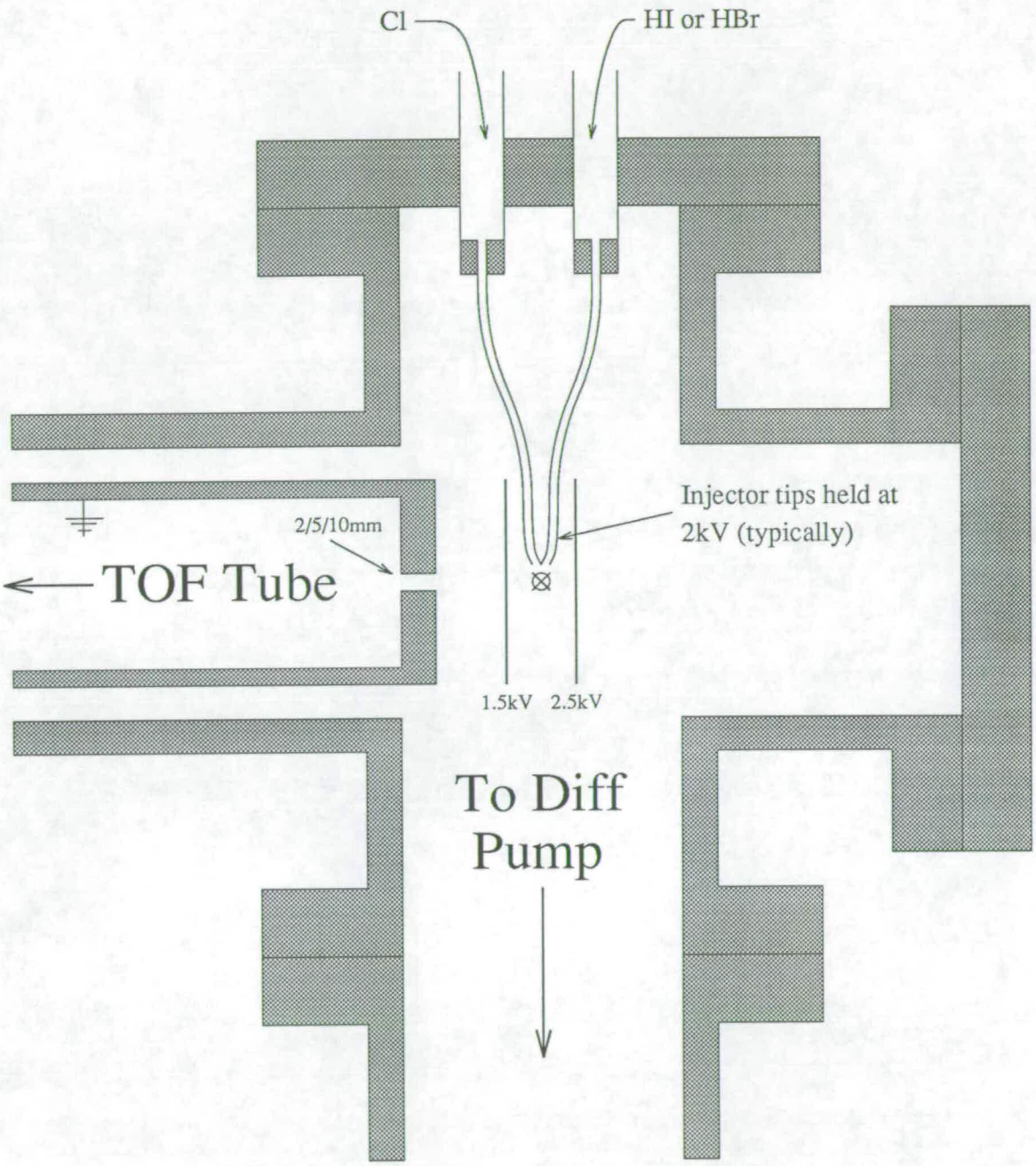

Figure 6–10: Schematic diagram of gas inlet arrangement using separate injectors for each reagent

6.4 Conclusions

For the Cl+HBr reaction the rate of change of the product HCl number density, ρ_{HCl}, is given by

$$\frac{d\rho_{\mathrm{HCl}}}{dt} = Cp_{HBr}p_{Cl}\sigma\langle v\rangle \tag{6.11}$$

where C is the square of Avogadro's number N_A divided by the number of litres occupied by one mole of gas at s.t.p, the pressures p_{HBr} and p_{Cl} are in mbar, σ is the reaction cross-section, $\langle v\rangle$ is the average relative translational velocity of the two reagents and the result has units $\mathrm{m^{-3}s^{-1}}$.

To allow for the fact that the chlorine atom number density at the reaction zone is a function of time this can be rearranged to give (assuming the HBr to be in excess)

$$\rho_{\mathrm{HCl}}(t) = p_{HBr}N_A^2\sigma\langle v\rangle/22.4^2\int_0^t p_{Cl}(\tau)d\tau \tag{6.12}$$

where τ has replaced t as the variable of integration, and it is assumed that no HCl escapes the observation zone over the timescale involved.

With the values used to plot figure 6–9 it was possible to calculate, approximately, the product HCl number density, ρ_{HCl}. This assumed an HBr partial pressure of approximately 10^{-2}mbar derived from foreground to background signal measurements assuming effusive injectors. The resulting values are shown in figure 6–11

As can be seen from figure 6–11 the pressure of HCl produced as a function of time levels out at approximately 2×10^{-6}mbar which corresponds to a number density of $5.5\times10^{16}\mathrm{m^{-3}s^{-1}}$, 75% of which is expected to lie in $v'' = 1$. This should be easily detectable with the current apparatus and had time been available it could be stated with reasonable confidence that the vibrationally excited HCl product would have been observed. In principle, the work could ultimately continue towards stimulated Raman pumping of the molecular reagent species, as described in section 7, for fully state-to-state reaction dynamics.

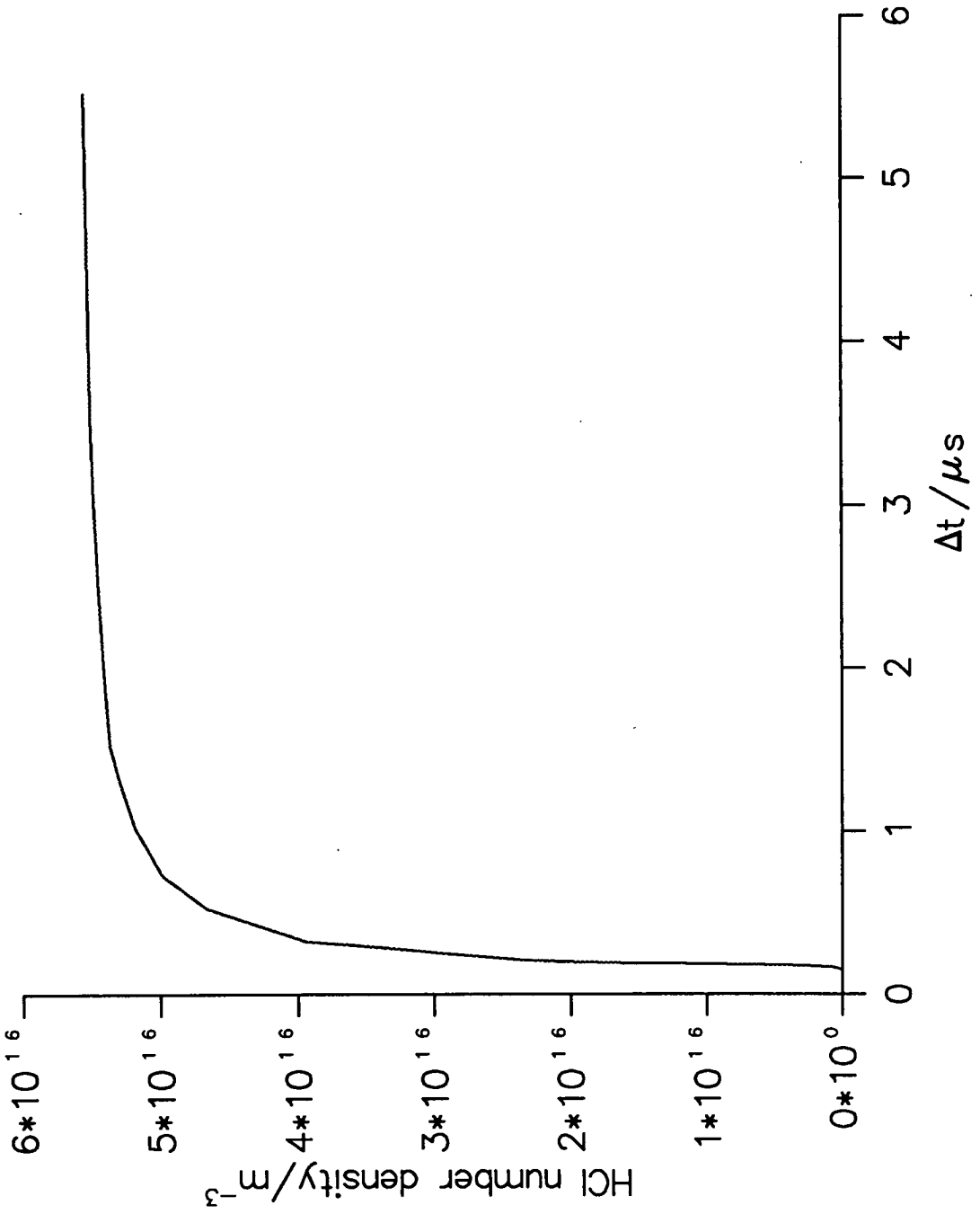

Figure 6–11: Plot showing expected HCl product number density ρ_{HCl} as a function of time. $t = 0$ corresponds to the firing of the photolysis laser

6.5 Future Work

More recently a pair of supersonic pulsed nozzles has been acquired. Initial $2+1$ REMPI studies suggest that a further order of magnitude increase in the reaction zone to background pressure ratio may be obtained when using these valves for a bimolecular study. This would have increased $\frac{d\rho_{HCl}}{dt}$ by approximately 10^2 making it the next logical step in the progress towards studies of bimolecular reactions.

Bibliography

[1] Park J., Lee Y., Flynn G. W., *Chem. Phys. Lett.*, **186**, 441 (1992)

[2] Mei C. C., Moore C. B., *J. Chem. Phys.*, **67**, 3936 (1977)

[3] Bergman K., Moore C. B., *J. Chem. Phys.*, **63**, 643 (1975)

[4] Maylotte D. H., Polanyi J. C., Woodall K. B., *J. Chem. Phys.*, **57**, 1547 (1972)

[5] Rubin R., Persky A., *J. Chem. Phys.*, **79**, 4310 (1983)

[6] Dolson D. A., Leone S. R., *J. Chem. Phys.*, **77**, 4009 (1982)

[7] Wickramaaratchi M. A., Setser D. W., *J. Chem. Phys.*, **87**, 64 (1983)

[8] Angular Momentum, *R. N. Zare* (Wiley Interscience, 1988)

[9] Matsumi Y., Tonokura K., Kawasaki M., *J. Chem. Phys.*, **97**, 1065 (1992)

[10] Callaghan R., Gordon R. J., *J. Chem. Phys.*, **93**, 4624 (1990)

Chapter 7

Stimulated Raman Pumping of HCl

7.1 Introduction

In the introduction to this work it was stated that the ultimate bimolecular reaction dynamics experiment would involve the preparation of at least one of the reagents in a single, or more realistically, very small set of, rovibronic quantum states before the reaction takes place. For this purpose the technique of stimulated Raman pumping, illustrated in the schematic energy level diagram in figure 7–1, has several advantages. Firstly it does not require the molecule being excited to possess a non-zero dipole moment thus allowing the excitation of homonuclear diatomics and, secondly, using modern pulsed lasers very high pumping efficiencies can be achieved.

In addition to this, the alignment in the prepared state can be controlled to a certain degree [1] by correct choice of pump laser polarizations and rotational branch. Populating the excited level through a Raman Q-branch using parallel pump laser polarizations results in pumping predominantly via the isotropic component of the Raman scattering tensor. Therefore, the excited state distribution is isotropic, i.e. there is no m_j dependence in the Raman transition probability. Pumping via anisotropic Q-branch transitions (with crossed pump polarizations) or via S or O-branches, on the other hand can produce anisotropic m_j distribu-

tions. In this way the experimentalist has some control over the relative alignment of the angular momenta of the reagents. Pumping in this way to produce anisotropic distributions is, however, very inefficient making it difficult to achieve significant populations.

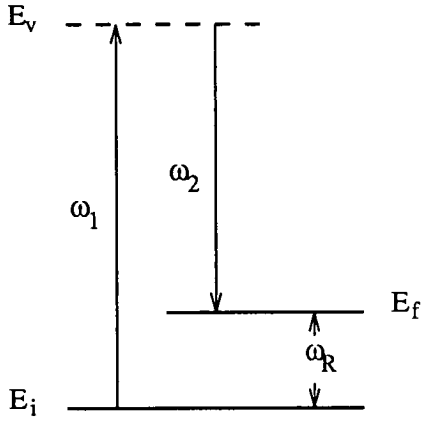

Figure 7–1: Diagram illustrating stimulated Raman pumping process. ω_1 and ω_2 denote the two photon frequencies used in the excitation, ω_R is a Raman active molecular transition and E_i, E_v and E_f label the initial, virtual and final energy levels respectively

To ascertain whether or not stimulated Raman pumping was feasible it was decided to perform Coherent Anti-Stokes Raman Spectroscopy (CARS) on an HCl sample. The decision to use HCl was the result of several factors. Firstly the wavelengths required to perform CARS of HCl were available using the Nd:YAG second harmonic at 532nm and the fundemental output from the dye laser. In addition there was the possibility of monitoring the excited state populations created by the CARS process directly via the two-photon REMPI schemes developed previously [2] during the brief period when two tunable laser systems were available. As can be seen from figure 7–2 CARS is effectively an extension of the stimulated Raman pumping process and therefore if a CARS signal was observed then stimulated Raman pumping must be taken place. CARS is outlined in the following section.

7.2 CARS Spectroscopy

The CARS technique combines the advantages of signal strength obtained in stimulated Raman spectroscopy with the general applicability of conventional Raman spectroscopy. The fact that the CARS signal is itself a laser beam makes it a fairly simple matter to redirect it into the detection system being used. In this technique, two incident waves with frequencies ω_1 and ω_2 respectively are passed through the sample, where $\omega_1 > \omega_2$. If the frequency difference $\omega_d = \omega_1 - \omega_2$ equals the frequency ω_R of a Raman active molecular transition as shown in figure 7–2 then Stokes and Anti-Stokes waves are generated. Two waves at frequency ω_1 and one at the Stokes frequency ω_2 are mixed by the non-linear polarization of the medium and a new Anti-Stokes wave at the frequency $\omega_a = 2\omega_1 - \omega_2$ is generated in a four-wave parametric mixing process.

Furthermore, for a CARS beam to be generated the beams present must be phase matched. For gaseous samples of up to moderate pressure this is achieved when the ω_1 and ω_2 pump beams are collinear. The theory of CARS rotational line strengths and line broadening effects can be found in references [3] and [4].

The apparatus used to collect the CARS data is shown in section 2.6.3, figure 2–10. The Nd:YAG second harmonic (532nm) and dye laser fundamental provide the ω_1 and ω_2 beams respectively. These two beams are spatially overlapped using a dichroic beam combiner before being focussed down into the gas cell containing approximately 300torr of HCl by a 20cm focal length lens. The emerging 532nm, dye laser, and CARS beams were collimated using a 30cm focal length lens and separated by a Pellin-Broca prism. The 532nm and dye laser beams passed into beam dumps while the CARS beam was diffusely reflected into a monochromator at centre wavelength 459.15nm and bandwidth (FWHM) 3.5nm. Finally the CARS signal emerging from the monochromator was detected using a photomultiplier tube .

The first CARS spectrum was recorded using the Spectron laser system described in section 2.2 for the $v = 0$ to 1 vibrational transition of room temperature

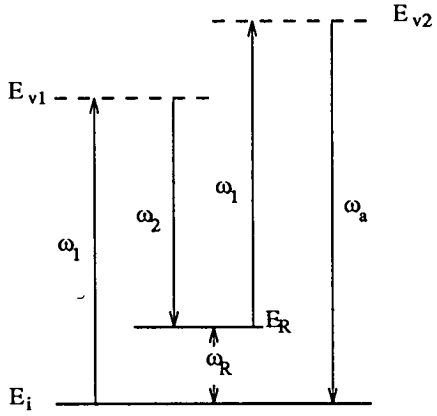

Figure 7–2: Schematic diagram of energy level scheme for Coherent Anti-Stokes Raman Spectroscopy (CARS) where ω_1 and ω_2 denote the two photon frequencies used in the excitation and ω_a represents the frequency of the resulting Anti-Stokes radiation

HCl in its ground electronic, $X^1\Sigma^+(0^+)$, state. This is shown in figure 7–3. A second CARS spectrum of the same transition was recorded using the Quanta-Ray laser system described in section 2.6 and is shown in figure 7–4.

The most obvious difference between the two spectra is the lower resolution of the Quanta-Ray spectrum. This is due to the fact that the Quanta-Ray Nd:YAG had no intra-cavity etalon and thus exhibited a much greater line width than did the Spectron system.

Both beams ω_1 and ω_2 had the same horizontal linear polarization for the two spectra shown which resulted in a reasonably intense signal with the CARS beam also being horizontally polarized. The effect of cross-polarized beams, ie the 532nm beam being vertical and the dye beam horizontal, was investigated and it was found that the CARS signal was reduced by approximately *two orders of magnitude.* This factor is a measure of the relative efficiency with which an aligned sample could be prepared but is not, however, a direct reflection since the steps involving the third and fourth photons will also depend on the relative polarizations of the two pump beams ω_1 and ω_2. The polarization of the CARS signal remained horizontal and linear, the same as the dye beam, for both the Q and S-branches irrespective of the polarization of the 532nm beam.

Having observed a CARS signal it was known that stimulated Raman pumping must be taking place and direct detection of the excited HCl in $v = 1$ using two-photon REMPI of the (1-1) band of the $F^1\Delta(2) \leftarrow X^1\Sigma^+(0^+)$ transition would have been the next obvious logical step. However, the very limited time for which the second tunable laser system was available (on loan from the SERC Laser Support Facility), exacerbated by a serious equipment failure towards the end of the loan period unfortunately prevented any further progress in this direction.

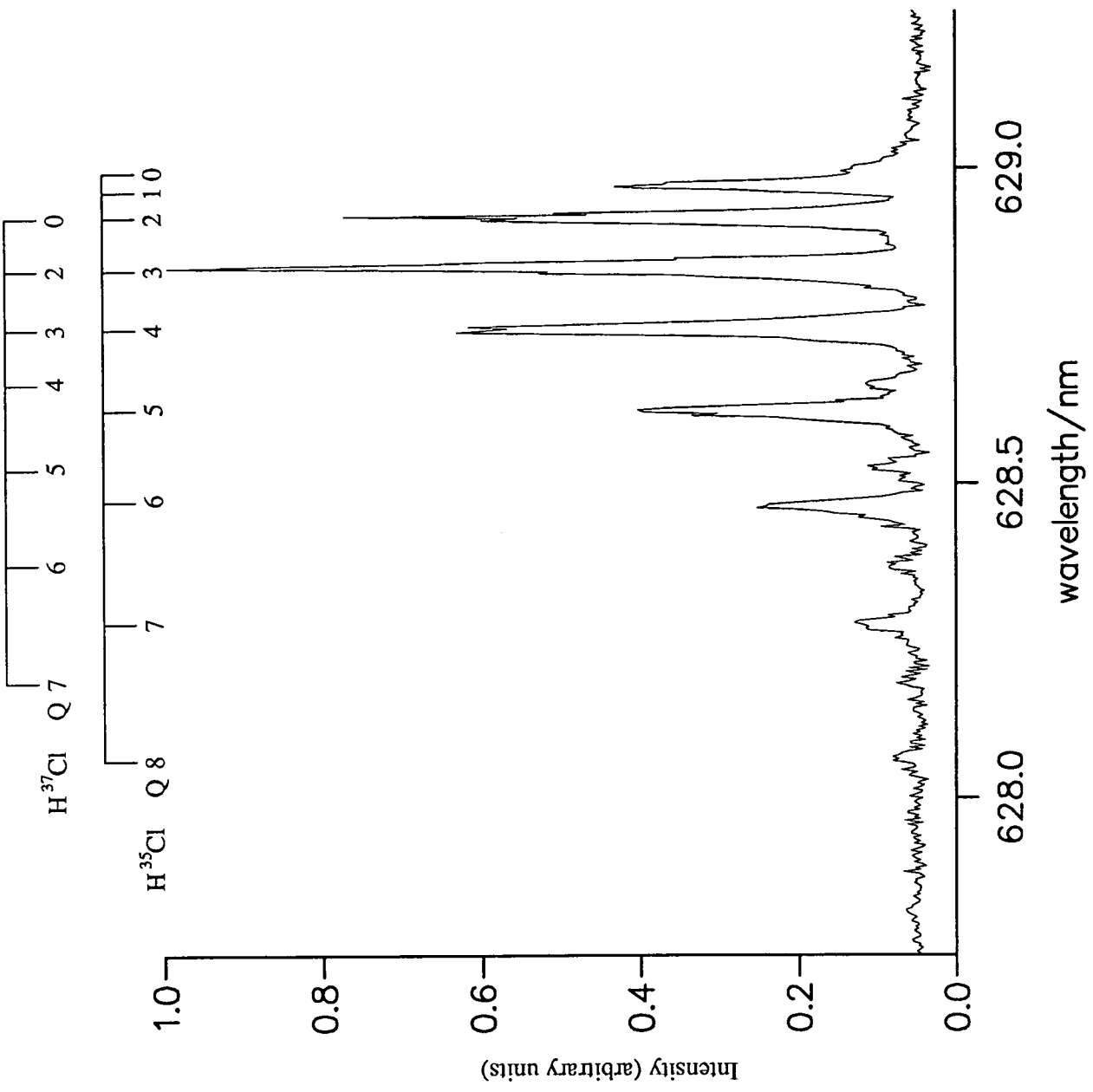

Figure 7–3: CARS spectrum showing the Q-branch of the (1-0) rovibrational transition in room temperature HCl in the ground electronic, $X^1\Sigma^+(0^+)$, state. Spectrum was recorded using the Spectron laser system. Both $H^{35}Cl$ and $H^{37}Cl$ isotopes are present

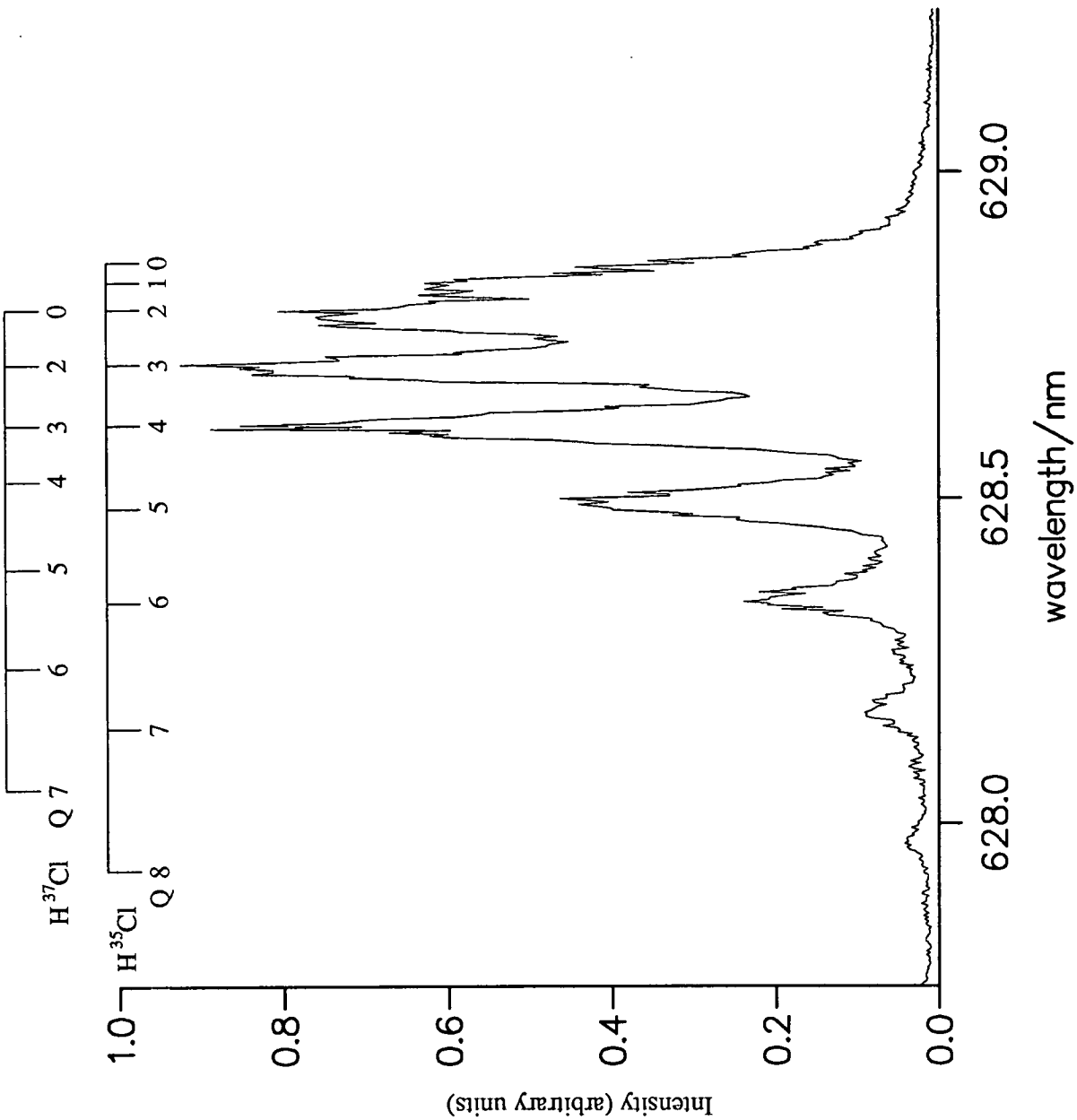

Figure 7–4: CARS spectrum showing the Q-branch of the (1-0) rovibrational transition in room temperature HCl in the ground electronic, $X^1\Sigma^+(0^+)$, state. Spectrum was recorded using the Quanta-Ray laser system. Both $H^{35}Cl$ and $H^{37}Cl$ isotopes are present

Bibliography

[1] Farrow R. L., Sitz G. O., *J. Opt. Soc. Am.*, **B5**, 865 (1989)

[2] Rohlfing E. A., Chandler D. W., *J. Chem. Phys.*, **87**, 5229 (1987)

[3] Attal-Trétout B., Monot P., Müller-Dethlefs K., *Mol. Phys.*, **73**, 1257 (1991)

[4] Spectroscopic Techniques (vol. 4), *J. J. Valentini (ed G. A. Vanesse)* (Academic Press, New York, 1984)

Appendix A

Data Acquisition Routine

A large part of the present work revolved around the design and implementation of the real-time data acquisition software used throughout. The central component of the software was the interrupt routine which was called automatically by the PC at the required repetition rate (10Hz) and is given in figures A–1 to A–4.

```
/*-------------------------------------
|   Data aquisition...
|-------------------------------------*/
if (_FLAGS._HARVEST._ON) {
    if (_FLAGS._HARVEST._ACTIVE) {
        if (_FLAGS._HARVEST._DELAY_SET_INCD) {
            H_delay_set_used = (H_delay_set+H_num_delay_sets-1)
                               % H_num_delay_sets ;
        }
        else {
            H_delay_set_used = H_delay_set ;
        }
        if (_FLAGS._HARVEST._DIGIT_ON) {
            CAMAC2001AXfer (xferbuf,(unsigned)atoi (_TD_REC_
                            [current_TD.RecLen])) ;
            _FLAGS._HARVEST._DIGIT_DATA_READY = 1 ;
        }
        for (H_i = 0 ; H_i < 3 ; ++H_i) {
            if (_FLAGS._HARVEST._ADC_ON[H_i]) {
                Camac_i16 (_ADC520_,_f0_,H_i,H_ADC_bin[H_i],_Q_,_X_) ;
                _FLAGS._HARVEST._ADC_DATA_READY[H_i] = 1 ;
            }
        }
        Camac_i16 (_ADC520_,_f0_,_A3_,H_ADC_bin[3],_Q_,_X_) ;
        if (_FLAGS._HARVEST._ADC_ON[3]) {
            _FLAGS._HARVEST._ADC_DATA_READY[3] = 1 ;
        }
    }
    Camac_ (_2001A_,_f9_,_A0_,_Q_,_X_) ;
    Camac_ (_2001A_,_f26_,_A0_,_Q_,_X_) ;
```

Figure A–1: Data Acquisition Code

```
Camac_ (_4222PDG_,_f24_,_A0_,_Q_,_X_) ;
_D24_ = H_delays[H_delay_set][0] ;
Camac_o24 (_4222PDG_,_f16_,_A0_,_D24_,_Q_,_X_) ;
_D24_ = H_delays[H_delay_set][1] ;
Camac_o24 (_4222PDG_,_f16_,_A1_,_D24_,_Q_,_X_) ;
_D24_ = H_delays[H_delay_set][2] ;
Camac_o24 (_4222PDG_,_f16_,_A2_,_D24_,_Q_,_X_) ;
_D24_ = H_delays[H_delay_set][3] ;
Camac_o24 (_4222PDG_,_f16_,_A3_,_D24_,_Q_,_X_) ;
Camac_ (_4222PDG_,_f26_,_A0_,_Q_,_X_) ;
if (_FLAGS._GENERAL._4222PDG_INTERNAL_TRIG ) {
    Camac_ (_4222PDG_,_f25_,_A0_,_Q_,_X_) ;
}
if (_FLAGS._HARVEST._FIRST) {
    --_FLAGS._HARVEST._FIRST ;
    return ;
}
_FLAGS._HARVEST._DELAY_SET_INCD = 0 ;
if (_FLAGS._HARVEST._ACTIVE) {
    if (_FLAGS._HARVEST._DIGIT_ON) {
        for (H_i = 0 ; H_i < H_num_masses ; ++H_i) {
            H_bg_first = H_bg_gates[H_i][0] ;
            H_bg_last = H_bg_gates[H_i][1] ;
            H_bg_bins[H_i] = 0 ;
            for (H_j = H_bg_first ; H_j <= H_bg_last ; ++H_j)
                H_bg_bins[H_i] += (float)(unsigned char)
                                  xferbuf[H_j] ;
            H_bg_bins[H_i] /= H_bg_last-H_bg_first+1 ;
            H_sig_first = H_mass_gates[H_i][0] ;
            H_sig_last = H_mass_gates[H_i][1] ;
```

Figure A–2: Data Acquisition Code (continued)

```
            H_mass_bins[H_i] = 0 ;
            for (H_j = H_sig_first ; H_j <= H_sig_last ; ++H_j)
                H_mass_bins[H_i] += (float)(unsigned char)
                                    xferbuf[H_j]-H_bg_bins[H_i] ;
            H_mass_bins[H_i] *= C1_polarity ;
            H_digit[H_i][H_delay_set_used][H_buf_pos] += H_mass_bins[H_i]
            PN_save (PN_TD,H_i,H_delay_set_used,H_muxed,H_mass_bins[H_i])
        }
    }
    for (H_i = 0 ; H_i < 4 ; ++H_i) {
        if (_FLAGS._HARVEST._ADC_ON[H_i]) {
            data = (ADC.POLARITY[H_i] == 1)
                   ? (H_ADC_bin[H_i]-ADC.ZERO[H_i])
                   : (ADC.ZERO[H_i]-H_ADC_bin[H_i]) ;
            H_ADC[H_i][H_delay_set_used][H_buf_pos] += data ;
            PN_save (PN_ADC,H_i,H_delay_set_used,H_muxed,data) ;
        }
    }
    H_delay_set = (H_delay_set+1) % H_num_delay_sets ;
    _FLAGS._HARVEST._DELAY_SET_INCD = 1 ;
    if (H_delay_set == 0) {
        if (++H_muxed >= H_mux_no) {
            if (_FLAGS._HARVEST._DIGIT_ON) {
                for (H_i = 0 ; H_i < H_num_masses ; ++H_i) {
                    for (H_j = 0 ; H_j < H_num_delay_sets ; ++H_j) {
                        H_digit[H_i][H_j][H_buf_pos] /= H_muxed ;
                    }
                }
            }
            for (H_i = 0 ; H_i < 4 ; ++H_i) {
```

Figure A–3: Data Acquisition Code (continued)

```
                    if (_FLAGS._HARVEST._ADC_ON[H_i]) {
                        for (H_j = 0 ; H_j < H_num_delay_sets ; ++H_j) {
                            H_ADC[H_i][H_j][H_buf_pos] /= H_muxed ;
                        }
                    }
                }
                H_muxed ^= H_muxed ;
                ++H_data_point ;
                H_buf_pos = H_data_point % H_num2buf ;
                _FLAGS._HARVEST._ACTIVE = 0 ;
                _FLAGS._GENERAL._SHIFT_WAVELENGTH = 1 ;
                if (H_buf_pos == 0) {
                    _FLAGS._HARVEST._FLUSH = 1 ;
                }
            }
        }
        ++H_shots ;
    }
    return ;
}
```

Figure A–4: Data Acquisition Code (continued)

Appendix B

Racah-Wigner Algebra in Angular Momentum Theory

B.1 Wigner Rotation Matrices (Representation Coefficients)

The Wigner rotation matrices, $D^{j}_{m'm}(\mathcal{U})$, are the matrix elements of the rotation operator $\mathcal{U} \equiv \exp(-i\psi\hat{n}\cdot\mathbf{J})$ where the rotation is denoted by the spinor transformation $\mathcal{U}(\psi,\hat{n})$ corresponding to a rotation of magnitude ψ about the axis specified by the unit vector $\hat{n}$ [1] . It can be shown that [2] a state having total angular momentum j and projection m along the z axis is characterized by the ket vector $|jm\rangle$ and that under a rotation of frames, z→z′, this state vector undergoes the transformation

$$|jm\rangle \rightarrow |jm\rangle' = \sum_{m'} D^{j}_{m'm}(\mathcal{U})|jm'\rangle \tag{B.1}$$

---

[1] This can easily be reformulated in terms of the Euler angles or the complex Euler-Rodrigues parameters [1]

The relationship between $D^j_{m'm}(\alpha\beta\gamma)$ and the corresponding reduced rotation matrices $d^j_{m'm}(\beta)$ is given by

$$D^j_{m'm}(\alpha\beta\gamma) = \mathrm{e}^{-im'\alpha} d^j_{m'm}(\beta)\, \mathrm{e}^{-im\gamma} \tag{B.2}$$

with $d^j_{m'm}(\beta)$ being given by [2]

$$\begin{aligned} d^j_{m'm}(\beta) &= \left[(j+m')!(j-m')!(j+m)!(j-m)!\right]^{1/2} \\ &\quad \times \sum_s \frac{(-1)^{m'-m+s} \left(\cos\frac{\beta}{2}\right)^{2j+m-m'-2s} \left(\sin\frac{\beta}{2}\right)^{m'-m+2s}}{(j+m-s)!s!(m'-m+s)!(j-m'-s)!} \end{aligned} \tag{B.3}$$

To arrive at the physical interpretation of the rotation matrices consider the action of the rotation operator $\mathcal{U}(\alpha\beta\gamma)$ which transforms the frame specified by (x, y, z) into the frame (x', y', z'). It is found that

$$\left|D^j_{m'm}(\alpha\beta\gamma)\right|^2 = \left[d^j_{m'm}(\beta)\right]^2 \tag{B.4}$$

is the probability that a system in the angular momentum state $|jm\rangle$ in the frame denoted by (x, y, z) will be found in the angular momentum state $|jm'\rangle$ in the rotated frame denoted by (x', y', z'). This is illustrated in figure B–1

B.2 Spherical Tensor Operators

The concept of a tensor operator is an important one in angular momentum theory and leads to the examination of the characteristic quantum states, $|(\alpha)jm\rangle$ [3] and their transformation properties.

---

[2] A full derivation of the reduced rotation matrices, $d^j_{m'm}(\beta)$, can be found in reference [4].

[3] Here α is used to denote those quantum numbers not associated with angular momentum.

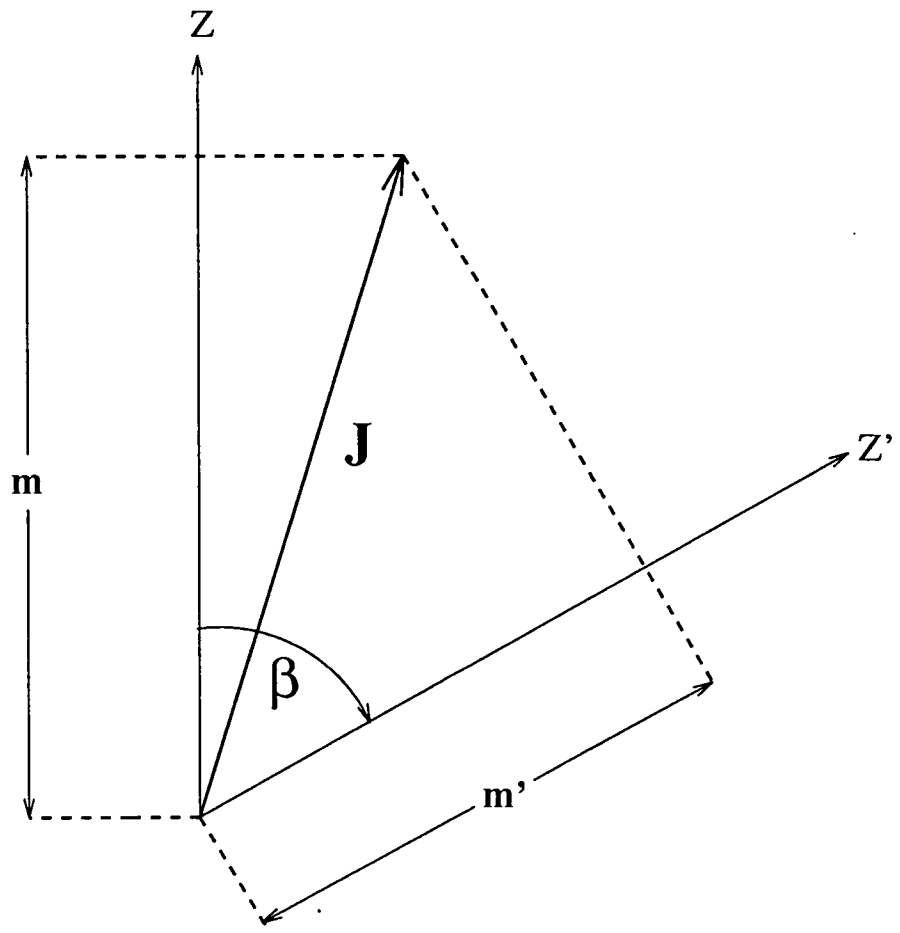

Figure B–1: Diagram showing physical interpretation of the Wigner rotation matrices $D^{j}_{m',m}(\alpha\beta\gamma)$

Consider an arbitrary operator, $\mathcal{O}$, that acts on the system. The action of the operator can be described by the set of matrix elements

$$\left\{\left\langle(\alpha')j'm'\left|\mathcal{O}\right|(\alpha)jm\right\rangle\right\} \tag{B.5}$$

Since these matrix elements are probability amplitudes, and since the physical probabilities must be invariant to the choice of coordinate frame it follows that

$$\left|\left\langle(\alpha')j'm'\left|\mathcal{O}\right|(\alpha)jm\right\rangle\right|^2 = \text{invariant to rotations of coordinate frames} \tag{B.6}$$

This implies either of two conditions, a) the probability amplitude is invariant or b) the probability amplitude transforms under the symmetry into its complex conjugate.

It has been shown by Wigner [5] that case b) corresponds to time reversal and thus for rotational symmetry it is the case that the probability amplitude itself is invariant. i.e.

$$\left\langle(\alpha')j'm'\left|\mathcal{O}\right|(\alpha)jm\right\rangle = \text{invariant to rotations of coordinate frames} \tag{B.7}$$

Since this relation is valid for all ket vectors $|(\alpha)jm\rangle$ and all bra vectors $\langle(\alpha)jm|$ it follows that

$$\langle\Psi\left|\mathcal{O}\right|\Phi\rangle = \text{invariant to rotations of coordinate frames} \tag{B.8}$$

where $|\Phi\rangle$ and $\langle\Psi|$ are arbitrary vectors in the Hilbert space and its dual respectively.

The action of the rotational symmetry operator $\mathcal{U} = \exp\left(-i\psi\hat{n}\cdot\mathbf{J}\right)$ [4] on the ket vector $|\Phi\rangle$ is the unitary transformation

$$|\Phi\rangle \rightarrow |\Phi'\rangle \equiv \mathcal{U}\,|\Phi\rangle \tag{B.9}$$

with a corresponding unitary transformation on the bra vector giving

$$\langle\Psi| \rightarrow \langle\Psi'| \equiv \langle\Psi|\,\mathcal{U}^{-1} \tag{B.10}$$

---

[4]The operator $\mathcal{U}(\psi,\hat{n})$ corresponds to a rotation of magnitude ψ about the axis $\hat{n}$.

Equation B.8 may now be written as

$$\langle \Psi \,|\mathcal{O}|\, \Phi \rangle = \langle \Psi' | \mathcal{O}' | \Phi' \rangle \tag{B.11}$$

where $\mathcal{O}'$ denotes the operator $\mathcal{O}$ relative to the rotated frame. Thus

$$\langle \Psi \,|\mathcal{O}|\, \Phi \rangle = \langle \Psi | \mathcal{U}^{-1} \mathcal{O}' \mathcal{U} | \Phi \rangle \tag{B.12}$$

for arbitrary $|\Phi\rangle$ and $\langle\Psi|$. It follows, therefore, that

$$\mathcal{O}' = \mathcal{U}\mathcal{O}\mathcal{U}^{-1} \tag{B.13}$$

For infinitesimal rotations, $\mathcal{U} = \exp(-i\delta\omega \cdot \mathbf{J})$, where $\omega = \psi\hat{n}$, $\mathcal{O}'$ can be expressed as

$$\mathcal{O}' = \mathcal{O} - i\delta\omega \cdot [\mathbf{J}, \mathcal{O}] \tag{B.14}$$

and

$$\delta\mathcal{O} \equiv \mathcal{O}' - \mathcal{O} = -i\delta\omega \cdot [\mathbf{J}, \mathcal{O}] \tag{B.15}$$

It is the appearance of a commutator of the general operator $\mathcal{O}$ with the angular momentum $\mathbf{J}$ which leads to the definition of an irreducible tensor operator of rank J $(J = 0, \frac{1}{2}, 1 \ldots)$. An irreducible tensor operator of rank J, denoted by $\mathbf{T}^J$, is defined to be a set of linear operators $\{\mathbf{T}^J_M : M = J, J-1, \ldots, -J\}$, where each operator is a mapping of the Hilbert space of ket vectors into itself and the commutator action of the angular momentum $\mathbf{J}$ on the set of operators is to map the set into itself according to the following rules:

$$\begin{aligned}
\left[J_+, \mathbf{T}^J_M\right] &= [(J-M)(J+M+1)]^{1/2}\, \mathbf{T}^J_{M+1} \\
\left[J_-, \mathbf{T}^J_M\right] &= [(J+M)(J-M+1)]^{1/2}\, \mathbf{T}^J_{M-1} \\
\left[J_z, \mathbf{T}^J_M\right] &= M\mathbf{T}^J_M
\end{aligned} \tag{B.16}$$

Having defined the tensor operator it is often convenient to write the commutation relations B.16 in a form in which the Wigner coefficients, described in

section B.3, are introduced. In this case the so called spherical components of the angular momentum **J** given by

$$\begin{aligned} J_{+1} &= -(J_x + iJ_y)/\sqrt{2} \\ J_0 &= J_z \\ J_{-1} &= (J_x - iJ_y)/\sqrt{2} \end{aligned} \tag{B.17}$$

are introduced and B.16 becomes

$$\left[J_m, \mathbf{T}^J_M\right] = [J(J+1)]^{1/2} C^{J\,1\,J}_{M,m,M+m} \mathbf{T}^J_{M+m} \tag{B.18}$$

From the definition of a tensor operator it follows that the components of a tensor operator of rank J transform under the similarity action of $\mathcal{U}$ in the same way as a ket vector does under the standard action of $\mathcal{U}$, i.e.

$$\begin{aligned} \mathcal{U} : \mathbf{T}^J_M \rightarrow \left(\mathbf{T}^J_M\right)' &= \mathcal{U}\mathbf{T}^J_M\mathcal{U}^{-1} \\ &= \sum_{M'} D^J_{M'M}(\mathcal{U})\, \mathbf{T}^J_M \end{aligned} \tag{B.19}$$

where the $D^J_{M'M}(\mathcal{U})$ are the Wigner rotation matrices described in section B.1.

B.3 Vector Coupling (Wigner) Coefficients

To find the physical interpretation of the vector coupling coefficients [5] consider the addition of two angular momenta j_1 and j_2. The resulting system can be described in terms of two separate basis sets given by

$\lvert j_1 m_1; j_2 m_2\rangle$	uncoupled representation
$\lvert (j_1 j_2)\, jm\rangle$	coupled representation

[5] Also called Wigner or Clebsch-Gordon coefficients.

This is illustrated in figure B–2. The physical interpretation of the vector coupling coefficient $C^{j_1 j_2 j}_{m_1 m_2 m}$ is then given by the following:

$$|\langle j_1 m_1; j_2 m_2 | (j_1 j_2) jm \rangle|^2 = \left| C^{j_1 j_2 j}_{m_1 m_2 m} \right|^2 \tag{B.20}$$

is the probability that a measurement of the three components of the angular momenta of the individual parts of the system, originally in the angular momentum state $|(j_1 j_2) jm\rangle$, will find the system in the state $|j_1 m_1\rangle \otimes |j_2 m_2\rangle$. The following expression gives the vector coupling coefficient in terms of finite sums:

$$\begin{aligned} C^{j_1 j_2 j}_{m_1 m_2 m} &= \delta_{m_1+m_2,m} \\ &\times \left[\frac{(2j+1)(j_1+j_2-j)!(j_1-m_1)!(j_2-m_2)!(j-m)!(j+m)!}{(j_1+j_2+j+1)!(j+j_1-j_2)!(j+j_2-j_1)!(j_1+m_1)!(j_2+m_2)!} \right]^{1/2} \\ &\times \sum_t (-1)^{j_1-m_1+t} \left[\frac{(j_1+m_1+t)!(j+j_2-m_1-t)!}{t!(j-m-t)!(j_1-m_1-t)!(j_2-j+m_1+t)!} \right] \end{aligned} \tag{B.21}$$

Although the vector coupling coefficient in this form is fundemental to the quantum theory of angular momentum it is usual to construct a more highly symmetric coefficient. This results in the 3j symbol given by

$$\begin{pmatrix} j_1 & j_2 & j \\ m_1 & m_2 & -m \end{pmatrix} \equiv (-1)^{j_1-j_2+m} (2j+1)^{-1/2} C^{j_1 j_2 j}_{m_1 m_2 m} \tag{B.22}$$

B.4 6j Symbols (Racah Coefficients)

The Racah coefficients are viewed as recoupling coefficients for systems of three angular momenta j_1, j_2 and j_3. Let the ket vector $|[(j_1 j_2)_{j'} j_3]_{jm}\rangle$ denote the state vector corresponding to the coupling scheme

$$j = (j_1 + j_2) + j_3 = j' + j_3 \tag{B.23}$$

Similarly, the ket vector $|[j_1 (j_2 j_3)_{j''}]_{jm}\rangle$ denotes the state vector corresponding to the coupling scheme

$$j = j_1 + (j_2 + j_3) = j_1 + j'' \tag{B.24}$$

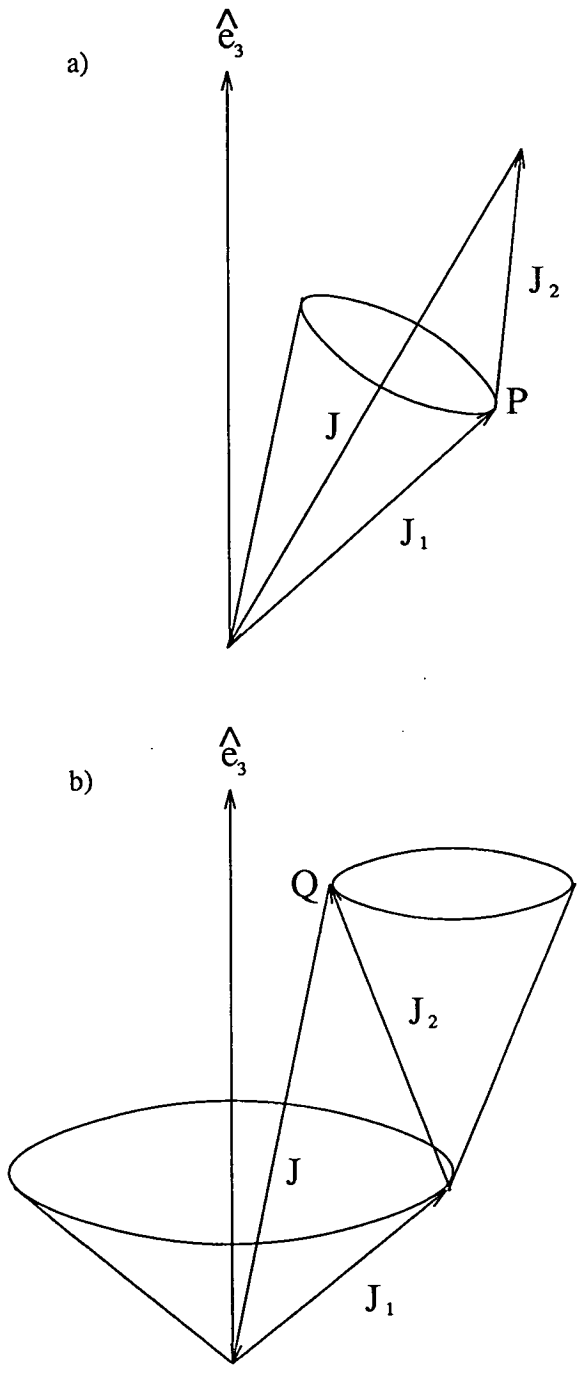

Figure B–2: Diagram showing the coupled representation a) and uncoupled representation b) for the combination of two angular momenta

This is illustrated in figure B–3. The Racah coefficient $W(j_1 j_2 j j_3; j' j'')$ expresses the transformation between these two schemes by the equation

$$\left|\left[(j_1 j_2)_{j'} j_3\right]_{jm}\right\rangle = \sum_{j''}\left[\left(2j'+1\right)\left(2j''+1\right)\right]^{1/2} \times W\left(j_1 j_2 j j_3; j' j''\right)\left|\left[j_1 (j_2 j_3)_{j''}\right]_{jm}\right\rangle \tag{B.25}$$

It follows from this result that the quantum mechanical probability, P, defined by

$$P \equiv \left(2j'+1\right)\left(2j''+1\right) W^2\left(j_1 j_2 j j_3; j' j''\right) = \left(2j'+1\right)\left(2j''+1\right)\left\{\begin{array}{ccc} j_1 & j_2 & j' \\ j_3 & j & j'' \end{array}\right\}^2 \tag{B.26}$$

is the probability that a system prepared in a state of the coupling scheme B.23, which assumes that j_1, j_2, j_3, j' and j have definite magnitudes, will be found to be in a state of the coupling scheme B.24, which assumes j_1, j_2, j_3, j'' and j to have definite magnitudes. The factor of

$$\left\{\begin{array}{ccc} j_1 & j_2 & j' \\ j_3 & j & j'' \end{array}\right\}$$

in equation B.26 is the so called 6j symbol. Analogous to the 3j symbol in section B.3 it is simply a 'highly symmetrized' Racah coefficient and can be expressed in terms of finite sums as [6]

$$\begin{aligned} \left\{\begin{array}{ccc} j_1 & j_2 & j' \\ j_3 & j & j'' \end{array}\right\} &= (-1)^{j_1+j_2+j_3+j} \\ &\times \delta(j_1, j_2, j')\delta(j', j_3, j)\delta(j_1, j, j'')\delta(j_2, j_3, j'') \\ &\times \sum_n \frac{(-1)^{j_1+j_2+j_3+j+n}(n+1)}{(n-j_1-j_2-j')!(n-j'-j_3-j)!(n-j_1-j-j'')!} \\ &\times \frac{1}{(n-j_2-j_3-j'')!(j_1+j_2+j_3+j-n)!} \end{aligned}$$

[6] From reference [1].

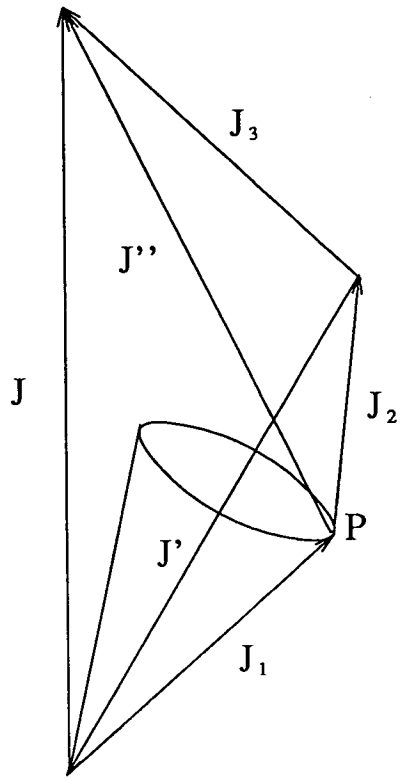

Figure B–3: Diagram showing the alternative schemes for the recoupling of three angular momenta and illustrating the physical interpretation of the 6j symbol

$$\times \frac{1}{(j_1 + j_{'} + j_3 + j_{''} - n)!(j_2 + j_{'} + j + j_{''} - n)!} \tag{B.27}$$

where

$$\delta(\alpha, \beta, \gamma) = \left[\frac{(\alpha + \beta - \gamma)!(\alpha - \beta + \gamma)!(-\alpha + \beta + \gamma)!}{(\alpha + \beta + \gamma + 1)!}\right]^{1/2} \tag{B.28}$$

B.5 9j Symbols (Fano Coefficients)

The 9j symbols, given explicitly by [7]

$$\begin{Bmatrix} j_{11} & j_{12} & j_{13} \\ j_{21} & j_{22} & j_{23} \\ j_{31} & j_{32} & j_{33} \end{Bmatrix} = (-1)^{j_{13}+j_{23}-j_{33}}$$

$$\times \frac{\Delta(j_{21},j_{11},j_{31})\Delta(j_{12},j_{22},j_{32})\Delta(j_{33},j_{31},j_{32})}{\Delta(j_{21},j_{22},j_{23})\Delta(j_{12},j_{11},j_{13})\Delta(j_{33},j_{13},j_{23})}$$

$$\times \sum_{\tau,\mu,\nu} \frac{(-1)^{\tau+\mu+\nu}}{\tau!\mu!\nu!} \times \frac{(2j_{23}-\tau)!(2j_{11}-\nu)!}{(2j_{32}+1+\mu)!(j_{11}+j_{21}+j_{31}+1-\nu)!}$$

$$\times \frac{(j_{21}+j_{22}-j_{23}+\tau)!(j_{13}+j_{33}-j_{23}+\tau)!}{(j_{22}+j_{23}-j_{21}-\tau)!(j_{13}+j_{23}-j_{33}-\tau)!}$$

$$\times \frac{(j_{22}+j_{32}-j_{12}+\mu)!(j_{31}+j_{32}-j_{33}+\mu)!}{(j_{12}+j_{22}-j_{32}-\mu)!(j_{31}+j_{33}-j_{32}-\mu)!}$$

$$\times \frac{(j_{12}+j_{13}-j_{11}+\nu)!}{(j_{11}+j_{21}-j_{31}-\nu)!(j_{11}+j_{13}-j_{12}-\nu)!}$$

$$\times \frac{(j_{11}+j_{21}+j_{33}-j_{32}-\mu-\nu)!}{(j_{21}+j_{32}-j_{12}-j_{23}+\tau+\mu)!(j_{12}-j_{23}-j_{11}+j_{33}+\tau+\nu)!} \tag{B.29}$$

where

$$\Delta(\alpha,\beta,\gamma) = \left[\frac{(\alpha-\beta+\gamma)!(\alpha+\beta-\gamma)!(\alpha+\beta+\gamma+1)!}{(-\alpha+\beta+\gamma)!}\right]^{1/2} \tag{B.30}$$

are associated with the coefficients of unitary transformations which connect state vectors corresponding to different coupling schemes of four angular momenta. Consider an addition of four angular momenta j_1, j_2, j_3 and j_4 to form a resultant

---

[7] From reference [6].

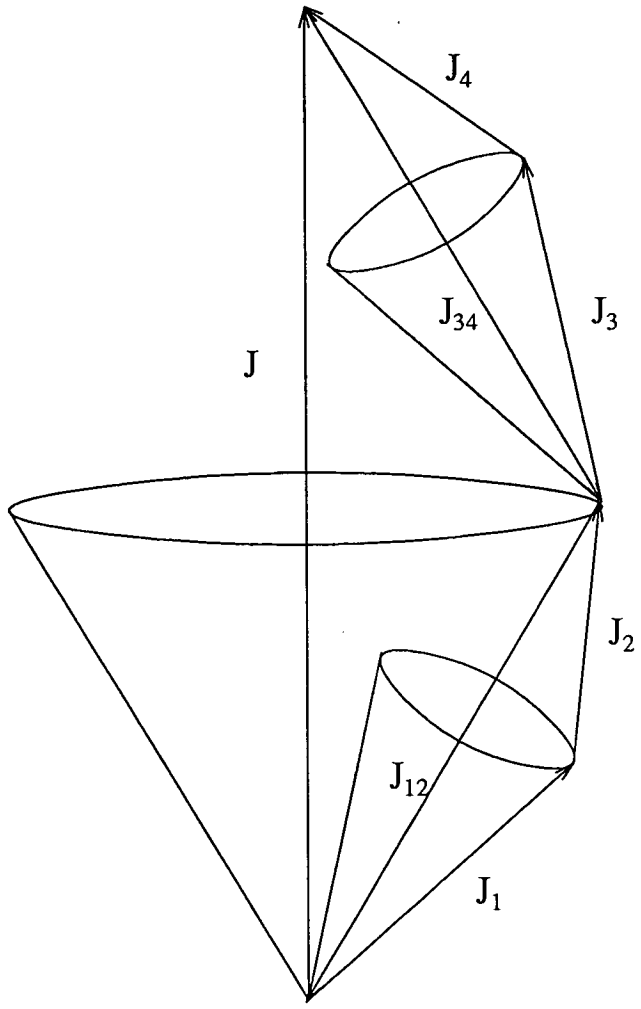

Figure B–4: Diagram showing the $j = (j_1 + j_2) + (j_3 + j_4) = j_{12} + j_{34}$ scheme for recoupling of four angular momenta

angular momentum j with projection m. There exist different coupling schemes of these angular momenta given by

$$j = (j_1 + j_2) + (j_3 + j_4) = j_{12} + j_{34} \tag{B.31}$$

$$j = (j_1 + j_3) + (j_2 + j_4) = j_{13} + j_{24} \tag{B.32}$$

$$j = (j_1 + j_4) + (j_2 + j_3) = j_{14} + j_{23} \tag{B.33}$$

The first of these coupling schemes is illustrated in figure B–4.

It should be noted that along with these coupling schemes there exist some others, e.g.

$$j = ((j_1 + j_2) + j_3) + j_4 = (j_{12} + j_3) + j_4 = j_{123} + j_4 \tag{B.34}$$

However, the coefficients of transformation which connects a state vector in this coupling scheme with vectors in coupling schemes B.31, B.32 and B.33 are related to the products of two 6j symbols rather than to the 9j symbols.

Bibliography

[1] Quantum Theory of Angular Momentum, *D. A. Varshalovich, A. N. Moskalev, V. K. Khersonskii* (World Scientific, 1988)

[2] Angular Momentum in Quantum Physics: Theory and Application, *L. C. Biedenharn, J. D. Louck* (Cambridge University Press, 1984)

[3] The Racah-Wigner Algebra in Quantum Theory, *L. C. Biedenharn, J. D. Louck* (Cambridge University Press, 1984)

[4] Mathematical Methods for Physicists, *G. Arfken* (Academic Press, 1985)

[5] Group Theory, *E. P. Wigner* (Academic Press, 1959)

[6] Angular Momentum, *R. N. Zare* (John Wiley & Sons, 1988)

Appendix C

Courses Attended

In accordance with the regulations of the Department of Chemistry, University of Edinburgh, I attended the following lecture courses and conferences during my period of study:

I) Departmental postgraduate lectures

II) 'C' programming course

III) Quantum mechanics 2

IV) Advanced quantum mechanics

V) Relativistic quantum mechanics

VI) Groups and symmetries

VII) Faraday Discussion 1991. "Structure and Dynamics of Reactive Transition States". (March 1991).

VIII) Second Annual Northern Universities Dynamics and Spectroscopy Group Meeting. (July 1991).

IX) Gas Kinetics Discussion Group of the Royal Society of Chemistry. "Reactions on Complex Potential Energy Surfaces". (January 1992).

X) European Meeting on Photons, Beams, and Chemical Dynamics. University of Paris XI Orsay. (July 1992).

In addition, all the regular departmental seminars and research group meetings were attended.